ATOMISTIC MODELLING OF NANOGRANULAR MAGNETIC MATERIALS

RICHARD FRANCIS LLEWELYN EVANS

A Thesis submitted for the degree of Doctor of Philosophy

THE UNIVERSITY of York

DEPARTMENT OF PHYSICS

JULY 2008

Abstract

The continuing development of advanced magnetic nanomaterials for electronic devices and medical applications necessitates an understanding of the origins of magnetism at the atomistic level. In this thesis current state of the art modelling methods are developed and applied to a variety of physical problems in order to better understand the origins and limitations of magnetic materials at the nanoscale. The dependence of the Curie temperature and magnetocrystalline anisotropy on the atomic level structure is shown to be significant, and can sometimes dominate the magnetic properties of nanoparticles. In particular, the addition of a silver coating to cobalt nanoparticles is shown to induce a transition of the internal crystal order to bulk-like crystal structure. A detailed investigation into the effects of Néel surface anisotropy on the magnetic properties of nanoparticles is made. This study revealed that the local atomic order at the surface can lead to radically different magnetic behaviour. A new constrained Monte Carlo modelling method is developed to enable the calculation of equilibrium properties of magnetic nanoparticles. This method is used specifically to calculate the temperature dependence of the magneto-crystalline anisotropy energy and exchange stiffness in bulk-like atomistic systems, where comparison is made to existing analytical theories. The physics of heat-assisted magnetic reversal at the nanoscale is investigated by simulation of iron-platinum nanoparticles, showing the emergence of a previously unknown elliptical reversal mechanism at temperatures close to the Curie temperature. An analytic description of the equilibrium reversal properties is formulated which describes the fundamental thermodynamic limit for heat assisted magnetic reversal. A large scale atomistic model of a heat assisted magnetic recording system is constructed to study the effects of inter-grain interactions and to assess the future feasibility of heat assisted recording in a hard disk drive.

Table of Contents

Table of Contents . . . 3

Acknowledgements . . . 9

Declaration . . . 10

1. Introduction . . . 11
- 1.1 Origins of Magnetism . . . 11
- 1.2 Motivation for Research . . . 15
- 1.3 Thesis Outline . . . 16

2. Modelling Methods . . . 18
- 2.1 Theoretical Background . . . 18
- 2.2 Classical Spin Hamiltonian . . . 19
- 2.3 Spin Dynamics . . . 22
- 2.4 Monte Carlo Methods . . . 24
- 2.5 Calculation of Atomic-Scale Parameters . . . 25
- 2.6 Atomic Scale Properties of $L1_0$ FePt . . . 26
- 2.7 Summary . . . 33

3. Computational Methods and Test Simulations . . . 34
- 3.1 Computational Methods . . . 34
- 3.2 Test Simulations . . . 37
- 3.3 Summary . . . 41

4. The Influence of Shape and Structure on the Magnetic Properties of Fe and Co Nanoparticles . . . 42
- 4.1 Modelling Methods . . . 42
- 4.2 Structural Analysis . . . 46
- 4.3 Results . . . 50
- 4.4 Conclusion . . . 56

5. The Influence of Surface Anisotropy on the Magnetic Properties of Nanoparticles . . . 57
- 5.1 Theoretical Background . . . 58
- 5.2 Results . . . 64
- 5.3 Conclusion . . . 80

6. Constrained Monte Carlo Algorithm . . . 82
- 6.1 Constraint Method . . . 82
- 6.2 Calculation of Free Energy via Restoring Torque . . . 84
- 6.3 Temperature Dependence of the Magnetocrystalline Anisotropy . . . 87
- 6.4 Temperature Scaling of the Micromagnetic Exchange Constant . . . 98
- 6.5 Conclusion . . . 105

7. An Atomistic Media Model for Tbit/in^2 Heat Assisted Magnetic Recording 106
7.1 Heat Assisted Magnetic Recording 106
7.2 Thermal Modelling 108
7.3 The Physics of Heat Assisted Magnetic Reversal 112
7.4 The HAMR Recording Process 129
7.5 The Write Process for a Single 3.5nm Grain 132
7.6 The Write Process for Media 138

Conclusions 141

Publications and Presentations 145
Published Papers 145
Papers under Preparation 145
Conference Presentations 146
Other Presentations 146

Appendix I - Code Optimisation Techniques 147
General Computational Techniques 147
Atomistic System Generation 151

References 157

List of Figures

1.1 Schematic Representation of Magnetic Spin Moments 12
1.2 Hysteresis loop for a generic magnet under an applied field 12
1.3 Illustration of thermal stability for a single domain particle 14

2.1 Visualisation of the $L1_0$ crystal structure of FePt. 27
2.2 Radial variation of effective exchange constant $\tilde{J}_{ij}$ for $L1_0$ FePt. . . . 29
2.3 Radial variation of 2-ion anisotropy energy for $L1_0$ FePt. 29
2.4 Visualisation of the exchange interactions for $L1_0$ FePt. 30
2.5 Visualisation of the Fe neighbours for the short range Hamiltonian. 31

3.1 Temperature dependence of the integration timestep 36
3.2 Hysteresis curve for single spin moment 38
3.3 Boltzmann distribution for a single spin moment 39
3.4 Effects of finite size on the Curie temperature 40

4.1 Visualisation of annealed Fe and Co nanoparticles 45
4.2 Radial variation of exchange energy in Cobalt and Iron 46
4.3 Schematic diagram of atomic spacing plots 47
4.4 Structural properties of a Co nanoparticle 48
4.5 Visualisation of a dislocation in a Co nanoparticle 48
4.6 Structural properties of a Fe nanoparticle 49
4.7 Shape dependence of T_c for Co 50
4.8 Shape dependence of T_c for Fe 51
4.9 Structure dependence of T_c for Fe 52
4.10 Structural properties of a CoAg nanoparticle 54
4.11 Visualisation of stacking order in CoAg nanoparticle 55

5.1 Visualisation of a simple cubic system with surface anisotropy . . . 60
5.2 Energy landscapes comparing uniaxial and cubic anisotropies. . . . 63
5.3 Visualisation of different particle shapes 64
5.4 Shape dependence of the energy barrier 65
5.5 Energy landscape for spherical particle for $K_{\text{Néel}} = 50K_u$ 66
5.6 Energy landscape for cubic particle for $K_{\text{Néel}} = -50K_u$ 67
5.7 Energy landscape for truncated octahedron particle for $K_{\text{Néel}} = 100K_u$ 68
5.8 Energy landscape for cubic particle for $K_{\text{Néel}} = 200K_u$ 69
5.9 Energy barriers for an elongated nanoparticle 70

5.10 Energy landscape for an elliptical particle for $K_{\text{Néel}} = 150K_u$ 71
5.11 Energy barriers for different crystal structures 72
5.12 Energy landscape for a spherical hcp particle for $K_{\text{Néel}} = -250K_u$. 73
5.13 Energy landscape for a spherical sc particle for $K_{\text{Néel}} = 95K_u$ 74
5.14 Comparison between simulation and experimental results for size scaling of the energy barrier 75
5.15 Visualisation of surface easy axes for elongated cuboid 78
5.16 Size dependence of the energy barrier for different magnitudes of K_s 80

6.1 Schematic of the torque on a spin 85
6.2 Torque curves for uniaxial anisotropy for different temperatures . . 88
6.3 Temperature dependence of uniaxial anisotropy 90
6.4 Temperature scaling of uniaxial anisotropy 91
6.5 Torque and energy curves for cubic anisotropy 92
6.6 Temperature dependence of cubic anisotropy 93
6.7 Temperature scaling of cubic anisotropy 93
6.8 Plot of normalised anisotropy energy for fcc 001 surface 95
6.9 Visualisation of thin film system 96
6.10 Temperature dependence of magnetisation and surface anisotropy for thin film 97
6.11 Temperature scaling of surface anisotropy with system magnetisation 98
6.12 Visualisation of interacting micromagnetic cells 100
6.13 Visualisation of a spin spiral 100
6.14 Visualisation of system used to calculate the exchange constant . . 102
6.15 Typical torque line for exchange scaling calculation 104
6.16 Temperature scaling of the micromagnetic exchange 105

7.1 Recording head and media arrangement 107
7.2 Visualisation of heat transfer model 110
7.3 Visualisation of thermal modelling grid dimensions 111
7.4 Spatial temperature profile for HAMR 111
7.5 Schematic plots of the different reversal modes 113
7.6 Effect of Temperature on Reversal Mechanism 115
7.7 Ultrafast reversal process above T_c 117
7.8 Snapshots of the HAMR Process for a Single Grain 118
7.9 Time dependence of the reversal success rate 120
7.10 Angular dependence of the applied and anisotropy energies 121
7.11 Angular dependence of the spin probability 122
7.12 Boltzmann Distribution for 3 nm^3 FePt Nanoparticle 123
7.13 Spin Distributions for Different Sized Particles 125

7.14 Equilibrium reversal probability for different sized FePt grains . . . 126
7.15 Blocking temperatures for different sized FePt grains 127
7.16 Reversal probability as a function of applied field strength 128
7.17 Illustration of how a granular recording media is generated 130
7.18 Grain size distribution for generated HAMR material 131
7.19 Visualisation of a single 3.5 nm FePt grain 133
7.20 Curie temperature of a 3.5 nm FePt grain 134
7.21 Coercivity of 3.5 nm FePt grain with surface anisotropy 135
7.22 Temperature and field profiles for a single grain 137
7.23 Plot of time dependence of a single grain magnetisation during HAMR 138
7.24 Final magnetisation configuration after write simulation. 139
A-1 Visualisation of integer lattice construction 151
A-2 Visualisation of simple cubic lattice 152
A-3 Visualisation of face centred cubic lattice 153
A-4 Visualisation of hexagonal close packed lattice 154

List of Tables

2.1 Table of exchange interactions for short-range FePt Hamiltonian . . 33

Acknowledgement

I would like to take this opportunity to express my thanks and gratitude to the many people who have in so many ways helped and supported me throughout my Doctoral studies.

First and foremost I would like to thank my supervisor, Roy Chantrell, without whom this work would not have been possible. He has been an inspiration and a great friend for the past three years, providing invaluable insight and constructive criticism to the research I have done. It has truly been a great pleasure and privilege to work with him on the many different areas of research, and his enthusiasm and willingness to help have allowed me develop to be a better scientist and more capable person.

I would also like to thank two other mentors who I have had the privilege of working closely with during my doctoral studies overseas: Oksana Chubykalo-Fesenko of the Institute for Materials Science, Madrid, Spain, and Pierre Asselin at Seagate Technology, Pittsburgh, PA, USA. They were both most welcoming and helpful, and provided fresh challenges and inspiration for my research.

I must also mention my coworkers at York, Denise Hinzke, Uli Nowak, Andreas Biternas, Natalia Kazantseva, and Jerome Jackson, who have always given the time to challenge ideas, help with technical and programming problems, and for providing a friendly and stimulating workplace. I am especially grateful to Denise for reading and correcting the draft thesis many times. I would also like to give special thanks to Matt Probert for the numerous occasions where he has helped overcome seemingly insurmountable programming problems, and for his help, advice and friendship throughout my studies at York.

Of course mention must also be made of the contribution of musicians who have provided assistance during writing the thesis, including but not limited to: Muse, Shooter Jennings, Metallica, Daniel O'Donnell, Run DMC, The BBC Symphony Orchestra, Creedence Clearwater Revival, and of course, the indomitable late Johnny Cash.

I would like to extend my gratitude to my parents, without whom's encouragement and guidance I would not have pursued a path in Physics. Last, but not least, I would like to thank my wife, Karen, for being so supportive of my research for the past 2 years, without whom life would not have been nearly as enjoyable.

Declaration

The author hereby declares that the following thesis is, excepting the previously acknowledged contributions, his own work. The following lists specific research which was done in collaboration with others, but is presented as part of the thesis for clarity and completeness.

The microstructural calculations of Fe and Co nanoparticles were performed by Dr. Florian Dorfbauer at the Vienna University of Technology, Austria. The calculations of surface anisotropy of nanoparticles were performed in collaboration with Dr. Oksana Chubykalo-Fesenko at the Institute for Materials Science, Madrid, Spain, forming a large body of work. The author's personal contribution to this work is that which is presented in this thesis. The constrained Monte Carlo method was developed in collaboration with Dr. Pierre Asselin at Seagate Technology, Pittsburgh, PA, USA. The simulations, testing and application of the method were all performed by the author.

The majority of the work presented in this Thesis has been shown previously at meetings and conferences by myself, and also published in a variety of scientific publications.

1. Introduction

Magnetism is a physical phenomenon first recorded around 600 BC by Greek philosophers studying ferrite rocks (lodestone). Today it is one of the most important properties of nature and is used in a multitude of technological devices from power plants to computer chips. This is largely due to the interaction of magnets with electricity, which is used to make electric motors. However, magnetic materials have, for some years now, also found a use in computers as hard disk drives. The reason for this is the huge capacity for storing digital information securely when compared to any other technology. This, however, has been the result of years worth of investment in the research and development of magnetic materials for hard disk recording. This investment has paid off since the storage capacity of typical hard drives has effectively doubled every few years since the 1980s [1]. However, a point will soon be reached where there are fundamental physical limitations on data density [2]. In order to continue increasing data density a deeper understanding of the underlying physics relating to the nanoscale is required, which is where theoretical magnetics comes into play.

1.1 Origins of Magnetism

Magnetism arises on the sub-atomic level from localised polarisation of the electron clouds of certain atoms arising from unpaired electrons. This causes the charge on the atom to have a net angular momentum. Any flow of charge causes additional physical effects on the surroundings, usually referred to as a 'magnetic' effect. In the case of atoms the net angular momentum of the charge cloud causes a magnetic field perpendicular to the rotation of the excess charge. The magnitude of this magnetic or spin moment is dependent on the species of atom [3]. How these spin moments interact with each other is critical to how different materials are characterised magnetically. When atoms are brought in proximity to each other there is a probability of an electron jumping from one atom to another, known as the Heisenberg exchange [4]. This interaction probability can indirectly couple the spin moments of the atoms, causing the spin moments to align parallel or anti-parallel. In most materials the spin moments are small and aligned randomly, leading to paramagnetism as shown in Figure. 1.1(a). In some materials however, specifically transition metals such as nickel, cobalt, and iron, the spin moments are large, and align in parallel

or ferromagnetically as shown in Figure. 1.1(b). This causes a net spontaneous magnetic moment in the material.

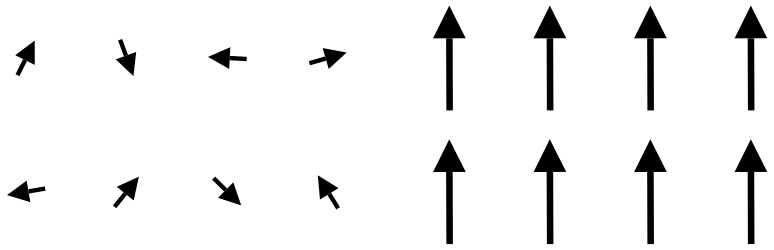

(a) Paramagnetic spin moments (b) Ferromagnetic spin moments

Figure. 1.1: Schematic Representation of Magnetic Spin Moments.

Material Magnetism

The magnetisation, $\boldsymbol{M}$, of a sample is defined by the size and direction of its net magnetic moment per unit volume. The magnitude of the magnetisation is affected by a number of factors, including atomic species, temperature, and shape of the sample. When a magnetic field, $\boldsymbol{H}$, is applied to a sample the magnetisation responds in a pattern known as a hysteresis loop, as shown in Figure. 1.2.

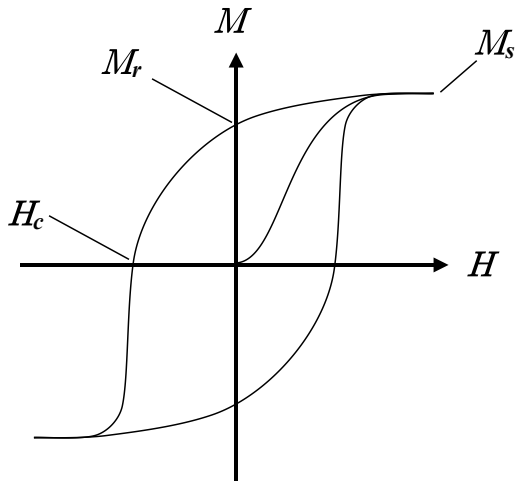

Figure. 1.2: Hysteresis loop for a generic magnet under an applied field shown as a plot of **M** vs **H**.

The critical parameters on this curve are the remanence, $\boldsymbol{M_r}$, the intrinsic coercivity, $\boldsymbol{H_c}$, and the saturation magnetisation, $\boldsymbol{M_s}$. The remanence is the magnitude of the magnetisation after an applied field is reduced to zero, the coercivity is the field required to return the magnetisation of the sample to

zero from saturation, and the saturation magnetisation is the maximum value of magnetisation and is purely dependant on the number of spin moments on the actual sample being measured. Another important feature of magnets is the effect of heating. As the temperature is increased beyond a critical point, known as the Curie temperature T_c, all ferromagnets become paramagnetic. These features, $\boldsymbol{M_r}$, $\boldsymbol{H_c}$, $\boldsymbol{M_s}$ and T_c, describe the fundamental behaviour of all magnets. Materials with a high remanence and coercivity are known as hard materials, while those with a low remanence and coercivity are denoted as soft materials.

Whenever a magnetised body exists there is always a field which attempts to oppose the magnetisation, known as the de-magnetisation field, $\boldsymbol{H_D}$. The size of this field is strongly size and shape dependent. This field leads to the idea of domains [5, 6]. A typically sized magnetic material in its natural form and in the absence of an externally applied field has no overall magnetic moment. This is because on the atomic scale moments are strongly coupled and group together to form a magnetic domain. Domains, however, are weakly coupled and as a result they can align randomly in certain materials, leading to an overall de-magnetised state. As the sizes of samples are reduced it is possible to have only a few domains. Additionally, most materials are anisotropic, meaning that the magnetisation prefers to align along particular crystal directions. This is known as the magnetocrystalline anisotropy. In these small samples the domains tend to align antiparallel in order to retain an overall magnetic moment of zero. There are a huge number of factors affecting the size of magnetic domains, but the critical point for magnetic recording is that formation of domains requires energy. For large samples it is energetically favourable to form domains, but if a particle is small enough a single-domain particle is formed.

Single Domain Particles

In a single domain particle all the atomic moments are aligned in parallel. This leads to improved magnetic characteristics, such as possessing a high coercivity and remanence, which is in turn ideal for magnetic recording. The magnetic properties of single domain particles have been described in detail by Stoner and Wohlfarth [7]. The critical parameter for single domain particles is the anisotropy, arising either from shape or magnetocrystalline effects. The uniaxial anisotropy locks the magnetic moment of the particle in one of two directions, thus making an ideal material for digital storage. The Stoner-Wohlfarth theory provides an effective basis for modelling the characteristics of conventional particulate recording media consisting of a collection of single domain particles [8].

A significant problem with very small magnetic particles of only a few nanometers in diameter, however, is their thermal stability. The thermal stability

of single domain particles is of critical importance to magnetic storage technology, since it is a key requirement that stored data persists for periods in excess of 10 years. The time dependent thermal stability of a single domain particle is described by an Arrhenius-Néel law [9, 10], and is principally dependent on the particle anisotropy and volume. As the particle volume is reduced, so is the energy barrier between stable magnetic states. This reduction in the energy barrier increases the chance that the direction of the magnetisation may reverse due to thermal fluctuations. For small nanoparticles with weak anisotropy the rapid thermal switching of nanoparticles can occur at room temperature, leading to an effect known as superparamagnetism [11]. A schematic diagram illustrating the thermal switching of a single domain particle is shown in Figure. 1.3.

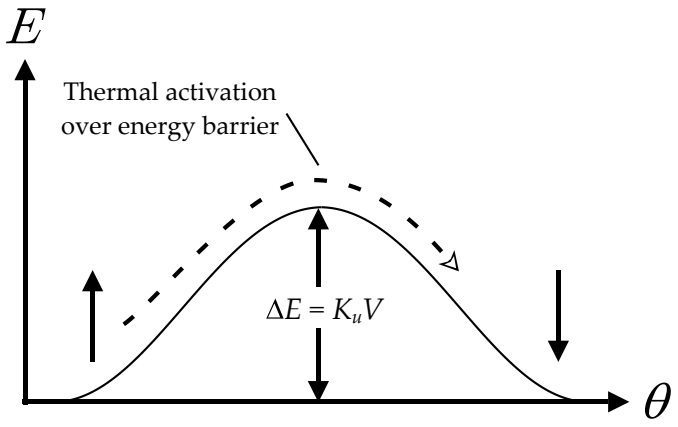

Figure. 1.3: Illustration of the anisotropy energy as a function of angle from the easy axis, θ, for a single domain particle. The plot shows that the existence of an energy barrier allows for the possibility of thermal activation.

The term superparamagnetism originates from the macroscopic behaviour of an array of particles, where in the absence of an applied field the overall magnetic moment is zero. When an external field is applied the transition rates between the two states are changed giving the material a net magnetisation, a behaviour which is similar to that of a paramagnet. In the case of magnetic data storage, thermal activation leads to a progressive loss of data. This has led to a significant amount of research into high anisotropy magnetic materials.

1.2 Motivation for Research

Magnetic Recording Media

Although magnetism has been critical to technological devices since the discovery of electricity, it was found in the late 1950's to make an excellent medium for long-term storage of digital information. Magnetic recording of digital information makes use of the ability to "flip" the direction of magnetisation in a uniaxial material. Traditionally arrays of elongated particles with a preferential easy axis were used on a thin film, but more recently the magnetocrystalline anisotropy of spherical particles has been used instead. The magnetic material is usually mounted on a circular rotating disk, allowing non-sequential access to the data on the disk. Each bit of digital data is recorded on a corresponding magnetic 'bit' on the disk. The first hard disks had only a few hundred bits on one square inch of magnetic material whereas modern disks have hundreds of billions of bits per square inch. This is more commonly referred to in terms of data density, with a disk possessing a number of Megabits (Mb) or Gigabits (Gb) per square inch. This increase in data density has been an order of magnitude per decade ever since the first disks were ever created and is achieved by decreasing the size of the bits on the disk. The main difficulty with reducing the bit size is magnetic stability [2], since at very high density each bit consists of only a few particles. This means that stray fields from nearby data bits have a much greater impact on the stored magnetic data, and the magnetisation can decay sufficiently so as to be unreadable. One solution to this is to use high anisotropy materials such as FePt [12], which help to "lock" the magnetic moment in the correct direction for a greater length of time. Another problem with increased data density is maintaining a good signal to noise ratio which is achieved by having several magnetic particles per data bit [13], typically around 50. If any one particle is incorrectly magnetised then the data is still correctly recorded and readable on the disk by the signal arising from the other particles in the data bit. A direct consequence of this is that in order to reduce the bit size, maintaining a similar signal to noise ratio requires the same number of smaller particles. To achieve the highest bit density therefore requires the use of particles of only a few nanometres in diameter, referred to as nanoparticles. This miniaturisation to the nanoscale also applies to other components used in hard disk recording such as the magnetic read and write heads.

Modelling of magnetic materials is now almost a necessity for complex components and particles such as those used in hard disks, since there are too many physical variables to reliably predict the magnetic behaviour of the system with a pencil and paper approach. The standard method of modelling magnetic

materials, known as micromagnetics [14], has been used to better understand the behaviour of magnetic materials with a large number of physical variables. Micromagnetics works by discretising the magnetic material into smaller spin components and looking at how these individual moments interact with the local physical surroundings. However, the fundamental problem when extending micromagnetics into the nanoscale is one of length scale. At some point it is more realistic to use atomic resolution as the basis of the discretisation, essentially the Heisenberg model [15]. This allows the input of ab-initio information directly into magnetic models forming a link between atomic parameters and larger systems comprising of a number of atoms. The way atomic moments interact at the nanoscale, however, can be substantially different from bulk material behaviour and this improvement in resolution allows such nanoscale magnetic systems to be modelled more effectively. For example, when looking at the process of writing magnetic data to nanoparticles on the disk the length of time and actual mechanism of magnetic reversal are very important to how fast data can be written to the disk.

Another reason for atomistic scale modelling, other than resolution, is the introduction of more complex magnetic materials. These are needed to increase the magnetocrystalline anisotropy of nanoparticles or to allow the use of bit-patterned media for example. This implies the use of magnetic materials consisting of two or more chemical elements which has a number of consequences. The Heisenberg exchange becomes much more complex in such materials, depending significantly on the particular crystal structure. Also some materials, such as platinum, are not normally magnetic and have a so-called induced spin moment arising from neighbouring ferromagnetic spins. Micromagnetics suffers significantly when calculating the Heisenberg exchange since it uses an exchange approximation which is only valid for long wavelength magnetization changes and as a result is incapable of describing multi-element materials on the nanoscale. Ultimately atomistic modelling of nanoparticles and components leads to a better understanding of their magnetic behaviour. This understanding in turn allows the focussed development of new materials and technological innovation in hard disk drives.

1.3 Thesis Outline

What follows is a general outline for the thesis. The first chapter will detail the modelling methods required to model magnetic materials at the atomistic level. This will start with a general introduction to the atomic origins of magnetism, followed by a detailed analysis of the Heisenberg model, spin dynamics and

equilibrium properties. The final section of the chapter will describe how the microscopic magnetic parameters relate to macroscopic phenomena such as the Curie temperature and coercivity, for example.

Chapter 2 will give a more technical overview of current state of the art modelling methods utilised in this thesis, including the methods used to obtain atomic-scale parameters from macroscopic material properties. Chapter 3 will then present a selection of simulation results used to test the atomistic model and also introduce some of the effects of finite size on the magnetic properties of nanoparticles.

Chapter 4 will present the first results of the thesis, describing the effects of atomic structure on the magnetic properties of cobalt, iron, and cobalt-silver core-shell nanoparticles. Chapter 5 will then extend this work to investigate the effects of surface faceting and crystal structure on the surface anisotropy of a wide variety of cobalt nanoparticles.

Chapter 6 will outline a new constrained Monte Carlo approach developed to investigate the equilibrium properties of magnetic nanoparticles, but with a physical constraint to force the system magnetisation along the desired direction. Results for the temperature dependence of the magnetocrystalline anisotropy based on this new algorithm are also presented and compared to existing theories. The method is then utilised to give the first calculations of the temperature dependence of surface anisotropy in thin films, and to calculate the temperature dependence of the micromagnetic exchange stiffness.

In Chapter 7 a detailed investigation into the physics of heat assisted magnetic reversal will be presented. This will start with a description of the new modelling methods developed to allow the investigation of the heating process by laser irradiation. Simulation results for the reversal processes for different sizes of FePt nanoparticles will then be presented, illustrating the emergence of a previously unknown elliptical reversal mechanism [16]. An analytical description of the equilibrium reversal properties for magnetic nanoparticles will then be presented, identifying the thermodynamic limits of heat assisted magnetic reversal. The final section of this chapter will describe the creation of an atomistic model of heat assisted magnetic recording (HAMR), as found in a future device. This model is then used to assess the feasibility of this promising technology at a data density in the $\mathrm{Tbit/in^2}$ regime.

The thesis will then conclude with a summary and conclusion, describing the main discoveries of the thesis and their relevance to developments in high performance magnetic nanomaterials.

2. Modelling Methods

This first chapter introduces the background to the atomistic magnetic model, which underpins the remainder of the thesis. The first section describes the fundamentals of atomic scale magnetism in the context of the Heisenberg model. The next section will address the physics of spin dynamics and thermal effects, followed by a section relating the macroscopic magnetic parameters, such as the coercivity and Curie temperature, to their atomistic equivalents. The final section will then address the formulation of an atomistic model for FePt, which is a complex magnetic material with significant potential for future technological applications.

2.1 Theoretical Background

The principal theoretical method used throughout this thesis is the atomic-scale modelling of magnetic materials using the classical limit of the Heisenberg localised spin model. The Heisenberg model describes the atomic scale exchange interaction with a local moment theory, considering the interaction between two electron spins on neighbouring atomic sites. By applying the Heitler-London approximation [17] for the linear combination of electron orbitals, Heisenberg developed a model which describes the energy of neighbouring atoms with spin [4], given by:

$$< \mathcal{H} >= -J_{ij}\tilde{\mathbf{S}}_i \cdot \tilde{\mathbf{S}}_j \tag{2.1}$$

where $\tilde{\mathbf{S}}_i$ and $\tilde{\mathbf{S}}_j$ are the quantum mechanical spins on atomic sites i and j respectively, and J_{ij} is the interaction energy arising from the probability of the two electrons exchanging atomic sites. The quantum nature of the electron spins leads to quantisation of the electron energy, which for a single spin was demonstrated by the Stern-Gerlach experiment [18]. In the above case, however, the quantum effects are far more complex due to the coupling of the electronic spin moments. In the limit of infinite spin angular momentum, the quantisation effects vanish, and the spin moments have continuous degrees of freedom. Such spins are said to be classical, leading to the classical Heisenberg spin model. It should be pointed out that there is a fundamental assumption within the Heisenberg model, namely that the electrons are localised onto the atomic sites. In general this is not the case, since the magnetic interactions arise from unpaired outer electrons, which in metals are loosely bound to the individual atomic sites.

The band theory of ferromagnetism proposed by Stoner [19] successfully explains why atoms possess non-integer spin moments by describing the exchange splitting of the spin-up and spin-down energy bands. However, the band theory reveals little about the fundamental magnetic properties due to its complexity, and so an assumption that on some, very short, timescale the local moment approximation is valid is not unreasonable, provided that it is acknowledged that in fact electrons are not confined to the atomic sites. Collectively this leads to an *effective* Heisenberg classical spin model, where the spins have some non-integer, time-averaged, value of the spin moment.

2.2 Classical Spin Hamiltonian

The Heisenberg spin model incorporates all the possible magnetic interactions into a single, convenient, formalism which can be used to investigate a myriad of magnetic phenomena at the fundamental level. The principal part of the model is forming the Spin Hamiltonian, describing the energetics of the magnetic system. Such a Hamiltonian is formed from a summation of energy contributions, E, each of which describes an interaction between an atomic spin moment, $\vec{\mu}_i$ and neighbouring moments or external magnetic fields. The Spin Hamiltonian typically takes the form:

$$\mathcal{H} = E_{\text{exchange}} + E_{\text{anisotropy}} + E_{\text{applied}} + E_{\text{dipolar}} + \text{others...} \tag{2.2}$$

Each of the individual contributions to the Hamiltonian are described in detail below. Note that it is usual in the literature to use a dimensionless normalised spin moment, $\boldsymbol{S}_i = \frac{\boldsymbol{\mu}_i}{|\mu_s|}$, where $|\mu_s|$ is the magnitude of the spin moment, and this convention is adopted for this thesis.

Exchange Energy

The dominant contribution to the Spin Hamiltonian in ferromagnetic materials comes from the internal or Weiss field, which attempts to align the atomic spin moments. The Weiss field in fact originates from the quantum mechanical exchange interaction, arising from the probability of an electron moving from one atomic site to another. The exchange interaction, as it is called, leads to very strong alignment of spin moments to their neighbours in ferromagnetic metals. The total exchange energy for each atom, i, is described by the sum over all neighbouring atomic spin moments:

$$E_{\text{exchange}} = -J_{ij} \sum_{ij} \boldsymbol{S}_i \cdot \boldsymbol{S}_j \tag{2.3}$$

where J_{ij} is the exchange interaction between the spins i and j, where $\boldsymbol{S}_i$ is the local spin moment and $\boldsymbol{S}_j$ are the spin moments of neighbouring atoms. If J_{ij} is positive (ferromagnetic), then the exchange contribution will attempt to align the spins in parallel, whereas if J_{ij} is negative (anti-ferromagnetic), then it will attempt to align the spins anti-parallel. In simple models it is possible to approximate the effects of exchange by only considering nearest neighbours with an overall exchange constant, but in reality the interaction is relatively long ranged, with ferromagnetic and anti-ferromagnetic contributions leading to an overall exchange value. For FePt, where the exchange interaction is particularly long ranged, this leads to enhanced finite size effects which cannot be properly described by an effective nearest neighbour exchange model.

Magnetocrystalline Anisotropy

One of the most basic parameters in a magnetic system is the magnetocrystalline anisotropy, namely the preference for spin moments to align with particular crystallographic axes. This arises from the effect of the local crystal environment on the spin-orbit coupling of the electron. The simplest form of anisotropy is single ion uniaxial, where the magnetic moments prefer to align along a single axis, $\boldsymbol{e}$, often called the easy axis. Such an anisotropy exists where the crystal lattice is distorted along a single axis, as in materials such as hexagonal Cobalt and $L1_0$ FePt. Indeed, recent experiments have utilised this property in an attempt to engineer a higher anisotropy in Fe_3Pt [20]. The uniaxial single ion anisotropy energy is given by:

$$E^{\text{uniaxial}}_{\text{anisotropy}} = d_e \left(\boldsymbol{S} \cdot \boldsymbol{e}\right)^2 \tag{2.4}$$

where d_e is the anisotropy energy per atom.

Another, less commonly known, form of uniaxial anisotropy energy is the 2-ion form. Unlike the single ion form described above, the 2-ion anisotropy originates from the interaction of neighbouring spins, in much the same way as the exchange interaction. The 2-ion anisotropy appears in magnetic Rare Earth alloys, where the outer electrons are weakly bound, but where the crystal structure imparts an anisotropic energy contribution to the exchange energy. This effect is described in detail in Section 2.6 for FePt, but a general form for the 2-ion anisotropy is given by:

$$E^{2-\text{ion}}_{\text{anisotropy}} = \sum_{ij} -d^e_{ij} \boldsymbol{S}_i \cdot \boldsymbol{S}_j \tag{2.5}$$

where d^e_{ij} is the local on-site 2-ion anisotropy constant, assuming an easy axis along $\boldsymbol{e}$.

Materials with a cubic crystal structure, such as Iron and Nickel, have a different form of anisotropy known as Cubic anisotropy. Cubic anisotropy is a much weaker effect than in uniaxial anisotropy, and has three principal directions which energetically are easy, hard and very hard magnetisation directions respectively. This is defined in terms of the value of the directional cosines of the spin moment relative to the cartesian axes, such that, to first order, the anisotropy energy density of a single spin is given by

$$E^{\text{cubic}}_{\text{anisotropy}} = d_2({S_x}^2{S_y}^2 + {S_x}^2{S_z}^2 + {S_y}^2{S_z}^2) \tag{2.6}$$

where d_2 is the cubic anisotropy energy per atom, and S_x,S_y, and S_z are the x,y, and z components of the spin moment respectively.

Applied Fields

Most magnetic problems involve interactions between the system and external applied fields, $\boldsymbol{H}_{\text{applied}}$. External fields can arise in many ways, for example a nearby magnetic material, or as an effective field from an electric current. In all cases the applied field energy is simply given by:

$$E_{\text{applied}} = -|\mu_s| \boldsymbol{H}_{\text{applied}} \cdot \boldsymbol{S} \tag{2.7}$$

Dipolar Fields

An important property when modelling the dynamics of ensembles of magnetic moments is the de-magnetising or dipolar field. This arises from law of continuity of flux, leading to the idea that any magnetised body will have a certain field opposing the overall magnetisation. The size of the dipolar field relates to the size and shape of the magnetic body and the separation of individual moments. In the point-dipole approximation the energy arising from the dipolar field is represented by a sum over all the moments such that:

$$E_{\text{dipolar}} = -\frac{{\mu_s}^2 \mu_o}{4\pi a^3} \sum_{i \neq j} \frac{3(\boldsymbol{S}_i \cdot \hat{\boldsymbol{r}}_{ij})(\hat{\boldsymbol{r}}_{ij} \cdot \boldsymbol{S}_j) - (\boldsymbol{S}_i \cdot \boldsymbol{S}_j)}{{r_{ij}}^3} \tag{2.8}$$

where μ_s is the magnitude of the spin moment, μ_o is the permeability of free space, a is the lattice spacing, $\hat{\boldsymbol{r}}_{ij}$ is the unit position vector between sites i and j,

and r_{ij} is the distance (in unit cells, a) between sites i and j.

Other Interactions

While the most common magnetic interactions have been described above, such a list is not comprehensive and so the possibility of other interactions within the Spin Hamiltonian has been included. These other interactions can arise from a range of phenomena, such as incorporating implicitly the magnetic effects of atomic vibrations, or special forms of anisotropy such as surface anisotropy which is utilised in Chapter 5.

2.3 Spin Dynamics

While the spin Hamiltonian describes the energetics of the magnetic system, it provides no information regarding its time evolution. The first understanding of spin dynamics came from ferromagnetic resonance experiments, where the time dependent behaviour of macroscopic magnetic spin moments is described by the Torque equation derived by Lifshitz and Landau [21]. The damping parameter in the Landau-Lifshitz equation has a linear relationship with the relaxation rate. Subsequently Gilbert introduced a critical damping parameter, with a maximum effective damping for $\alpha = 1$, to arrive at the Landau-Lifshitz-Gilbert equation [22]. It should be noted that although this equation was originally derived from the motion of macroscopic spin moments, the same equation can also be derived from the quantum mechanical formulation of the Heisenberg model under an applied field [23].

The Landau-Lifshitz-Gilbert Equation

The time dependent motion of atomic spin moments is described by the Landau-Liftshitz-Gilbert equation (LLG), which, in its modern form, is given by:

$$\frac{\partial \boldsymbol{S}}{\partial t} = -\frac{\gamma}{(1+\alpha^2)}[\boldsymbol{S} \times \boldsymbol{H}_{\text{eff}} + \alpha \boldsymbol{S} \times (\boldsymbol{S} \times \boldsymbol{H}_{\text{eff}})] \tag{2.9}$$

where $\boldsymbol{S}$ is the normalised magnetic spin moment, γ is the gyromagnetic ratio, α is the Gilbert damping parameter, and $\boldsymbol{H}_{\text{eff}}$ is the net magnetic field. The LLG equation describes the interaction of an atomic spin moment with an effective magnetic field, which is obtained from the negative first derivative of the complete spin Hamiltonian, such that:

$$\boldsymbol{H}_{\text{eff}} = -\frac{\partial \mathcal{H}}{\partial \boldsymbol{S}} \tag{2.10}$$

The LLG equation has two distinct parts, the first part, $\boldsymbol{S} \times \boldsymbol{H}_{\text{eff}}$ induces spin precession around the net field direction $\boldsymbol{H}_{\text{eff}}$, while the second, $\alpha \boldsymbol{S} \times (\boldsymbol{S} \times \boldsymbol{H}_{\text{eff}})$ describes spin relaxation towards $\boldsymbol{H}_{\text{eff}}$. The phenomenological damping constant, α, determines the rate of relaxation towards the net field direction, representing the coupling of the spin system to a heat bath. As the spin system is excited the precession is damped, eventually leading the spin to align with the net field direction. The physical origin of the damping comes from a range of different atomic scale phenomena, including lattice vibrations and electron-spin interactions, although a full theoretical understanding of its origin is still lacking. Critical damping, where $\alpha = 1$, aligns the spin moment in the shortest possible time, while most real magnetic materials have a damping constant in the range $0.01 - 0.1$. It should be noted that there is, as yet, no first principles derivation of the damping constant and at present it can only be measured directly from experiment [24].

Langevin Dynamics

In its standard form the LLG equation is strictly only applicable to simulations at zero temperature. The effects of temperature are taken into account by using Langevin Dynamics, an approach developed by Brown [25]. The basic idea behind Langevin Dynamics is to assume that the thermal fluctuations can be represented by a Gaussian white noise term. As the temperature is increased, the width of the Gaussian distribution increases, thus representing stronger thermal fluctuations. In reality the thermal and magnetic fluctuations are correlated at the atomic level, arising from the Coulomb interactions of the atoms. New approaches such as coloured noise [26] and combined magnetic and molecular dynamics simulations [27] aim to better understand the underlying physics of the thermal interactions at the atomic level.

Nevertheless the established Langevin Dynamics method is used throughout the thesis and incorporates an effective thermal "field" into the LLG equation to simulate thermal effects [28]. The magnitude of the thermal field in each spatial dimension is represented by a gaussian distribution with a mean of zero and a variance given by:

$$\sigma = \sqrt{\frac{2k_B T \alpha}{\gamma \mu_s \Delta t}} \tag{2.11}$$

where k_B is the Boltzmann constant, T is the system temperature in Kelvin, α is the damping parameter, γ is the absolute value of the gyromagnetic ratio, μ_s is the magnitude of the spin moment, and Δt is the integration time step [29].

While spin dynamics are particularly useful for obtaining dynamic information about the magnetic properties, such as magnetic reversal, they are often not the

most efficient method for determining the equilibrium properties for a system. A better method, known as Monte Carlo simulation, is described in the next section.

2.4 Monte Carlo Methods

Monte Carlo Metropolis algorithms are an excellent way to study the energetics of a physical system under equilibrium conditions [30, 31]. The basic idea is to make an adjustment to a physical system and calculate the change in energy, ΔE. This change is then accepted or rejected in relation to the Boltzmann distribution for the system given the temperature. In the case of a classical spin model a single spin is speculatively moved in space and the difference in energy is evaluated. The move is then accepted with probability $\mathcal{P}$ according to

$$\mathcal{P} = \max\left(1, \exp\left[-\frac{\Delta E}{k_B T}\right]\right) \tag{2.12}$$

where k_B is the Boltzmann constant, and T is the absolute temperature. When using Monte Carlo algorithms the manner in which a trial move is made is important since it must obey the principle of detailed balance [32]. For a simple Monte Carlo algorithm, this principle is satisfied if the trial steps are uniformly random on the unit sphere. An efficient computational method for such a move was devised by Marsaglia [33]. The Marsaglia method is efficient for high temperatures since the uniform distribution of trial points gives a good sampling of the phase space. For low temperatures, however, only moves which have a small change in energy will be accepted. Due to the exchange energy this generally requires a small angular change in the spin moment direction. Since only a small fraction of moves are small angles with the Marsaglia method, a tuned step size will be a far more efficient at low temperatures.

Tuned Gaussian Trial Step

One method of improving the Monte Carlo algorithm efficiency is to use a tuned Gaussian step. This method ensures a uniform distribution of points but allows the angular displacement of the spin moments to be tuned to the temperature. A trial step, S', is made from the initial spin position, S by:

$$S'_\alpha = S_\alpha + \delta_\alpha \tag{2.13}$$

where $\alpha = x, y, z$ and δ_α is a Gaussian random number with a mean of zero and width σ where σ is a function of temperature. The new trial spin position is then normalised to unit length [34]. The width of the Gaussian distribution is chosen

so that the acceptance rate for Monte Carlo moves is around 50%, which leads to an optimal sampling of the phase space.

2.5 Calculation of Atomic-Scale Parameters

In order that atomistic models represent real materials as closely as possible, parameters from the atomistic model must be derived from experimental data or ab-initio calculations. To illustrate this, the process of obtaining a spin Hamiltonian for Co, a common magnetic element, is outlined below.

Material Parameters

The principal interaction in the classical spin Hamiltonian is the exchange energy, J_{ij}, which defines the temperature of the magnetic phase transition, or Curie temperature. Using the Curie-Weiss mean field model [5, 6], it is possible to relate the total exchange energy per atom to the Curie temperature by the expression:

$$\sum_{ij} J_{ij} = \frac{3k_B T_c}{\varepsilon} \tag{2.14}$$

where k_B is the Boltzmann constant and ε is an interaction constant which is equal to 1 in the mean-field model (where all interactions are equal in size) and less than one for increasingly localised interactions. For a *2D* Ising model $\varepsilon \approx 0.66$ while for a *3D* Heisenberg model $\varepsilon \approx 0.86$. Once the total exchange energy is found it must then be divided between neighbouring atoms. The actual distribution and range of the exchange interaction can only be found by ab-initio calculations, however an approximation that the interaction is uniformly confined to nearest neighbours only is a reasonable approximation for cobalt. Cobalt has either a face-centred cubic (fcc) or hexagonal (hcp) crystal structure, both of which have 12 nearest neighbours. Assuming an isotropic distribution of the exchange energy, and an experimental Curie temperature of $\sim$ 1390 K, this gives a J_{ij} of 5.6 $\times 10^{-21}$ Joules/link.

The magnitude of the uniaxial anisotropy constant, d_{atomic}, is derived from material parameters, using the expression

$$d_{\text{atomic}} = \frac{K_1 M_{\text{atomic}}}{\rho N_A} \tag{2.15}$$

where K_1 is the anisotropy energy density, M_{atomic} is the atomic mass, ρ is the density, and N_A is Avogadro's number. For Cobalt this yields a value of 4.644 $\times$ 10^{-24} J.

Another parameter in the LLG equation requiring ab-initio information is the magnitude of the spin moment, $|\mu_s|$. In general $|\mu_s|$ is atomic species dependent and arises from the resultant orbital angular momentum of electrons in the outer shells of the atom. Strongly magnetic materials have spin moments of the order of a Bohr magneton, μ_B, for example Cobalt has an average spin moment of ~ 1.4 Bohr magnetons. This is approximated in this model by assuming a time averaged value of the spin moment, μ_s, though in reality its magnitude can vary slightly on very short timescales due to its electronic origin. One situation where there are significant changes in the size of the spin moment is at the surface of nanoparticles, where typically the spin moment becomes much larger [35]. While the enhancement of surface spin moments can be significant for very small systems, it is generally neglected due to the complexity in determining its actual size, though it is intended that future work might incorporate a variable spin moment into the atomistic model. Generally the bulk magnetic spin moment is used for all calculations.

In order to demonstrate that these atomistic parameters lead to the correct macroscopic behaviour, such as the correct Curie temperature and coercivity, test simulations for cobalt are presented in Chapter. 3. Although the above methods work well for generic modelling of magnetic materials, some materials have more complicated Hamiltonians which have specific effects on the macroscopic material parameters, particularly at elevated temperatures. The next section describes one such material, where the atomistic parameters are taken directly from ab-initio calculations.

2.6 Atomic Scale Properties of $L1_0$ FePt

For the most part, magnetic materials used in technological applications today are alloys containing one of the three principal magnetic elements, Fe, Co, and Ni. Alloyed magnetic materials develop complex characteristics due to the interactions with non-magnetic elements. These can range from magnetic nanoparticles which are oxidised on the surface, to alloyed thin films containing a wide variety of elemental ingredients. Accurately modelling such materials presents a significant number of challenges due to the close relationship between local atomic structure and the magnetic properties [36]. In order to understand the properties of complex magnetic materials other modelling approaches, such as the use of ab-initio calculations, are required. Due to the computational effort required for such calculations, it is usual to make a number of physical assumptions, such as the material having a fixed periodic atomic crystal structure. Nevertheless it is possible to extract a significant amount of information about the

magnetic properties, such as the exchange interactions and magnetic anisotropy. Using these parameters it is then possible to model the spin dynamics and much larger problems using the atomic-scale magnetic model.

FePt is a material which has received a lot of attention from the magnetics research community due to its exceptionally high magnetocrystalline anisotropy of around 10^7 Joules/m^3 [12]. Because of this high anisotropy, FePt potentially has a particular application in future magnetic recording media, since it is the anisotropy which determines the thermal stability of written information. For FePt to possess this property, however, it must have an alternating Fe-Pt-Fe-Pt layered structure known as $L1_0$. A visualisation of this structure is shown in Figure. 2.1.

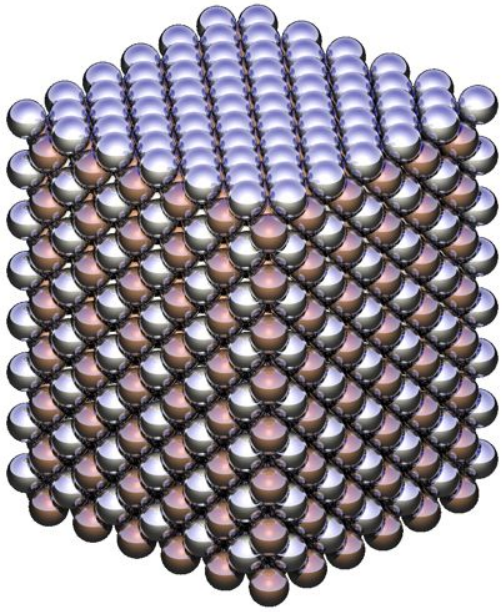

Figure. 2.1: Visualisation of the $L1_0$ crystal structure of FePt. Grey spheres represent the Pt sites, while the brown spheres represent the Fe sites. The layered nature of the crystal stacking gives $L1_0$ FePt its exceptionally high anisotropy.

Ab-initio calculations of the $L1_0$ phase of FePt by Mryasov et al [37] show that the Iron moments (i) are reasonably well localised, while the Platinum moments (ν) are delocalised. This presents a problem for the Heisenberg model since it assumes that moments are localised to the atomic sites. However, the ab-initio calculations also show that the Fe moments polarise the Pt moments, so that the effective Platinum moment, $\boldsymbol{m}_\nu$, can be expressed in terms of the surrounding Fe moments, given by:

$$\boldsymbol{m}_\nu = \frac{\chi_\nu}{M_\nu^0} \sum_i J_{i\nu} \boldsymbol{S}_i \tag{2.16}$$

where χ_ν is the local Pt susceptibility, M_ν^0 is the local Pt saturation magnetisation,

$J_{i\nu}$ is the Fe-Pt exchange interaction, and $\boldsymbol{S}_i$ is the Fe moment. With the above expression for the Pt moment it is then possible to construct an effective Hamiltonian consisting of the localised and delocalised moments of the form:

$$\mathcal{H} = -\sum_{i\neq j} J_{ij}\boldsymbol{S}_i \cdot \boldsymbol{S}_j - \sum_i k_{\mathrm{Fe}} \left[\boldsymbol{S}_i^z\right]^2 - \sum_\nu \tilde{I}\boldsymbol{m}_\nu^2 - \sum_\nu k_{\mathrm{Pt}} \left[\boldsymbol{m}_\nu^z\right]^2 \tag{2.17}$$

where respectively J_{ij} and $\tilde{I}$ are the Fe-Fe and Pt-Pt exchange interactions, and k_{Fe} = -0.097 meV and k_{Pt} = 1.427 meV are the Fe and Pt anisotropy constants. Since the Pt moment can be described in terms of the Fe moments, a reduction of equation 2.17 purely in terms of the Fe degrees of freedom can be made, and is given by:

$$\mathcal{H} = -\sum_{i\neq j} \tilde{J}_{ij}\boldsymbol{S}_i \cdot \boldsymbol{S}_j - d_i^z \left(\boldsymbol{S}_i^z\right)^2 - \sum_{i\neq j} d_{ij}^z \boldsymbol{S}_i^z \boldsymbol{S}_j^z \tag{2.18}$$

where $\tilde{J}_{ij} = J_{ij} + \tilde{I}\left(\frac{\chi_\nu}{M_\nu^0}\right)^2 \sum_\nu J_{i\nu}J_{j\nu}$ is the effective Fe-Fe exchange constant, and d_i and d_{ij} are the effective single-ion and two-ion anisotropy constants, given by:

$$d_i^z = k_{\mathrm{Fe}} + k_{\mathrm{Pt}}\left(\frac{\chi_\nu}{M_\nu^0}\right)^2 \sum_\nu J_{i\nu}^2 \tag{2.19}$$

and

$$d_{ij}^z = k_{\mathrm{Pt}}\left(\frac{\chi_\nu}{M_\nu^0}\right)^2 \sum_\nu J_{i\nu}J_{j\nu} \tag{2.20}$$

respectively. This reduced effective spin Hamiltonian clearly shows the effect of the delocalised moments on the overall magnetic properties for FePt, by inducing a 2-ion anisotropy which depends on the effective Fe-Pt exchange interaction, $J_{i\nu}$. It is this 2-ion anisotropy which forms the dominant part of the overall macroscopic anisotropy constant, since the single-ion anisotropy is approximately ten times weaker and in fact easy plane. For computational efficiency one usually includes the two-ion anisotropy term into the exchange interaction, forming an anisotropic exchange. In this form of the Hamiltonian in vector components becomes:

$$\begin{aligned}
\mathcal{H}_x &= -\sum_{i\neq j} \tilde{J}_{ij}\boldsymbol{S}_i^x \cdot \boldsymbol{S}_j^x \\
\mathcal{H}_y &= -\sum_{i\neq j} \tilde{J}_{ij}\boldsymbol{S}_i^y \cdot \boldsymbol{S}_j^y \\
\mathcal{H}_z &= -\sum_{i\neq j} \left[\tilde{J}_{ij} - d_{ij}^z\right] \boldsymbol{S}_i^z \cdot \boldsymbol{S}_j^z - d_i^z \left(\boldsymbol{S}_i^z\right)^2
\end{aligned} \tag{2.21}$$

One characteristic shown by the ab-initio calculations is that the magnetic interactions are long-ranged, with each Fe moment having over 1000 interactions with neighbouring moments, as illustrated in Figures. 2.2 and 2.3. A visualisation of the exchange interactions within an Fe-plane, as shown in Figure. 2.4, show that they are also highly anisotropic, though symmetric around the crystal planes. The complex long-ranged nature of the exchange energy makes computing the magnetic properties of FePt with the atomistic model very slow, even when using computational techniques such as Fast Fourier Transform (FFT) to calculate the long range interactions [38]. While this is not a problem for small systems, it prohibits the simulation of large problems. In the next section, an attempt will be made to express the core physics of the full FePt model described above in terms of a shorter ranged, truncated Hamiltonian with fewer interactions between the Fe moments. This allows the computation of much larger problems without significant loss of accuracy.

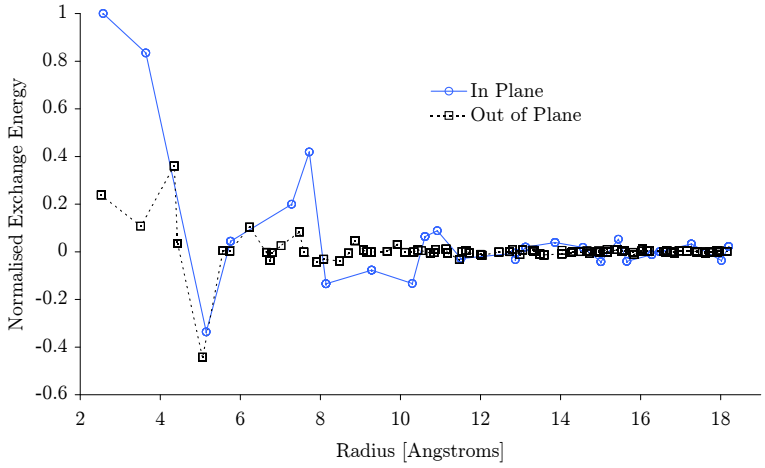

Figure. 2.2: Plot of normalised effective exchange constant $\tilde{J}_{ij}$ vs radius [Å] for $L1_0$ FePt.

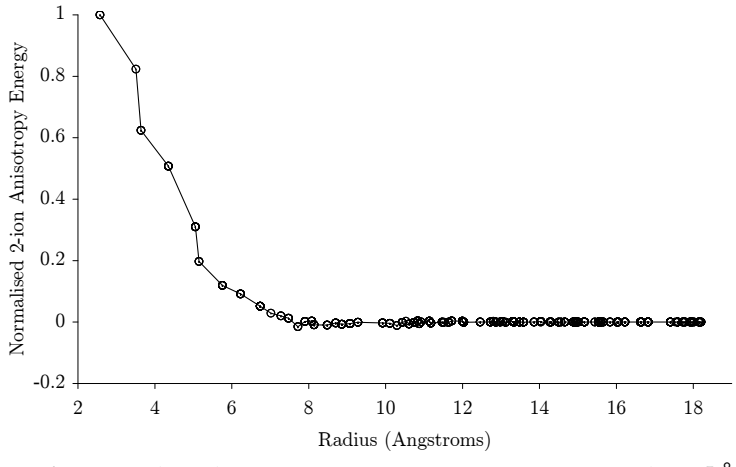

Figure. 2.3: Plot of normalised 2-ion anisotropy energy vs radius [Å] for $L1_0$ FePt.

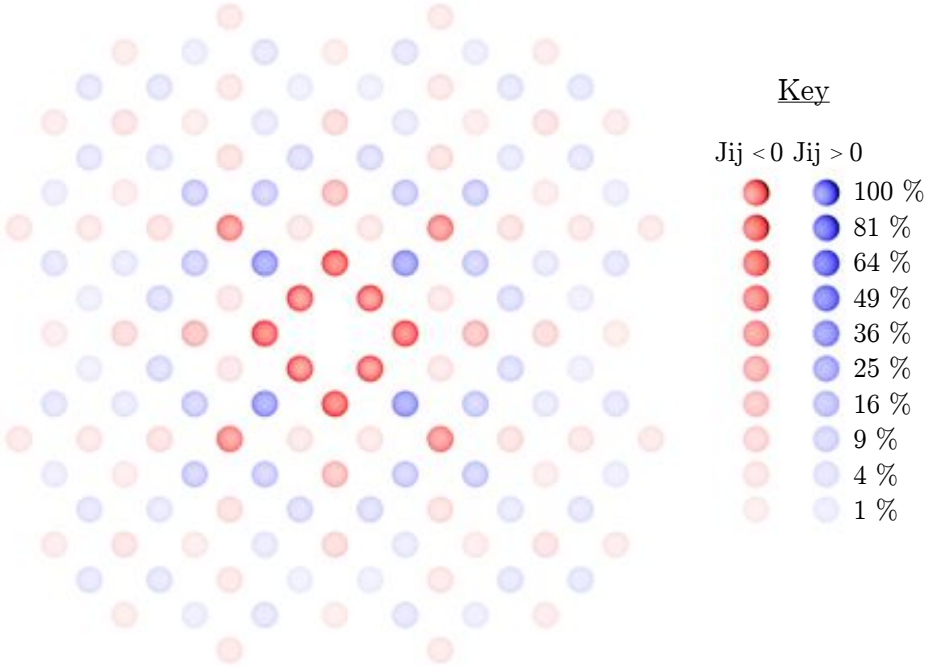

Figure. 2.4: Visualisation of the exchange interactions in $L1_0$ showing the anisotropic nature of the interaction. Red spheres represent ferromagnetic interactions, while the blue spheres represent the anti-ferromagnetic interactions. The colour depth shows the relative strength of the interactions as indicated in the key.

Short-range Spin Hamiltonian for FePt

Due to the computational complexity of the full FePt Hamiltonian, a new truncated Hamiltonian has been developed to enable the simulation of much larger systems, or systems requiring extensive statistics. This new truncated Hamiltonian is utilised in Chapter 7 to investigate the physics of Heat Assisted Magnetic Recording (HAMR). In order to achieve the best approximation, the truncated Hamiltonian is derived directly from the full range version calculated from ab-initio calculations. This aims to preserve the bulk properties of FePt, such as the Curie temperature and anisotropic nature of the exchange energy. Although the magnetic interactions are long ranged, the strength of the interactions decreases exponentially with distance, and so a short range Hamiltonian in principle should be a good approximation.

A Hamiltonian incorporating 26 nearest neighbours has been adopted, where the values of the exchange constants are chosen initially from the original Hamiltonian. A visualisation of these neighbours for the fcc lattice is shown in Figure. 2.5. Due to the slight compression of the lattice along the z-direction,

there are five unique neighbours, each indicated by the different colouring and each with a different exchange interaction, J.

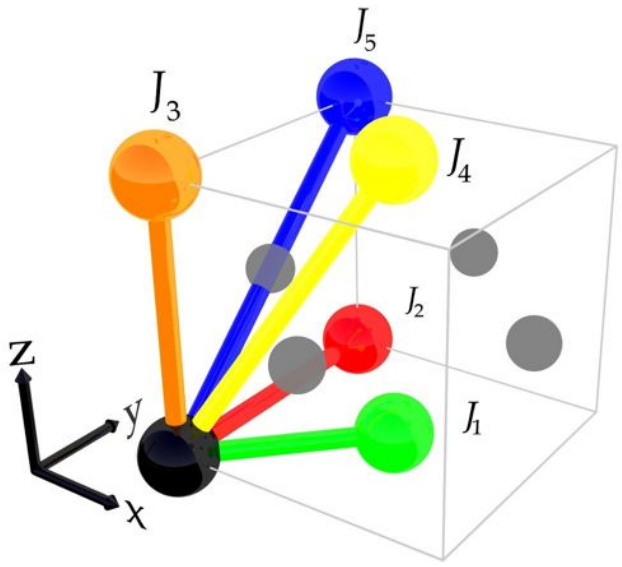

Figure. 2.5: Visualisation of the Fe neighbours for the short range Hamiltonian for FePt, showing the five unique neighbours with different colouring. The Pt atoms are indicated in grey but are incorporated into the effective hamiltonian utilising only the Fe degrees of freedom. Each of the five neighbours have an associated effective exchange interaction, J.

These 26 interactions form around 80% of the total strength of the exchange interactions which define the Curie temperature of the material. In order for the short range Hamiltonian to maintain the correct bulk Curie temperature of 750K the remaining exchange energy must be distributed between the 26 neighbours. There are a number of alternative methods for determining the distribution of this remainder between the 26 neighbours, such as an even distribution, a weighted distribution or some other scheme. A characteristic of the full FePt Hamiltonian is the anisotropic nature of the micromagnetic exchange constant, A [39].

In order to preserve the spatial anisotropy in the exchange energy the remaining exchange energy is distributed so that both the full and short-range Hamiltonians have the same anisotropic micromagnetic exchange constants. The directional component of the micromagnetic exchange constant, $\boldsymbol{A}_\alpha$, is given by a sum over all the exchange interactions between atoms i and j:

$$\boldsymbol{A}_\alpha = \sum J_{ij} \frac{|\boldsymbol{r}_{ij_\alpha}|}{|r_{ij}|} \tag{2.22}$$

where α is the dimension in Cartesian coordinates, J_{ij} is the exchange energy, $|r_{ij}|$ is the distance between atoms i and j, and $\boldsymbol{r}_{ij_\alpha}$ is the vector component of r_{ij} along

α. For the full FePt Hamiltonian, A_α is calculated numerically as a direct sum over all atoms.

For the short range Hamiltonian, however, the small number of interactions means that the individual contributions to the micromagnetic exchange can be evaluated as:

$$A_\alpha^{\text{short-range}} = a_1^\alpha J_1 + a_2^\alpha J_2 + a_3^\alpha J_3 + a_4^\alpha J_4 + a_5^\alpha J_5 \tag{2.23}$$

where a_n^α is the fractional contribution of the nth exchange interaction, J_n, to the micromagnetic exchange, A. Each of the atomistic exchange constants above refer to interactions with atoms which lie along different crystallographic axes. This means that along the principal x,y, and z axes, each exchange value contributes differently to the anisotropic micromagnetic exchange. These contributions, a_n^α, are evaluated numerically for the $L1_0$ crystal phase.

In the first instance, all interactions in the short-range Hamiltonian are set to the same value as they would have in the full Hamiltonian, meaning that the interactions will have some initial contribution to the micromagnetic exchange constant. So in order to have a good approximation to the full range Hamiltonian, the following condition is required:

$$A_\alpha^{\text{full}} = A_\alpha^{\text{sr}} + \Delta A_\alpha^{\text{sr}} \tag{2.24}$$

where A_α^{full} is the α-contribution to the micromagnetic exchange for the full Hamiltonian, A_α^{sr} is the contribution of the nearest neighbour interactions in the short-range (sr) Hamiltonian, and $\Delta A_\alpha^{\text{sr}}$ is the remaining contribution of the nearest neighbour interactions in the short-range Hamiltonian. Thus we arrive at an expression for the remaining contribution to the micromagnetic exchange in the short-range FePt Hamiltonian of:

$$\Delta A_\alpha^{\text{sr}} = a_1^\alpha \Delta J_1 + a_2^\alpha \Delta J_2 + a_3^\alpha \Delta J_3 + a_4^\alpha \Delta J_4 + a_5^\alpha \Delta J_5 \tag{2.25}$$

A similar equation also exists for the remainder of all exchange interactions, $\Delta \sum_{ij} J_{ij}$, which is given by:

$$\Delta \sum_{ij} J_{ij} = n_1 \Delta J_1 + n_2 \Delta J_2 + n_3 \Delta J_3 + n_4 \Delta J_4 + n_5 \Delta J_5 \tag{2.26}$$

where $n_{1,2,...5}$ are the number of neighbours of each type. Here the summation of the atomistic exchange energy is scalar, and so the contributions of each exchange energy is known simply from the number of neighbours.

If it is assumed that the first two exchange contributions, J_1 and J_2 are

unchanged from their usual value from the full Hamiltonian, then by setting ΔJ_1 and ΔJ_2 to zero, equations 2.25 and 2.26 can be solved simultaneously to give the exchange parameters shown in Table. 2.1. These total exchange energy coefficients are related to the atomic positions as shown in Figure. 2.5 and result in a short-range Hamiltonian with the correct Curie temperature and reasonable value for the micromagnetic exchange constant, A.

Constant	$n_{\text{neighbours}}$	x	y	z	Exchange Energy (10^{-21} Joules)
J_1	$n_1 = 4$	± 1	± 1	0	-1.7809570580
J_2	$n_2 = 4$	$\pm 2, 0$	$0, \pm 2$	0	-1.4866740680
J_3	$n_3 = 2$	0	0	± 2	0.01200762678
J_4	$n_4 = 8$	± 1	± 1	± 2	-0.6068754807
J_5	$n_5 = 8$	$\pm 2, 0$	$0, \pm 2$	± 2	-0.0075810829

Table. 2.1: Table of exchange interactions for short-range FePt Hamiltonian

This truncated FePt Hamiltonian is utilised in Chapter 7 to investigate heat assisted reversal, where its macroscopic properties such as Curie temperature and coercivity are investigated in detail to ensure good agreement with the full range Hamiltonian.

2.7 Summary

This chapter has covered in detail the current modelling methods used to simulate magnetic materials on the atomic level, including Langevin Dynamics, Monte Carlo methods and the determination of atomistic parameters. In particular an approximation to the full FePt Hamiltonian has been developed in order to reduce the computational effort required to simulate this technologically important material. In the next chapter these methods will be tested to ensure that both the atomic scale parameters exhibit the correct macroscopic magnetic properties, such as coercivity and Curie Temperature, and that the methods yield the correct behaviour. These results will also be compared to the established Stoner-Wohlfarth model for single domain particles, as described previously in the Introduction.

3. Computational Methods and Test Simulations

In order to investigate the magnetic properties on the atomic scale, one must resort to using fast computers, since the complexity of the atomistic model makes the analytical solution intractable, except for 1 and 2-spin systems. Most atomic scale systems of interest include thousands of atoms and so advanced computational techniques are needed to investigate their magnetic properties. In this chapter these techniques are outlined and then applied to test systems of Cobalt. This serves to test the atomistic material parameters and the correctness of the computer code by comparison with known results and macroscopic magnetic properties, such as the Curie temperature.

3.1 Computational Methods

The first section of this chapter illustrates the computational approaches used to model magnetic materials on the atomic scale, including how the particles are generated and time integration using the Heun scheme.

Atomistic System Generation

In order to effectively model real materials it is important to recreate their crystal structures. Since the work in this thesis primarily relates to small particles, different shapes and sizes of particles needed to be created. This was achieved by writing a stand-alone program capable of creating any required particles of a predefined size, shape, and crystal structure. Many examples of these particles are shown in later sections of the thesis. A method for generating materials with different crystal structures and also a fast neighbour list method are presented in the Appendix.

Time Integration of the LLG Equation

In order to solve the LLG equation, as given by Equation. 2.9, numerically, it is necessary to perform some form of discretised time integration. The most basic time integration scheme is the Euler method [40], which assumes a linear change in the spin direction in a single discretised time step, Δt. An improved integration scheme, known as the Heun method [41], allows the use of larger time steps

because of its use of a predictor-corrector algorithm. The first (predictor) step calculates the new spin direction, $\boldsymbol{S}'$, by performing a standard Euler integration step, given by:

$$\boldsymbol{S}' = \left(-\frac{\gamma}{(1+\alpha^2)} [\boldsymbol{S} \times \boldsymbol{H}_{\text{eff}} + \alpha \boldsymbol{S} \times (\boldsymbol{S} \times \boldsymbol{H}_{\text{eff}})] \right) \Delta t \tag{3.1}$$

The second (corrector) step then uses the predicted spin position to calculate the final spin position, resulting in a complete integration step given by:

$$\boldsymbol{S}\left(t + \Delta t\right) = \boldsymbol{S}(t) + \frac{1}{2}\left[\Delta \boldsymbol{S}(\boldsymbol{S}, t) + \Delta \boldsymbol{S}(\boldsymbol{S}', t + \Delta t)\right] \Delta t \tag{3.2}$$

where

$$\Delta \boldsymbol{S}(\boldsymbol{S}, t) = -\frac{\gamma}{(1+\alpha^2)} [\boldsymbol{S} \times \boldsymbol{H}_{\text{eff}} + \alpha \boldsymbol{S} \times (\boldsymbol{S} \times \boldsymbol{H}_{\text{eff}})] \tag{3.3}$$

The integration is performed on every spin in the system to make one complete time step. This is then repeated many times so that the time evolution of the system can be simulated. As discussed in the previous chapter, the effective field, $\boldsymbol{H}_{\text{eff}}$, includes the effective thermal field as well as contributions from the spin Hamiltonian. Although the Heun scheme was derived specifically for a stochastic equation with multiplicative noise, in the absence of the noise term the Heun method reduces to a standard second order Runge-Kutta method [42]. Consequently the Heun method is used throughout the thesis for all time integration of the LLG equation.

One point not yet discussed is the appropriate choice of timestep, Δt. Ideally one would like to use the largest time step possible so as to simulate systems for the longest time. However, in order to maintain the precessional nature of the LLG equation, the time step is fundamentally related to the size of the effective field, H_{eff}. For large fields the precession frequency is large, and so a small time step is required. Since the exchange is by far the largest interaction in an atomistic system, it dominates the effective field. Unfortunately this limits the timestep to a maximum value of around 1 femtosecond (10^{-15} s) to allow for correct integration of the LLG equation. In order to ascertain the maximum allowable timestep, plots of the equilibrium magnetisation as a function of the timestep for different temperatures are plotted in Figure. 3.1 for a generic material of 30,000 spins with a Curie temperature of 700K and for $\alpha = 1$.

The plots show that for small timesteps and low temperatures, the equilibrium magnetisation remains roughly constant until $\Delta t \sim 5 \times 10^{-15}$. For larger timesteps the Heun scheme begins to break down causing a reduction in the equilibrium magnetisation. It is interesting to note the effect of different timesteps near the Curie temperature of 700K. Here the Heun scheme breaks down at lower

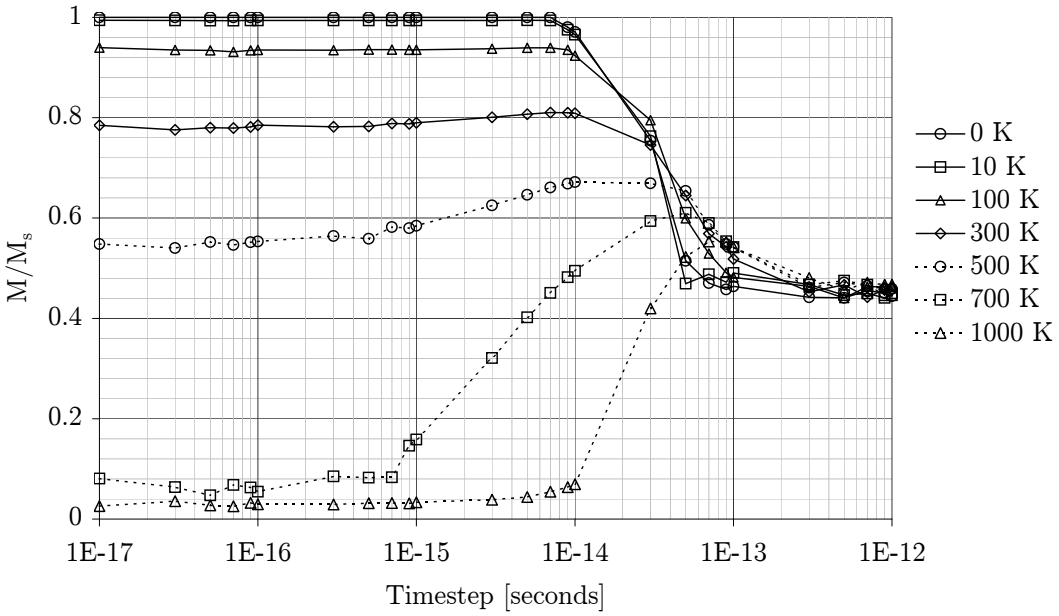

Figure. 3.1: Plot of equilibrium magnetisation vs timestep, showing the divergence of the integration timestep near the Curie temperature of 700K. For simulations near T_c a minimum timestep of 5.0×10^{-16} s is needed to yield the correct solution of the LLG equation.

timesteps, leading to a higher than expected equilibrium magnetisation. Thus for temperatures close to T_c a timestep of around 5×10^{-16} is required to ensure the stability of the integration scheme. At higher temperatures the behaviour of the Heun scheme is similar to that at low temperatures, and larger timesteps are permissible.

Random Number Generators

Another important consideration for computer simulation is the generation of "random" numbers. These are required for simulations at finite temperature in order to generate the random thermal fields for the LLG equation or random trial spin positions for the Monte Carlo algorithm. The main difficulty with computers, of course, is that they are designed to consistently generate predictable results and as a consequence a truly random number is impossible to achieve. Therefore algorithms have been developed to generate a sequence of so-called *pseudo-random* numbers, producing either a binomial, uniform or Gaussian distribution of numbers between between 0 and 1. A critical parameter with these pseudo-random numbers is the period, i.e. the number of numbers in the generated sequence before the series repeats itself. The main difficultly with these algorithms is ensuring they are sufficiently "random" and don't produce sequences of correlated numbers. A long sequence of random numbers is needed

and so a recently developed algorithm called the Mersenne Twister [43] with a period of $2^{19937} - 1$ is used instead of the intrinsic generators included with the programming language.

3.2 Test Simulations

Having outlined the methods for the computational simulation of atomistic magnetic materials, the following section will apply these methods to a test system of Cobalt. The initial tests will investigate the properties of a single isolated spin moment with anisotropy, looking at the solution of the LLG equation for an external field and for different temperatures. The later tests will calculate the Curie temperature for a range of different Cobalt nanoparticles.

Angular variation of the Coercivity

The first test involves calculating the angular variation of the coercivity, or reversing field, of a single spin moment under the action of an external field. A significant amount of theoretical work has been done on the magnetic properties of single-domain particles and a key characteristic is the angular variation of the coercivity [7]. Although the theory was derived for particles, it applies equally well to single atoms, although the simulation is somewhat artificial. Nevertheless such a simulation serves to test the static solution for the LLG equation. For a single isolated Cobalt atom in an external field, the Hamiltonian is given by:

$$\mathcal{H} = d_z S_z^2 + \boldsymbol{S} \cdot \boldsymbol{H}_{\text{applied}} \tag{3.4}$$

where d_z is the on-site uniaxial anisotropy constant and $\boldsymbol{H}_{\text{applied}}$ is the external applied field vector. The spin is initialised pointing along the applied field direction, and then the LLG equation is solved for the system, until $\boldsymbol{S} \cdot \boldsymbol{H}_{\text{eff}} \leq 0.0001$ The field strength is then decreased in steps of 0.01 Tesla and solved again for the same condition. This generates a hysteresis loop showing the response of the spin moment to the external field. When the external field is applied along the anisotropy axis (z-axis), the anisotropy and applied fields act along the same direction, producing a square hysteresis loop. When an angle ϕ is set between the field and anisotropy directions the fields begin to compete, leading to a reduction in the coercivity. A plot of the resulting $M - H$ curve for a single spin at zero K is plotted in Figure. 3.2.

The $M - H$ hysteresis curve conforms exactly to the Stoner-Wohlfarth solution, showing a 50% reduction in the coercivity for the applied field at an angle of 45° to the easy axis, and no coercivity for $\phi = 90°$.

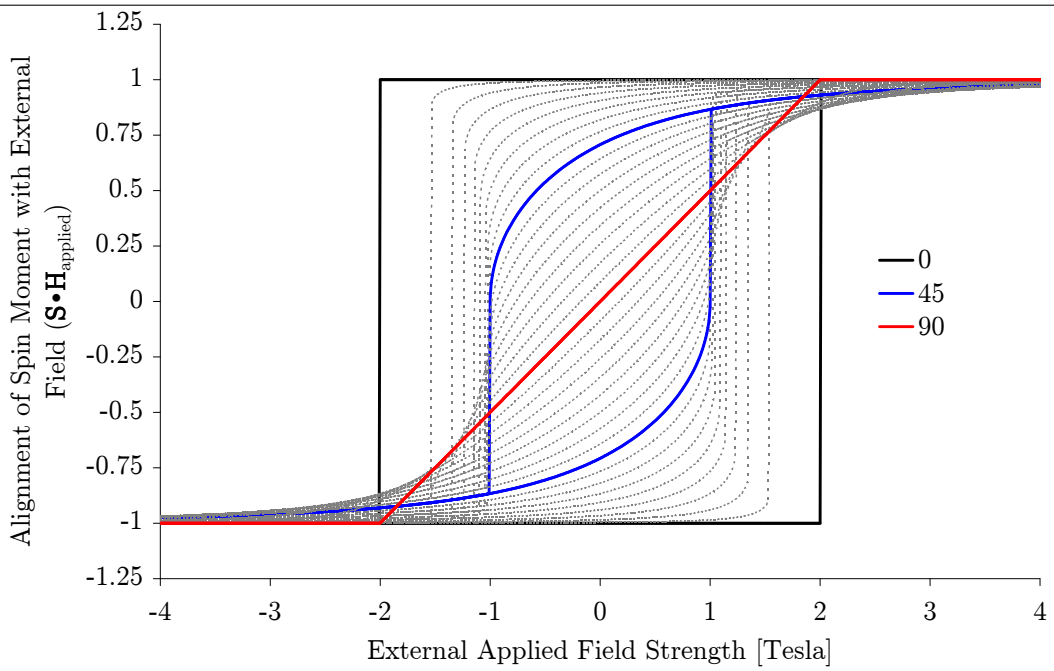

Figure. 3.2: Plot of M vs H for different angles of H (degrees) from the easy axis for a single spin moment.

Boltzmann Distribution for a Single Spin

To quantitatively test the thermal effects in the model, the probability of the spin moment lying at a certain angle from the easy axis in a system with uniaxial anisotropy was investigated. The distribution is characteristic of the temperature and the anisotropy energy and in the form of a Boltzmann distribution, given by:

$$P(\theta) \propto \sin(\theta) \exp\left(\frac{E(\theta)}{k_B T}\right) \propto \sin(\theta) \exp\left(\frac{d_z \sin^2(\theta)}{k_B T}\right) \tag{3.5}$$

where θ is the angle from the easy axis, d_z is the on-site atomistic anisotropy constant, k_B is the Boltzmann constant, and T is the absolute temperature. The $\sin(\theta)$ weighting normalises the probability to the surface area of the unit sphere. For the calculations the spin was initialised pointing in the easy axis direction and the system was allowed to evolve for 10^8 timesteps after equilibration, recording the angle of the spin to the easy axis each time. Since the anisotropy energy is known to be symmetric along the hard axis, the probability distribution is reflected and summed about the 90^o point to improve the statistics. For low temperatures the spin never leaves the initial spin direction and so the reflection of the probability distribution allows the full Boltzmann probability to be seen. Figure. 3.3 shows the normalised probability of the spin being at a particular angle from the easy axis as a function of angle from the easy axis for 3 different temperatures.

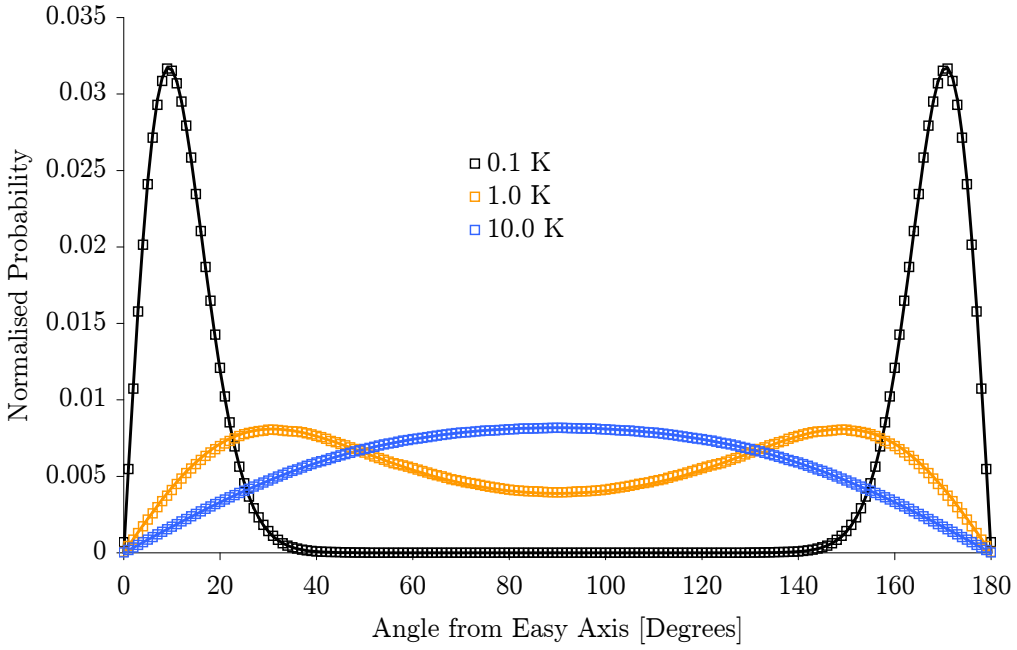

Figure. 3.3: Plots of the probability of the spin moment lying at an angle θ to the easy axis vs θ for different temperatures. The fits to equation 3.5 are shown by the solid lines.

As can be seen, at a temperature of 0.1 K the spin moment is confined entirely to small angles from the easy axis. As the temperature is increased the distribution is broader, showing superparamagnetic behaviour as the spin flips between the two anisotropy directions. This is seen by the finite probability of the spin lying along the hard axis. At a higher temperature the spin has sufficient thermal energy to overcome the anisotropy energy and as a result the distribution is flat on the unit sphere. The fits to equation 3.5 show excellent agreement with the theory.

Curie Temperature

Although the above tests confirm the behaviour of isolated moments, all real systems consist of an ensemble of spins connected by the interatomic exchange interaction. The Curie temperature of a particle is dominated by the strength of the exchange interaction between spins and so made an ideal test. For Cobalt the expected Curie temperature is around 1390 K. However, this is only for a bulk system with an infinite volume to surface ratio. Since it is impossible to simulate such a system, bulk like systems are modelled using a reasonably large system ($\sim 10^5$ spins) with periodic boundary conditions. This eliminates the surface effects due to missing exchange links, and minimises the effect of small system size, known generally as finite size effects. However, the increasing areal

density of hard disk drives requires smaller and smaller magnetic grains, where eventually the effects of finite size become important. In order to investigate the effect of system size on the Curie temperature, the equilibrium magnetisation for different sizes of truncated octahedron nanoparticles was calculated as a function of temperature. For comparison a 32,000 atom cube with periodic boundary conditions was also simulated in order to approximate a bulk-like system. The simulations were performed by initialising the spin moments along the +z-direction. A Monte Carlo algorithm was then used to find the equilibrium magnetisation as a function of temperature. The temperature was increased in 25 K increments and 20,000 Monte Carlo steps were calculated for each temperature. The system was allowed to equilibrate for the first 5000 steps, after which a snapshot of the magnetisation was sampled every three steps. The reason for only taking one snapshot in three is that the usual statistical methods assume that all samples taken of a variable are random. However, it is likely that snapshots from sequential Monte Carlo steps are correlated, and so only one in three snapshots is used to gather the statistics. Each of these samples of the magnetisation is then added to a running total which is averaged at the end to find the mean equilibrium magnetisation for a given temperature. A snapshot of the system spin configuration is then used as the starting point for the next temperature in order to minimise the equilibration time from one temperature to another. The results of these simulations are plotted in Figure. 3.4.

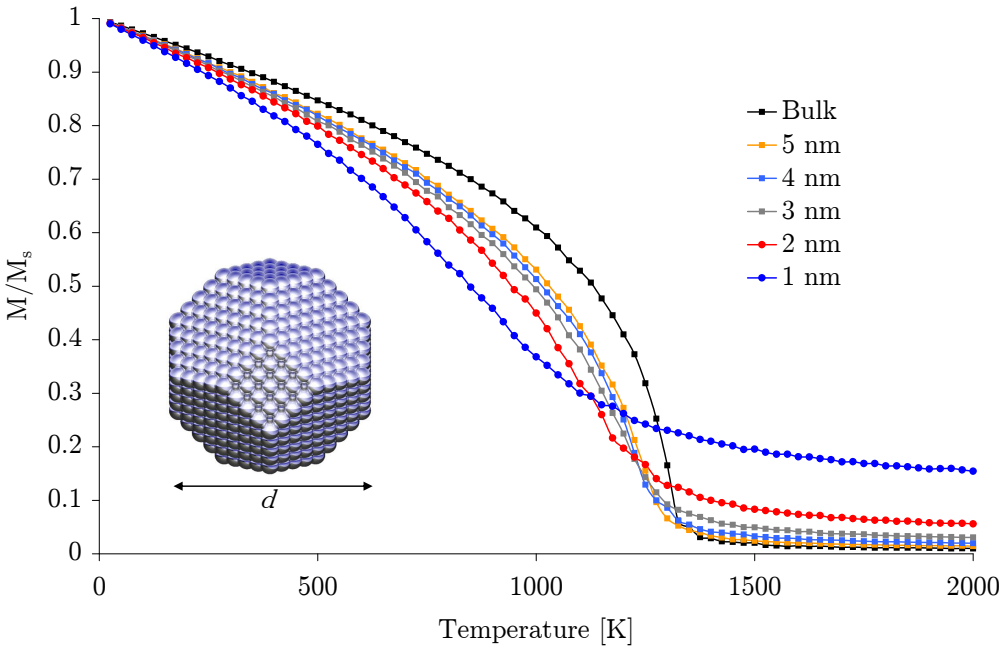

Figure. 3.4: Plots of the equilibrium magnetisation M/M_s as a function of temperature for different sized truncated octahedral Cobalt particles. A visualisation of a 3nm particle is inset.

The first point to note is the data for the bulk-like simulation for a large cube of Cobalt with periodic boundary conditions, showing a Curie temperature of around 1375 K, which is very close to the expected value of 1390 K. For the 5 nm diameter particle, the principal effect of the surface is to reduce the *criticality* of the temperature dependence of the magnetisation. This effect has been studied in detail by Binder et al [44], and arises due to the reduction in atomic coordination number at the particle surface. However, the Curie temperature for the 5 nm particle remains close to that of the bulk value. For the 3 and 4 nm diameter particles, the criticality of the curve is reduced, but for the 1 and 2 nm diameter particles another effect appears; namely a persistent magnetisation above the expected Curie temperature. This effect is distinguishable from the surface effect of the reduction in the criticality, and arises due to the (small) finite size of the system. The persistent magnetisation can be described by considering any two magnetic moments from the system. For a truly bulk system above T_c, it is possible to find a pair of moments which are aligned anti-parallel, due to the effectively infinite number of available spins. This means that above T_c, in the absence of an applied field, a bulk system will have zero net magnetisation. For a finite sized system, however, there is a probability that at any instant all moments are not perfectly aligned, leading to a persistent magnetisation above T_c. However, this persistent magnetisation is disordered, in so much as the correlations in spin direction are correlated only in space, not in time.

3.3 Summary

In this chapter the methods and models described in Chapter 2 have been applied to a single spin and ensembles of spins to test the correctness of their implementation, and to discern the underlying physics of the atomistic model. The remainder of the thesis will apply these methods to a variety of different problems and situations, to further our understanding of magnetism at the atomic level. The next Chapter will start with an investigation into the effects of atomic structure on the magnetic properties of Co and Fe nanoparticles.

4. The Influence of Shape and Structure on the Magnetic Properties of Fe and Co Nanoparticles

Materials at the nanoscale behave differently from the bulk form due to their finite size and surface effects. One example of such an effect was demonstrated in the previous chapter, with the smallest particles showing a persistent magnetic ordering above the Curie temperature. Physical effects due to the size of particles are broadly given the name of finite size effects, while surface effects are dealt with separately. Characterising and understanding these effects is important as the use of nanomaterials becomes more widespread, especially in the development of future materials for magnetic recording. When modelling nanomaterials it is usually assumed that their fundamental properties are the same as those of the same material in bulk form. Since the size range of nanomaterials is quite large (anything up to a few hundred nanometres), this approximation is justifiable for most nanomaterials. For the smallest of nanomaterials, however, the finite size, and particularly surface effects, begin to play a very important role in their magnetic properties.

In this chapter the effects of surface and finite size on the magnetic properties of small nanoparticles will be investigated. The challenge with understanding these effects is taking into account changes to the atomic structure due to the small size and large surface to volume ratio. This was achieved by generating simulated annealed Co and Fe nanoparticles using a molecular dynamics approach, provided by collaboration with Florian Dorfbauer at the Technical University of Vienna, Austria. The first part of this chapter describes the new theoretical approaches developed to model particles with a non-bulk atomic microstructure. The structural effects of the surface and finite size of the annealed nanoparticle are then described in detail, finally followed by various magnetic results, showing a change in the Curie temperature.

4.1 Modelling Methods

In order to obtain realistic particle shapes molecular dynamic annealing of the particles was performed. The basic idea behind molecular dynamics is to simulate the motion of atoms with classical equations of motion using an

assumed interatomic potential. For certain elements, such as Argon, the interatomic potential can be well approximated by the Lennard-Jones potential[45]. However, simple pair-potentials, like Lennard-Jones potentials, are unable to reproduce certain specific properties of metals, such as elastic constants. Therefore a more complicated method known as the Embedded Atom Method (EAM) was utilized [46] to create the microstructures. The main idea of EAM is to consider each atom as being an impurity in the host with an additional energy term dependent on the surrounding electron density. The total energy of the system is given by:

$$E = \frac{1}{2} \sum_{i,j,i \neq j} \phi_{ij}(r_{ij}) + \sum_{i} F_i(\rho_{i,host}), \tag{4.1}$$

where Φ_{ij} denotes the short range, double screened electrostatic interaction between the cores i and j; $F_i(\rho)$ is the energy related with the embedding of atom i in the host; and $\rho_{i,host}$ is just the sum over all electronic densities of all other atoms at the position of atom i,

$$\rho_{i,host} = \sum_{j \neq i} \rho_{j,atom}(r_{ij}). \tag{4.2}$$

A well-established set of EAM-potentials was used to model the interatomic interactions. The employed potentials were fitted to bulk properties like lattice constants, elastic constants, vacancy free energies and heats of solution [47].

The time evolution of the atomic system was computed using a velocity Verlet algorithm, which shows a much better stability and time-reversability than a conventional Euler integration scheme. The instantaneous atomic positions are used to compute the forces on the atoms which are then moved according to the velocity Verlet algorithm[48].

One problem with molecular dynamics is controlling the temperature of the system so that the atomic structures can be cooled. One basic method of controlling the temperature is to perform velocity scaling, since the temperature of the system is related to the kinetic energy of the atoms. Velocity scaling works by simply changing the length of the velocity vector so that the thermal energy equates to the correct temperature. However, this leads to incorrect thermal statistics. A much better method of controlling the temperature comes from assuming a heat bath in thermal equilibrium with the system, more commonly known as a Nosé-Hoover (NH) thermostat [49]. The NH thermostat works by assuming that there is a thermal reservoir, with an effective fictitious mass, Q, in thermal equilibrium with the system. The total Hamiltonian for a system with the NH thermostat is given by:

$$L_{Nosé} = \sum_{i=1}^{N} \frac{m_i}{2} s^2 \dot{r_i}^2 - U(r_1, r_2, ...r_N) + \left(\frac{Q}{2}\right)\left(\frac{ds}{dt}\right)^2 - (f+1)k_B T \ln s \qquad (4.3)$$

where m_i is the mass of atom i, $\dot{r}_i$ is the instantaneous velocity, $U(r)$ is some distance dependent interatomic potential, f is the number of degrees of freedom of the system (typically 3N), and s is a dynamical variable. The evolution of s is governed by $\dot{s} = \frac{sp_i}{Q}$, where p_i is the momentum of the system. The effect of s is to effectively re-scale time during the simulation, since the time evolution of the system depends on the total Hamiltonian in equation 4.3 above. The size of the fictitious mass, Q, is an adjustable parameter in the NH thermostat. If Q is too large then the flow of energy between the reservoir and the system is very slow, resulting in slow equilibration of the system to the desired temperature. If Q is too small then unphysical oscillations in the system energy appear, making equilibration difficult. Generally the size of Q is taken to be some multiple of fk_BT found by trial and error for the specific system being modelled. The temperature of the thermostat can be freely controlled and thus heat is then transferred to the molecular dynamic system.

The desired number of atoms (672 for Cobalt and 432 for Iron) was initialised in a perfect crystal structure and then successively cooled through the ordering temperature to produce a low temperature ordered state. Because of the small size of the cluster, typically only a few hundred atoms, the final structure is quite different to that of the bulk form. As can be seen in Figure. 4.1, the annealed particles show faceting on the outer surface due to the surface structural optimisation, which is not present in bulk microstructure particles.

The dynamic magnetic calculations were performed largely using the methods described above in Chapter 2. To investigate the effects of particle shape on the Curie temperature, the variation of the magnetisation with temperature was simulated for particles with a perfect crystal structure, being body centred cubic (bcc) for Fe and hexagonal close packed (hcp) for Co, with spherical and cubic particle shapes. For comparison, similar calculations were also performed for annealed particles with a static low temperature atomic configuration, which determines the sole effect of the geometric arrangement of atoms in the particle.

The spin moments are initialised pointing in the easy axis direction, i.e. an ideal zero temperature configuration. The temperature was then increased in 20K steps in keeping with the molecular dynamic calculations, and the system was equilibrated before taking time-averaged measurements of the mean magnetization of the particle. The system was then reset and the simulation repeated 500 times to calculate the average magnetization and the standard

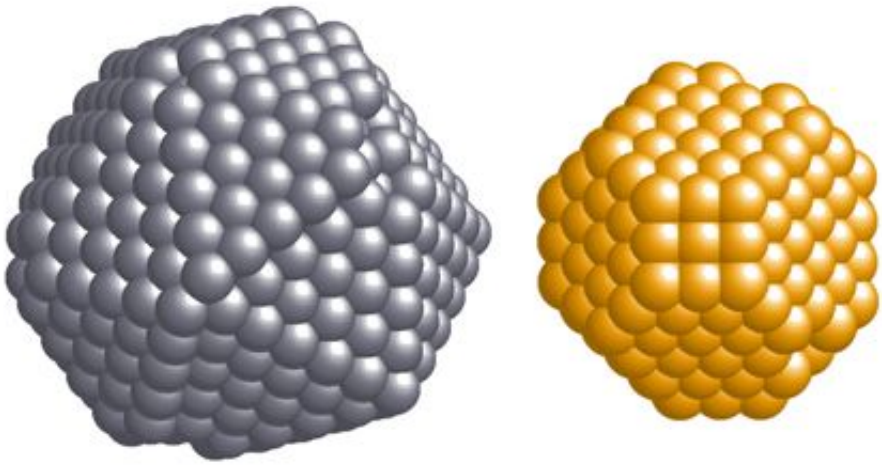

Figure. 4.1: Visualisation of simulated annealed 672 atom Co [left] and 432 atom Fe [right] nanoparticles, showing the different types of faceting induced for the different materials. The Co particle shows icosahedral like faceting, while the Fe particle shows truncated octahedral faceting.

error. During the annealing process the structure of the particle changes significantly and so additionally the variation of magnetization with temperature was calculated for the dynamic particle as well, at each temperature step incorporating any structural changes following from the Molecular Dynamic calculations, and by default any corresponding changes in exchange energy. The main difficulty in performing the dynamic simulations for the annealed particles is calculating the Heisenberg exchange energy between neighbouring atoms, since the particles no longer have a perfect bulk structure for which the exchange constants are known. The exchange interaction also varies considerably with atomic separation, and subtly in different crystallographic directions. As a result it was necessary to find a functional variation of exchange energy with atomic separation. Such ab-initio calculations have been described by Pajda et al [50]. Due to the complexity in calculating the exchange energy the calculations performed by Pajda et al were for a perfect crystal and the values quoted were along specific crystallographic directions. However, there were insufficient data points to allow the Ruderman-Kittel-Kasuya-Yosida (RKKY) - type interaction function to be reliably fitted to the data, since the curve has a different form along different crystallographic directions. As an approximation a polynomial fit to the data was used as shown in Figure. 4.2, approximating the magnitude of the exchange but neglecting any anisotropic directional variation.

For dynamic magnetic simulations in Cobalt it is the usual convention to include only nearest atomic neighbours when calculating exchange energy. However, as Figure. 4.2 shows, there are significant contributions to the Heisenberg

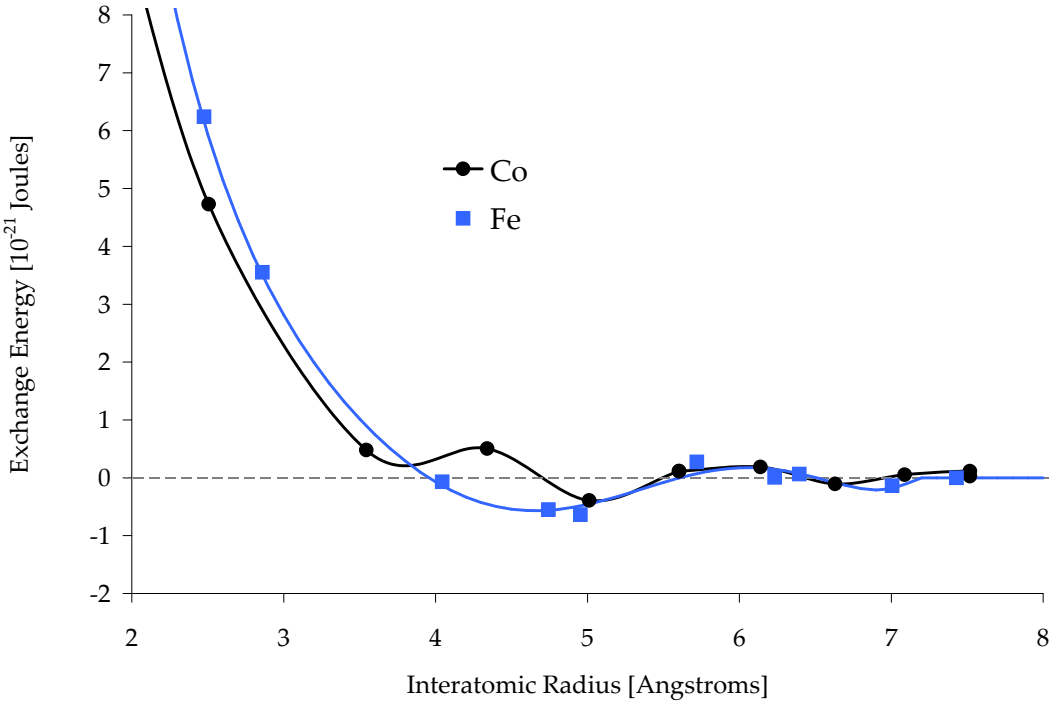

Figure. 4.2: Plot of the site-to-site exchange energy for Cobalt and Iron as a function of interatomic separation. The points correspond to those calculated by Pajda et al [50], while the solid line indicates the fitted polynomial functions. Values above zero show ferromagnetic interactions, while values below indicate anti-ferromagnetic interactions. It can be seen that both interactions for Fe and Co are long ranged, although beyond an interatomic separation of 6 Åthey become less significant.

exchange up to fourth nearest neighbours. For completeness all the calculations performed used the full range of the interaction. Another problem arises from thermal fluctuations in the positions of the atoms in the particle, even though the particle structure is notionally 'frozen'. For a given snapshot of atomic positions, the atoms are not in an instantaneous equilibrium state due to the finite temperature of the system. In order to take account of this, several snapshots of the atomic structure were taken for each temperature. All the magnetic calculations were repeated for each of these different structures and averaged, effectively eliminating any artifacts introduced by using only a single snapshot of the atomic structure.

4.2 Structural Analysis

Having found a satisfactory method of approximating the Heisenberg exchange, the influence of the annealing process on the structural properties of the nanoparticles

was investigated. To observe any expansion or relaxation of the interatomic spacing, a plot of the mean atomic spacing of an atom from its nearest neighbours as a function of its radial distance from the centre of the particle is shown below in Figure. 4.4 for Co and Figure. 4.6 for Fe. Before going on to analyse the results, it is appropriate to explain why the data is plotted in this way. Figure. 4.3 shows a schematic diagram of the data plotted. First consider a target atom coloured in blue, where the distance from the centre of the particle, r, is indicated by the black arrow. The blue atom has 6 nearest neighbours, coloured in red. The atomic separation distance, a, is totalled for all the nearest neighbours. This is done for all atoms in the particle, showing any compression or expansion in the mean atomic spacing as a function of the radial distance from the centre.

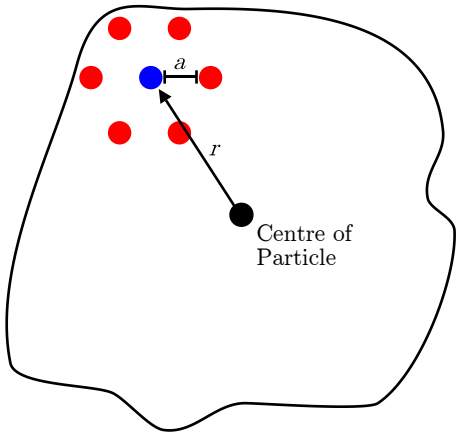

Figure. 4.3: Schematic diagram of atomic spacing plots. The target atom (in blue) has 6 nearest neighbours (in red) and lies at a distance r from the centre of the particle. The interatomic distance, a, is averaged over all the nearest neighbours, showing any compression or expansion of the lattice as a function of radial distance from the centre of the particle.

The first point to note is the extent of the scatter in the mean atomic spacing in Figure. 4.4, clearly showing thermal fluctuations in the interatomic spacing. The dark lines represent the weighted mean of the points. In the case of the 672 atom Co particle, there is a reduction in the mean atomic spacing near both the centre and surface of the particle. This reduction indicates a region of compression when compared to a bulk interatomic spacing of $\sim$ 2.507 Å. The compression at the surface of nanoparticles has previously been reported in ab-initio calculations [51] and arises from the reduction in coordination number at the surface. Due to the long range nature of the interatomic potential, surface atoms feel a net attractive force towards the centre of the particle, which induces a reduction in the mean atomic spacing.

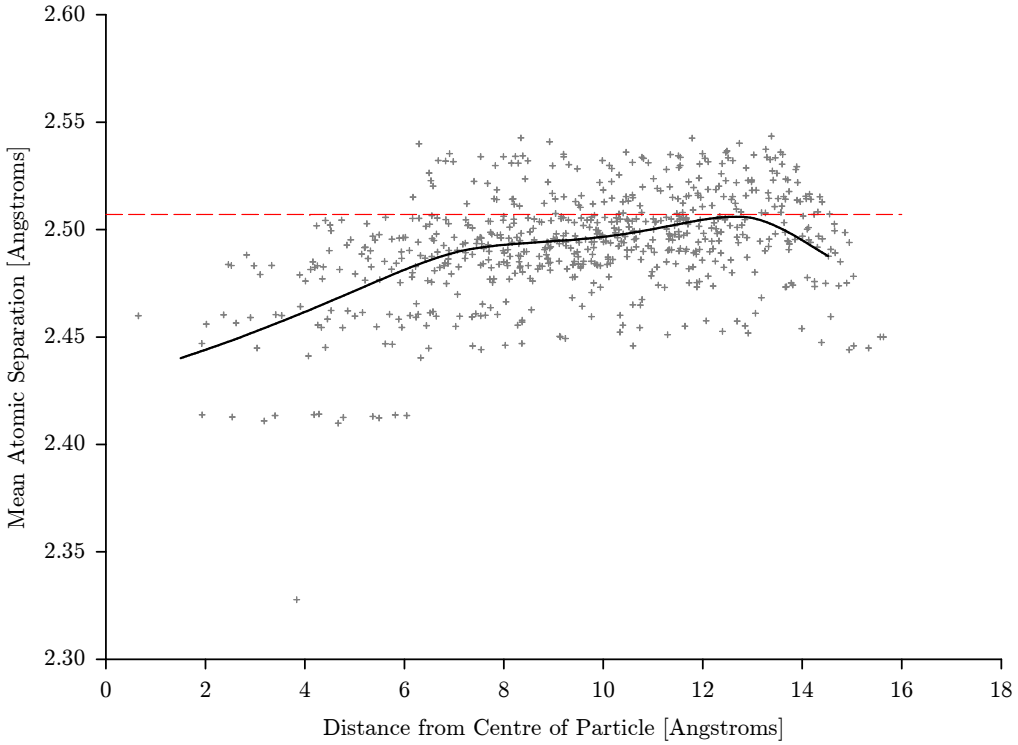

Figure. 4.4: Plot of mean interatomic separation as a function of radial distance from the centre for a 672 atom Co particle. The black line is a guide to the eye, while the dashed red line indicates the interatomic spacing for bulk Cobalt. The graph shows compressions in the mean atomic spacing at the surface and in the centre due to a dislocation in the crystal structure.

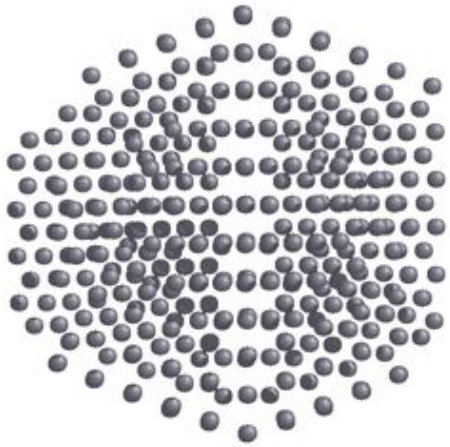

Figure. 4.5: A transparent visualisation of the 672 atom Co particle showing the screw defect thought to be responsible for the compression towards the centre of the particle.

The compression towards the centre of the Co particle is thought to be due to a visible dislocation in the atomic structure, as shown in Figure. 4.5. The dislocation appears to show a low density region, which, as with the surface, induces a compression of the mean atomic spacing.

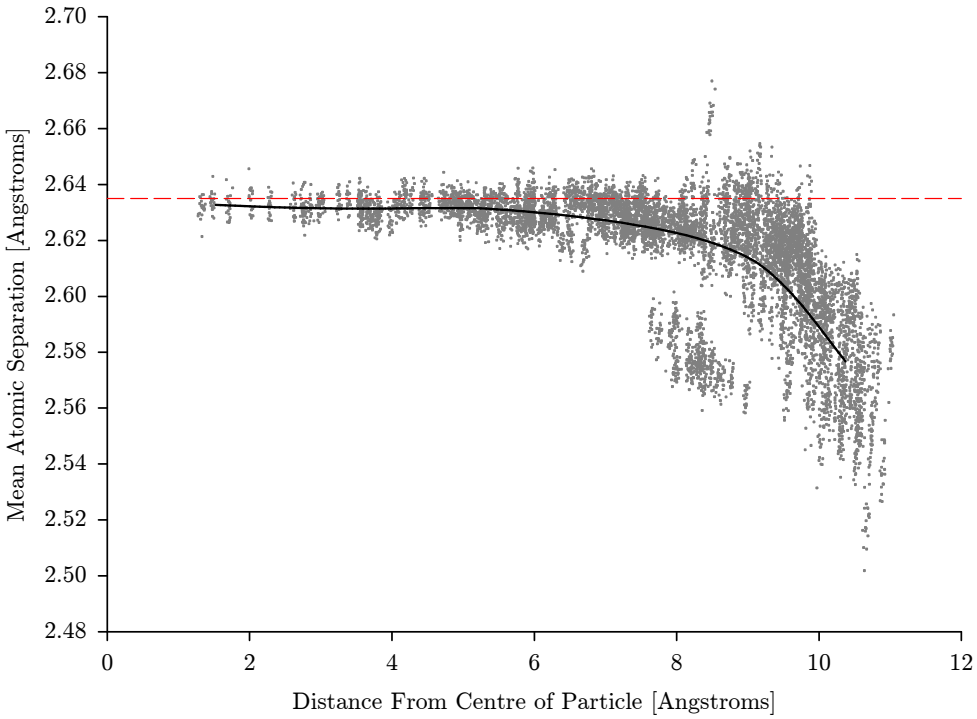

Figure. 4.6: Plot of mean interatomic separation as a function of radial distance from the centre for a 432 atom Fe particle. The black line is a guide to the eye, while the dashed red line indicates the interatomic spacing for bulk Iron. The graph shows a compression in the mean atomic spacing at the surface, but not in the centre as for the Co particle.

The Fe particle as shown in Figure 4.6, by comparison, only shows a characteristic compression at the surface of the particle, while the centre of the particle shows a mean atomic spacing comparable to the bulk value of $\sim$ 2.635 Å. However, the reduction in coordination number also means that the surface atoms are less tightly bound to their local environment, and thus experience bigger thermal fluctuations in their position compared with atoms at the centre of the particle. These compressions can significantly affect the Curie temperature of these particles, since the exchange energy (which, overall, essentially defines the Curie temperature) varies strongly with interatomic separation.

4.3 Results

Shape Dependence of the Curie Temperature

Since the overall exchange in the annealed particles is different from that of a particle of the same size but with a bulk structure, one would expect that the Curie temperature of these particles would be different. The calculation of the Curie temperature was performed by incrementally increasing the temperature of the system and letting the system equilibrate and calculating the mean magnetisation and standard error. Calculations were repeated 500 times for the smaller particles and the results averaged to achieve reliable statistics. In order to maintain consistency the same form of the interatomic exchange energy, $J_{ij}(r)$, was used for all the particles which includes long range interactions up to 8 nearest neighbours. Figure. 4.7 shows comparative plots of M vs T for the annealed particle, spherical and cubic particles of the same size, and for an 8nm diameter particle approximating bulk.

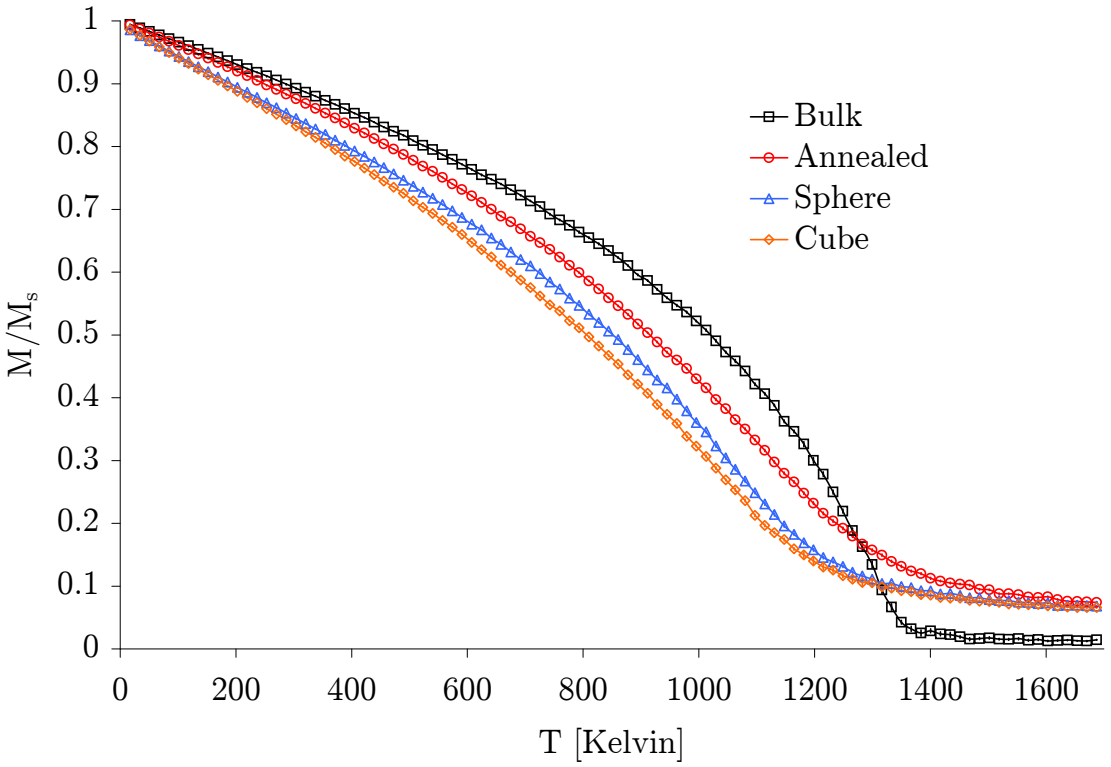

Figure. 4.7: Plot of M/M_s vs T for a 672 atom Co nanoparticle of differing shapes. The cubic shaped particle shows the lowest Curie temperature, while the annealed particle possesses the most highly optimised geometry leading to an enhancement of the Curie temperature. All particles show a sizeable reduction in their Curie temperature when compared to bulk.

As can be seen all the smaller particles exhibit a significant reduction in their

Curie temperature compared with the larger particle, but also there is a significant difference between different shapes. As previously reported [52], the spherical particle has a higher Curie temperature than the cubic particle. This arises from the fact that the cubic particle has a greater number of surface atoms and hence a lower coordination number. This lowers the overall exchange leading to a reduced Curie temperature. The annealed particle, however, has a higher Curie temperature than that of the spherical particle, even though the shapes are nearly identical. This then suggests that the compression at the surface of the annealed particle causes an increase in the Curie temperature, although still below the bulk value. This effect is also more significant for the Co compared to the Fe particles, as shown in Figure. 4.8, and is likely due to the different distance dependence of the exchange interaction for Fe and Co. The difference between the form of the exchange interactions in Fe and Co means that any compression in the lattice spacing, or change in the number of missing neighbours, will lead to a larger increase in the overall exchange in Co compared with Fe.

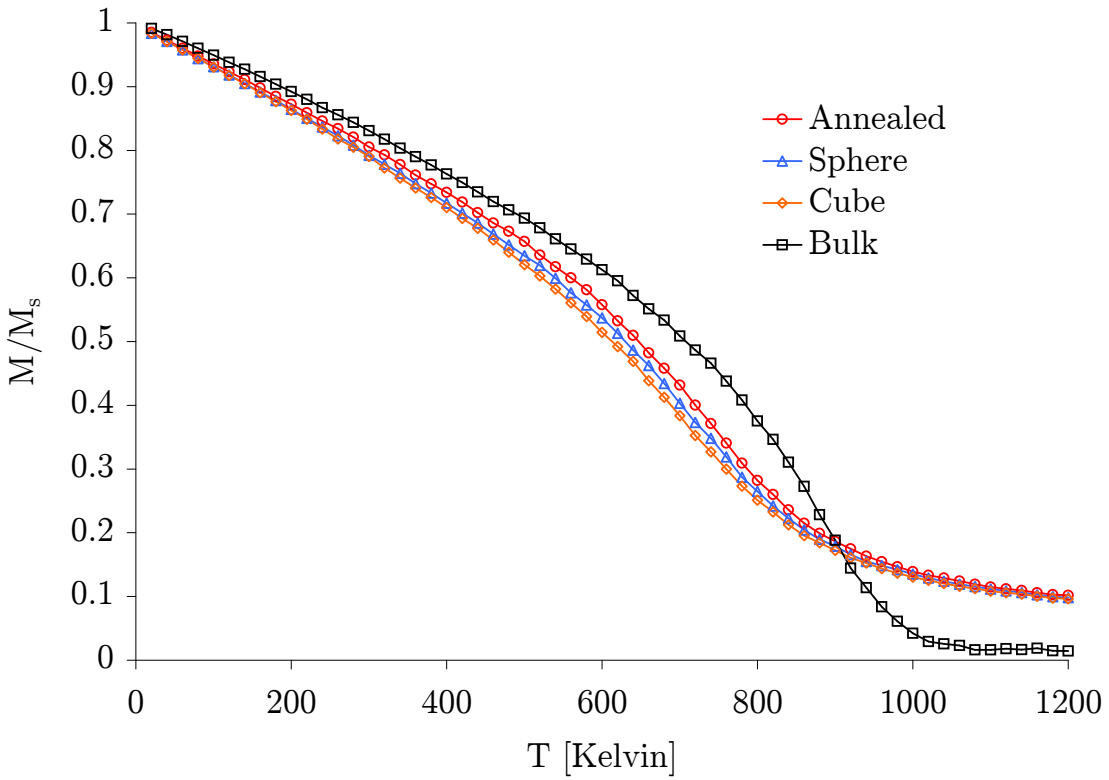

Figure. 4.8: Plot of M/M_s vs T for a 432 Atom Fe nanoparticle of differing shapes. As with the Co particles, the cubic shaped particle shows the lowest Curie temperature, while the annealed particle possesses the highest, although the effect is much less pronounced than with Co. This is likely due to differences in the attenuation of the exchange interaction with increasing interatomic distance between the two materials.

Structure Dependence of the Curie Temperature

In atomistic simulations it is usual to use a bulk microstructure at 0K. However, when simulating a system at finite temperature, this structure does not take into account the expansion of the lattice. This effect was simulated by taking snapshots of the microstructure for a 432 atom Fe particle in 20K steps from the molecular dynamic annealing simulation. The correct structure for a given temperature was then used in the atomistic spin simulation of the Curie temperature in the same way as above. At each temperature the atomic positions change so it is necessary to recalculate the exchange parameters for each different particle structure. It should be noted that any given snapshot from the molecular dynamic annealing simulation does not take into account the fact that in reality the individual atoms are not static. To correct for this calculations were performed over 20 different snapshots, effectively averaging over the thermal fluctuations in the atomic positions and giving an effective mean exchange for the whole particle at the given temperature.

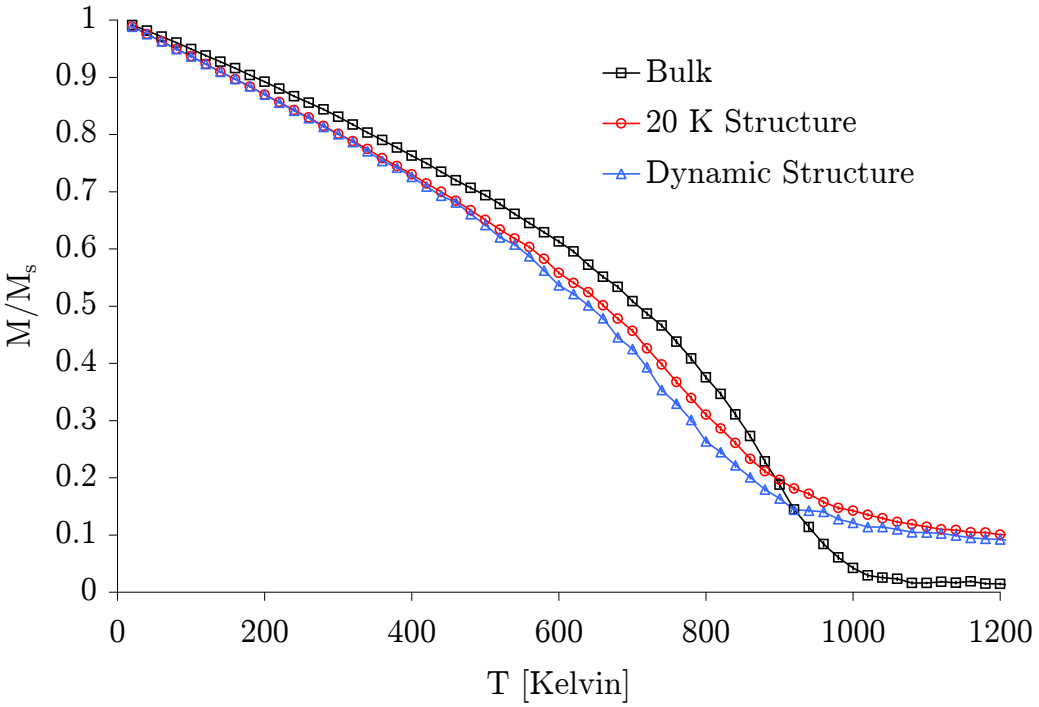

Figure. 4.9: Plot of M/M_s vs T for a 432 atom Fe nanoparticle, comparing the difference between static and temperature dependent atomic structures. The dynamic structure shows a reduced Curie temperature due to the expansion of the lattice, caused by a reduction in the exchange interaction.

The comparative results of a 432 atom annealed Fe particle with a "frozen" or

static structure with the same particle with a dynamic microstructure changing with temperature is shown in Figure. 4.9. Here the dynamic structure shows a reduction in the Curie temperature compared with the static structure. This is to be expected since an expansion of the lattice with increasing temperature will lower the exchange energy, although the size of the reduction is of course material dependent. In the final section of this chapter the effects of structural changes on the magnetic anisotropy energy will be investigated in detail for CoAg core-shell nanoparticles.

Structure Dependence of the Anisotropy

Although the exchange energy is the largest interaction within magnetic nanoparticles, the form of the anisotropy energy is also particularly important for applications. Single ion anisotropy energy arises from spin-orbit coupling between a magnetic atom and its immediate neighbours, and is typically one thousand times weaker than the exchange interaction energy. Given the localised origin of the anisotropy energy, in principle it should be possible to understand qualitatively the effects of atomic structure on the form of the anisotropy, without resorting to ab-initio calculations. Nevertheless, to obtain a definitive value and precise form for the anisotropy in mixed systems would still require the use of ab-initio calculations. This approach certainly fails for magnetic alloys, such as FePt, where an additional 2-ion anisotropy arises from the interaction between the Fe and Pt ions.

An interesting material to investigate in terms of its anisotropy is Cobalt. This is because there are two common structural forms of Co, namely fcc and hcp. In the bulk, the hcp structure has a slightly lower configuration energy, which forms the high anisotropy hcp phase at room temperature, and transitions to an fcc phase at around 500K. For Co nanoparticles [53] and ultrathin films [54] it is possible for the normally high-temperature fcc phase to become stable at room temperature. This arises due to the effect of the surface on the lattice spacing, making the fcc phase more stable. Although the two structural phases of Cobalt are very close in energy, magnetically they are very different. This arises due to the slight compression of the hcp lattice along the [0001] direction, giving a large uniaxial contribution to the anisotropy energy along this axis. The fcc structure is symmetric along all three principal axes, and so the contribution to the anisotropy energy is small and cubic.

For the pure Cobalt particles simulated above, the atomic structure was icosahedral in form, consisting of multiple twinned fcc regions. Resolving the magnetic anisotropy energy for such a structure is complex since no definable orientation axis exists, but due to the radial nature of the twinned regions the

anisotropy energy is likely to be very small. A detailed investigation of the anisotropy energy of perfect icosahedral nanoparticles was investigated by Morel et al[55].

The addition of silver to the Cobalt nanoparticle forms a so-called core-shell nanoparticle, where the silver is ejected to the surface[56]. Figure. 4.10 shows the radial variation of mean atomic spacing for a simulated annealed CoAg nanoparticle.

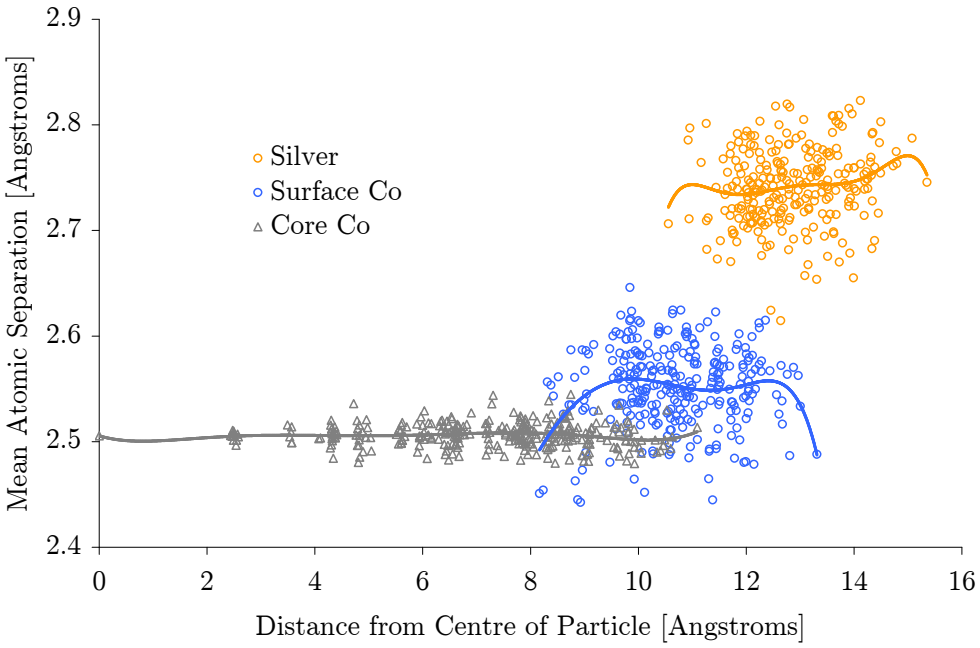

Figure. 4.10: Plot of mean interatomic separation as a function of radial distance from the centre for a 864 atom CoAg core-shell nanoparticle. The scatter plots are categorised for core Cobalt [grey], surface Cobalt (atoms with less than 12 nearest neighbours [blue]), and Silver atoms [orange]. The lines are guides to the eye. The graph shows that all the Ag is ejected to the surface of the particle, while all the core Co has a mean atomic spacing very close to the bulk value of 2.51 Å. The surface Co has an increased mean lattice spacing due to the presence of the Ag coating, which has a higher equilibrium lattice constant.

As can be seen, the compression at the centre of the pure cobalt particle, as shown in Figure. 4.4, is not present in the CoAg particle. Also the equilibrium atomic spacing of the silver is much larger than that of Cobalt, causing the compression of the surface cobalt to be replaced with a surface expansion.

The most profound effect of the addition of silver is to alter the internal structure of the Cobalt core. The silver coating optimises the surface potential of the Cobalt, inducing the formation of close packed stacking within the cobalt core. Since the two types of close packed stacking can be locally defined, based on

the arrangement of atomic neighbours, it is possible to show the stacking order within the particle, as illustrated in Figure. 4.11.

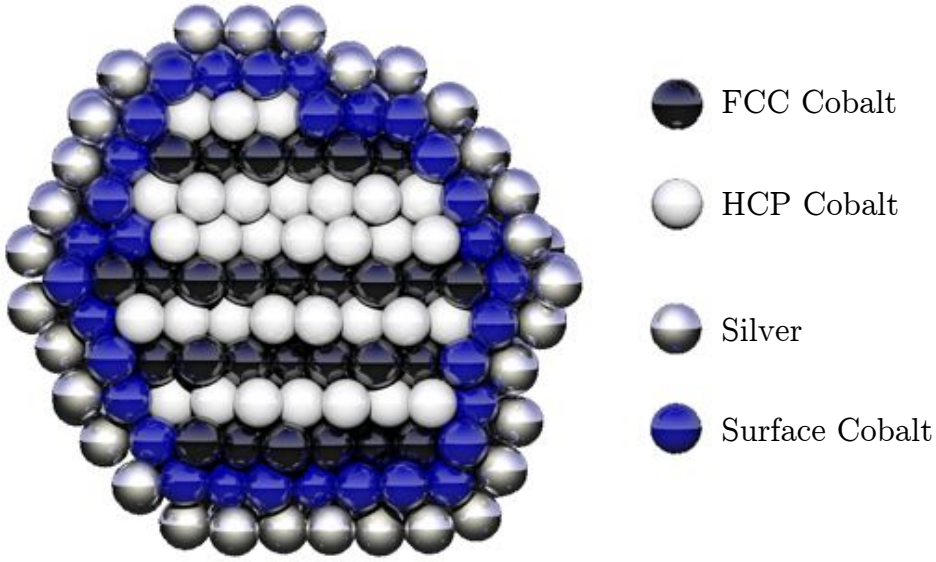

Figure. 4.11: Visualisation of the local close packed stacking order in a CoAg nanoparticle. The different colours indicate whether the stacking is hcp (white) or fcc (black). The blue colouring indicates cobalt atoms with less than 12 nearest neighbours, while the silver atoms are fully migrated to the surface of the particle.

As can be seen, the stacking is approximately 50% fcc and 50% hcp. It is also interesting to note that the stacking is totally consistent within the layers, so that there are no in-plane stacking faults. In order to assess the effect of the alternating stacking on the anisotropy energy, it was assumed that the anisotropy is entirely local in origin, and depending on the local atomic arrangement, a particular atom was attributed bulk cubic (fcc) or bulk uniaxial (hcp) anisotropy. The surface atoms have no crystal symmetry and so were treated as having Néel surface anisotropy. The effects of surface anisotropy are many and varied, and will be considered in much more detail in the next chapter. For the purposes of this calculation the effects of surface anisotropy were assumed to be small and so the strength of the surface anisotropy constant, K_s, was set to the same value as the bulk uniaxial constant for Cobalt. Due to symmetry, the surface anisotropy contributes virtually nothing to the effective anisotropy energy. Since the uniaxial anisotropy is an order of magnitude larger than the cubic anisotropy, the overall anisotropy energy density for the particle was found to be $\sim$ 2.5 times larger than that of an equivalently sized particle made of bulk fcc Cobalt, calculated by measuring the difference in configuration energy along the magnetically hard and easy axes. This anisotropy energy is an order of magnitude higher than the value reported for a single 4 nm cluster by Jamet et al [57]. In these simulations

the increased anisotropy arises from the hcp contribution of the core rather than the surface. Since the actual number of hcp layers probably depends on the particle fabrication methods employed, it is not unreasonable to suggest that some discrepancy between results is likely.

4.4 Conclusion

In this chapter the effects of atomic structure and surface geometry on the magnetic properties of nanoparticles have been investigated. In general it has been found that the atomic structure of nanoparticles is considerably different than that of bulk material, featuring dislocations, faceting, and other phenomena. Each of these structural differences contributes to a change in the Curie temperature, dependent on the nature of the exchange interaction. The addition of silver to a small cobalt particle was found to change the internal structure so that regular close packed stacking was formed. The influence of this stacking on the anisotropy energy is significant, suggesting an alternative origin for high anisotropy in core-shell nanoparticles.

5. The Influence of Surface Anisotropy on the Magnetic Properties of Nanoparticles

Traditionally, when calculating the energy barrier in single domain particles for the purposes of assessing magnetic stability, the particle has been assumed to have a magneto-crystalline anisotropy equivalent to a block of bulk material of the same size. The anisotropy energy essentially determines the thermal stability of a single domain particle through the Arrhenius-Néel law[9, 10]. The Arrhenius-Néel law relates thermal fluctuations of the magnetisation in a minimum energy state to a characteristic attempt frequency, f_o. Given an estimate of f_o (usually assumed to be around 10^9 Hz), it is possible to estimate the time over which a magnetisation state is stable, τ, given by:

$$\tau^{-1} = f_o \exp\left(\frac{K_u V}{k_B T}\right) \tag{5.1}$$

where K_u is the anisotropy energy density, V is the particle volume, k_B is the Boltzmann constant, and T is the absolute temperature. As the particle volume is decreased, this leads to a reduction in the thermal stability. However, for very small particles of a few nanometres in diameter, surface effects can begin to play a significant, sometimes dominant, part in determining the overall magnetic stability of nanoparticles.

Significant research has been conducted investigating the magnetocrystalline anisotropy at interfaces between different materials in thin films [58, 59], where a special surface anisotropy has been found. Magnetocrystalline anisotropy arises from the crystal symmetry in the lattice, but at the surface this atomic symmetry is broken leading to a surface anisotropy arising from the reduced coordination at the atomic surface. Since the fundamental origin of surface anisotropy is the same as magnetocrystalline anisotropy, it is possible to model the effects of surface anisotropy by taking into account the local atomic environment.

In thin films, the surface anisotropy generally gives a strong preference for the surface magnetic moments to lie either in the film plane, or perpendicular to the film, dependent on the materials used, growth methods, and crystal orientation. In some cases, usually in ultrathin films, the surface anisotropy can be so strong that the magnetisation of the film is forced to lie perpendicular to the film plane in competition with the demagnetising field, which usually orientates the magnetisation in plane. Understanding surface anisotropy is particularly

important for any applications utilizing ultra thin magnetic films, such as layers in a read head element in a hard disk. The contribution of the surface anisotropy in thin films is established experimentally by varying the thickness of the film and measuring the resultant anisotropy energy. The total anisotropy energy, K_{eff} is then described as a summation of the volume, K_{v}, and surface, K_{s}, contributions, given by:

$$K_{\text{eff}}V = K_{\text{v}}V + K_{\text{s}}S \tag{5.2}$$

where V is the system volume, and S is the surface area of the film. Dividing through equation 5.2 by the system volume, V, gives:

$$K_{\text{eff}} = K_{\text{v}} + \frac{K_{\text{s}}}{t} \tag{5.3}$$

where t is the film thickness. By plotting the effective anisotropy against the inverse of the film thickness it is straightforward to extract the surface (gradient) and volume (intercept) contributions to the overall anisotropy energy. While the effect of surface anisotropy in thin films is easy to quantify, though limited to a specific case, the effect on nanoparticles is substantially more complex due to the geometry. A similar scaling behaviour is often used for nanoparticles, though as the following chapter aims to illustrate, the use of such a formula is only valid for a very particular case.

In the following chapter the Néel model of surface anisotropy is introduced. This model is then applied to investigating the effects of surface anisotropy on the magnetic properties of nanoparticles for a number of different particle topologies and crystal structures. The effects of each on the thermal stability of the nanoparticles is then evaluated using the established Lagrange Multiplier technique by giving an estimate of the zero-temperature energy barrier between magnetic states.

5.1 Theoretical Background

The origin of magneto-crystalline anisotropy is the spin-orbit coupling between electron orbitals of atoms within a crystal. This coupling gives a preferred directionality for the electron orbit, aligning the spin moment. Ab-initio calculations [60, 61] and experimental results [57, 62] on clusters of atoms at a surface have shown that the electronic structure is significantly different at the surface when compared with a bulk crystal. This results in a different anisotropy, known generally as surface anisotropy. The specifics of surface anisotropy depend on the material at the surface, for example an inert metal coating would give very

different results from surfactant coating or vacuum for example. There are two significant models for surface anisotropy, namely transverse and Néel. In the transverse model the surface anisotropy is assumed to be uniaxial (or easy plane, depending on the sign of the anisotropy constant) perpendicular to the surface. This is often acceptable for thin films in micromagnetic modelling since the surface plane is usually well defined. For an atomic discretisation however, the surface roughness means the definition of a flat surface is problematic. The Néel model varies the direction and magnitude of the anisotropy based on the local atomic geometry at the surface and also the local spin configuration, and thus is more suitable for atomistic scale modelling of surface anisotropy. A study also showed that in general the Néel model is the more realistic [63] of the two, and is described in detail below.

Néel Model of Surface Anisotropy

The Néel surface anisotropy (NSA) model is formed by a pairwise interaction between two surface atoms, i and j, given by:

$$E_{\text{surface}}^{\text{anis}} = L_N(\boldsymbol{S}_i \cdot \boldsymbol{r}_{ij})^2 = L_N \cos^2 \varphi, \tag{5.4}$$

where $\boldsymbol{S}_i$ is the atomic spin, $\boldsymbol{r}_{ij}$ is the unit vector between atomic sites i and j, and L_N is the Néel surface anisotropy constant. L_N depends on the interatomic distance r according to the following expression:

$$L_N(r) = L_N(r_0) + \left(\frac{\partial L_N}{\partial r}\right)_{r_0} r_0 \eta, \tag{5.5}$$

where r_0 is the bulk unstrained bond length and η the bond strain. In the simple case of a perfect crystal, with no change in the bond length at the surface, the surface anisotropy energy reduces to:

$$E_{\text{surface}}^{\text{anis}} = L_N(r_0)(\boldsymbol{S}_i \cdot \boldsymbol{r}_{ij})^2 \tag{5.6}$$

Taking a sum over all neighbouring atoms, and replacing the Néel constant with an effective surface anisotropy constant, $K_{\text{Néel}}$, the on site surface anisotropy energy is:

$$E_{\text{surface}}^{\text{anis}} = \frac{1}{2} K_{\text{Néel}} \sum_{j=1}^{n_{NN}} (\boldsymbol{S}_i \cdot \boldsymbol{r}_{ij})^2 \tag{5.7}$$

where n_{NN} is the number of nearest neighbours. In general for an atom located within a bulk crystal structure the contributions r_{ij} from all the neighbouring atoms cancel, resulting in a zero contribution to the anisotropy. Interestingly

for some materials, such as hcp Cobalt, there is some compression along the easy axis. Taking this compression into account within the NSA the asymmetry induces a uniaxial anisotropy along the c-axis, as is seen in bulk hcp Cobalt. At the surface, however, there are missing neighbours from the bulk magnetic material and this always gives a non-zero contribution to the surface anisotropy. Due to the wide variety of surface atomic arrangements, understanding the nature of the surface anisotropy is somewhat complex. For simple geometries however it is possible to determine explicitly the local anisotropy for a given atomic arrangement. The simplest case to is to take a particle with a simple cubic crystal structure cut in the shape of a cube. This yields three distinct surface geometries which, with their corresponding surface anisotropy energy surfaces, are illustrated in Figure. 5.1. Each of the different geometries yields a different surface anisotropy, dependent on the on-site spin direction. The energy surface for each configuration is displayed as a function of the polar and rotational angle of the atomic spin direction from the z and x axes respectively.

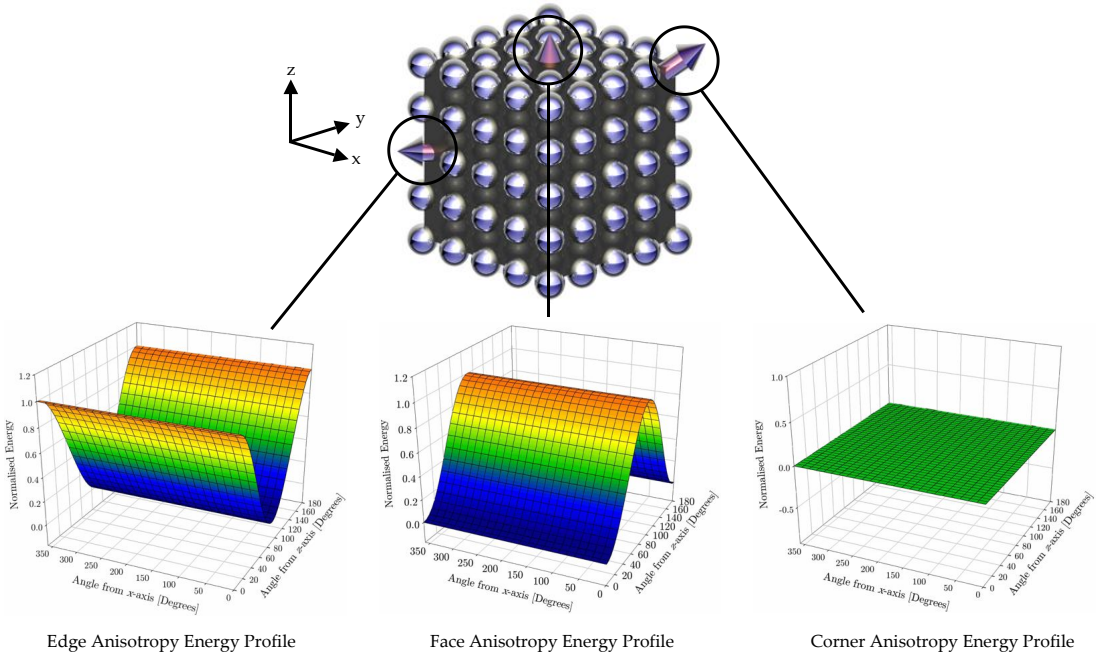

Figure. 5.1: Visualisation of a simple cubic system with surface anisotropy. The arrows relate a particular local geometry to a different single-spin anisotropy surface, shown below. The edges and faces yield easy axis and easy plane anisotropies, while the corner site has no preferential magnetisation axis. The energies are normalised for a positive value of the surface anisotropy constant, K_s.

As can be seen, the three cases induce different forms of anisotropy. The edge and face cases show a uniaxial or easy plane anisotropy with opposite

signs, while the corner arrangement yields an isotropic zero contribution to the anisotropy energy. Of course for more complex surface arrangements and crystal structures the situation becomes more complicated. In these cases the precise contribution of the surface anisotropy is difficult to identify.

By convention the strength of the surface anisotropy is given relative to that of the core uniaxial anisotropy K_u or mean inter-atomic exchange energy, J. For some materials the magnitude of the surface anisotropy is several times that of the core anisotropy. In this case the surface anisotropy can begin to truly dominate the energetics of the magnetic system. Extracting an exact value for $K_{\text{Néel}}$ from experimental results for a given material is problematic due to the complex non-linear effects of surface anisotropy, as will be illustrated in the following sections. As a result we usually assume the magnitude of the surface anisotropy to be a parameter in the simulations.

Constrained Minimisation

Having a description for anisotropy both in the core and surface of a nanostructure it is then possible to investigate the effects of surface anisotropy on the thermal stability of nanoparticles. In a simple uniaxial system below the Stoner-Wohlfarth size limit (so that there are no domains) and neglecting surface effects there are two stable magnetic states, spin up and spin down. These two magnetic states are separated by an energy barrier, preventing the magnetisation from reversing. In this situation this energy barrier is well defined since it is entirely symmetric. In the case of cubic anisotropy the energy barrier is less well defined since there is the usual energy barrier associated with reversal along the cubic easy axis, but additionally there is a barrier to reversal around the easy axis, otherwise known as a rotational energy barrier.

The introduction of surface anisotropy, however, can contribute to the energy barrier in a complex way so it is necessary to use a special technique to study the energy surface which can assess its impact on the energy barrier.

Lagrange Multiplier Technique

The Lagrange Multiplier Technique is an energy minimisation scheme which uses a constraint method to calculate the configuration energy of a magnetic state [64]. The average magnetisation of the system is constrained to point along a certain direction $\boldsymbol{\nu}_o$ by the addition of an additional energy term to form the following amended spin Hamiltonian:

$$\mathcal{F} = \mathcal{H} - \mathcal{N}\boldsymbol{\lambda} \cdot (\boldsymbol{\nu} - \boldsymbol{\nu}_o) \tag{5.8}$$

where $\mathcal{F}$ is the total energy of the system, $\mathcal{H}$ is the standard Hamiltonian for a magnetic system, $\mathcal{N}$ is the number of spins, $\boldsymbol{\nu}$ is the instantaneous direction of the macrospin magnetisation, and $\boldsymbol{\lambda}$ is the Lagrange Multiplier. The method essentially works by forcing the system magnetisation to lie along $\boldsymbol{\nu}_o$ with a large Lagrange field, calculated as the derivative of $\mathcal{F}$ with respect to $\boldsymbol{S}$. The system is solved using the relaxational component of the LLG equation ($\dot{\boldsymbol{S}} = \alpha \boldsymbol{S} \times (\boldsymbol{S} \times \boldsymbol{H})$). The time evolution of the Lagrange multiplier is given by:

$$\dot{\boldsymbol{\lambda}} = \frac{\partial \mathcal{F}}{\partial \lambda} = \mathcal{N}(\boldsymbol{\nu} - \boldsymbol{\nu}_o) \tag{5.9}$$

and is solved iteratively for the instantaneous system conditions. The system is initialised such that $\boldsymbol{\nu} = \boldsymbol{\nu}_o$ and $\boldsymbol{\lambda} = 0$, and then solved until the total torque ($\boldsymbol{S} \times \boldsymbol{H}$) is zero with some tolerance, typically 10^{-5}. When the intended and actual system magnetisation directions are aligned then the second term of equation 5.8 becomes zero, leaving the original Hamiltonian for the system. Although the system magnetisation is constrained to point along a certain direction, individual spin moments are allowed to choose their direction freely provided the global constraint is preserved. This permits the existence of canted spin structures and deviation from a fully aligned state which can often be caused by strong values of surface anisotropy.

The Lagrange Multiplier technique is used to generate energy surfaces, showing the variation of the system energy as a function of the azimuthal (θ) and rotational (ϕ) angles of the system magnetisation from arbitrary vectors in spherical polar coordinates. If the system possesses a bulk easy-axis anisotropy, then the azimuthal angle is usually measured from the easy axis.

Calculation of Energy Surfaces

Energy surfaces are calculated by initialising all spins along the desired direction, $\boldsymbol{\nu}_o$. The system is then allowed to relax to a minimum energy state given the constraint, where the final configuration energy normalised to the exchange energy is measured. This is repeated for values of θ and ϕ in spherical polar coordinates over the whole particle generating a plot of the "energy landscape"[65]. Examples of energy landscapes for a particle with purely z-axis uniaxial anisotropy (a) and cubic anisotropy (b) as seen in Fe are shown below in Figure. 5.2.

The energy landscape for the uniaxial case Figure. 5.2(a) shows that there is an increase in energy as the azimuthal angle θ increases, which reaches a maximum at $\theta = 90^\circ$, as expected for uniaxial anisotropy. The particle also shows no rotational anisotropy, ie the energy for all values of the rotational angle ϕ are

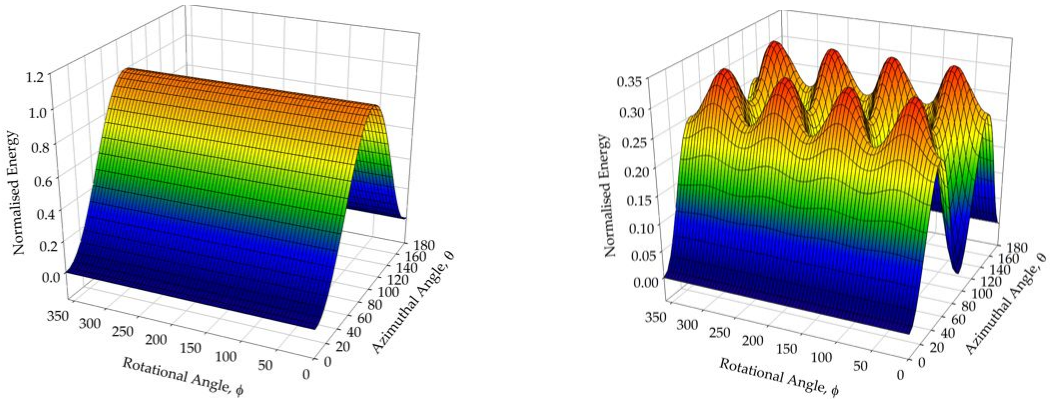

(a) Energy landscape for uniaxial anisotropy.

(b) Energy landscape for cubic anisotropy.

Figure. 5.2: Energy landscapes for purely uniaxial (a) and cubic (b) forms of anisotropy.

the same. In contrast, the energy landscape for the cubic anisotropy case in Figure. 5.2(b) shows both azimuthal and rotational anisotropy. The global energy maxima for this case lie at $\theta = 54.74°, \phi = 45°$ [111], while there is also a saddle point at $\theta = 90°, \phi = 45°$ [110], corresponding to the very hard and hard axes respectively. The easy axis appears along the principal [001] axes, having the lowest energy states. It should be noted that a change in the sign of the anisotropy constant has the effect of inverting the energy surface along the energy axis, so that peaks become troughs and vice versa. In the case of uniaxial anisotropy with a negative constant, the energy surface yields an easy plane anisotropy, while for cubic anisotropy the [111] axis becomes the easy axis.

Energy Barriers

In order to estimate the thermal stability of these particles, one must evaluate the energy barrier to the system magnetisation escaping from the deepest energy minimum of the energy landscape. Depending on the azimuthal and rotational anisotropy, the reversal path can trace complex routes via intermediate metastable states. If one assumes that the energy barriers are large with respect to the thermal energy, $k_B T$, then the only barrier of interest is the lowest. The lowest energy barrier, ΔE, is obtained by evaluating the expression from the calculated energy landscape:

$$\Delta E = \min(E_{\text{max}}) - \min(E_{\text{min}}) \tag{5.10}$$

where $\min(E_{\text{max}})$ is the minimum energy of the local energy maxima, and $\min(E_{\text{min}})$ is the minimum of the local energy minima, or the global energy minimum. In the case of uniaxial anisotropy, the only energy barrier is to reversal along the azimuthal direction, which separates the two stable states of spin up

and spin down. For cubic anisotropy, the energy barrier is between the easy and hard directions, while the very hard anisotropy direction plays no part in the thermal stability of the particle.

In the following section the above techniques will be used to investigate the effect of various physical variables, specifically crystal structure, particle size, and particle volume on the energy surfaces and thermal stability of nanoparticles with surface anisotropy.

5.2 Results

Shape Dependance of the Energy Barrier

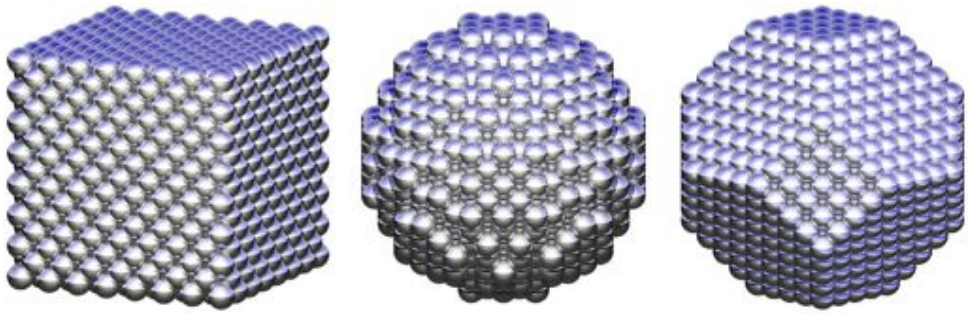

Figure. 5.3: Visualisation of cuboid, sphere, and truncated octahedron particle shapes with a face-centred cubic crystal structure simulated using surface anisotropy. Each of the different shapes shows very different faceting, which in turn influences the effect of surface anisotropy on the energy barrier.

The simplest case to consider first is the effect of different particle geometries on the energy barrier. Normally one would expect this effect to be small, but for strong values of the surface anisotropy constant the particular surface topology can become important. In order to investigate the effects of changing the particle shape, similarly sized particles of around 2000 atoms were created using the same face-centred-cubic crystal structure. For comparison, particles in the shape of a cube, sphere, and truncated octahedron were generated, as shown in Figure. 5.3.

A uniaxial anisotropy was assumed for the non-surface atoms, ie those with the full 12 nearest neighbours, in order to ascertain the influence of the surface anisotropy on a pre-existing energy barrier. The bulk uniaxial easy axis in all cases was chosen to be along the z-axis. The energy surfaces are plotted relative to the z-axis, so the easy axis angle is the angle from the z-direction, while the rotational angle is taken from the x-axis. Due to the small size of the particles, around 40 % of atoms are on the surface which means that surface effects can be

quite significant. Since the strength of the surface anisotropy constant is specific to particular cases, the magnitude of $K_{\text{Néel}}$ is varied for each particle shape to investigate its effect on the energy barrier. The variation of both the easy axis energy barrier and the rotational barrier between local minima, normalised to the equivalent bulk energy barrier, with increasing strength of the surface anisotropy for a cube, sphere, and truncated octahedron are plotted in Figure. 5.4. Note that the effects on the energy barrier of both signs of $K_{\text{Néel}}$ have been investigated, since the effects can be quite different for the two cases.

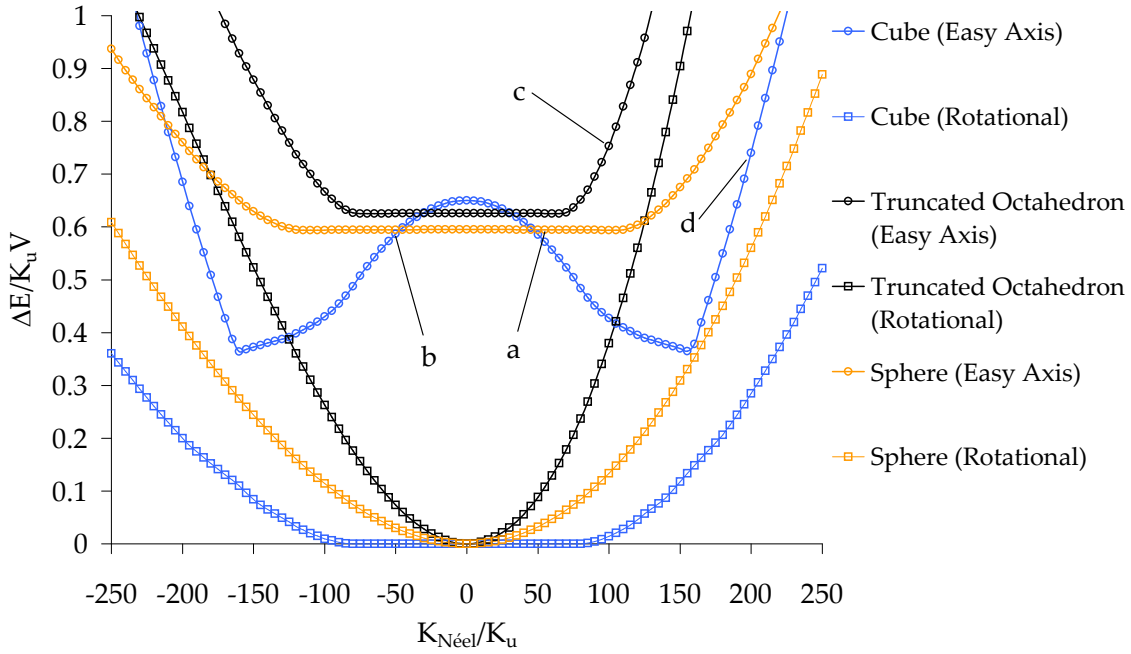

Figure. 5.4: Plot of the energy barriers of different FCC particle geometries as a function of the normalised strength of the surface anisotropy constant. For analysis see accompanying text.

As can be seen the effects of surface anisotropy can be complex and so what follows is a detailed analysis of this graph. The first result to note is the effect when the surface anisotropy constant is zero. All the particles show a reduction in the energy barrier, which is equal to the fraction of surface atoms in the particle. This is due to the surface atoms having no anisotropy and so the effective anisotropic volume is decreased. If all atoms had a bulk anisotropy, then the magnitude of the energy barrier would be 1. This effect can be seen experimentally for some nanoparticle preparation methods, where a magnetic core can be surrounded by a magnetically dead layer with no anisotropy.

The next case to consider is that of small values of $K_{\text{Néel}}$. For the spherical and truncated octahedron particles, the effect of increasing $K_{\text{Néel}}$ on the energy barrier is very small. This is due to the almost continuous variation of the surface

normal, leading to a continuous variation of surface easy axis. This effect can be seen for the spherical particle in the energy landscape plotted in Figure. 5.5 (point *a* in the graph in Figure. 5.4), showing a weak angular variation in the system configuration energy in the energy maximum at $\theta = 90°$.

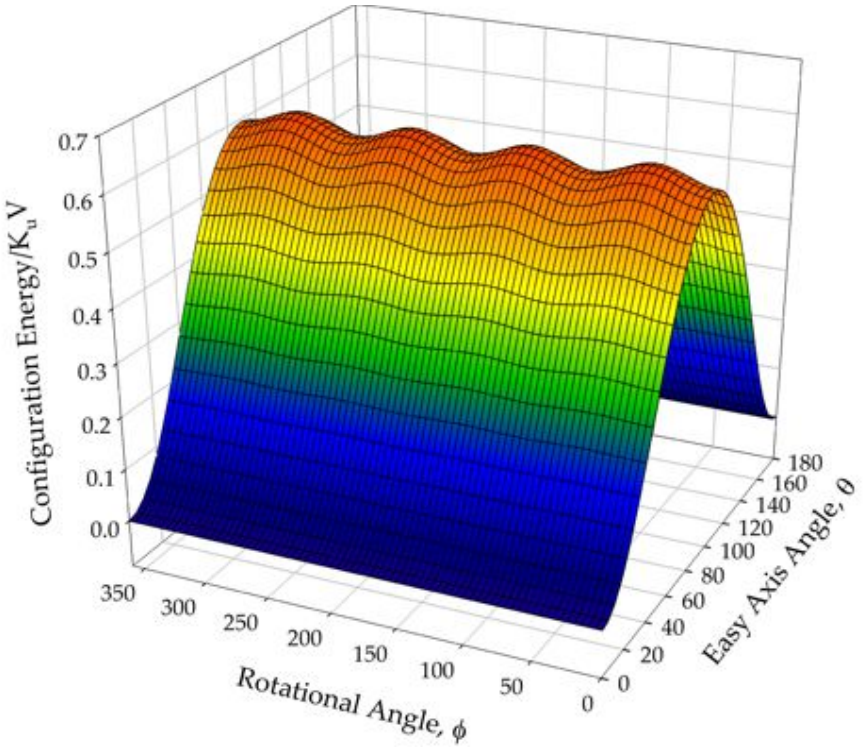

Figure. 5.5: Energy landscape for a spherical particle for $K_{\text{Néel}} = 50K_u$ showing a weak angular variation of the configuration energy in the energy maximum at $\phi = 90°$.

Even for small values of $K_{\text{Néel}}$, spin non-collinearities due to surface pinning can begin to influence the form of the energy surface. Due to the near radial symmetry of the spherical and truncated octahedron particles, the underlying cubic crystal structure begins to influence the energy surface by forming a cubic surface energy potential. The breakdown of the regime where the energy barrier changes very little with increasing $K_{\text{Néel}}$ occurs at a lower value of $K_{\text{Néel}}$ for the truncated octahedron due to the surface faceting - essentially creating edges. Edges are important since they form discontinuities in the direction of the local spin easy axis between adjacent facets. This effect is illustrated by the cube shaped particle even at low values of $K_{\text{Néel}}$, where the energy barrier decreases sharply with increasing $K_{\text{Néel}}$. This is caused by the strong directionality in the surface facets and edges. For both signs of $K_{\text{Néel}}$ the minimum surface energy state exists where the system magnetisation lies along the cube edges. This causes a marked reduction in the configuration energy when the system magnetisation lies along these edges, which in turn lowers the energy barrier between the two

states induced by the core uniaxial anisotropy. The effect of barrier lowering can be clearly seen in the energy landscape plotted in Figure. 5.6 (point *b* in the graph in Figure. 5.4). The lowering of the energy barrier is periodic, arising from the surface geometry, where the cube edges lie at 45° to the principal axes.

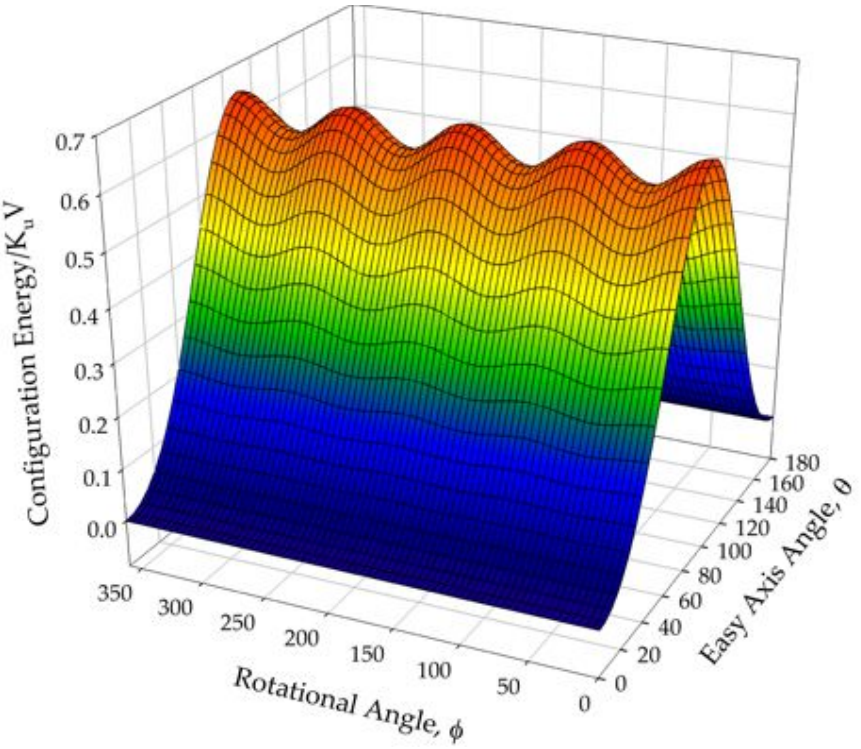

Figure. 5.6: Energy landscape for a cubic particle for $K_{\text{Néel}} = -50K_u$ showing lowering of the energy barrier along the cube edges.

It is interesting to note that the energy barriers for the spherical and truncated octahedron particles only increase, rather than exhibit a barrier lowering as seen for the cube. For the truncated octahedron, this is due to the particular surface faceting, where the alignment of the system magnetisation with the square faces forms a minimum energy state, deepening the energy barrier arising from the core anisotropy. This can be seen in the energy surface by looking in the region of the energy maximum at $\theta = 90°$, as plotted in Figure. 5.7 (point *c* in the graph in Figure. 5.4). The square facets lie at $\phi = 0°$, where a visible reduction in the configuration energy can be seen when compared with the edge configuration energy at $\phi = 45°$. Due to symmetry, a similar reduction in energy occurs in the global energy minimum, deepening the minimum energy well, leading to an effective increase in the energy barrier. The effect of edges in the case of the truncated octahedron is somewhat different to that of the cube edges, actually causing an increase in the system configuration energy.

The final case to consider is that of large values of $K_{\text{Néel}}$, where the energy barrier increases rapidly for all particle shapes with increasing $K_{\text{Néel}}$. For such

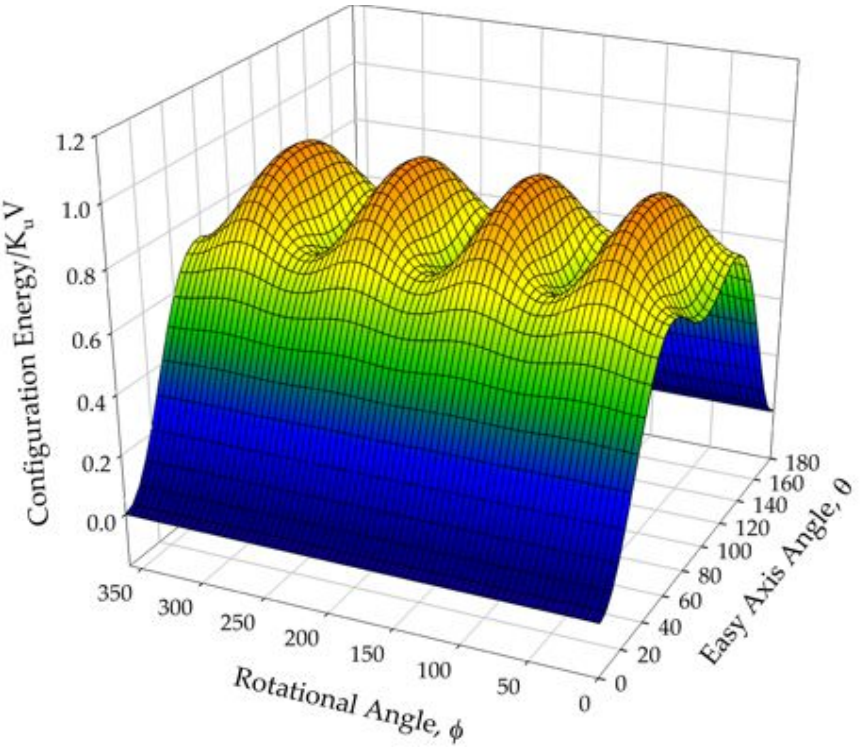

Figure. 5.7: Energy landscape for a truncated octahedron particle for $K_{\text{Néel}} = 100K_u$, showing lowering of the configuration energy at the square facets at $\theta = 90^\circ$, $\phi = 0^\circ$.

large values of $K_{\text{Néel}}$, approaching a sizeable fraction of the exchange energy, the energy landscapes become highly distorted, as shown in Figure. 5.8 (point *d* in the graph in Figure. 5.4). Here the energy landscape represents a cubic energy surface, with deep global minima away from the original easy axis. The reason for the huge increase in the energy barrier comes entirely from the spin non-collinearity. In the fully collinear magnetic state, the surface anisotropy makes an isotropic contribution to the configuration energy due to the symmetric nature of the particles. Allowing for deviations from the collinear state, however, adds a direction dependent contribution to the configuration energy caused by a reduction in the system magnetisation along the cube edges [64]. Even though the reduction in magnetisation is less than 0.1%, the strength of the exchange interaction means that this small change in the magnetisation can make a large contribution to the effective energy surface, and thus the energy barrier. This spin non-collinearity effect gives rise to the cubic energy surface in Figure. 5.8, and relates to the underlying cubic crystal lattice, although the effect originates at the surface.

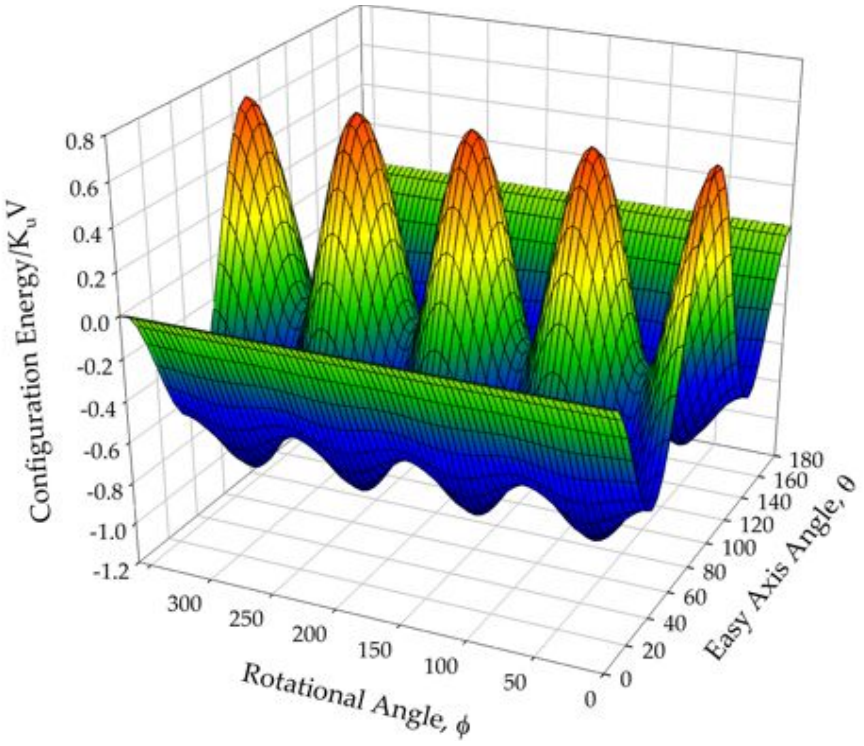

Figure. 5.8: Energy landscape for a cubic particle for $K_{\text{Néel}} = 200K_u$, showing a form of cubic anisotropy landscape, arising from the underlying crystal symmetry.

Elongation Dependence of the Energy Barrier

One geometric effect not yet discussed is that of elongating particles along one axis. Elongation of particles is known to give the magnetisation a preferential orientation along the elongation axis due to the shape anisotropy. In order to investigate the effects of elongation on the energy barrier, a spherical particle with an FCC crystal structure and uniaxial core anisotropy is elongated along the magnetic easy axis by 50%. The energy barrier is then evaluated for increasing positive and negative values of the surface anisotropy constant, $K_{\text{Néel}}$. Note that no dipolar fields are included in these calculations, which in reality would give a small demagnetising effect with the magnetisation lying along the long axis. This is for computational efficiency reasons, and the effect is nevertheless very small. Compared to the strength of the core anisotropy, the strength of the dipolar fields is small and so can be neglected. Figure. 5.9 shows a plot of normalised easy axis and rotational energy barriers for the elongated nanoparticle for different values of $K_{\text{Néel}}$. A visualisation of the particle is inset.

The first point to note is that, as with the non-elongated particle shapes discussed above, there is a reduction in the energy barrier for $K_{\text{Néel}} = 0$, arising from a reduction in the anisotropic magnetic volume due to the surface atoms. What is very noticeable for elongated particles is the effect of the surface

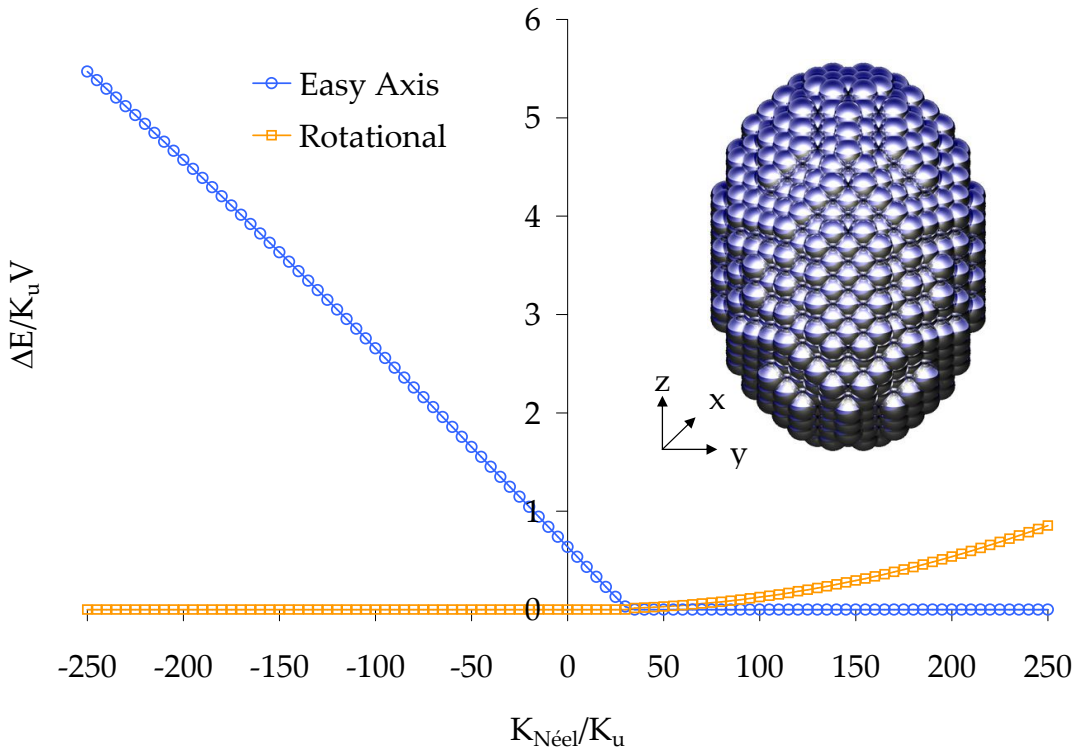

Figure. 5.9: Plot of easy axis and rotational energy barriers as a function of the normalised surface anisotropy constant for a 1964 atom FCC elliptical nanoparticle (inset). The core magnetic easy and elongation axes are both aligned along the z-direction. For negative values of $K_{\text{Néel}}$ the principal easy-axis energy barrier increases near-linearly to values much greater than one, while for positive values the easy axis energy barrier disappears, leaving only a rotational barrier within the easy plane.

anisotropy on the energy barrier for different signs of $K_{\text{Néel}}$. For the case of negative $K_{\text{Néel}}$, the uniaxial energy barrier shows an almost linear increase with $|K_{\text{Néel}}|$. This can be explained by the fact that a negative surface anisotropy constant yields an easy plane configuration with respect to the surface normal. When the particle magnetisation is aligned along the easy axis, the side faces are all in a minimum energy state, while the top and bottom faces are not. Conversely, when the particle magnetisation is orientated along the core hard axis, two side faces are in a maximum energy state, while the other two side faces and the top faces are in a minimum energy state. Due to the elongation of the particle, the surface area of the side faces is greater than that of the top faces, leading to a large difference in energy between the two different orientations of the magnetisation. This adds to the anisotropy due to the core, and leads to a much increased energy barrier which is linear in $K_{\text{Néel}}$.

For the case where $K_{\text{Néel}}$ is positive, the influence on the energy barrier is markedly different. The different sign leads to a local easy axis parallel to the surface normal. The effect of this on the overall energy surface is qualitatively the same as for negative $K_{\text{Néel}}$, except that the minimum energy surface configuration is now in the plane of the core anisotropy axis, as can be seen in the energy surface plotted in Figure. 5.10 for $K_{\text{Néel}} = 150K_u$. Since the overall energy surface is an easy plane, there is no longer a large easy axis energy barrier separating two energy states, although the strength of the easy plane anisotropy is considerable. The spin non-collinearities caused by the surface faceting and underlying cubic symmetry give rise to a small rotational energy barrier in the plane, which forms the only energy barrier in the case of the easy plane system. For smaller values of positive $K_{\text{Néel}}$, the surface contribution is insufficient to overcome the core contribution, but works in direct competition with the core anisotropy. This yields to a rapid reduction in the energy barrier for increasing $K_{\text{Néel}}$, until the surface contribution begins to dominate.

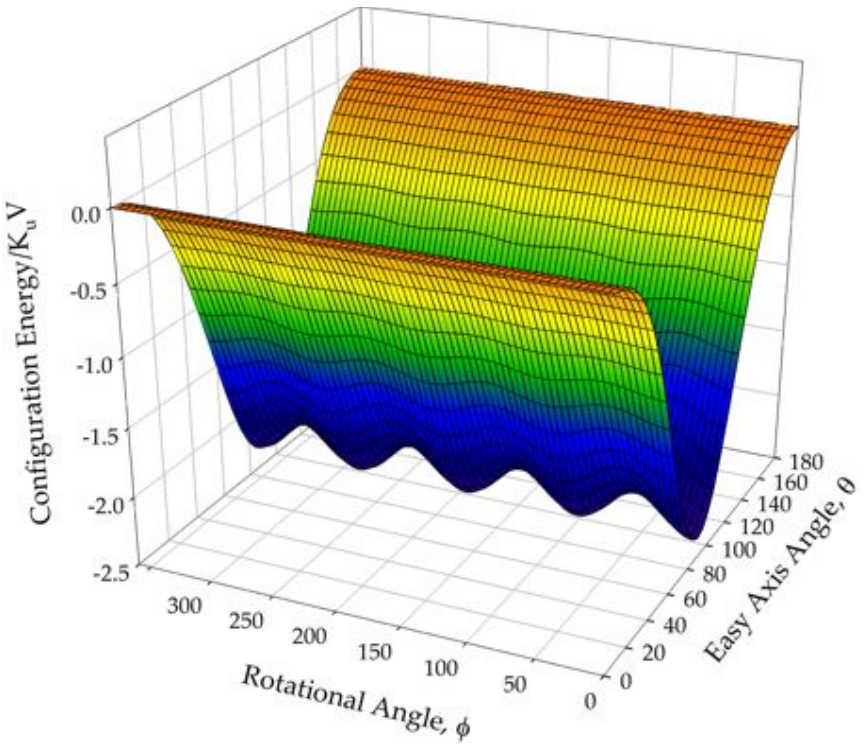

Figure. 5.10: Energy landscape for an elliptical particle for $K_{\text{Néel}} = 150K_u$, showing an easy plane configuration with respect to the core easy axis. The surface faceting still gives rise to a small rotational energy barrier in the energy minimum.

Crystal Structure Dependance of the Energy Barrier

The next effect to consider is that of the crystal structure dependence of the energy barrier. At first sight it might seem somewhat strange that the crystal structure has much effect on the energy at all, particularly since the models used here are somewhat simplified. However, as the following section will show, the effect of the crystal structure can be significant. The effect of crystal structure on the energy barrier has been investigated by generating energy surfaces for spherical particles with simple cubic (sc), face centred cubic (fcc), and hexagonal close packed (hcp) crystal structures. Figure. 5.11 below shows the normalised energy barriers for the particles with different crystal structures as a function of the strength of the surface anisotropy constant, $K_{\text{Néel}}$.

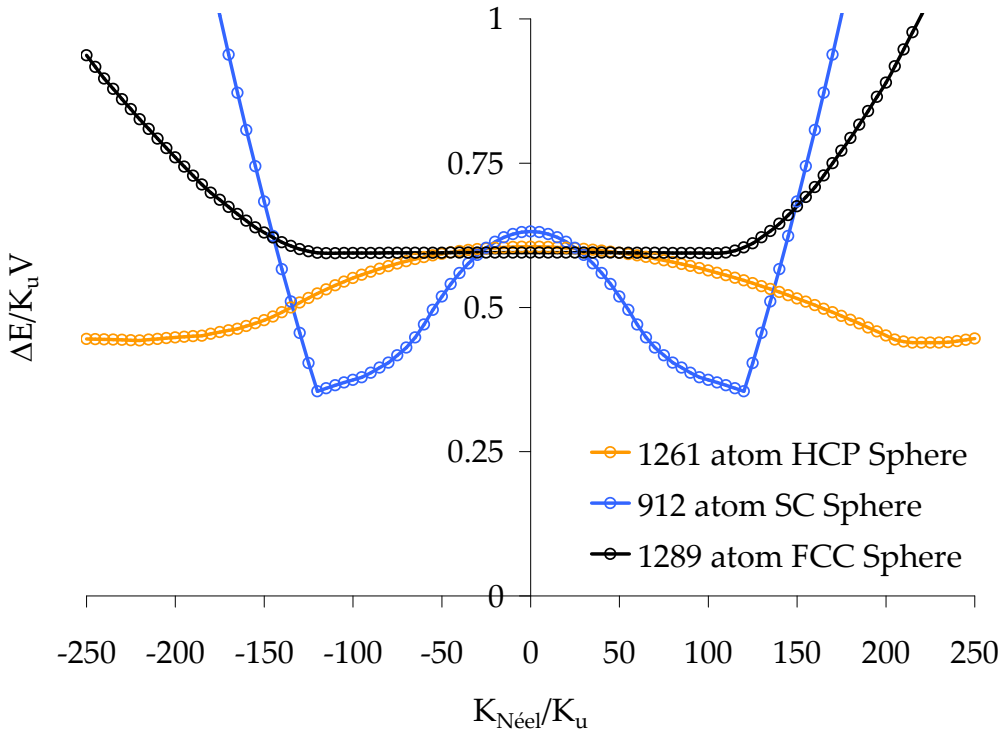

Figure. 5.11: Plot of easy axis energy barriers as a function of the normalised surface anisotropy constant for spherical particles with different internal crystal structures. The effect of increasing $K_{\text{Néel}}$ is largely symmetric for all the particles. See text for further analysis.

Each of the particles has an approximately equivalent fraction of surface atoms, but, as can be seen, the different crystal structures respond very differently to increasing $K_{\text{Néel}}$. The plots are also largely symmetric for both positive and negative values of $K_{\text{Néel}}$. The first case to consider is that of the particle with hcp crystal structure. The energy surface for the particle with an hcp structure is

plotted in Figure. 5.12.

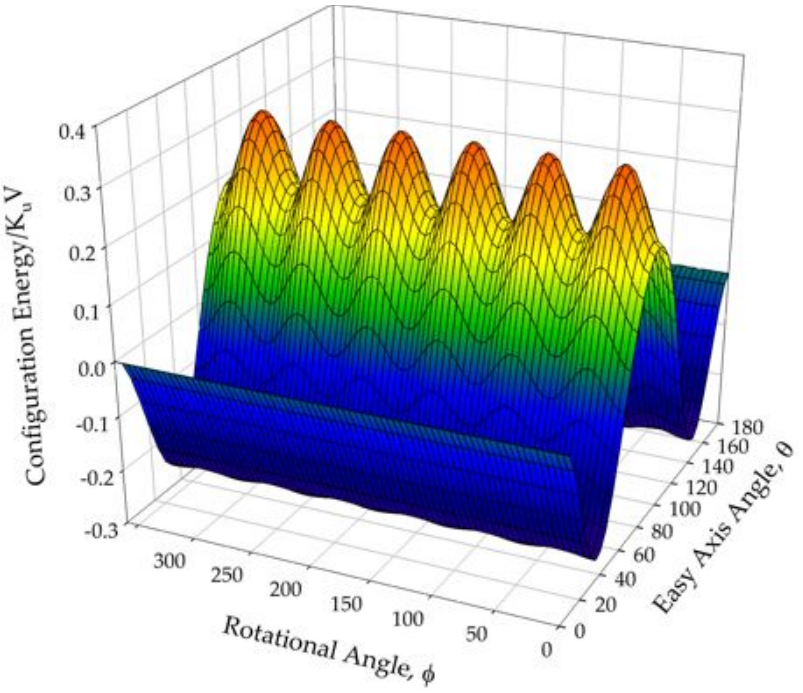

Figure. 5.12: Energy landscape for a spherical hcp particle for $K_{\text{Néel}} = -250K_u$ showing six fold symmetry arising from the underlying crystal structure.

The energy surface shows a six fold symmetry which comes from the underlying crystal symmetry. Note that this result illustrates that the spin non-collinearities follow the crystal symmetry, and are not necessarily cubic as suggested by Garanin et al [64]. Also, the global energy minimum moves to an angle of $\theta = 30^\circ$ from the core easy axis, in alignment with the principal crystal axes. This is one situation where the particular surface faceting is of secondary importance to the underlying crystal symmetry. The influence of the hcp crystal structure on the energy barrier in this case is to reduce it which is in contrast with the fcc structure where the opposite occurs. Qualitatively the same effect occurs with the simple cubic crystal structure, though due to the increased coordination in the hcp structure the relative strength of $K_{\text{Néel}}$ is much smaller.

The final case to consider is that of particles with a simple cubic crystal structure. From a practical perspective the simple cubic structure is less important since there are no real ferromagnetic materials with this crystal structure. However, it is common to use this structure for "toy" models which illustrate the underlying physics without being tied to a particular magnetic material. This is one situation, however, where the specific crystal structure *is* important. Increasing $K_{\text{Néel}}$ for the simple cubic structure initially causes a reduction in the energy barrier, while at a value of $|K_{\text{Néel}}| \approx 125$ the effect becomes very large, strongly enhancing the

energy barrier. The reason for the strong effect of increasing $K_{\text{Néel}}$ partly comes from the reduced coordination number of 6 compared to 12 for bulk structures when comparing simple cubic and face-centred cubic structures. This reduces the effective exchange coupling on the surface, which in turn enhances the relative strength of the surface anisotropy due to spin non-collinearities. The cubic nature of the lattice introduces a highly cubic potential energy surface even for relatively low values of $K_{\text{Néel}}$, as plotted in Figure. 5.13. It is this cubic energy surface induced by spin non-collinearities which causes the rapid increase of the energy barrier at high values of $K_{\text{Néel}}$.

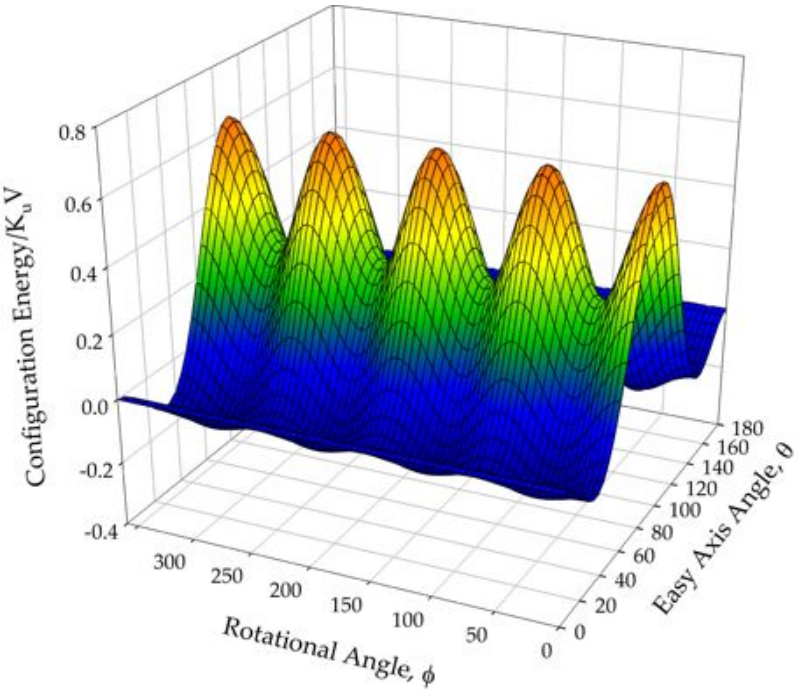

Figure. 5.13: Energy landscape for a spherical particle with a simple cubic crystal structure for $K_{\text{Néel}} = 95K_u$. The energy surface is highly cubic, reflecting the underlying cubic symmetry and the effect of reduced coordination number.

Size Dependance of the Energy Barrier

One important implication of surface anisotropy, with respect to nanoparticles, is the scaling of the energy barrier with size. Experimental measurements by Bødker et al on Fe nanoparticles [66] showed a linear scaling of the energy barrier with inverse particle diameter. They assumed that the particles were spherical but, as has been shown in the above sections, an enhancement of the energy barrier only occurs when the surface anisotropy is very strong and an appreciable fraction of the internal exchange energy. Such strong surface anisotropy induces a cubic energy surface, where the energy barrier

increases primarily with increasing surface area, which is inconsistent with the experimental results. The only situation where the correct scaling occurs is specifically limited to elongated particles with a negative value for the surface anisotropy constant, $K_{\text{Néel}}$. In order to investigate the size scaling of the energy barrier for this situation, elliptical FCC nanoparticles with a 50% elongation and $K_{\text{Néel}} \ll J$ for a range of particle sizes have been simulated. The elongation of 50 % has been chosen so that the surface contribution to the energy barrier is relatively large, while the choice of $K_{\text{Néel}} \ll J$ ensures that there are no visible cubic effects in the energy surface, and so the anisotropy remains uniaxial. The results for these simulations are plotted in Figure. 5.14(a) alongside the experimental results from Bødker et al [66] in Figure. 5.14(b).

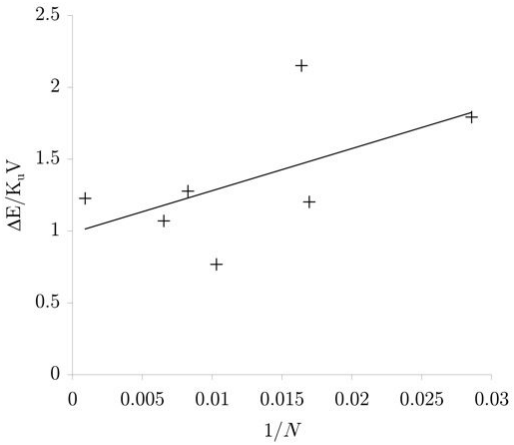

(a) Plot of normalised energy barrier against inverse number of atoms for simulated elliptical nanoparticles with surface anisotropy.

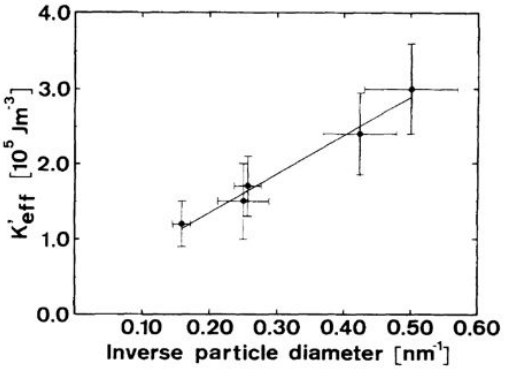

(b) Plot of K_{eff} against inverse particle diameter from [66].

Figure. 5.14: Comparison between simulation (a) and experimental results (b) for size scaling of the energy barrier in nanoparticles with surface anisotropy. Although the units for the two plots are slightly different, they both measure the same physical effect. Both plots show a convergence of the energy barrier to the bulk value for increasing particle size (bulk K_{eff} for Fe is around 0.5 MJ/m^3). The qualitative results from (a) and (b) agree well, showing a general enhancement of the energy barrier above the bulk value for decreasing particle size.

Qualitatively the plots show the same behaviour - a decrease in the particle size gives an increase in the energy barrier. Also both plots converge in the limit of very large particles, where the energy barrier tends to the bulk value. The large scatter in the data points from the simulated particles arises purely from the stepped rearrangement of the atomic surface faceting with changing particle size, and is not at all statistical in nature. This is because particles of this size are not smooth and have rough atomic surfaces, leading to magic numbers of atoms as

the size is gradually increased. Such an effect would not be seen in experimental data due to the size dispersion of the particles and the fact that measurements are usually averaged over several particles. In the experimental paper and in the literature in general [67], it is assumed that, if the volume and surface easy axes are aligned, the energy barrier, ΔE, can be described as a combination of surface and volume contributions, where

$$\Delta E = K_{\text{eff}} V = K_{\text{v}} V + K_{\text{s}} S \tag{5.11}$$

where K_{v} is the volume anisotropy, K_{s} is the surface anisotropy, V is the particle, S is the surface area, and K_{eff} is the *effective* anisotropy constant. Assuming the particles are spheres with diameter d, the effective anisotropy constant can be described by:

$$K_{\text{eff}} = K_{\text{v}} + \frac{6K_{\text{s}}}{d}. \tag{5.12}$$

By plotting the measured effective anisotropy constant against $1/d$ one can obtain the volume and surface contributions to the energy barrier. Unfortunately the assumption that the particles are spherical is almost certainly incorrect. Assuming that the particles are elongated along the easy axis does, however, provide the correct condition where in principle equation 5.11 would apply. The key difficulty in the case of ellipses is accurately determining the extent of the elongation, since this is directly proportional to the surface contribution to the anisotropy. Another issue is ensuring that the elongation occurs only along the magnetic easy axis, since any misalignment will cause the core and surface anisotropy contributions to compete. For these reasons it is difficult, if not impossible, to determine a reasonable estimate of the surface anisotropy constant from nanoparticle measurements. A much more reliable approach is to use a thin film arrangement with very tightly controlled interfaces. In the case of a perfectly flat interface the surface anisotropy always yields an easy plane or easy axis contribution to the anisotropy energy which is relatively easy to extract by variation of the the film thickness.

Nevertheless, it is interesting to consider the case of elongated particles since in principle it is at least possible to extract the surface anisotropy constant from experimental measurement of the size scaling of the anisotropy energy. In order to simplify the analysis the following calculations simulate simple cubic cuboids extended by 50% along the easy axis. The reason for the somewhat arbitrary choice of system is that the contribution of individual surface atoms to the surface anisotropy is simple to evaluate. One could also do the same for face-centred cubic ellipses, though the analysis would be much more involved. It is also

interesting to relate the on-site Néel surface anisotropy constant, $K_{\text{Néel}}$ to the macroscopic surface anisotropy constant K_s taken from the calculation of the energy barrier.

The first issue to address is that of the surface and volume contributions assumed in equation 5.12. In arriving at the results they assumed that the surface area and volume are related empirically for mathematical spheres, neglecting that in fact the magnetic contributions come from discrete atoms. The principal consequence of this is that the surface is in fact a layer of atoms with a certain thickness, which for very small particles significantly increases the surface/volume ratio. It also has the consequence that the core contribution to the energy barrier, having bulk anisotropy, is overestimated. The fraction of core atoms can be represented by a fractional volume contribution, V', which takes into account the fact that surface atoms do not possess a bulk anisotropy. Equation 5.12 also assumes that the whole surface area, S, contributes to the surface part of the energy barrier, which generally is only true for thin films. For non-elongated nanoparticles and small values of K_s, the surface anisotropy typically has an insignificant effect on the energy barrier due to the particle symmetry. In elongated particles, *some* fraction of the surface area, S' contributes to the energy barrier, although the actual value of S' is highly geometry dependent.

With this in mind, it is possible to formulate an expression for the size dependence of the energy barrier for elongated particles along similar lines to equation 5.11, given by:

$$\Delta E = K_{\text{eff}} V = K_u V' + |K_s| S' \tag{5.13}$$

where V' and S' are the fractional volume and surface contributions to the energy barrier. Normalising equation 5.13 with respect to the bulk volumetric energy barrier, $K_u V$, gives the general expression for an elongated particle for $K_s \ll J$ and $K_s < 0$:

$$\frac{\Delta E}{K_u V} = \frac{K_{\text{eff}}}{K_u} = \frac{V'}{V} + \frac{|K_s|}{K_u}\frac{S'}{V}. \tag{5.14}$$

In order to utilize equation 5.14 to extract the surface anisotropy constant from energy barrier measurements or calculations, one must first evaluate the constants V' and S'. The fractional volume constant, V'/V, is relatively easy to calculate by assuming a surface shell of thickness a, where a is the interatomic spacing, essentially defining the thickness of the surface layer. The volume fraction is then the inverse ratio between the total surface volume for a particle of length L and the core volume of length $L - 2a$. Assuming the cuboid particle is extended by a constant δ, then the analytic expression for the volume fraction is

$$\frac{V'}{V} = \frac{(L-2a)^2(\delta L - 2a)}{\delta L^3}. \tag{5.15}$$

Interestingly, exactly the same formula applies for elongated ellipses, replacing the length L with the equatorial particle diameter, D. For simple cubic cuboid particles the above expression is exact, though for very small elliptical nanoparticles with less than $\sim$ 1000 atoms the mathematical expression becomes a poor approximation for the volume fraction.

The *effective* surface fraction, S', is much harder to evaluate even for the simplest of particles, as it is primarily dependant on the surface faceting. For the simplest case of a simple cubic cuboid with angular facets, however, the situation is relatively easy to understand. A visualisation of a simple cubic cuboid in two different magnetic configurations is shown in Figure. 5.15.

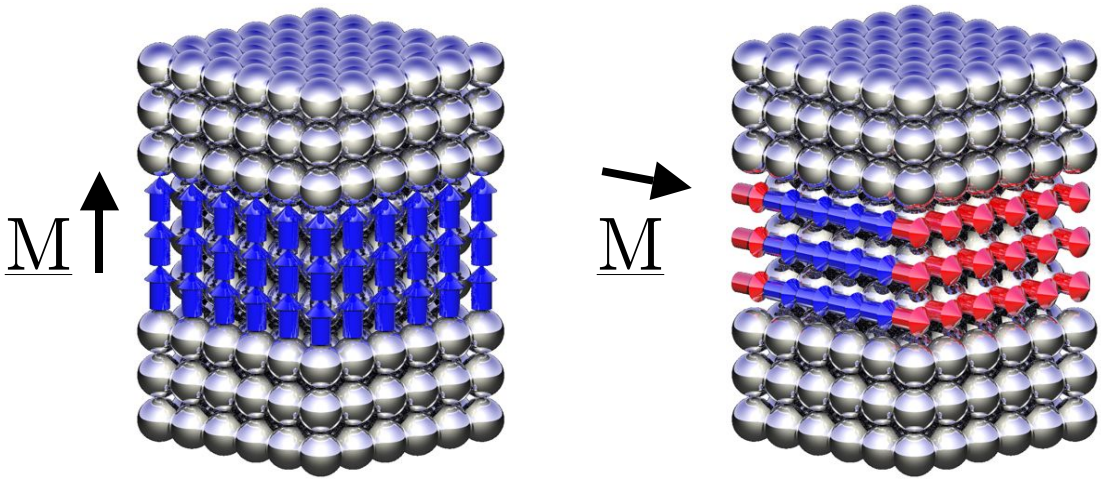

(a) Energy configuration of surface spins when the system magnetisation is aligned along the core easy axis.

(b) Energy configuration of surface spins when the system magnetisation is aligned along the core hard axis.

Figure. 5.15: Visualisation of an elongated cuboid where the system magnetisation is oriented along the core easy axis (a) and core hard axis (b). Red colouring of the spins indicates local maximum energy state, while blue indicates a local minimum energy state. Only the central band of atoms contribute to the energy barrier due to symmetry. See text for further details.

As was shown previously for cube shaped particles, the surface anisotropy makes no contribution to the energy barrier due to symmetry. For elongated particles, however, the side contributions are no longer equal to the end contributions, and so the surface anisotropy then contributes to ΔE. Nevertheless, the symmetric part of the surface can be discounted, and so only the central band of the surface (effectively the elongated part) contributes to the energy barrier, indicated by the coloured spins in the figure. When the system is aligned along the core easy

axis, as illustrated in Figure. 5.15(a), all the spins on the side and edge faces lie in their local easy axis direction, indicated by the blue colouring. When the system magnetisation is aligned along the core hard axis direction, as shown in Figure. 5.15(b), the spins on two faces are in a minimum energy state. However, the edge spins and the spins on two faces are in a maximum energy state, since their spins, indicated in red, are forced into a high energy state by the exchange energy.

Using this information it is possible to express the fraction of surface atoms that contributes to the energy barrier analytically. Contributing atoms are those which change their energy state between the system magnetisation lying in the core easy and hard axis directions. As can be seen from Figure. 5.15 above, this consists of the edge spins, and spins from two of the side faces. Using the same terminology as before when considering a system of length L, elongation δ, and atomic spacing a, we have:

$$\begin{aligned} S' &= 4La(\delta-1) + 2L(\delta-1)(L-2a) \\ &= L(\delta-1)[4a + 2L - 4a] \\ S' &= 2L^2(\delta-1) \end{aligned} \tag{5.16}$$

The total volume of the particle is given by δL^3, which gives the volume fraction of contributing surface atoms:

$$\frac{S'}{V} = \frac{2L^2(\delta-1)}{\delta L^3} = \frac{2(\delta-1)}{\delta L} \tag{5.17}$$

For the case of a cuboid particle with $\delta = 1.5$, this gives:

$$\frac{S'}{V} = \frac{1}{3L} \tag{5.18}$$

In order to test the analytical solution, the energy barrier of particles of different sizes were calculated for three different values of the surface anisotropy. A plot of the normalised energy barrier, taking into account the changing volume fraction, V/V', against $1/3L$ is shown in Figure. 5.16.

As can be seen, the effective measured K_s per atom, taken from the gradient of the line, is very close to the Néel constant used as an input parameter, suggesting that, in principle at least, it is possible to extract the Néel surface anisotropy constant from experimental measurements of the size scaling of the energy barrier in nanoparticles. Of course the system used for the calculations here is largely artificial in terms of its crystal structure and surface geometry. Ideally one would prefer to do the analysis for slightly elliptical, or properly faceted particles

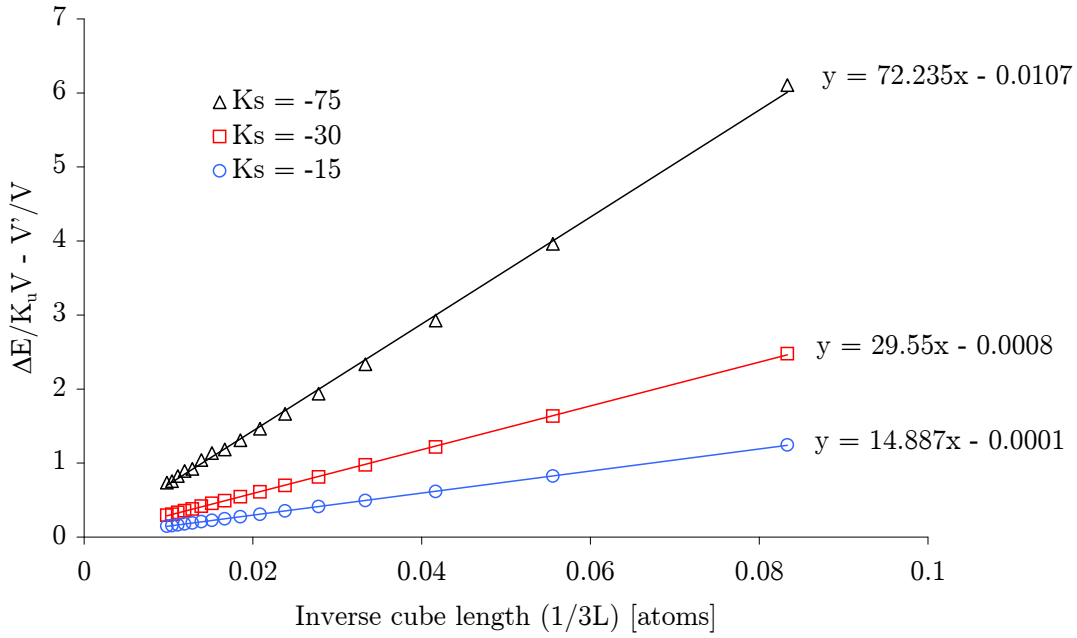

Figure. 5.16: Plot of normalised energy barrier vs inverse cube length for simple cubic cuboidal nanoparticles for different strengths of the surface anisotropy constant, K_s.

with a more realistic crystal structure. However, this significantly complicates the analysis and the analytical expressions can become a little woolly since accurately determining the volume fraction V'/V and surface contribution S'/V is difficult. In general the best method of determining the surface anisotropy constant is with very good thin film interface measurements, since the surface anisotropy contribution is always easy plane or easy axis.

5.3 Conclusion

As has been illustrated in this chapter, the effects of surface anisotropy in nanoparticles can be many and varied, even in the case of weak surface anisotropy. For strong surface anisotropy, the situation is far more complex, with spin non-collinearities inducing a high order energy surface depending on the underlying crystal lattice and surface faceting. However, as $K_{\text{Néel}}$ approaches an appreciable fraction of the exchange energy one must begin to question whether such values are realistic.

The volume scaling of elongated particles with surface anisotropy has also been investigated, showing that, in general, experimental measurements of high anisotropy in small nanoparticles is likely due to en elongation effect. The connection between the macroscopic surface anisotropy constant, K_s, and the microscopic Néel surface anisotropy constant, $K_{\text{Néel}}$, has also been determined

for elongated particles and weak surface anisotropy.. One significant limitation of the Lagrange multiplier technique is that, strictly speaking, it is only applicable for zero temperature, since there is no account of thermal fluctuations in the magnetisation. Given that the surface anisotropy is a surface effect, the reduced surface coordination leads to a reduced criticality in the surface magnetisation, which in principle leads to a more rapid temperature dependence of the surface when compared to bulk anisotropy. In order to investigate this effect one must develop new techniques which use a constraint method with temperature. In the next chapter such a new method is derived and used to investigate the temperature dependence of anisotropy in general, as well as a simple case of a thin film with surface anisotropy.

6. Constrained Monte Carlo Algorithm

A conventional Monte Carlo algorithm is often used to determine equilibrium properties in a wide variety of physical systems, such as the equilibrium magnetisation. Sometimes, however, it is desirable to investigate magnetic systems in quasi-equilibrium situations. One such situation is the temperature dependence of the magnetocrystalline anisotropy energy. In true thermal equilibrium the magnetisation lies along the easy axis (in the case of uniaxial anisotropy). In order to determine the strength of the anisotropy constant, however, one must somehow force the magnetisation to lie along the hard axis. The usual method in this case is to apply a large external field along the magnetic hard axis, forcing the magnetisation along the field direction. This forces the system into a quasi-equilibrium state, so that, by taking into account the effect of the external constraint field, the strength of the anisotropy energy can be estimated. However, the influence of the external field on the thermodynamics is not always clear, and so an alternative constraint method is needed. In collaboration with Dr. P. Asselin, during an internship at Seagate Research, a constrained Monte Carlo approach was developed as outlined in the following.

6.1 Constraint Method

The principal requirement of our constrained Monte Carlo method is to constrain two spatial components of the system magnetisation to be zero, while allowing the other component to vary in magnitude. This essentially conserves the direction of the system magnetisation but the directions of individual spin moments are allowed to vary. For simplicity the following describes the conservation of the z-component of the magnetisation but the method can, of course, be generalised to three dimensions. The method uses a single spin move followed by a corrective move of another spin so that the components of magnetization perpendicular to the z-axis are conserved. The moves are performed as follows:

1) Randomly move spin $\boldsymbol{S}_i$ to $\boldsymbol{S}_i'$ and speculatively accept the move with no conditional change in energy.

2) Move a second spin $\boldsymbol{S}_j$, where $i \neq j$ to $\boldsymbol{S}_j'$, to compensate for the change in the perpendicular components of magnetization, in this case M_x and M_y, such that:

$$S_{j_x}' = S_{i_x} + S_{j_x} - S_{i_x}' \tag{6.1}$$

$$S'_{j_y} = S_{i_y} + S_{j_y} - S'_{i_y} \tag{6.2}$$

$$S'_{j_z} = \text{sign}(S_{j_z})\sqrt{1 - S_{j_x}^2 - S_{j_y}^2} \tag{6.3}$$

As one can see the x and y spin components are forced to remain zero. If $S_{j_x}^2 + S_{j_y}^2 > 1$ then the moves of both spins are rejected as unphysical. If the second move is not rejected this way then it is accepted speculatively. The change in energy for both moves, ΔE_i and ΔE_j are then evaluated as follows:

$$\Delta E_i = E(S'_i, S_j) - E(S_i, S_j) \tag{6.4}$$

$$\Delta E_j = E(S'_i, S'_j) - E(S'_i, S_j) \tag{6.5}$$

Note that the change in energy for the second move is calculated assuming the first move is accepted. The total energy, ΔE_{ij}, for the combined moves is then calculated as follows:

$$\Delta E_{ij} = \Delta E_i + \Delta E_j \tag{6.6}$$

It is essential for a Monte Carlo algorithm to obey the principle of detailed balance, that is to be time reversible. By constraining the direction of the magnetisation, the probability of transitions away from the constraint direction is greater than the converse due to the increase in the number of available states. In order to correct for this, one must find the relationship between a spherical surface element and its projection in the xy plane. This relationship leads directly to a Jacobian prefactor, $\mathcal{J}$, which modifies the acceptance probability to retain ergodicity in the constrained algorithm, given by:

$$\mathcal{J} = \left(\frac{M'_z}{M_z}\right)^2 \left|\frac{S_{j_z}}{S'_{j_z}}\right| \tag{6.7}$$

where M'_z is the z-component of the magnetization after moving both spins, and M_z is the z-component of the magnetization before. In order to constrain M_z to point along $+z$ an additional condition that $M'_z > 0$ is implemented. The total probability of both moves, p, being accepted is now given by:

$$p = \max(1, \mathcal{J} e^{-\frac{\Delta E_{ij}}{k_B T}}) \tag{6.8}$$

Since only one move is random (the other being deterministic), each pair of moves is classed as a single Monte Carlo step. As with the conventional Monte Carlo algorithm, the absolute conservation of total energy leads to the generation of the Micro-canonical thermodynamic ensemble.

Outline

As the constrained Monte Carlo method is new, this chapter will firstly investigate physical situations for which the solution is known, in order to assess the correctness of the method. One test which the constrained Monte Carlo method can compute is the temperature dependence of the magnetocrystalline anisotropy energy (MAE). The temperature dependence of the MAE for both single-ion uniaxial and cubic anisotropies was investigated fully by Callen and Callen in the 1960's [68] and so provides an ideal test of the constrained Monte Carlo method. Since we are dealing with thermodynamic variables, one must take care when calculating an 'energy'. At finite temperatures, due to the entropy, one must compute the *free* energy of the system, which is generally not equal to the internal system energy. One method of calculating the free energy is to calculate the thermodynamic average of the restoring torque on the system magnetisation, the details of which are described in the next section.

The second part of this chapter applies the constrained Monte Carlo method to situations without known solutions. The first of these, already mentioned previously, is the temperature dependence of the Néel surface anisotropy for the case of a thin film. The second is the temperature dependence of the micromagnetic exchange energy, which is a fundamental input parameter for micromagnetic simulations.

6.2 Calculation of Free Energy via Restoring Torque

When a calculation of a system is performed one usually wants to assess the variation of the energy of the system with spatial direction or temperature for example. At temperatures above zero however, the required parameter is the *free* energy, $\mathcal{F}$, which is the total amount of energy in a physical system which can be converted to do work. The free energy of the system can be expressed as:

$$\mathcal{F} = U - TS \tag{6.9}$$

where U is the internal energy, T is the absolute temperature and S is the entropy. The total differentiation of equation 6.9 is given by:

$$d\mathcal{F} = dU - TdS - SdT \tag{6.10}$$

Applying the first and second laws of thermodynamics, where $dU = \delta Q + \delta W$ for isolated systems, and $\delta Q = TdS$ for reversible processes, we have:

$$d\mathcal{F} = \delta W - SdT \tag{6.11}$$

where δW is the *reversible* work done by the system. If the work done by the system is performed at constant temperature then dT is zero. Integrating over the total work done moving between two states a and b yields the difference in free energy between those states, $\Delta\mathcal{F}$, given by:

$$\Delta\mathcal{F} = \int_a^b dW = \sum_i^n W_i \Delta W \tag{6.12}$$

where W_i is the work done in moving from the initial state a to an intermediate state i of n intermediate states [69].

In magnetic systems one generally deals with the influence of magnetic fields of force on the magnetic state of a system. In such a case the work done on the system is equivalent to the torque on the system as a whole. In a spin system the magnitude of the torque is defined by the first derivative of the free energy with respect to θ, the angle from the z-axis, and given by:

$$|\mathcal{T}| = -\frac{\partial\mathcal{F}}{\partial\theta} = |\boldsymbol{S} \times \boldsymbol{H}| \tag{6.13}$$

A schematic of a spin system under the influence of an external applied field is shown in Figure. 6.1. The effect of the field is to induce a torque perpendicular to both $\boldsymbol{S}$ and $\boldsymbol{H}$. In general external and anisotropic fields have an angular dependence with respect to the z-direction, that being the easy axis or external field direction respectively. The magnitude of the torque is directly proportional to the derivative of the free energy.

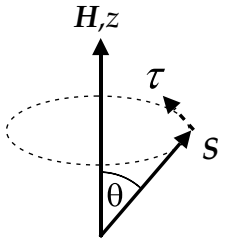

Figure. 6.1: Schematic diagram of the torque on a spin induced by an external field along the z-direction. External and anisotropic fields have an angular dependence with respect to the field direction, indicated by θ.

In order to calculate the free energy from the relationship given in equation 6.12, one must relate the element of work done, δW, to the torque. The element of work done is given by the inexact differential:

$$\delta W = \boldsymbol{F} \cdot d\boldsymbol{s} \tag{6.14}$$

and so one must find the effective force analogous to a mechanical system. For a spin system the generalised force is *always* perpendicular to the spin vector, $\boldsymbol{r}$, and so one can make the following substitution:

$$\mathcal{T} = \boldsymbol{r} \times \boldsymbol{F} = |\boldsymbol{r}||\boldsymbol{F}|\hat{\boldsymbol{n}} \sin\phi = Fr\hat{\boldsymbol{n}} \tag{6.15}$$

where F and r are the magnitudes of the force and spin vector respectively. The magnitude of the torque, $|\mathcal{T}| = Fr$, can be used to obtain the magnitude of the generalised force, which can then be substituted into equation 6.14. Finally an expression for the position vector is required, which is given simply by the arc subtended by the spin, $d\boldsymbol{s} = rd\theta$. Substituting expressions for $\boldsymbol{F}$ and $d\boldsymbol{s}$ into equation 6.14 then gives:

$$\delta W = \frac{|\mathcal{T}|}{r} \cdot rd\theta = |\mathcal{T}|d\theta \tag{6.16}$$

showing the equivalence of an element of work and the magnitude of the torque for a spin system. The equivalent relationship for equation 6.13 for the *difference* in free energy is then found by integration of the total torque between two states a and b, and given by:

$$\Delta\mathcal{F} = -\int_a^b |\mathcal{T}|d\theta \tag{6.17}$$

In order to calculate the total vector torque in an atomistic magnetic system, the total torque, $\mathcal{T}$, is given by a summation of the microscopic torques for all atoms , $\mathcal{T}_i$:

$$\mathcal{T} = \sum_i \mathcal{T}_i = \sum_i \boldsymbol{S}_i \times \boldsymbol{H}_i \tag{6.18}$$

where $\boldsymbol{H}_i$ is the net field and $\boldsymbol{S}_i$ the spin moment at site i. Due to the vectorial nature of the torque, the thermodynamic average of the torque is computed while maintaining the vector components of torque, $\mathcal{T}_x$,$\mathcal{T}_y$ and $\mathcal{T}_z$ as separate summations. The magnitude of the total torque is then calculated from the thermodynamic average of the vector components, ie. $|\mathcal{T}| = |<\mathcal{T}>|$.

By calculation and integration of the system torque one can obtain the free energy difference between two states by the relationship given in equation 6.18. In some situations the variation of a physical parameter with temperature can be consistent, and so the integral over elements of work can be replaced with a one-point Gaussian quadrature rule, namely that a single physical state is exactly representative of the entire integral[1]. The use of the quadrature rule must be

[1] The one-point Gaussian quadrature rule allows the representation of a finite integral by a single value of the integrated function [70].

exercised with caution, however, as is is not applicable to all systems.

6.3 Temperature Dependence of the Magnetocrystalline Anisotropy

Magnetocrystalline anisotropy is of critical importance in magnetism, defining domain structures within bulk material and having a direct application in the stability of magnetic recording media. Calculating the temperature dependence of the magnetocrystalline anisotropy provides an ideal test of the constrained Monte Carlo method since the physical origin is at the atomic level and there is a well established analytical theory by Callen and Callen [68] describing the temperature variation for single-ion uniaxial and cubic forms of anisotropy for all temperatures.

Since we are only interested in the fundamental physics of the temperature dependence of the anisotropy energy, a generic atomistic model system with a face-centred cubic crystal structure and a Curie temperature of 1000K has been chosen. As the anisotropy is a bulk property a relatively large system of around 16000 atoms, with periodic boundary conditions, was used to minimise the possibility of finite size effects and eliminate surface effects.

Uniaxial Single-ion Anisotropy

Single-ion uniaxial anisotropy arises from the interaction of localised electrons within a magnetic metal with the local atomic crystal environment through spin-orbit coupling. In some materials this induces a single axis along which the atomic magnetic moment prefers to orientate, known as uniaxial anisotropy. In order to calculate the uniaxial free energy for a given temperature, one must compute an integral of work, as described by equation 6.12. Since the uniaxial anisotropy energy at the atomic level is dependent on the angle of the atomic spin from the easy axis, θ, this provides a good variable over which to integrate. The integral is computed by taking the thermodynamic average of the torque from an angle of $\theta = 0^\circ$ to $\theta = 90^\circ$, generating a so-called torque curve. Plots of the restoring torque as a function of angle from the easy axis at temperatures of 10 K, 100 K and 500 K are shown in Figure. 6.2. For comparison, the system anisotropy energy as a function of angle is also plotted alongside the torque curves. The anisotropy energy is calculated as a sum over all atoms of the on-site anisotropy energy.

The first point to note regarding the torque curves is that both the x and z components of the torque are effectively zero for all temperatures. This

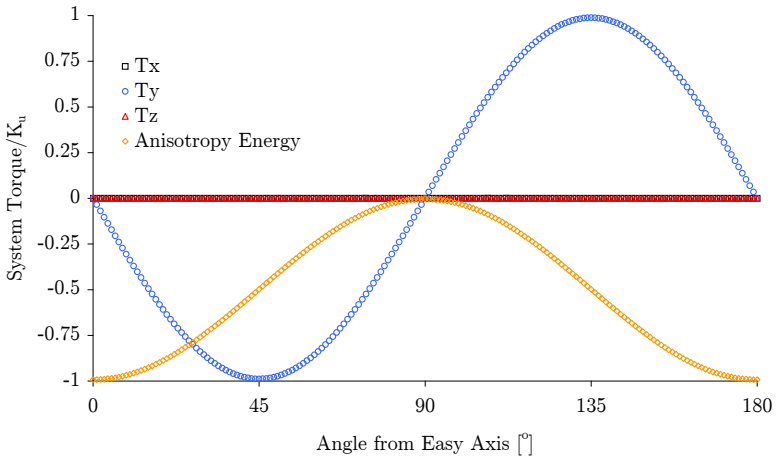

(a) Plot of system torque normalised to the system uniaxial anisotropy as a function of angle from the easy axis at 10 K.

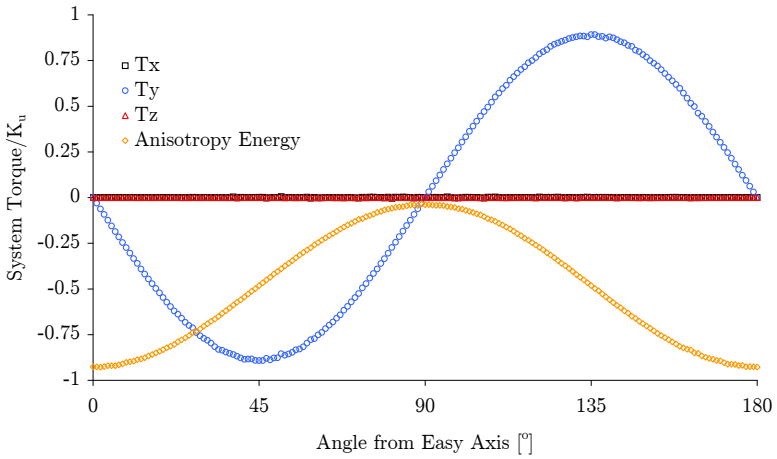

(b) Plot of system torque normalised to the system uniaxial anisotropy as a function of angle from the easy axis at 100 K.

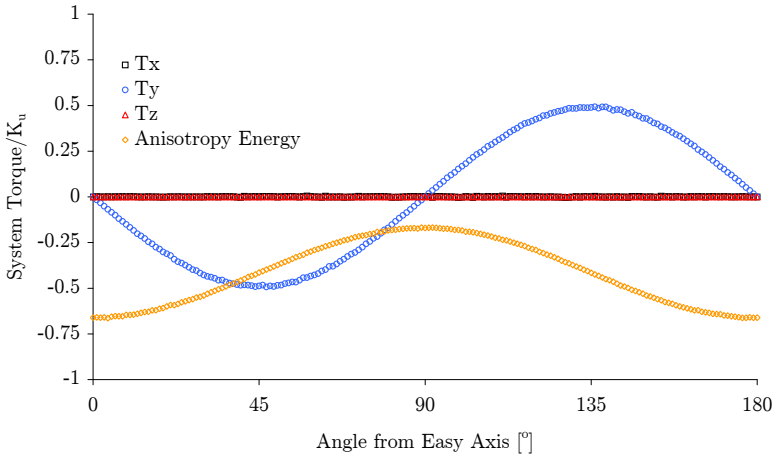

(c) Plot of system torque normalised to the system uniaxial anisotropy as a function of angle from the easy axis at 500 K.

Figure. 6.2: Plots of system torque and anisotropy energy for a system with uniaxial anisotropy as a function of angle from the easy axis for 10 K, 100 K, and 500 K.

is expected since the torque acts perpendicular to the net field (along the z-direction), so $\mathcal{T}_z$ is zero. Similarly, the x-component of the torque, $\mathcal{T}_x$, is zero since the system magnetisation is constrained to point along the x-axis. This leaves only the y-component of the torque, which varies sinusoidally with increasing angle from the easy axis. It is interesting to note that the $\sin(2\theta)$ shape of the torque curve is independent of temperature, while the increased temperature simply reduces the amplitude of the torque curve. In order to calculate the free anisotropy energy difference at each temperature, one needs to calculate an integral of the torque from $\theta = 0, 90^\circ$. At zero temperature the torque is given by the derivative of the total internal energy, U, which for the case of uniaxial anisotropy is:

$$U = K_u \sin^2\theta + J(\phi) \tag{6.19}$$

where K_u is the uniaxial anisotropy constant. Taking the derivative with respect to the angle from the easy axis, noting that the exchange contribution is isotropic in ϕ, gives:

$$|\mathcal{T}| = -\frac{\partial U}{\partial \theta} = -2K_u \sin\theta\cos\theta = -2K_u \frac{1}{2}(\sin 2\theta + \sin 0) = -K_u \sin 2\theta \tag{6.20}$$

If the above relationship extends to all temperatures, then one would expect that the amplitude of the anisotropy energy function and that of the torque curve are the same, which is indeed seen in Figure. 6.2. The data for all three plots show that the torque at $\theta = 45^\circ$ is exactly equivalent to the difference in anisotropy energy between $\theta = 0^\circ$ and $\theta = 90^\circ$, which essentially defines the effective anisotropy constant for the system. This means that the change in free anisotropy energy can be represented by a one-point Gaussian quadrature rule by calculating the restoring torque at an angle of $\theta = 45^\circ$. A final point to note is the evident barrier lowering of the anisotropy energy with elevated temperatures, since the anisotropy energy no longer goes to zero at $\theta = 90^\circ$. This comes from the statistical contribution of the spin dispersion at elevated temperatures, and has the effect of increasing the energy minimum and reducing the energy maximum equally.

Having established that the one-point quadrature rule applies to uniaxial anisotropy, one can then go and easily calculate the temperature dependence of the uniaxial anisotropy constant, as shown in Figure. 6.3.

As can be seen, the calculated value of the uniaxial anisotropy constant at low temperatures converges very well towards the zero temperature value. The temperature dependence of K_u is much stronger than that of the magnetisation.

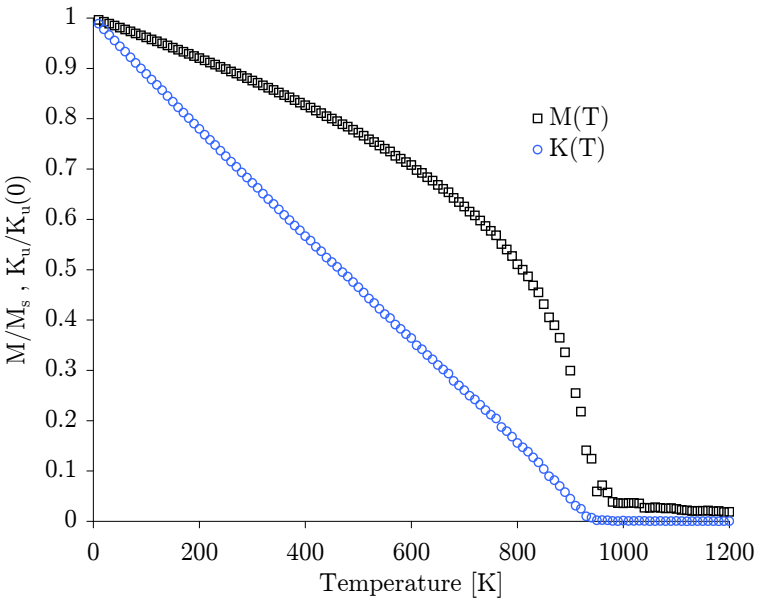

Figure. 6.3: Plot of temperature dependence of normalised magnetisation and uniaxial anisotropy calculated from the torque method. The anisotropy constant is much more temperature dependent than the magnetisation.

In order to investigate the temperature dependent scaling of the uniaxial anisotropy with magnetisation, a plot of the natural logarithm of $K_u/K_u(0)$ against M/M_s is shown in Figure. 6.4. This shows the exponent of K with M, which can be directly compared with the Callen-Callen theory for uniaxial anisotropy described earlier. Also plotted is the expected low temperature exponent of $K \propto M^3$.

As can be seen at low temperatures, the data show excellent agreement with the theory, showing a temperature scaling of $K \propto M^3$. At higher temperatures (lower M/M_s) the anisotropy energy varies less rapidly with the system magnetisation, in qualitative agreement with the Callen-Callen theory. The discrepancy between the calculated data and theory could come from the fact that the theory assumed a mean-field approach, where the exchange interactions are equal and long ranged. In the simulations exchange interactions were limited to nearest neighbours only.

Having calculated the temperature scaling of uniaxial anisotropy, the next section does the same for cubic anisotropy. Here the nature of the cubic anisotropy energy surface means that its temperature dependence is substantially different.

Cubic Anisotropy

Another form of anisotropy is cubic anisotropy, commonly seen in Fe and Ni magnets. Generally cubic anisotropy is much weaker than uniaxial anisotropy

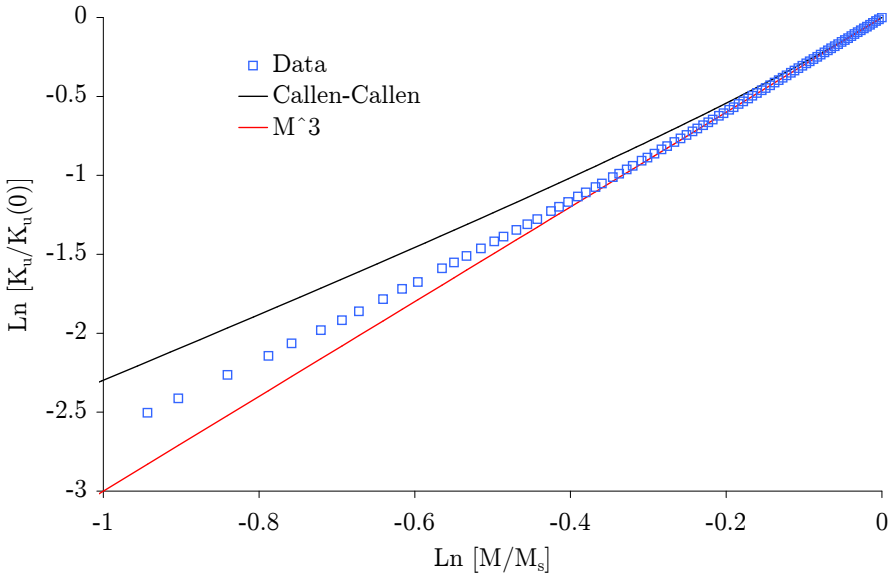

Figure. 6.4: Plot of magnetisation dependence of normalised uniaxial anisotropy calculated compared with Callen-Callen theory and low temperature limit of $K_u \propto M^3$.

due to the symmetry of the lattice [71]. Callen and Callen also studied the temperature dependence of cubic anisotropy and derived an M^{10} dependence for low temperatures. The cubic nature of the energy surface means that the restoring torque depends on the azimuthal and rotational angles, unlike uniaxial anisotropy where only the angle from the easy axis was important. However, due to symmetry, only two rotational angles are important for the determination of the temperature dependence of cubic anisotropy, namely $\phi = 0^\circ$ and $\phi = 45^\circ$. Torque curves and the corresponding anisotropy energies for these two angles are plotted in Figure. 6.5.

As can be seen, the two different rotational angles each give a different torque curve due to the cubic nature of the anisotropy energy. For $\phi = 45^\circ$, the x and y components of the torque are equal, since the restoring torque acts perpendicularly to the constraint direction. In this case the anisotropy energy is extracted from the magnitude of the total torque vector. As in the case of uniaxial anisotropy the shape of the torque curves do not change their shape with temperature; they are only scaled. Thus in the same way as before, one can represent the whole torque integral by calculating the torque at a single point. This point was chosen at the maximum of the torque curve, where $\theta = 22.5^\circ$ and $\phi = 0^\circ$, where the anisotropy energy is given by:

$$K_{cubic} = \frac{\mathcal{T}_y(22.5, 0)}{2}. \tag{6.21}$$

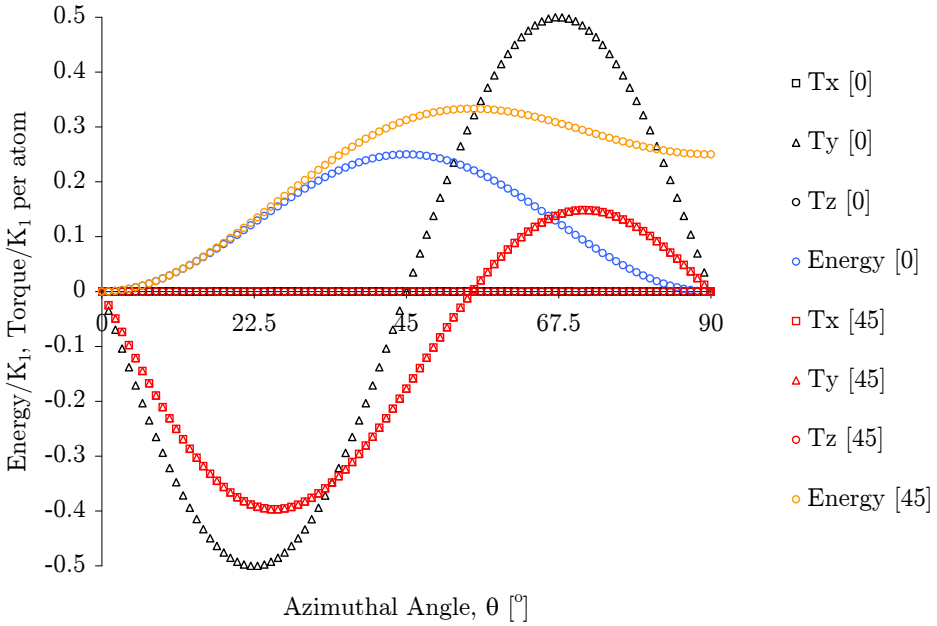

Figure. 6.5: Plot of normalised torque and anisotropy energy as a function of azimuthal angle, θ for rotational angles of $\phi = 0°$ [black] and $\phi = 45°$ [red]. The cubic nature of the energy surface gives two different torque curves. The maximum torque for $\phi = 0°$ is related to the cubic anisotropy energy by a factor 2, allowing the use of a one-point quadrature rule to represent the entire torque integral.

This result can also be derived by taking the negative first derivative of the zero temperature anisotropy energy with respect to the azimuthal angle. Using this approach the temperature dependence of the cubic anisotropy and system magnetisation for the same simulation is plotted in Figure. 6.6.

As can be seen, the cubic anisotropy constant is much more strongly temperature dependent compared to uniaxial anisotropy. As before, the temperature scaling of the cubic anisotropy with system magnetisation is shown in Figure. 6.7. Again this shows excellent agreement with the Callen-Callen theory of a low temperature scaling exponent of $K_c \sim M^{10}$.

Having now validated the constrained Monte Carlo method by calculating the known temperature dependencies of bulk anisotropy constants, the next section will investigate the temperature dependence of the surface anisotropy for a perfect thin film.

Surface Anisotropy

As illustrated previously in Chapter 5, the effects of Néel surface anisotropy can be many and varied, due to the complex interaction between the underlying crystal lattice and surface faceting. Calculating the temperature dependence of the surface anisotropy in nanoparticles presents a significant challenge in

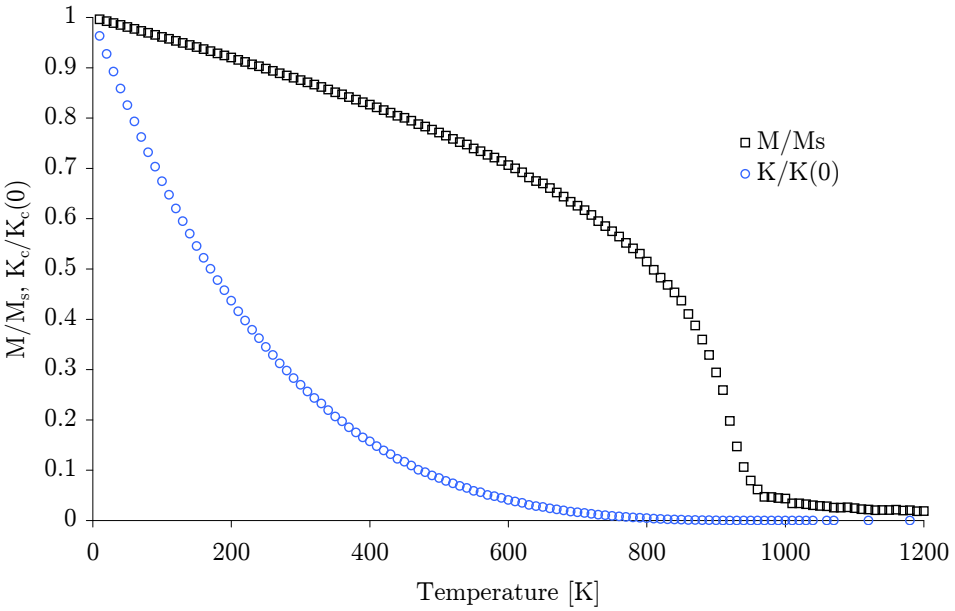

Figure. 6.6: Plot of temperature dependence of normalised magnetisation and cubic anisotropy calculated from the torque method. Compared with uniaxial anisotropy cubic anisotropy is considerably more temperature dependent.

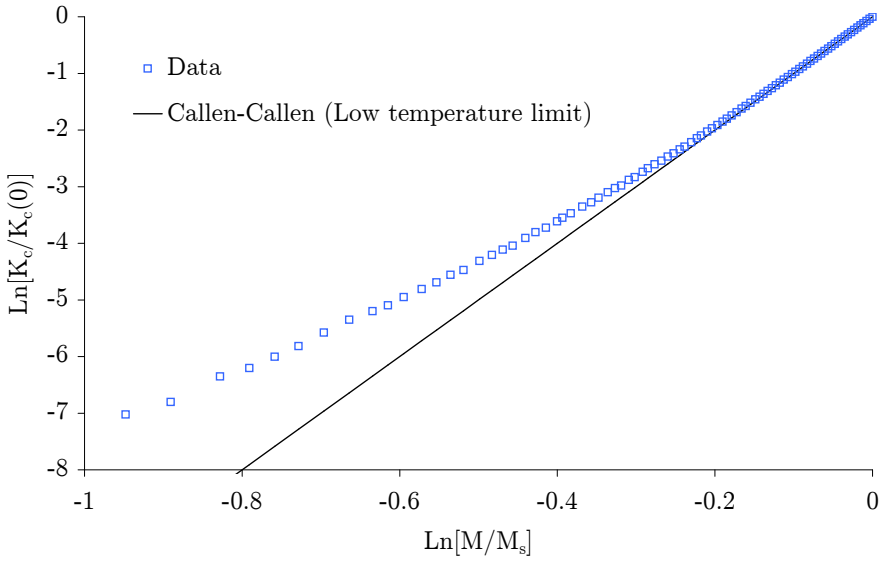

Figure. 6.7: Plot of magnetisation dependence of normalised cubic anisotropy calculated compared with Callen-Callen theory for the low temperature limit of $K_c \sim M^{10}$.

terms of methods and in computational effort. For materials with a cubic lattice, where the surface anisotropy is very large, the spin non-collinearities induce cubic energy surfaces. The "cubicness" of these surfaces will be very strongly temperature dependent since the anisotropy arises from surface atoms with reduced coordination and thus reduced effective Curie temperature. A full treatment of this problem would require significant computer resources since, in order to calculate the surface anisotropy, one must calculate the entire torque surface for each temperature, rather than using the Gaussian quadrature rule to calculate a single point. Nevertheless, a special case where the surface anisotropy can be studied in nanoparticles arises for FePt, where the layered nature of the material yields a purely uniaxial or easy plane anisotropy for weak values of $K_{\text{Néel}}$. This is covered in more detail with reference to the simulation of Heat Assisted Magnetic Recording in Chapter 7.

There is one common situation where the temperature dependence of surface anisotropy can be studied in detail, namely that of thin films. Thin films have attracted a great deal of research interest over the past 50 years and so a large body of experimental data exists. Nevertheless, achieving good experimental data on the temperature dependence of surface anisotropy requires the creation of very thin films with very sharp interfaces, which has only been technologically feasible within the last decade. This is because the influence of surface anisotropy is usually determined by varying the thickness of the magnetic layer, so that volume and surface contributions can be separated. For thick films the volume component strongly dominates the overall anisotropy, leading to a large degree of uncertainty in the strength of the surface contribution. Another problem arises with temperature dependent atomic migration, structural changes and interface mixing, which cause a change in the surface properties [72]. Taking proper account of all these temperature dependent effects would require a combined molecular dynamics and magnetic model similar to that described in Chapter 4, where the structural changes of the magnetic and interface materials are included explicitly. Nevertheless, one can still investigate the idealistic case where a perfect interface remains at all temperatures, and thus garner an understanding of the temperature dependence of the Néel surface anisotropy.

In the case of a perfect single crystal magnetic film with a face-centred-cubic crystal structure with interfaces cut along the [001] direction, the on-site Néel surface anisotropy yields a purely uniaxial anisotropy, as shown in Figure. 6.8. A visualisation of the surface atomic arrangement is inset. Since the surface anisotropy is purely uniaxial, the torque method described above can be used. Thus the overall anisotropy energy for the system can be obtained by calculating the restoring torque when the system magnetisation is held at 45° to the easy axis.

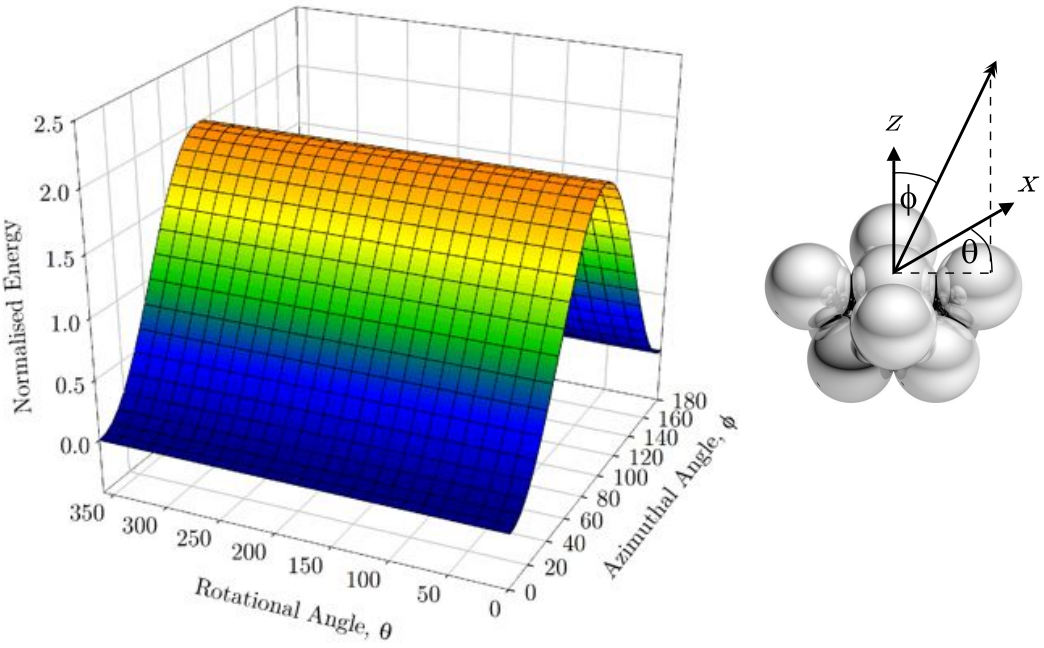

Figure. 6.8: Plot of normalised anisotropy energy for the fcc [001] surface. A visualisation of the atomic surface arrangement is inset. The energy surface is entirely uniaxial, allowing the temperature dependence of the surface anisotropy contribution to be easily studied.

In order to simulate a section of thin film, a generic magnetic material with an fcc crystal structure and a T_c of around 1300 K was chosen, as shown in Figure. 6.9. The surface atoms are coloured in copper, while the bulk atoms are coloured silver. In order to eliminate edge effects within the film, periodic boundary conditions in the film plane were used.

Although the material has an fcc crystal structure, a uniaxial bulk anisotropy was chosen in order to better reflect experiments. The symmetry of the lattice also allows the choice of either an in-plane or out-of-plane easy axis. For the purposes of these simulations only the case where the surface and bulk anisotropy directions are aligned in the perpendicular direction was investigated. Generally, surface anisotropy is found to be much stronger than bulk-type anisotropy, and so a value of $K_\mathrm{s} = 10K_\mathrm{u}$ was chosen. Since the surface atoms must be identified in order to calculate the Néel surface anisotropy, it is trivial to separate the surface and core components of anisotropy and magnetisation. This allows the investigation of the temperature scaling of the surface anisotropy separately with respect to the surface magnetisation, M_surface, and core magnetisation, M_core.

Since the energy surface for surface atoms is uniaxial in nature, one would expect that the scaling of the surface anisotropy with respect to the surface magnetisation should follow $K_s \sim M^3_\mathrm{surface}$, as was found in the bulk case. In

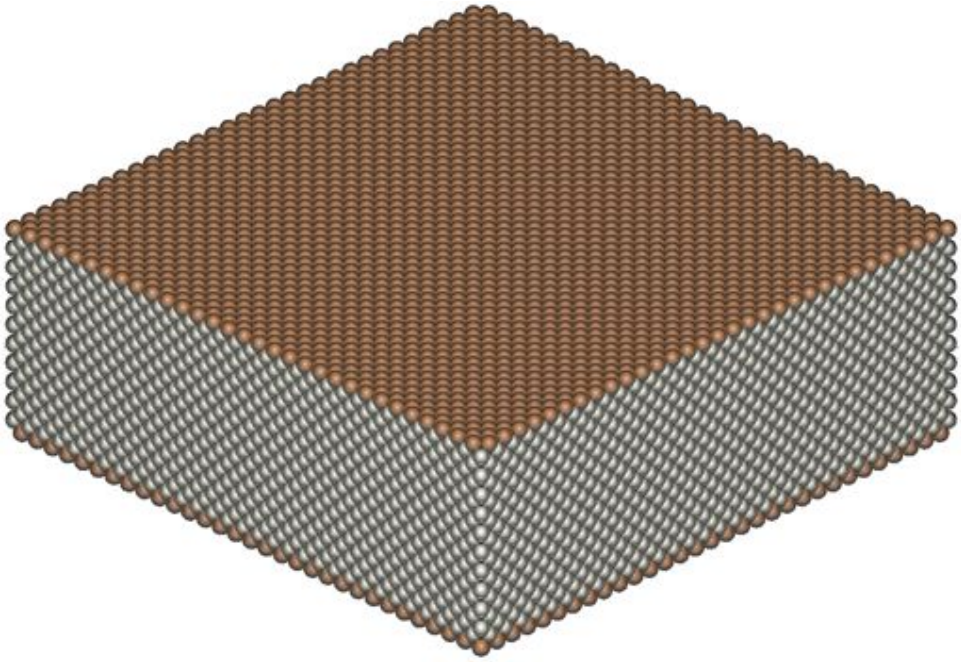

Figure. 6.9: Visualisation of a section of a thin film system with an fcc crystal structure containing around 45,000 atoms. Surface atoms are indicated by the copper colouring, while silver indicates the bulk atoms. The bulk edges have periodic boundary conditions in order to eliminate edge effects.

principle this effect could be measured experimentally using a monolayer of magnetic material, though such a structure is generally unstable at anything other than cryogenic temperatures. However, a thicker layer of magnetic material, with more bulk-like properties, should show a different scaling of the surface anisotropy with the core magnetisation. The scaling of the surface anisotropy with core magnetisation is unknown a-priori, and is coordination number and material dependent. Nevertheless, it is this scaling which would be measured experimentally.

A plot of the normalised system magnetisation and surface anisotropy calculated via the torque method as a function of temperature is plotted in Figure. 6.10. The surface, core and volume average magnetisation are plotted, each having the same Curie temperature but with a different criticality, as previously reported by Binder et al [44].

The stronger criticality in the surface magnetisation arises from a reduction in coordination number. An isolated surface layer would also have a reduced Curie temperature, but due to the thickness of the magnetic material the surface layer is polarised by the core and thus has the same T_c as the core of around 1300 K.

Figure. 6.11 shows the temperature scaling of the surface anisotropy with the surface and average system magnetisation. Inset is a linear regression fit of the

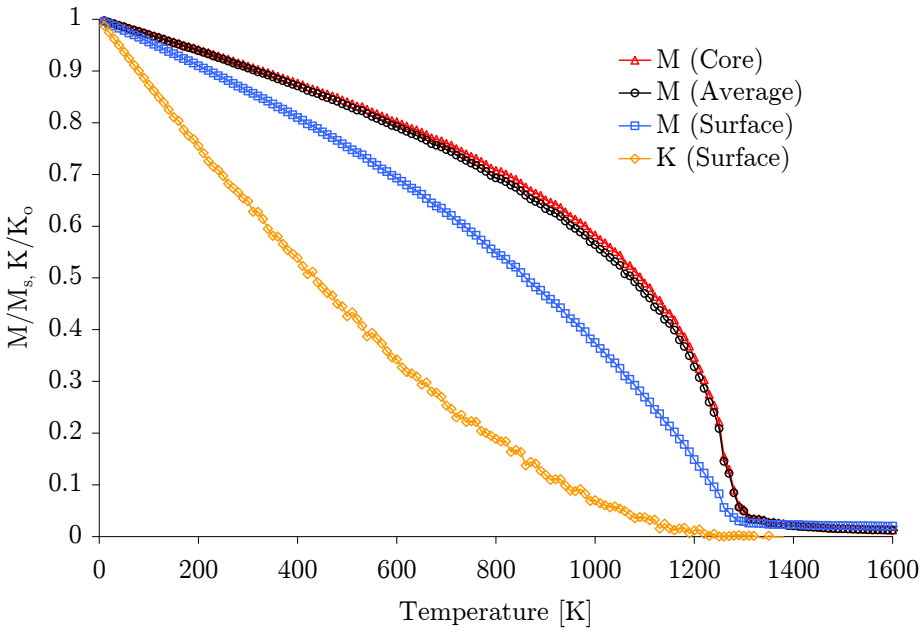

Figure. 6.10: Plot of normalised magnetisation and surface anisotropy against temperature for a small section of thin film. The surface magnetisation shows stronger criticality than the core and average magnetisation.

low temperature scaling of the surface anisotropy with surface magnetisation, giving a low temperature exponent of $K_{\text{surface}} \sim M^{3}_{\text{surface}}$, in excellent agreement with the Callen-Callen theory for single ion uniaxial anisotropy.

The scaling of the surface anisotropy with average system magnetisation shows an exponent of $K_{\text{surface}} \sim M^{4.57}_{\text{average}}$, which is somewhat rapid compared to bulk uniaxial anisotropy. This arises due to the increased criticality of the surface magnetisation, and thus the result is quite expected. In contrast, experimental results for Gd show a largely linear temperature dependence of surface anisotropy[73]. The origin of the discrepancy could be due to a number of factors, including structural changes with increased temperatures or a lattice mismatch which could be influencing the bulk-type anisotropy. One other possibility is that of an enhanced exchange interaction at the surface of the material [74]. An increased exchange interaction would lead to a *reduction* in the criticality of the surface layer and similarly the temperature scaling of the surface anisotropy.

The temperature dependence of the surface anisotropy also leads to a number of interesting effects, such as a temperature dependent re-orientation of the magnetisation direction from in plane to out-of plane [72]. Such an effect can occur when the easy directions of the surface and core anisotropies compete. At low temperatures the magnetisation lies along the surface easy axis. As the temperature is increased the surface contribution to the anisotropy energy

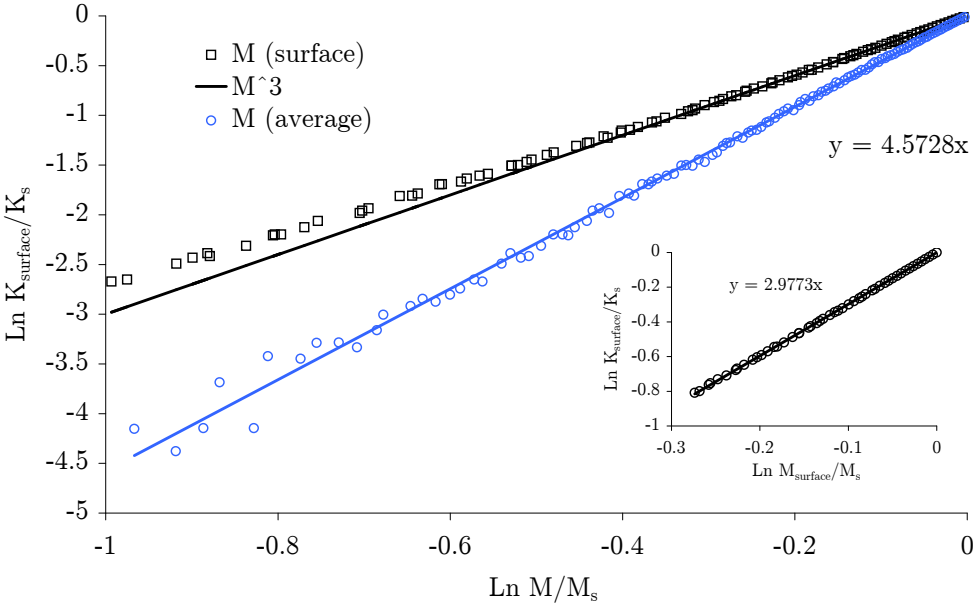

Figure. 6.11: Plot of temperature scaling of surface anisotropy with surface and average system magnetisation. Inset is the low temperature scaling of the surface anisotropy with surface magnetisation, showing excellent agreement with the Callen-Callen theory. Compared with the average magnetisation the surface anisotropy varies with an exponent of $M^{4.57}$ for a wide range of temperatures.

rapidly decreases, so the system magnetisation lies along the bulk easy axis.

The final section of this chapter describes the application of the constrained Monte Carlo algorithm to calculate the temperature scaling of the micromagnetic exchange constant.

6.4 Temperature Scaling of the Micromagnetic Exchange Constant

The micromagnetic exchange constant, A, is a key parameter for micromagnetic simulations, describing the strength of magnetic correlations in neighbouring micromagnetic cells. Generally such simulations do not explicitly take account of temperature effects, but simply use *effective* parameters for exchange and anisotropy at elevated temperatures. At zero temperature, the micromagnetic exchange constant is related to the atomistic Heisenberg exchange for a simple cubic system by the expression:

$$A = \frac{\sum_{ij} J_{ij}}{2a} = \frac{\mathcal{J}}{2a} \tag{6.22}$$

where a is the interatomic spacing. In order to account for elevated temperatures, an effective Heisenberg exchange constant, $\mathcal{J}$ is used instead of J_{ij} with an assumed temperature dependence from experimental measurements. This temperature dependence is of course material specific, depending on the range and form of the exchange integral.

However, it is not clear from a theoretical perspective that the temperature dependence of the micromagnetic exchange constant is the same as that of the microscopic exchange interaction, $\mathcal{J}$, which scales with the square of the system magnetisation. Indeed, the micromagnetic exchange describes correlations in atomistic spin direction over a certain length scale. Clearly, at elevated temperatures, thermal fluctuations produce some degree of disorder on the atomic scale, which are not present at the micromagnetic scale. These extra degrees of freedom at the atomic level suggest that the temperature scaling of the micromagnetic exchange constant *should* be different from the atomistic temperature dependence of the exchange. In order to accurately determine the temperature dependence of the micromagnetic exchange, one must replicate the effect of long-range spin correlations within an atomistic spin model. The strength of these correlations can then be calculated directly, which equates to the micromagnetic exchange constant.

Statement of the Problem

The simplest possible case is to consider a simple material with no anisotropy or demagnetisation fields and with no external field, essentially only having an internal exchange field. On the micromagnetic level, we then assume we have two adjacent magnetic cells of this material, whose magnetisation directions are M_1 and M_2. The internal energy for this system is then given by:

$$U = A\boldsymbol{M}_1 \cdot \boldsymbol{M}_2 = A|M_1||M_2| \cos\varphi \tag{6.23}$$

where φ is the angle between the adjacent micromagnetic spins, as illustrated in Figure. 6.12.

At the atomic level, the angle between the two micromagnetic spins is represented by a continuous spin spiral, as shown in Figure. 6.13(a). The blue colouring indicates spins which are orientated in the positive z-direction, the green colouring indicates spins pointing in the y-direction, and the red colouring indicates spins pointing in the negative z-direction.

At zero temperature the spins in each plane are aligned in parallel, and so this can be represented as a series of $\mathcal{N}_{\text{planes}}$ atomic planes, as shown in Figure 6.13(b). Each plane has a magnetisation vector $\vec{m}$ which lies at an angle of θ to each of the

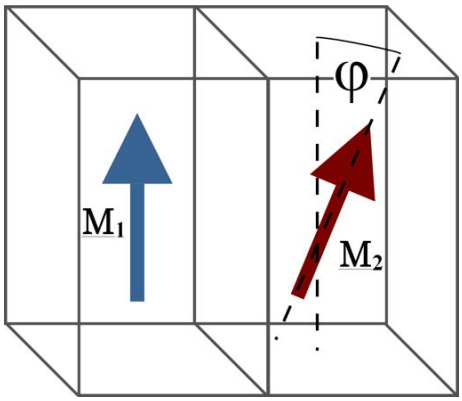

Figure. 6.12: Visualisation of two interacting micromagnetic cells, M_1 and M_2, separated by an angle φ.

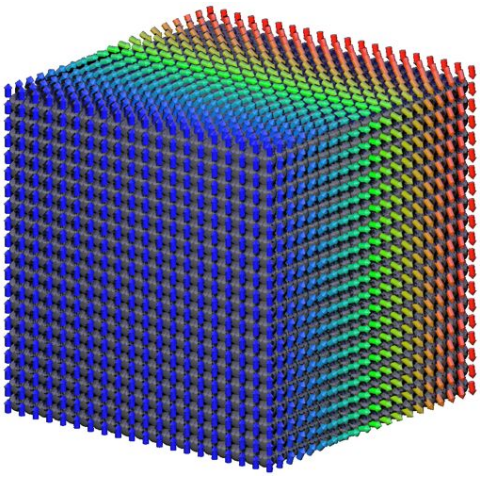

(a) Visualisation of an atomistic spin spiral, showing surface spins only. This represents the micromagnetic cell model in Figure. 6.12 at the atomic level, with an angle of separation of π radians.

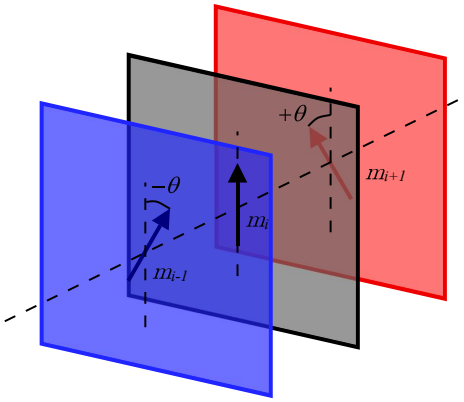

(b) Schematic diagram showing planes of atoms with magnetisation m. The neighbouring planes lie at an angle $\pm\theta$.

Figure. 6.13: Visualisation of an atomistic spin spiral (a) and schematic diagram of neighbouring atomic planes within the spin spiral (b). The spin spiral represents the atomic level spin configuration at zero K, showing planes of parallel spins. This can be represented by a series of atomic planes, with each plane separated by an angle $\pm\theta$.

neighbouring planes. The angle between neighbouring planes is given by:

$$\theta = \frac{\varphi}{\mathcal{N}_{\text{planes}} - 1}. \tag{6.24}$$

Since all the spins within the plane are aligned in parallel, and assuming that θ is a small angle, then the internal energy of each plane is defined by its two neighbouring planes and given by:

$$U = \frac{\mathcal{J}}{2}\left(\boldsymbol{m}_i \cdot \boldsymbol{m}_{i+1} + \boldsymbol{m}_i \cdot \boldsymbol{m}_{i-1}\right) = \mathcal{J}\cos\theta \tag{6.25}$$

Note that the factor 2 arises from the double sum, since the energy between planes is added twice for each plane. Given the above expression for the energy of each plane, and noting that θ is the same for all planes, one can calculate the difference in energy between a system with and without a spin spiral. For a system without a spin spiral, essentially the minimum energy configuration, the angle between planes is zero. Thus the total increase in internal energy caused by the insertion of a spin spiral is given by:

$$\Delta U = \mathcal{J}\mathcal{N}_{\text{planes}}\left(\cos\theta - \cos 0\right) = \mathcal{J}\mathcal{N}_{\text{planes}}\left(\cos\theta - 1\right) \tag{6.26}$$

If it is assumed that the thermodynamic average of the magnetisation within a plane is the same for all planes, and that the angle between all planes is the same, then this idea can be extended to higher temperatures, where the internal energy is replaced by the *free* energy. Thus an effective exchange parameter, $\mathcal{J}(T)$, can be calculated as a function of the system temperature, and through Equation. 6.22 related to the micromagnetic exchange constant, A.

Calculation of the Free Energy of a Spin Spiral using the Torque Method

In order to calculate the effective exchange parameter, one must first compute the free energy of the system. The torque, $—\mathcal{T}—$, is defined as the negative first derivative of the free energy with respect to some generic thermodynamic variable, as previously described in Section. 6.2. In this case the variable was chosen to be the angle between adjacent planes, θ. Thus we have:

$$|\mathcal{T}| = -\frac{\partial \mathcal{F}}{\partial \theta} = -\frac{\partial \langle U \rangle}{\partial \theta} \tag{6.27}$$

Taking the derivative of equation. 6.25 with respect to θ then gives:

$$|\mathcal{T}| = \mathcal{J}\sin\theta \simeq \mathcal{J}\theta \text{ for small angles} \tag{6.28}$$

In order to check that the torque yields the system energy at zero temperature, one can integrate with respect to the angle between planes, so that:

$$\Delta U_{\text{torque}} = -\int_0^{\theta} \mathcal{J}\mathcal{N}_{\text{planes}} \sin\theta d\theta = \mathcal{J}\mathcal{N}_{\text{planes}} (\cos\theta - 1) \tag{6.29}$$

which is indeed the same expression as derived in equation 6.26.

Simulation Method

The micromagnetic exchange constant is calculated using a simple cubic atomic system of size $40 \times 20 \times 20$ atoms with periodic boundary conditions, as shown in Figure. 6.14. The Hamiltonian for the system is formed purely of the Heisenberg exchange interaction, which is limited to nearest neighbours only with an exchange constant of $J_{ij} = 6.82 \times 10^{-21}$ Joules/link, giving a Curie temperature of 750 K.

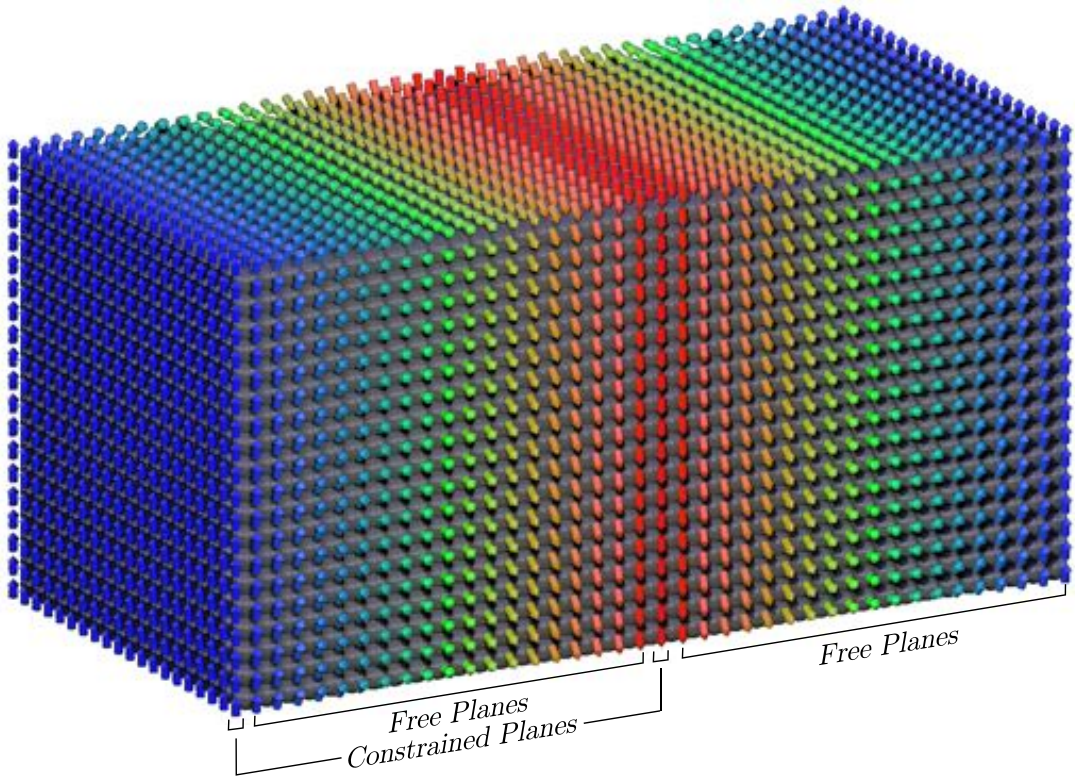

Figure. 6.14: Visualisation of the atomistic system used to calculate the micromagnetic exchange constant. Two of the planes are constrained to point along different directions, while the other planes are equilibrated using the standard Monte Carlo algorithm. The constrained spins at the centre of the system are set at an angle φ to the z-axis.

In order to force a spin spiral into the system, two constraints must be used, holding the magnetisation of one plane along the z-axis, and the magnetisation

of another plane at an angle of φ to the z-axis. In order to eliminate surface effects arising from reduced coordination number at the constrained planes, the system is constructed to be double length, where the sense of rotation of the spin planes is opposite at either side of the constrained planes. The remaining planes do not need to be constrained and so they are minimised using a standard Monte Carlo Metropolis algorithm. The system is initialised in a spin spiral between the two constrained planes, which is the ideal configuration at zero temperature.

The restoring torque is the same for all the planes in the system due to symmetry, and so one could calculate the torque for a single plane and multiply by the number of planes. Since the algorithm requires identification of the constrained planes anyway, these planes were used to calculate the restoring torque. Since the sense of rotation is opposite for the two constrained planes, the torque also has a different sign for each plane, though the magnitude is the same.

In order to calculate the difference in free energy between a system with and without a spin spiral, the total angle between the constrained planes is varied from $\varphi = 0$ and $\varphi = \pi$. From equation 6.28, the restoring torque as a function of the angle between planes ($\theta = \varphi/[N_{\text{planes}} - 1]$) should approximately be a straight line. The difference in the free energy of the system between $\varphi = 0, \pi$ is given by the integral of the torque between those limits. Due to thermal fluctuations, especially at high temperatures, the error associated with the restoring torque for a particular angle of θ can be quite large. Consequently it is more accurate to perform a linear regression on the torque line and compute the area under the line analytically. Where the gradient of the torque line, $m_{\mathcal{T}}$, is given by $m_{\mathcal{T}} = \partial|\mathcal{T}|/\partial\theta$ and the torque is given by $|\mathcal{T}| = m_{\mathcal{T}}\theta$, the difference in free energy between $\varphi = 0, \pi$ is:

$$\Delta\mathcal{F} = \int_0^{\theta} m_{\mathcal{T}}\theta d\theta = \left[\frac{m_{\mathcal{T}}\theta^2}{2}\right]_0^{\theta} = \frac{m_{\mathcal{T}}\theta^2}{2} \tag{6.30}$$

A plot of a typical torque line is plotted in Figure. 6.15 for a system temperature of 500K. The figure shows that the torque is linear in φ, since the angle between neighbouring planes is very low. The small scatter of the points about the regression line at such high temperature is indicative of the robustness of the method. It should be noted that it is possible to use a one-point quadrature rule as for the anisotropy calculations. However, the errors associated with a single date point are much larger, and so calculating the entire torque integral is a more reliable method in this case.

The temperature dependence of the free energy is calculated from torque lines at 10 K increments. In order to extract the effective exchange parameter, $\mathcal{J}$, it is

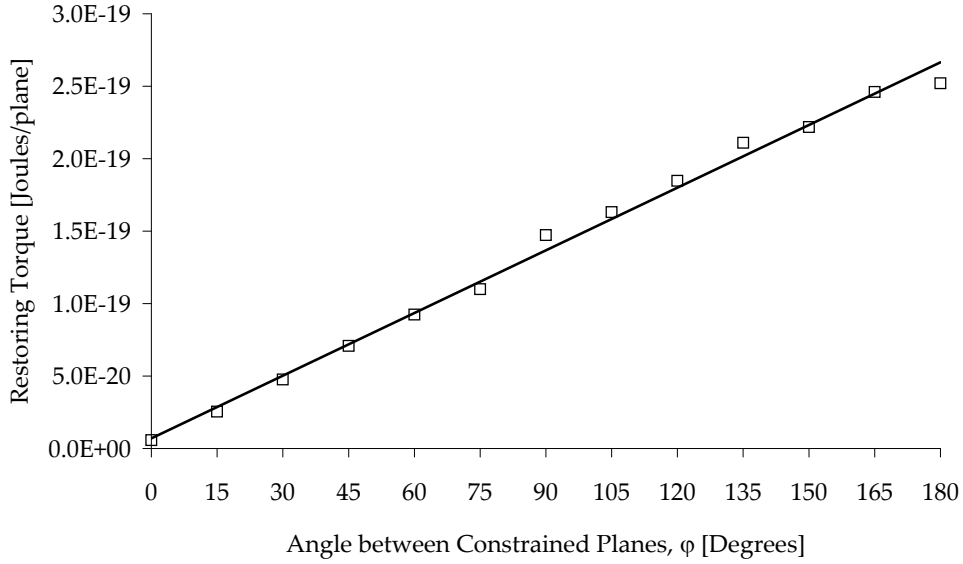

Figure. 6.15: Plot of restoring torque against angle between constrained planes, φ, at a temperature of 500 K. The gradient of the torque line is shown by the black line.

necessary to take into account its angular dependence. If it is assumed that the angular dependence of $\mathcal{J}$ is independent of temperature, then from equation 6.26 we have:

$$\mathcal{J} = \frac{\Delta \mathcal{F}}{\cos \theta_{\max} - 1} \tag{6.31}$$

where $\theta_{\max}$ is the maximum angle between adjacent planes.

The reduced exchange energy, $\mathcal{J}/J_{ij}$, is plotted as a function of temperature compared with the system magnetisation in Figure. 6.16(a), while a plot of the scaling of $\mathcal{J}/J_{ij}$ with reduced magnetisation is plotted in Figure. 6.16(b).

The micromagnetic exchange constant is more strongly temperature dependent than the system magnetisation, showing that long range spin correlations do not exist at high temperatures. Also the error in the results is still quite visible, since the exchange values fluctuate quite strongly. The temperature scaling of the micromagnetic exchange for temperatures up to 200 K shows a low temperature exponent of $\mathcal{J}/J_{ij} \sim M^{1.71}$. This result is close to that of other methods [75], where the exponent was found to be $\mathcal{J}/J_{ij} \sim M^{1.66}$. The slight discrepancy between the results is due to the sensitivity of the exchange scaling and the scatter in the calculated data points. The reason for the scaling behaviour of $M^{\sim 1.66}$ is not yet understood, and a more detailed investigation of this phenomenon is needed to fully determine the source of the strange exponent.

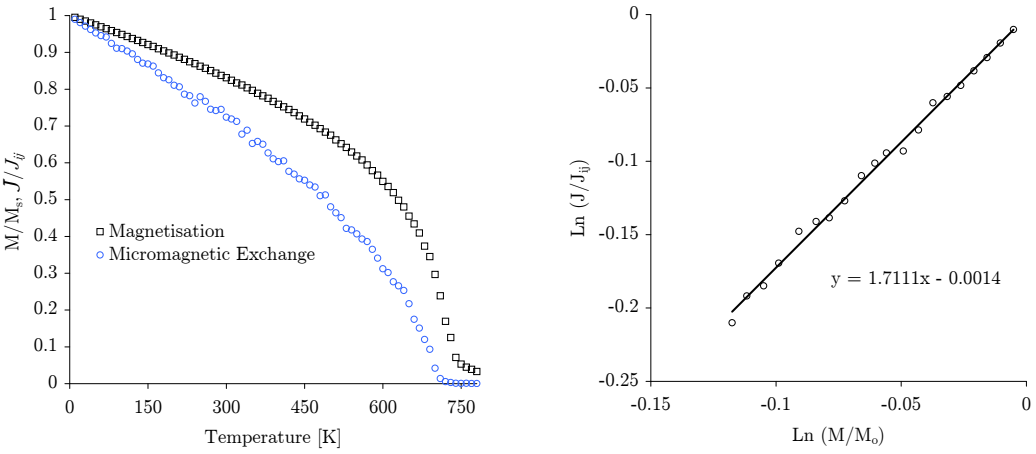

(a) (b)

Figure. 6.16: Temperature dependence (a) and scaling (b) of the reduced effective micromagnetic exchange constant, $\mathcal{J}/J_{ij}$. The temperature scaling of the micromagnetic exchange shows a low temperature exponent of $\mathcal{J}/J_{ij} \sim M^{1.71}$.

6.5 Conclusion

This chapter has presented a new constrained Monte Carlo method which has been applied to investigate the temperature dependencies of a number of magnetic properties. A method for calculating the change in free energy of a system by integration of the system torque has also been shown. The results for the temperature dependence of uniaxial and cubic anisotropies show good agreement with the analytical theories, showing M^3 and M^{10} scaling at low temperatures respectively.

The method has also been used to investigate the temperature dependence of the surface anisotropy in thin films of Cobalt. Due to the flat surfaces the surface anisotropy yields either an easy plane or easy axis configuration for the surface spins. This characteristic avoids the complicated cubic energy surfaces seen in Chapter 5, and thus allows the simple calculation of the temperature dependence of the surface anisotropy. This calculation showed that the surface anisotropy free energy scales with the surface magnetisation.

Finally the temperature scaling of the micromagnetic exchange parameter, A was calculated, by creating a spin spiral using the constrained Monte Carlo method. This calculation shows that the micromagnetic exchange parameter scales with the system magnetisation as $M^{1.71}$, which is different from the assumed mean field temperature dependence.

The final chapter of this thesis will apply the techniques and methods developed so far to investigate a more practical problem, that of Heat Assisted Magnetic Recording.

7. An Atomistic Media Model for Tbit/in^2 Heat Assisted Magnetic Recording

At the time of writing the highest areal density in commercial hard disk drive products is around 240 GBit/in^2 [76]. In order to increase the performance and capacity of disk drives in the future it is necessary to increase the storage density. This presents a number of unique engineering and physical challenges [77].

A critical problem for increased data density is the thermal stability of the written information. The principle of magnetic recording is to write a magnetic bit in one of two magnetic states, each separated by an energy barrier. The size of the energy barrier in a single domain particle is primarily determined by the magnetocrystalline anisotropy energy of the material and the particle size [78]. Clearly increasing data density requires smaller bit sizes, and thus materials with a much higher magnetocrystalline anisotropy energy, such as $L1_0$ FePt. Such materials do exist but the high anisotropy energy also hugely increases the coercivity of the material, making it impossible to write the data with existing recording heads. This is an intractable problem requiring novel approaches to overcome the physical limitations.

7.1 Heat Assisted Magnetic Recording

It is well known that the magnetocrystalline anisotropy energy reduces significantly with increasing temperature. By using a heat source to raise the temperature of the material, it is possible to make use of this property for magnetic recording. The heat source reduces the material coercivity for the writing process, while retaining good thermal stability at room temperature due to the high anisotropy energy. The most effective form of heating utilizes a high power laser mounted directly on the recording head; a process known as Heat Assisted Magnetic Recording (HAMR). Other common names include Optically Assisted Magnetic Recording (OAMR) or Thermally Assisted Magnetic Recording (TAMR). A typical layout of the recording arrangement for HAMR is illustrated in Figure. 7.1.

A number of micromagnetic models have previously been developed to model the HAMR process [77, 79], but make a number of assumptions which are certainly not true as the grain size of magnetic media decreases well into the sub 10 nanometre regime. Micromagnetics is essentially a continuum formulation, in its original form valid at zero temperature only. However,

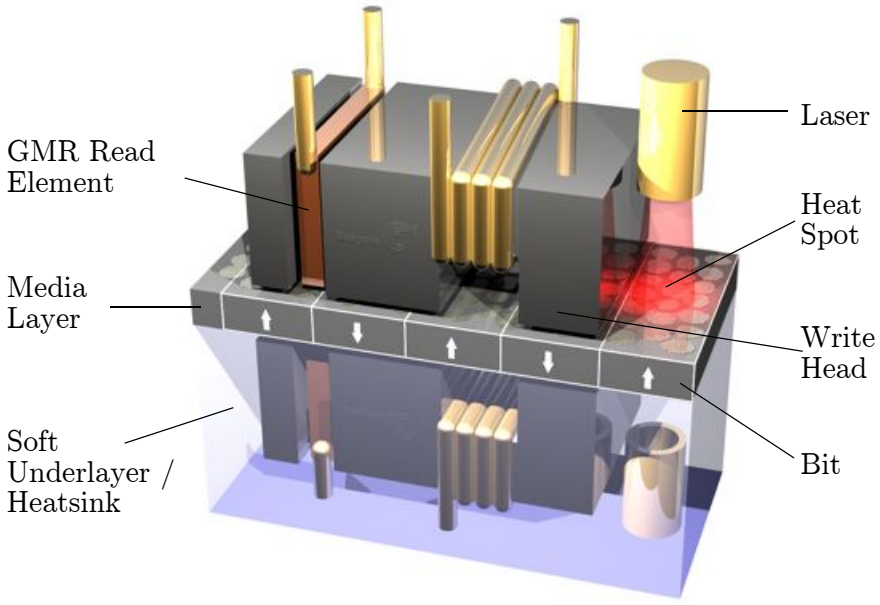

Figure. 7.1: Visualisation of the arrangement of the recording head and media for HAMR, showing key components with typical dimensions. The proximity of the field head to the laser is closely related to the rate of cooling and maximum temperature for the writing process.

improvements to the model over time have allowed temperature effects to be incorporated into micromagnetics, principally by scaling the length of the magnetisation vector, exchange energy, anisotropy energy and other material parameters with temperature. The Landau-Lifshitz-Gilbert equation of motion for the micromagnetic spin system with temperature incorporates Langevin dynamics in a similar manner to the atomistic model, except it is applied at the granular macrospin rather than atomistic level. In this case the width of the thermal field distribution for a single micromagnetic cell is given by:

$$\sigma = \sqrt{\frac{\alpha k_B T}{M_s V \gamma \Delta t}} \tag{7.1}$$

where α is the damping constant, k_B is the Boltzmann constant, T is the absolute temperature, M_s is the saturation magnetisation of the cell, V is the cell volume, γ is the gyromagnetic ratio, and Δt is the integration timestep. These ideas are certainly applicable in the case of reasonable micromagnetic cell sizes (tens of nanometres) and for temperatures much lower than the Curie temperature, where the length of the micromagnetic macrospin does not change significantly. However, for small system sizes and high temperatures the above assumptions are definitely not applicable and thus will provide incorrect results [80, 81].

For small micromagnetic cell sizes, the cell only represents a few atoms. Because of this, near the Curie temperature the atomic scale thermal fluctuations

are significant enough to considerably affect the length of the macrospin magnetic moment, which in turn can be critical for fast reversal processes. For these reasons micromagnetic models as they currently stand are wholly unsuitable to accurately model the HAMR process. New approaches, such as the Landau-Lifshitz-Bloch (LLB) macrospin equation [82, 83], may well accurately reflect the influence of atomic scale fluctuations.

In order to better understand the core physics of the HAMR process, an atomic-scale model of the recording medium has been developed. Such a model is not limited by the same restrictions as micromagnetics regarding the continuum approximations, and so can accurately reflect the magnetisation dynamics on a sub-picosecond timescale. The supreme disadvantage with such an approach is computational effort due to the requirements of simulating over a hundred 3.5 nm grains, but the simulations do provide valuable insight into the details of the recording process. Information from these results can then be fed into macrospin models, such as the LLB, allowing much larger systems to be modelled which much better reflect the underlying physics of HAMR [84].

The chapter is structured as follows; the first part of this chapter will describe the modelling methods developed to model the thermal effects arising from rapid laser heating. The next section will then address the fundamental physics of HAMR, by investigating the process for single isolated FePt grains in the range 2-10 nm in diameter. The second part will then apply this knowledge to the creation of a working atomistic model of the recording process on realistic recording media, where the effects of variable grain size, media rotation speed, laser power and other phenomena can be properly taken into account. Finally the feasibility of using conventional media to achieve a recording density in the range 1-2 Tbit/in^2 is discussed.

7.2 Thermal Modelling

The first section of this chapter addresses the thermal modelling of laser heating within a magnetic recording medium and also isolated grains, where the spatial and temporal temperature profile is important for the magnetisation dynamics. Usually a two-temperature model is employed to model the effects of heat transfer in isolated laser-heated systems [85, 86, 87, 88]. The two-temperature model treats the electrons as a separate system to the lattice and models the heat transfer between the two systems. However, such a model takes no account of the spatial temperature profile essential for a large-scale recording model. In order to effectively model the spatial and temporal heat profile a simple, purely classical, electron heat transfer model was developed. Recently more advanced treatments

of the problem, such as the Lattice-Boltzman method [89], have been suggested, but the simple classical model suffices for the purposes of a recording simulation in the first instance. From a magnetic standpoint, the electron temperature is the characteristic magnetic temperature, and so the heat transfer model deals only with this temperature.

The heat transfer model works by dividing the recording layer or grain into small blocks (0.5 nm cubed) with an electron specific heat capacity at constant volume, $|c_m|_v$, and a thermal conductivity of k_m. Underneath the recording layer is a thick heatsink layer with a thermal conductivity of k_h. Neighbouring blocks of material exchange thermal energy dependent on the temperature gradient, timestep, and specific heat capacity. The bottom of the heatsink is held at room temperature so that excess heat is always removed from the recording layer. The heat is added from the laser by assuming a normalised Gaussian energy distribution. Therefore, for each cell in the magnetic layer we can express the total change in thermal energy per unit time, $\Delta E_{\text{thermal}}$, as:

$$\begin{aligned} \frac{\Delta E_{\text{thermal}}}{\Delta t} &= \Delta E_{\text{laser}} - \Delta E_{\text{magneticlayer}} - \Delta E_{\text{heatsink}} \\ &= P_{\text{laser}} \exp\left(\frac{-r^2}{2r_o^2}\right) - \frac{1}{2}\sum_{j=1,4} \frac{k_m A_{\text{cell}} \Delta T_m^{ij}}{L_{\text{cell}}} - \frac{k_h A_{\text{cell}} \Delta T_h}{L_{\text{heatsink}}} \end{aligned} \quad (7.2)$$

where P_{laser} is the laser power, r is the distance of the cell from the centre of the laser spot, $2r_o\sqrt{2\ln 2}$ is the full-width-half-maximum of the laser, A_{cell} is the area of the discretised cell, L_{cell} is the centre-to-centre cell separation distance, ΔT_m^{ij} is the temperature gradient between neighbouring cells i and j, ΔT_h is the temperature gradient between the cell and the base of the heatsink, and L_{heatsink} is the thickness of the heatsink, as shown in Figure. 7.2.

The change in thermal energy is then converted to a temperature rise by the relation:

$$\Delta T = \frac{\Delta E_{\text{thermal}}}{|c_m|_v V_{\text{cell}}} \quad (7.3)$$

where ΔT is the temperature rise in the cell, and V_{cell} is the volume of the cell. These equations are then solved for each cell to generate the thermal profile in the magnetic layer. This model allows certain material parameters, such as the heat sink thermal conductivity or laser power, to be tuned for optimal recording results.

The actual grid size for the thermal modelling is considerably larger than the simulated magnetic area, as shown in Figure. 7.3. This is due to the fact that the heat from the laser tends to spread out over a wide area. If the thermal array is

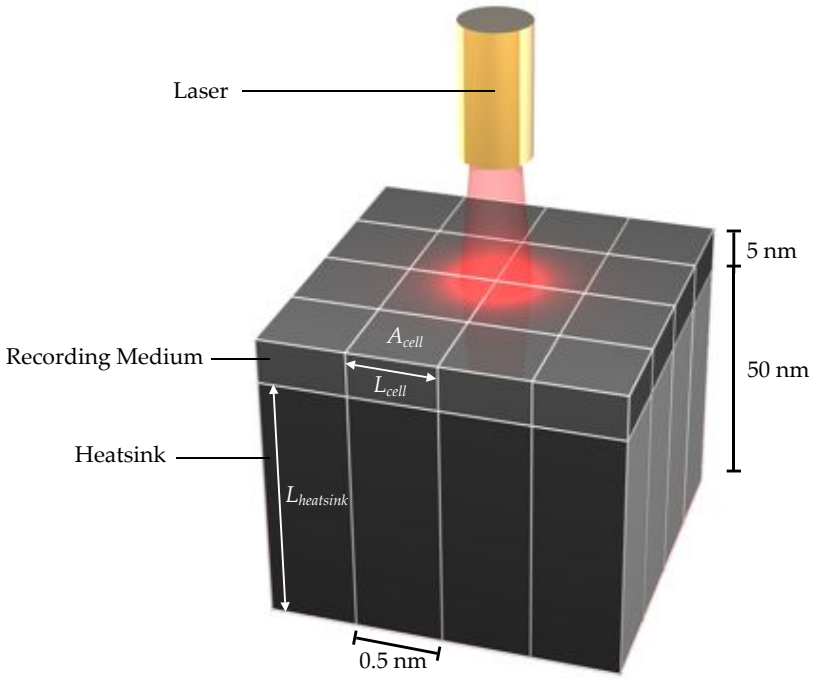

Figure. 7.2: Visualisation of a classical heat transfer model, showing key elements and dimensions.

limited to the magnetic area then there is an artificial concentration of heat at the ends of the array which leads to an unphysical increase in the temperature under the laser spot. This problem is solved by having a large thermal modelling area.

A typical temperature profile is shown in Figure. 7.4. The asymmetry of the profile is due to the proximity of the laser source and write head, causing a substantial proportion of the laser power to be absorbed by the write head above the medium. This is modelled by truncating part of the light profile from the laser in Equation. 7.2.

The thermal conductivity of the heatsink material essentially determines the lateral extent of the hot spot in the magnetic layer, as this is the only mechanism which removes heat from the system (laterally the heat is only distributed). Since the laser spot size is already much bigger than the size of a magnetic bit, aggressive heatsinks are needed to localise the heating, thus preventing adjacent magnetic data from being erased, however highly conducting materials also require much more powerful lasers to heat the material. As such Silicon is an optimal heatsink material as it has a high thermal conductivity of 140 W/mK. The thermal conductivity of the magnetic layer is primarily determined by its chemical composition and the actual structure. Due to its granular nature, the thermal conductivity of the media layer is quite low, typically around 5 W/mK.

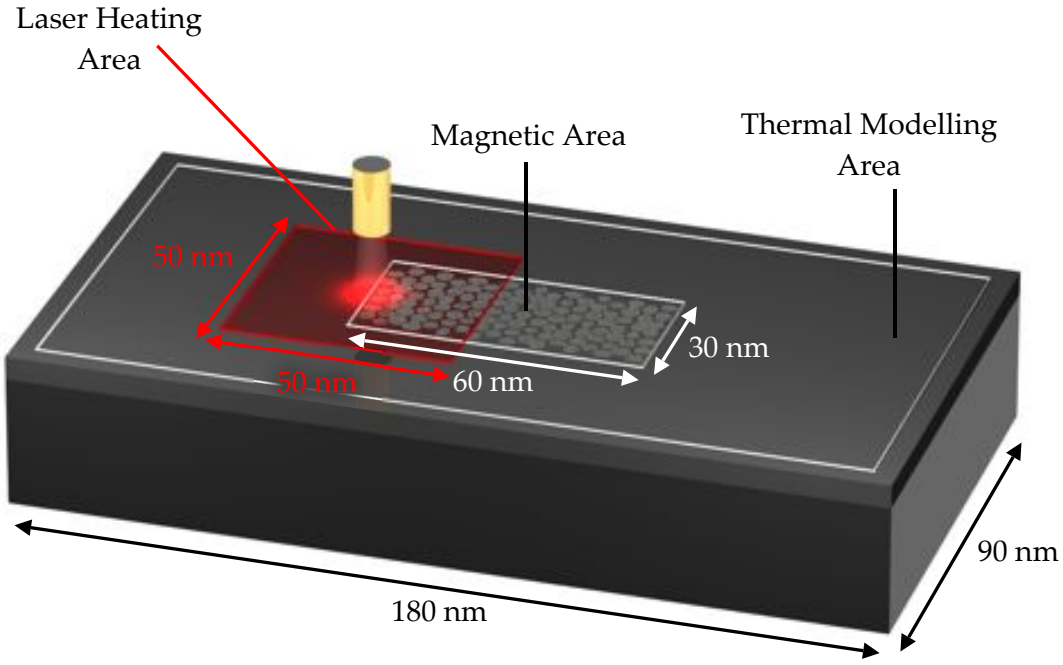

Figure. 7.3: Visualisation of thermal modelling grid and magnetic area, showing key dimensions.

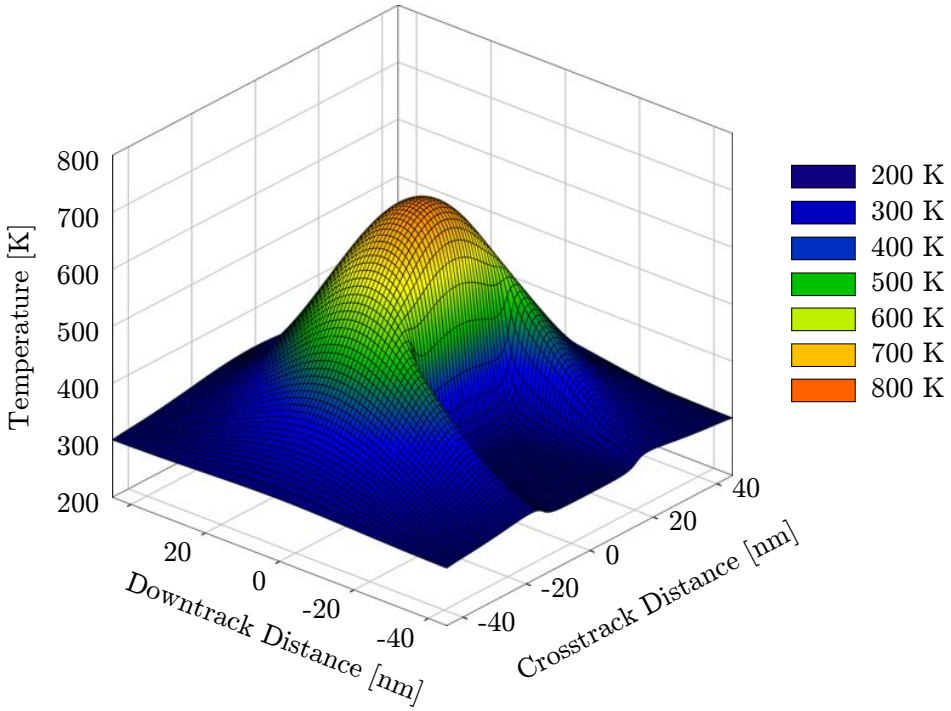

Figure. 7.4: Representation of a typical spatial temperature profile of a laser pulse centred on a magnetic recording medium. The laser power is 3.0 mW and the FWHM of the laser is set at 40 nm. The asymmetry in the profile is caused by the proximity of the laser source and write head.

In fact, due to the granular structure of the medium, it is likely that heat will be localised within the magnetic grains due to the high thermal conductivity of the packing medium. In general, of course, a lot of the so-called "constants" in such a model are in fact temperature dependent, and future models will likely take such effects into account.

7.3 The Physics of Heat Assisted Magnetic Reversal

In order to better understand the fundamental reversal mechanism during the HAMR process, the reversal of a single, isolated grain was investigated first. A critical requirement of any magnetic recording process is repeatability - a single grain must reliably reverse every time. HAMR significantly complicates this requirement since the reversal mechanism is dominated by the thermal fluctuations induced by the rapid heating. By investigating these effects for a single, isolated magnetic grain, ideal conditions for a larger scale system can be found much more quickly due to the much reduced computation time.

Magnetic Reversal Mechanisms near the Curie Point

For conventional magnetic recording, the magnetic grains are reversed through rotation of the magnetic moments by the external field, so-called precessional reversal. During the conventional reversal process the length of the magnetic moment remains essentially constant, since it is related to the temperature of the system. Note that this is the only possible mechanism when simulating systems using the LLG equation.

Near the Curie temperature, however, the length of the system magnetisation can vary during the reversal process due to the strength of the anisotropy and applied fields compared with the exchange energy. A similar effect has been observed previously in investigations into domain walls in FePt [39], where at elevated temperatures the high anisotropy field caused a reduction of the length of the magnetisation at the centre of the wall (in the magnetically hard direction), generating elliptical domain walls [1].

The relevance of this phenomenon to magnetic reversal is that it allows for another, previously unknown, route for the reversal process, namely a reduction in the length of magnetisation which aids the transition between energy states along and against the applied field direction. Due to the anisotropy

[1] Elliptical domain walls are a perturbation of the usual Néel domain wall, where the wall is formed by a gradual circular rotation of the magnetisation vector along the plane of the wall. For elliptical walls, the length of the magnetisation is reduced at the centre (in the magnetic hard axis) due to the strength of the anisotropy energy and thermal fluctuations. This gives the wall an elliptical profile in M, hence the name.

field, the maximum reduction in magnetisation length occurs when the system magnetisation is orientated along the magnetic hard axis. This is because the high anisotropy competes with the exchange interaction along the hard axis, whereas along the easy axis the exchange and anisotropy energies are complementary. Since the anisotropy and applied field energies are ultimately dependent on the length of the system magnetisation, this leads to a reduced configuration energy along the magnetic hard axis, and thus a reduction in the energy barrier between the two minimum energy states.

The path of the system magnetisation vector under this process (in zero field) is an ellipse, and hence this is given the name elliptical reversal. In its extreme form the reversal process is entirely due to the reduction in the length of the system magnetisation, and this is classified as linear reversal, where no precessional component exists. Schematic diagrams for all three reversal modes are shown in Figure 7.5. It should be emphasised here that these effects occur only at temperatures in the vicinity of the Curie point, since at lower temperatures the exchange energy prevents any significant reduction in the length of the system magnetisation. In fact the linear and elliptical reversal mechanisms each have different temperature regimes, a detailed analysis of which can be found in [90].

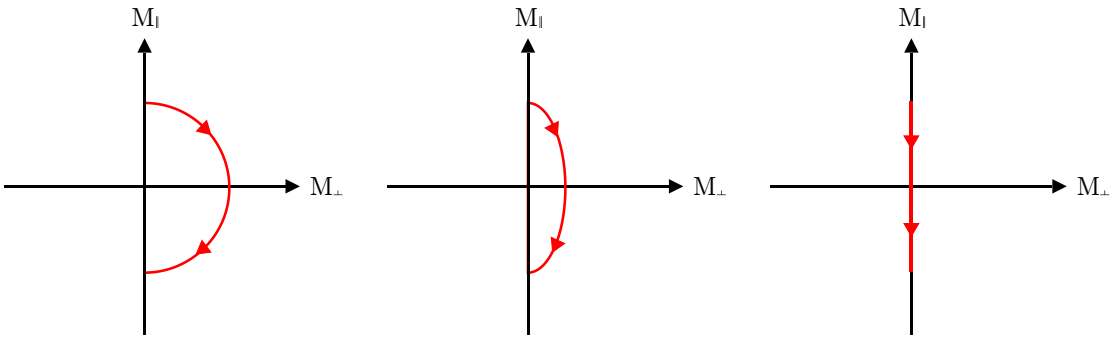

(a) In the precessional reversal mode, the magnitude of the system magnetisation remains constant, as it precesses around the external applied field.

(b) In the elliptical reversal mode, the magnitude of the system magnetisation reduces to a minimum as it crosses the magnetic hard axis, and recovers as the magnetisation realigns along the easy axis direction.

(c) In the linear reversal mode, the magnitude of the system magnetisation reduces to zero as the M_z component of magnetisation crosses zero.

Figure. 7.5: Schematic plots of precessional (a), elliptical (b) and linear (c) reversal modes of the system magnetisation under the influence of an external applied field. The red lines indicate the path of the system magnetisation for the different modes relative to its alignment to the easy axis.

In order to illustrate the effect of temperature on the heat assisted reversal process, simulations of the reversal of 10 nm diameter FePt nanoparticles were performed. This particle size is much larger than that needed for a recording

density of 1TBit/in^2, but as will be illustrated later, the success of the HAMR process is significantly volume dependent. The model utilises the truncated FePt Hamiltonian described in section 2.6, which incorporates the effects of anisotropic exchange coupling, which are important for modelling FePt realistically. The simulations were performed on a single isolated cylindrical grain, with a moving laser pulse with a varying laser power. The laser is initialised directly above the grain, and then moved away at constant speed, resulting in a cooling time to room temperature of approximately 300 ps. The effect of the laser is to heat the material to the desired temperature, which is determined by the laser power. The Curie temperature of the grains is $\sim$ 700K, and so maximum temperatures of 673 K, 691 K, 710 K and 800 K were chosen. All of these temperatures are above the minimum write temperature, where the external applied field is greater than the anisotropy field, $H_k = 2K_u(T)/M_s$. In principle this means that magnetic reversal should be energetically favourable for all the above temperatures. The grain magnetisation is initialised in the positive z-direction, and an external reversing field of 0.8 Tesla was applied along the negative z-direction. The system is first equilibrated for 5 ps, at which point the laser is then activated. The simulations were repeated 100 times so that the relative reliability of the reversal process could be assessed. The first ten results for each temperature are plotted in Figure. 7.6.

The data in Figure. 7.6(a) for the lowest temperature of 673 K, which is around 25K below T_c, shows only one reversal in ten is successful. As can be seen, the reversal process in this case is largely precessional, since at no point do all three magnetisation components go to zero. This corresponds to the case where the elevated temperatures, and thus reduced anisotropy, allow the field to reverse the magnetisation via precession. The fact that reversal occurs at all suggests that for long timescales the reversal process is energetically favourable, however, the low success rate suggests that the precessional reversal process is insufficiently fast for successful HAMR. If the cooling time is increased significantly, then one would expect to achieve a much higher reversal success rate. However, such a long time is not possible in a practical device.

For a maximum temperature of 691K, as shown in Figure. 7.6(b), the reversal success rate is much higher than for the lower temperature, at approximately 50 %. Firstly this shows a very sharp temperature dependence of the reversal success rate, given the small increase in temperature. In general the data also show a mixture of elliptical and near-linear reversal mechanisms. Counting from the left of the figure, reversals *1*, *2*, and *5* show a significant component of magnetisation perpendicular to the easy axis, indicating an elliptical reversal mode. However, reversal *9* shows a nearly pure linear transition, since all

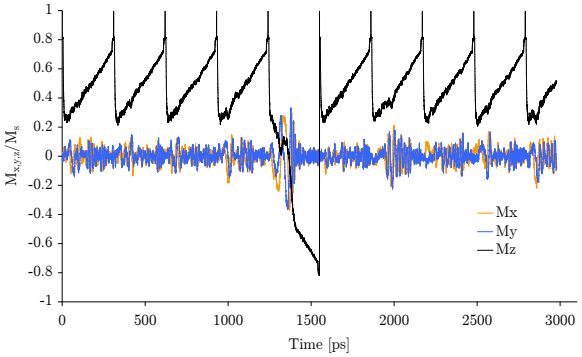

(a) Magnetisation components vs time for T_{max} = 673 K.

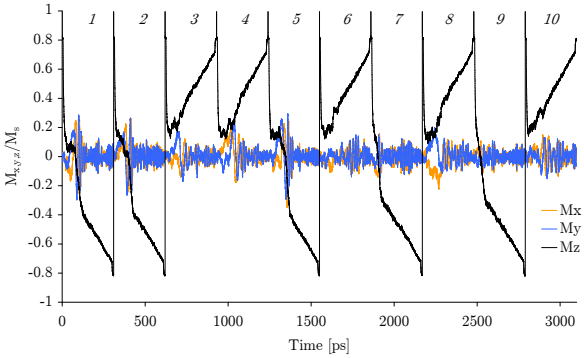

(b) Magnetisation components vs time for T_{max} = 691 K.

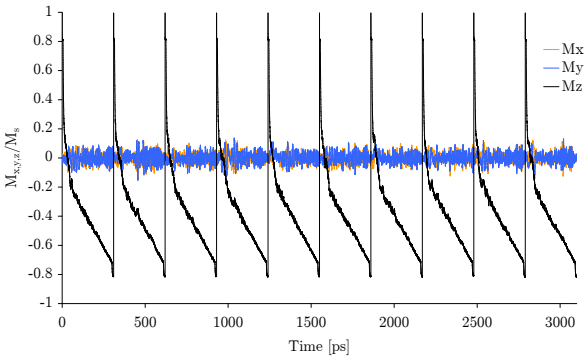

(c) Magnetisation components vs time for T_{max} = 710 K.

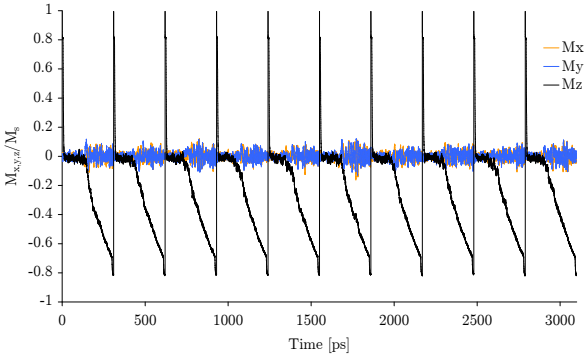

(d) Magnetisation components vs time for T_{max} = 800 K.

Figure. 7.6: Effect of temperature on the reversal mechanism for maximum temperatures, T_{max}, of 673K (a), 691K (b), 710K (c), and 800K (d).

components of magnetisation go very close to zero. The final successful reversal, *7*, shows a stronger reduction of all three magnetisation components compared with reversals *1,2*, and *5*, suggesting a more elliptical reversal mode. Although the elliptical reversal mode seems to be energetically favourable, the rapid cooling time means that the reversal success rate is still only 50%, since there is insufficient time to allow the system to fully equilibrate. As with the previous example, if a longer cooling time is used then one would expect the process to be much more successful.

In order to see true linear reversal, practically one must heat the material significantly above the Curie temperature, as shown in Figure. 7.6(d). The reason for this originates from the small size of the grains. In a bulk material, the magnetisation at T_c is zero, but as shown previously in Chapter 3, small particles possess a persistent average magnetisation at and above T_c. This persistent magnetisation means that, on average, there is likely to be some non-easy axis magnetisation component due to the random thermal fluctuations, in which case the reversal mechanism is closer to elliptical than linear. If the system temperature is increased to above T_c then the anisotropy energy disappears, since the thermal fluctuations in the length of magnetisation are truly random. This then allows the linear reversal mechanism to appear, since the magnetisation vector can take up any orientation with equal probability.

The data in Figure. 7.6(d) show a 100% reversal success rate, which is primarily due to the linear reversal mechanism. As can be seen, the very high $T_{\max}$ of 800K rapidly reduces the magnetisation to a very small value. Above T_c the anisotropy energy disappears, leaving only the external applied field. In the vicinity of T_c the susceptibility of the material diverges, strongly enhancing the effect of the external applied field on the magnetisation orientation. The combination of these effects is to orientate the (small) magnetisation vector along the field direction within 10 ps of activating the laser. An expanded view of this is shown in Figure. 7.7.

Although the z-component of magnetisation does occasionally oppose the field direction, it is much more likely to lie along the field direction. As the grain is cooled through T_c, the susceptibility becomes very large, forcing the magnetisation to point along the field direction. Under further cooling the increasing anisotropy field prevents the magnetisation escaping from the field aligned direction, resulting in a very robust reversal mechanism.

The final result to discuss is that for a maximum temperature of 710 K, which is just above T_c, as shown in Figure. 7.6(c). As for the case of $T_{\max}$ = 800 K, the reversal process is 100% reliable, although due to the persistent magnetisation above T_c, the reversal process is generally more elliptical rather than linear.

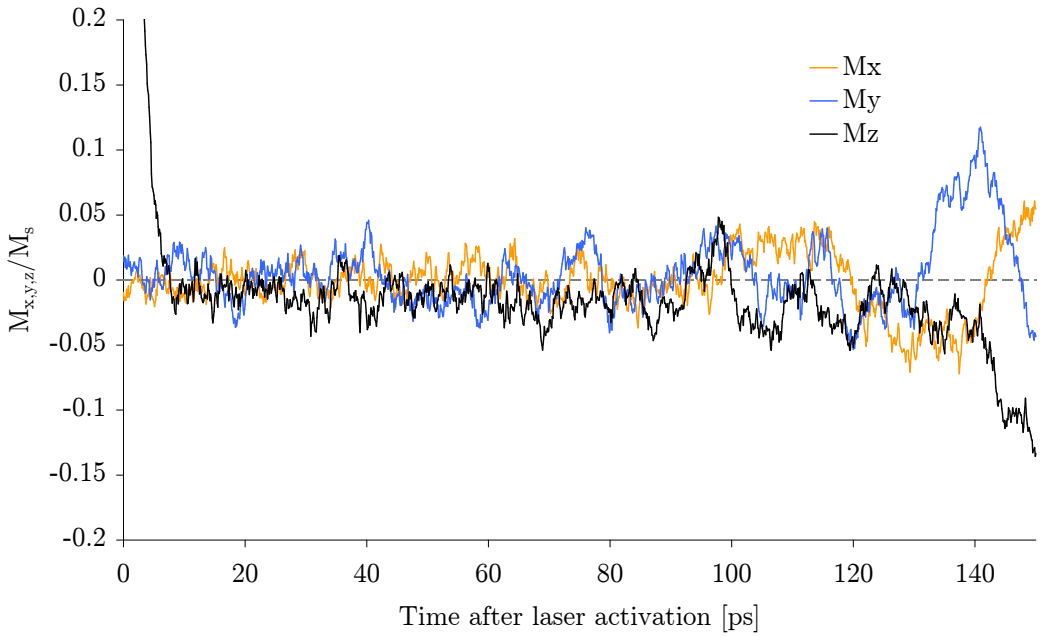

Figure. 7.7: Plot of Magnetisation components vs time for T_{max} = 800 K showing initial reversal within 10 ps of laser activation. As the system cools the grain exhibits superparamagnetic behaviour, with multiple switching events. At t=125 ps the field orients the magnetisation in the negative z-direction, at which point it is stable due to the lower system temperature.

Visualisation snapshots of the reversal process at different times are shown in Figure. 7.8. On the left of each image is a cutaway view of the grain with atomic moments, while on the right is the single macroscopic spin which shows the magnetisation volume and direction of the collective grain.

Initially, at a time of 5 ps, the grain magnetisation is orientated along the +z-axis. The laser is then activated, causing a rapid reduction in the length of the system magnetisation due to the increased temperature, as shown in Figure. 7.8(b). In Figures. 7.8(c) and 7.8(d) the magnetisation length becomes very small and rotates across the hard axis. The enhanced damping due to the high temperature causes a near linear change of M_z across the magnetic hard axis, though M/M_s is finite throughout. Note that even at temperatures near T_c there are visible short range correlations in the magnetisation. As the system is cooled the length of magnetisation begins to recover, as shown in Figure. 7.8(e) until the grain becomes near-uniformly magnetised in the field direction as shown in Figure. 7.8(f). During the recovery there is a slight precession arising from the magnetisation not recovering precisely along the easy direction.

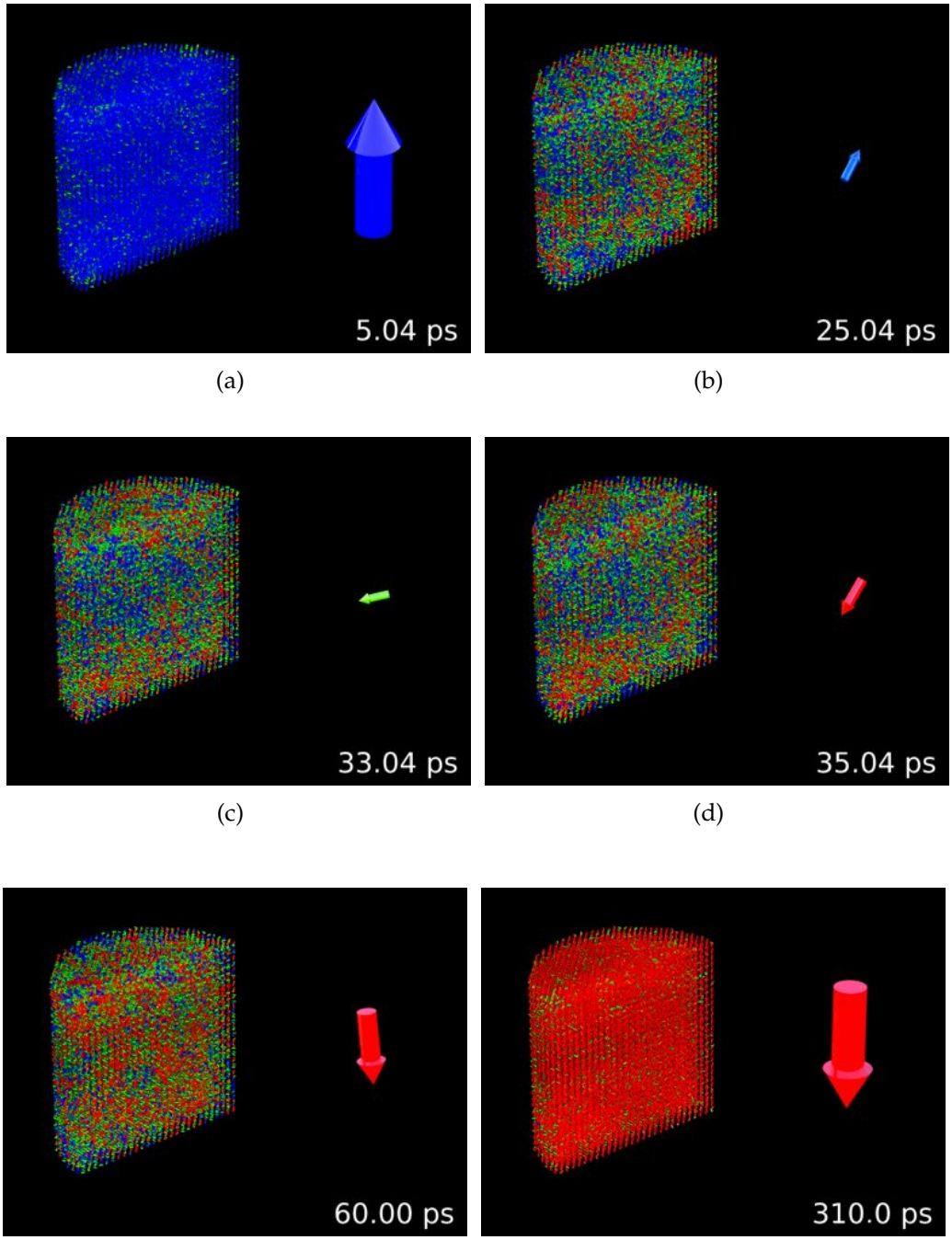

(a) (b)

(c) (d)

(e) (f)

Figure. 7.8: Visualisation snapshots of the HAMR process for a single 10nm diameter FePt grain for a maximum temperature of 710 K.

Time Dependence of Reversal below T_c

One important effect not yet addressed is the time dependence of the reversal success rate. For single domain particles at low temperatures, where the anisotropy energy is much greater than the thermal energy, the escape rate is well described by an Arrhenius-Néel law [9, 10]. At higher temperatures, however, the transition rates are not easily calculated, since they depend on the actual shape of the energy surface. However, taking a generic system with some energy surface not in an equilibrium state, one can certainly say that the longer the system has to equilibrate, the closer the system will be to thermal equilibrium. This effect is central to understanding the physics behind ultrafast reversal processes, since even if a certain equilibrium state favours reversal, if there is insufficient time to reach equilibrium then the reversal success rate will not reflect the equilibrium distribution.

In order to determine the time to reach equilibrium, a simplified reversal simulation was performed. The system chosen was a 6nm diameter FePt nanoparticle, with a magnetisation initialised in the positive z-direction. An external applied field is applied in the negative z-direction, which attempts to reverse the grain magnetisation, for the duration of the simulation. After equilibration at room temperature, the grain is instantly heated to 670K, simulating a fast laser pulse. After a certain pulse time, Δt, the grain is instantly cooled to 423K, simulating deactivation of the laser, but with some remaining heat in the material. At this lower temperature the system magnetisation direction is stable on the timescale of the simulation and does not change. Since the maximum temperature is below T_c, the reversal mechanism is entirely elliptical, and the system magnetisation remains non-zero at all times. At the end of the simulation the final magnetisation direction is recorded and the simulation repeated 100 times. The number of grains which are orientated along the field direction are then counted, giving a measure of the reversal success rate. The laser pulse time is varied between 10 and 110 picoseconds to determine the time dependence of the reversal success probability. A plot of the percentage write success rate as a function of laser pulse time for applied field strengths of 0.8 and 2.0 Tesla is shown in Figure. 7.9.

The difference between the two field strengths is quite stark for this simulation, with the 0.8 Tesla external field showing a very slow convergence to the equilibrium energy state, while the 2 Tesla external field has a very fast convergence, showing 100% reversal after only 20 ps. This effect can be explained by noting that for this temperature the coercivity is approximately 0.5 Tesla, so for the 2 Tesla external field the magnetisation transitions very rapidly to lie along the field direction. For the 0.8 Tesla external field, the transition to equilibrium relies more heavily

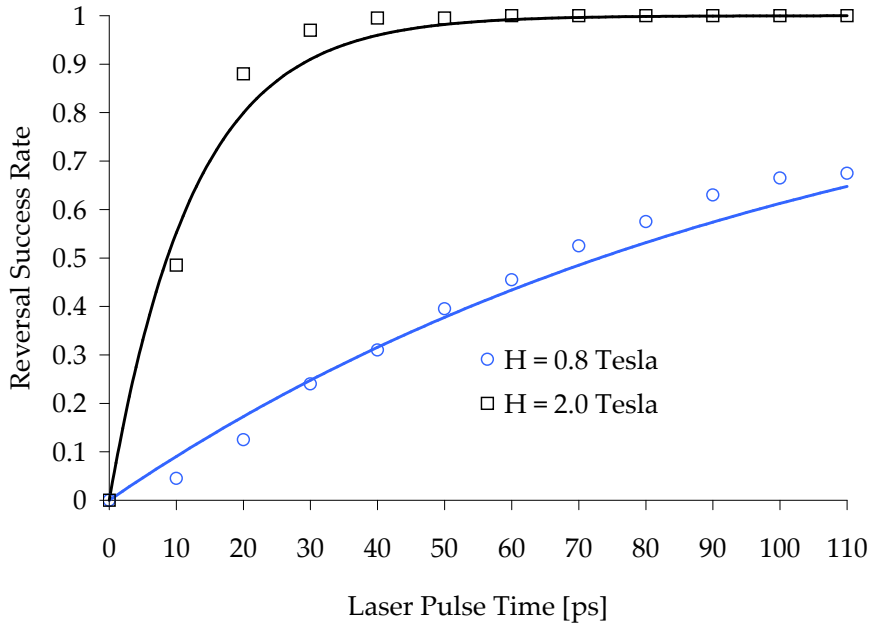

Figure. 7.9: Plot of the time dependence of the reversal success rate for a 6nm diameter FePt grain, for different laser pulse times and applied field strengths. The line provides a guide to the eye.

on thermal activation and thus progresses much more slowly. The underlying trend for both cases shows a transition to equilibrium for increasing laser pulse times, in keeping with the qualitative prediction of the Arrhenius-Néel Law.

Given that a realistic head field in a practical device is approximately 0.8 Tesla, this simulation shows that, for a temperature of 670 K, reliable magnetic reversal will not occur on the timescale of 100 ps. This problem can be overcome on the physical level either by the application of a much stronger applied field, or by increasing the temperature closer to T_c, where the coercivity is lower and the transition rates are increased.

Volume Dependence of Heat Assisted Magnetic Reversal

Although the details of the temperature and cooling time are critical to achieving successful heat assisted reversal, understanding the precise temperature and volume dependence of the process is important for determining the limits of the technology. If one neglects the time dependence of the write success rate, excepting that the cooling time must allow the system to reach thermal equilibrium, one can consider the equilibrium distribution of the magnetic moment as representing, on the fundamental level, the physics of heat assisted reversal.

For conventional magnetic recording, where the strength of the external

applied field exceeds the anisotropy field, $2K/M_s$, the effect of the field is to bias the energy so that the minimum configuration energy exists where the system magnetisation lies along the field direction. The total energy of the system is given by the summation of the anisotropy and applied field energies, given by:

$$E_{\text{total}}(\theta) = E_{\text{applied}}(\theta) + E_{\text{anis}}(\theta) = MVH\cos\theta + KV\sin^2\theta \tag{7.4}$$

where θ is the angle from the positive z-direction, M is the particle magnetic moment, H is the applied field strength, K is the anisotropy constant, and V is the particle volume. A plot of the angular dependence of the anisotropy, applied field and total energies for an arbitrary system with $E_{\text{applied}} = 2E_{\text{anis}}$ is shown in Figure. 7.10.

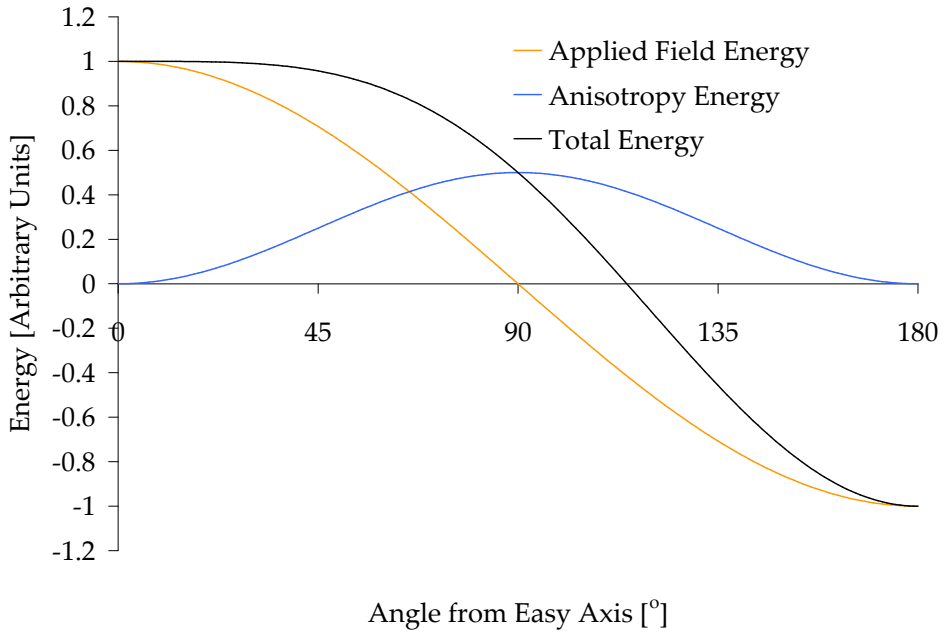

Figure. 7.10: Plot of the normalised applied field, anisotropy, and total energies as a function of angle from the positive z-axis, where $E_{\text{applied}} = 3E_{\text{anis}}$.

As can be seen, the effect of the external field is to bias the energy so that the minimum energy state is along the field direction. In order to obtain the statistics for this system, for an ensemble of identical moments, one can calculate the probability of the magnetic moment lying at a certain angle from the positive z-axis, $P(\theta)$, using the Boltzmann distribution of the form:

$$P(\theta) = \sin\theta\exp\left(\frac{\Delta E}{k_B T}\right) = \sin\theta\exp\left(\frac{MVH\cos\theta + KV\sin^2\theta}{k_B T}\right) \tag{7.5}$$

where k_B is the Boltzmann constant and T is the absolute temperature. The $\sin\theta$

prefactor arises from the relative area on the unit sphere, which is maximised at the equator. The Boltzmann distribution for the same system as above is shown in Figure. 7.11 for the low temperature case ($\Delta E/k_BT = 0.1$).

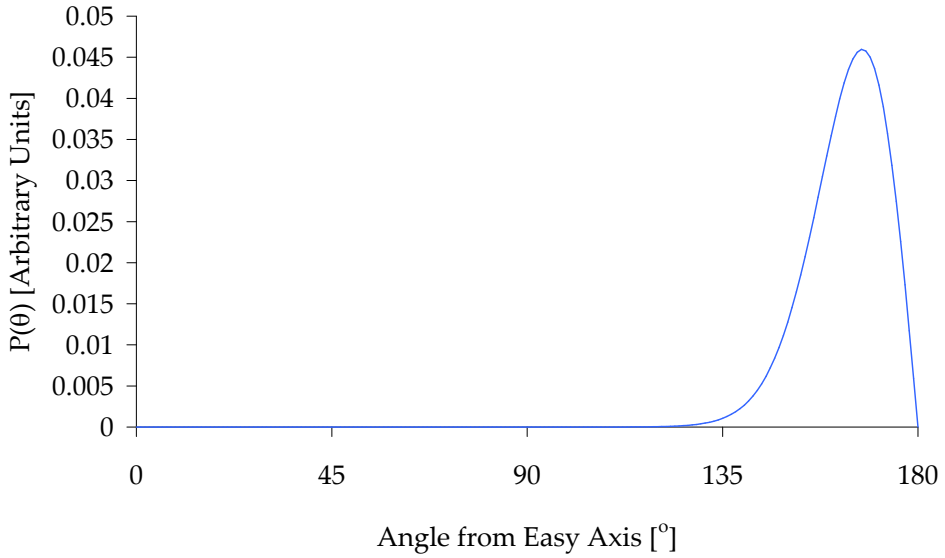

Figure. 7.11: Plot of the normalised probability of the magnetic moment lying at an angle θ from the positive z-axis for $E_{\text{applied}} = 3E_{\text{anis}}$.

As can be seen, the probability of the magnetic moment being aligned against the field direction in equilibrium is effectively zero. This agrees with the plots of the energy in Figure. 7.10, showing the minimum along the field direction.

For heat assisted reversal, however, the situation is more complex than this picture, since both the applied field energy and anisotropy energy are temperature dependent. However, an analytic expression for the free energy of a ferromagnet at all temperatures exists which can be used to correctly describe the energetics of a magnetic system close to the Curie Temperature. The Garanin expression for the free energy of a ferromagnet per unit magnetisation and volume, $\mathcal{F}$, taken from the derivation of the Landau-Lifshitz-Bloch equation [82], is given by:

$$\mathcal{F} = \frac{\mathcal{F}_e}{V} + \boldsymbol{H}\cdot\boldsymbol{m} + \frac{m_x^2 + m_y^2}{2\chi_\perp} + \frac{\left(m^2 - m_e^2\right)^2}{8\chi_\parallel m_e^2} \tag{7.6}$$

where $\boldsymbol{m}$ is a vector describing the magnitude and direction of the system magnetisation. Note that the above expression is valid only for temperatures below T_c - above T_c a different expression exists which can be found in reference [82]. The first term, $\frac{\mathcal{F}_e}{V}$, is an isotropic ground state energy which is independent of temperature. The second term describes the coupling of the system to an external magnetic field, $\boldsymbol{H}$, while the third term, $\frac{m_x^2+m_y^2}{2\chi_\perp}$, describes the anisotropy

free energy, assuming a uniaxial easy axis along the z-direction. The temperature dependence of the free anisotropy energy is described by the temperature dependent perpendicular susceptibility, $\chi_\perp$, which is fitted to atomistic simulations or derived from mean field theory. The final term, $\frac{\left(m^2-m_e^2\right)^2}{8\chi_\parallel m_e^2}$, describes a change in energy associated with deviations from the equilibrium magnetisation for a given temperature, m_e, and arises from the internal exchange energy. As for the anisotropy, there is a temperature dependent parallel susceptibility, $\chi_\parallel$, which describes the temperature dependence of this effect. For the purposes of the following analytical work, the temperature dependence of m, and the parallel and perpendicular susceptibilities were all calculated from atomistic simulations of FePt in reference [91].

This simple description of the free energy of a ferromagnetic system hides a myriad of complex physics, some of which is investigated in detail by Kazantseva [90]. For the purposes of the following, however, we are primarily interested in the Boltzmann spin distribution for systems of different sizes for different temperatures. Unlike previously, however, the Boltzmann distribution cannot be described in terms of a unique value of θ, since the magnetisation is able to go to zero. Also the Boltzmann distribution describes a population of states over the x, y, and z components of the magnetisation. Since the Garanin free energy is rotationally invariant perpendicular to the z-axis, the problem can be reduced to the x-z plane. Plots of the two dimensional Boltzmann distribution for a 3 nm^3 FePt nanoparticle for three different temperatures are shown in Figure. 7.12.

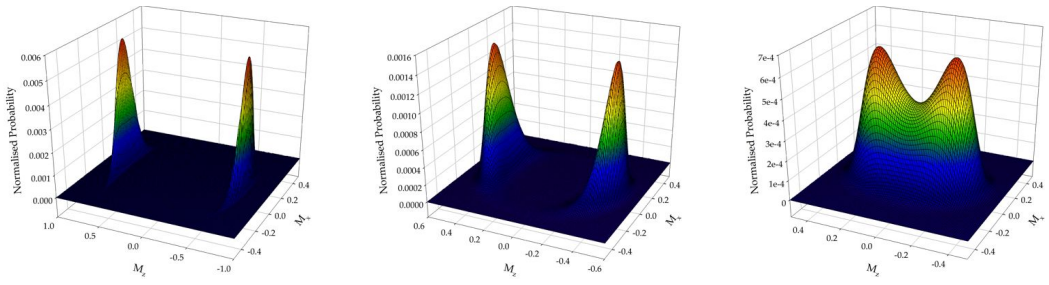

(a) (b) (c)

Figure. 7.12: Boltzmann Distribution for 3 nm^3 FePt Nanoparticle for 400 K (a), 600 K (b), and 650K (c).

As can be seen, at a temperature of 400 K the magnetisation tends to align along the $\pm z$ direction, indicated by the maximum probability. At low temperatures the length of the magnetisation is forced to be very close to the equilibrium length, leading to a very narrow distribution in the length of $\boldsymbol{m}$, while the anisotropy ensures that the magnetisation is orientated along the $\pm z$ direction. As the temperature is increased to a temperature of 600 K, the equilibrium magnetisation is decreased to approximately 40%. However, the

distribution in the direction and length of magnetisation is much broader, due to the increased parallel susceptibility and reduced anisotropy energy. Very close to T_c, at a temperature of 650 K, the Boltzmann distribution is still a maximum at $\pm m_e^z$, but now there is a significant probability of the magnetisation lying at $m_z = 0$, indicating a superparamagnetic state. What is particularly interesting is that, for the line along $m_z = 0$, the maximum probability lies where $m_x = 0$, essentially showing that the most likely reversal mode is via the linear mechanism, as described earlier.

In order to calculate the Boltzmann distribution for a single variable, such as m_z, then the distribution of probabilities over m_x must be taken into account. This is done by taking a sum over all m_x probabilities for a unique value of m_z. Utilising the Boltzmann distribution of the free energy for different values of m_z allows the investigation of the equilibrium spin distribution for different sized particles, for different field strengths and temperatures. This new approach allows one to take into account elliptical and linear reversal modes explicitly within the Boltzmann distribution to determine the reversal probability for a given system. Plots of the equilibrium spin distribution for 2 nm, 3 nm, 4.5 nm and 6 nm diameter particles are shown in Figure. 7.13 for different temperatures and an external applied field of 0.8 Tesla in the positive z-direction.

Considering first the case of the larger 6nm diameter particles, as shown in Figure. 7.13(d), one can see that in equilibrium the probability of the macrospin moment being aligned against the field direction is effectively zero for temperatures below 640 K. This equates to the low temperature case for conventional reversal, where the reversal process is totally reliable provided the system is given sufficient time to reach equilibrium. As the grain diameter is reduced to 4.5 nm, as shown in Figure. 7.13(c), one can see that the zero probability of the spin moment aligning against the field direction occurs at a lower temperature of 620 K. For successful reversal to occur in this system one must therefore equilibrate the system at a temperature of 620K or below.

For the 3 nm diameter grains, as shown in Figure. 7.13(b), another problem in achieving successful reversal arises, namely that in equilibrium there is always a probability of the spin moment lying against the field direction. This is a volume effect and arises from the fact that the applied field and anisotropy energies relate directly to the particle volume. For small grain sizes, the difference in the configuration energies along and against the field direction, compared with the thermal energy, become much smaller. This means that it is possible for a spin moment initially lying along the field direction to escape into the opposite energy well against the field direction. This is a statistical process, illustrated by the equilibrium spin distribution as shown in the figure. This illustrates the

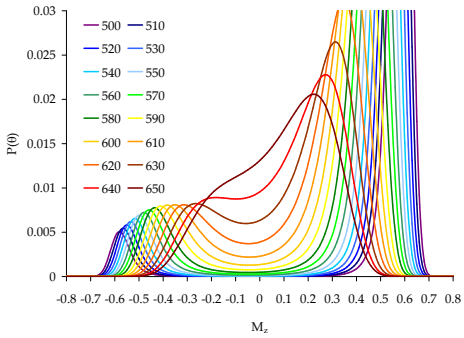

(a) Spin distribution for a 2nm x 5nm Grain.

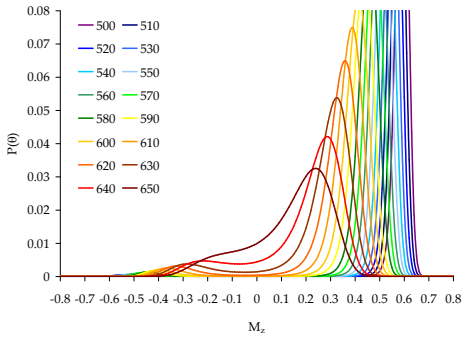

(b) Spin distribution for a 3nm x 5nm Grain.

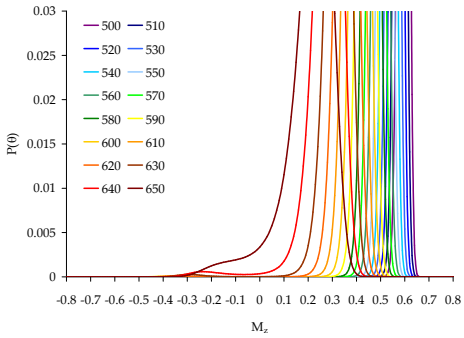

(c) Spin distribution for a 4.5nm x 5nm Grain.

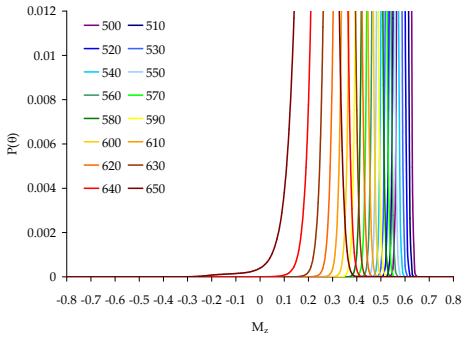

(d) Spin distribution for a 6nm x 5nm Grain.

Figure. 7.13: Spin distributions for different temperatures for 2nm (a), 3nm (b), 4.5nm (c), and 6nm(d) diameter grains in an external field of 0.8 Tesla along the positive z-direction.

appearance of the fundamental small volume limit of heat assisted magnetic reversal, since the equilibrium spin distribution no longer allows for reliable magnetic reversal. The spin distribution for the 2 nm diameter grains shows this effect clearly, with a significant probability of the macrospin aligning against the field direction, even for temperatures much less than the Curie temperature.

In order to assess the overall equilibrium temperature dependent reversal probability for different grain sizes, one can simply calculate the area under the spin distribution curve along the field direction. This would represent the reversal success rate if the grains were instantly cooled to zero from the equilibrium temperature, but gives an indication of the general reversal reliability for different grain sizes and also the minimum equilibration temperature (equating roughly to the temperature that the medium must be cooled through in an actual device). A plot of this reversal reliability as a function of temperature for a realistic head field of 0.8 Tesla is plotted in Figure. 7.14.

The plot shows that for 6 nm diameter grains, the reversal reliability converges to 100% very close to T_c, while the smaller grains converge at increasingly lower temperatures, requiring much longer cooling times. As evident from the equilibrium spin distribution, the 2 nm diameter grains never reach a 100%

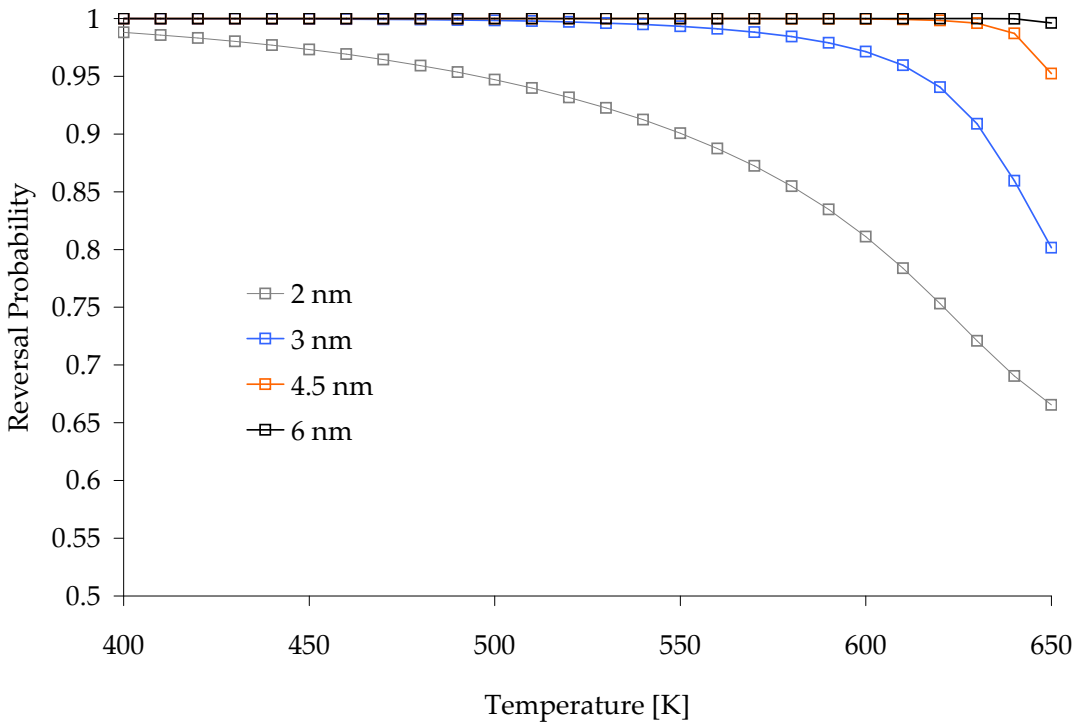

Figure. 7.14: Plot of the temperature dependence of the equilibrium reversal probability for 2 nm, 3 nm, 4.5 nm and 6 nm diameter FePt grains. The external field is set at 0.8 Tesla.

success rate due to their small volume. The question then remains, what is the limiting factor for the equilibration temperature for use in a functional device, since the data above show that ideally the equilibration temperature should be as low as possible? The solution comes from the concept of a time-dependent blocking temperature. The blocking temperature arises from the Arrhenius-Néel law, where the critical blocking temperature, T_B is given by:

$$T_B = \frac{\Delta F}{k_B \ln t f_o} \tag{7.7}$$

where ΔF is the free energy barrier between the easy and hard direction, k_B is the Boltzmann constant, and f_o is the attempt frequency. This expression associates a critical temperature to a given timescale. It should be noted that strictly this expression is valid only in the limit of $\Delta E \gg k_B T$, and so for the high temperatures there is likely some small error in the analytic calculation of the blocking temperature. The other point to note is the value of the "attempt frequency", f_o. Conventionally this is taken to be around 10^9 s^{-1}, whereas a more realistic value [83] for higher temperatures and lower volumes is around 10^{12} s^{-1}, and so this higher value is assumed for the following. In a functional device, the cooling time in a field is effectively limited to about 100 ps. Using the above expression for the blocking temperature, it is possible to find the minimum

allowable equilibration temperature for an equilibration time of 100 ps. In order to determine this minimum equilibration temperature, one must first calculate the energy barrier, ΔE.

Due to the applied field, there are in fact two energy barriers to reversal; the first being against the field direction, and the second being along the field direction. Due to the asymmetry in the applied field energy with respect to the magnetic easy axis, the energy barrier for the magnetisation to escape from lying against the field direction is the lower of the two. Since we are interested in the reversal probability, ie the probability of the magnetisation lying along the field direction, then it is this lower energy barrier that is the one of interest. However, there is a complication with this approach, in that the energy barrier, ΔE, is temperature and field dependent. A plot of the blocking temperature as a function of system temperature for different sized grains is shown in Figure. 7.15.

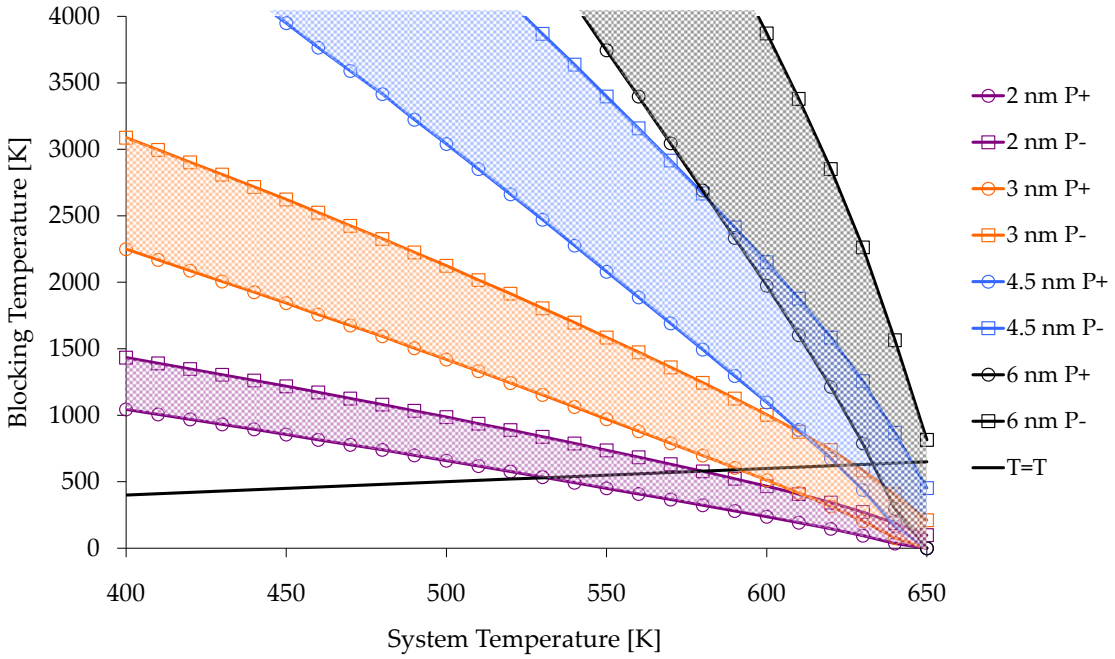

Figure. 7.15: Plot of the temperature dependence of the Blocking temperature for 2 nm, 3 nm, 4.5 nm and 6 nm diameter FePt grains. The external field is set at 0.8 Tesla.

The blocking temperatures for both energy barriers along (P-) and against (P+) the field direction. For zero field the two lines for each particle size are coincident, since the energy barriers are the same. Also plotted is the line for the equivalence of the blocking and system temperature, indicating the temperature at which the system goes from a blocked to non-blocked state. Clearly it is this temperature which is the actual blocking temperature, and, by comparison with the data in Figure. 7.14, one can see that for a reliable recording method the grain size is limited to sizes of 3 nm x 5nm or larger (assuming a 95% success rate is required),

which limits the use of HAMR for ultrahigh recording densities, at least with conventional granular recording media.

Finally the influence of the external field strength on the reversal probability will be addressed. For conventional recording, the increased strength of the applied field allows higher coercivity materials to be used for recording media. For HAMR, however, the effect is quite different, since the coercivity is independent of particle size provided the material remains single domain. The influence of increased field strength is to increase the bias of the minimum configuration energy along the field direction. This effect can partially alleviate the finite volume problem discussed above, where the thermal fluctuations allow the spin moment to escape the minimum energy state. A plot of the probability of the spin moment lying along the field direction at the field dependent blocking temperature as a function of applied field strength for different particle sizes is plotted in Figure. 7.16.

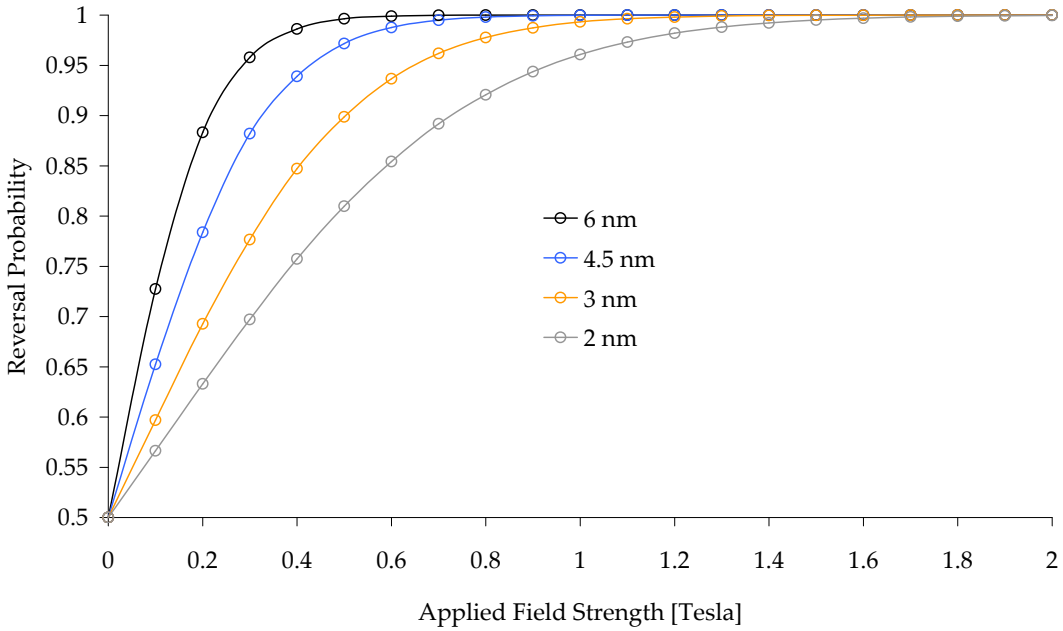

Figure. 7.16: Plot of the external field strength dependence of the equilibrium reversal probability for 2 nm, 3 nm, 4.5 nm and 6 nm diameter FePt grains at the blocking temperature.

As can be seen, for the intermediate grain sizes the influence of increasing the field is significant, suggesting that if write fields can be enhanced then HAMR can be used to write information to grains with a diameter as small as 3nm in diameter. For the 2 nm diameter grains the small volume means that even for very large fields the reversal probability remains below 100%.

In the next section the physics described here will be applied to an atomistic recording model for a data density of 1-2 TBit/in^2. Such a recording media

would utilise grains which are 3.5 nm in diameter, which is near the fundamental physical limit of heat assisted magnetic reversal.

7.4 The HAMR Recording Process

In a hypothetical future device which uses HAMR, the write process essentially involves a write head with an attached laser passing over a high density recording media. The laser heats the medium to near or above the Curie temperature and the write head records the magnetic information. A fast hard drive will spin up to 15000 rpm and so the speed of the medium relative to the head is around 50 ms^{-1}, or in more "atomic scale units" 0.05 nm/ps. Given that a typical bit length for 1 $\mathrm{Tbit/in}^2$ is $\sim$ 15 nm then a typical raw recording rate will be around 3 GBit/s.

Designing an Ultra High Density Recording Medium

A conventional perpendicular recording medium utilises a granular thin film material where the magnetic grains are separated by a non-magnetic padding material, such as a metal-oxide. This attempts to make each grain a largely separate magnetic entity which can be written independently of other grains. When a recording pass is made it is possible that a grain is not written as intended, usually due to undesired exchange coupling to nearby grains. To ensure that the written data can be read back reliably each data bit consists of 50-60 grains. Thus if a single grain is not written successfully there will still be many other grains with the correct magnetisation and thus give back a correct reading to the read head.

The media material for the HAMR process has two key requirements: it must have a high anisotropy energy, K_u, and also a relatively low Curie temperature, T_c. Candidate materials for HAMR are presently confined to rare earth / transition metal alloys such as FePt and CoPt. FePt with an $\mathrm{L1}_0$ crystal structure is an ideal candidate as it has a room temperature K_u of around 10^7 $\mathrm{J/m}^3$ and $T_c \sim$ 750K [37]. Creating the $\mathrm{L1}_0$ structure requires annealing at a high temperature for a number of hours. However, the annealing process has a tendency to destroy the granular nature of the medium and so obtaining all the desired parameters for a perfect recording medium is proving somewhat difficult in practice [92, 93, 94]. For the purposes of this study it is assumed that these technical limitations can be overcome. The magnetic modelling utilises a truncated FePt Hamiltonian as described in section 2.6, which incorporates the effects of anisotropic exchange coupling, which are important for modelling FePt realistically.

For realistic modelling of a recording media, a close approximation to the real granular structure is required. An illustration of how this is achieved is shown in Figure. 7.17.

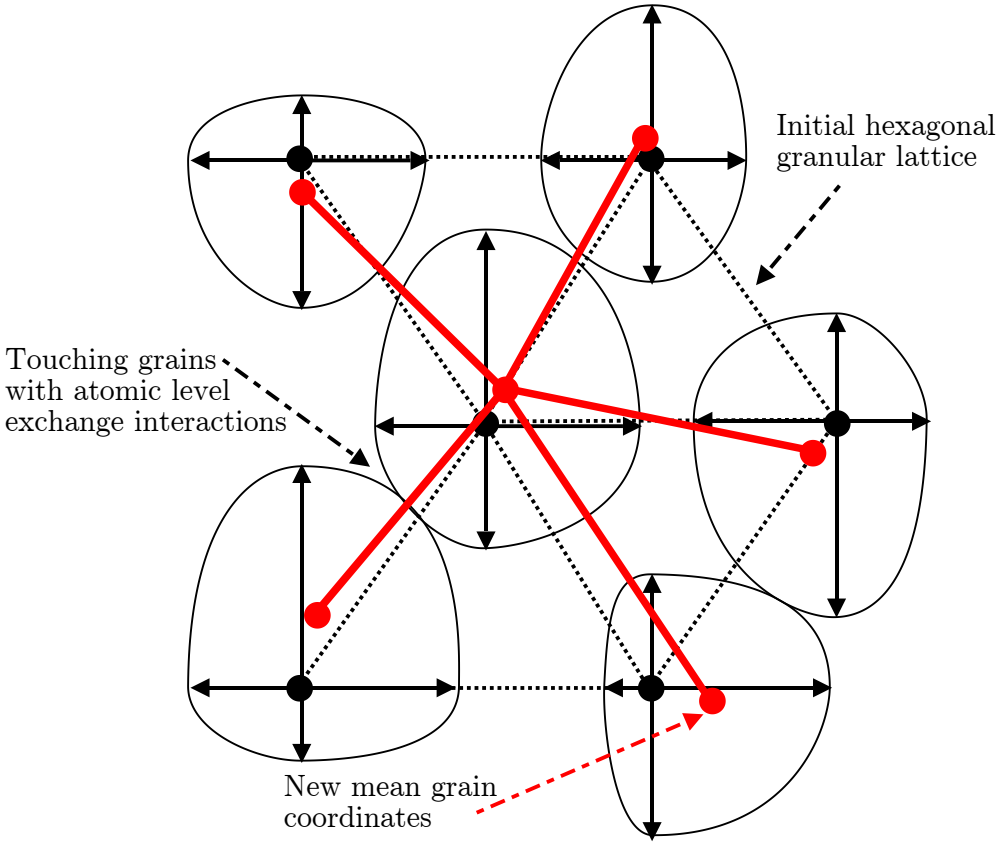

Figure. 7.17: Illustration of how the granular recording media is generated. The grain template starts with a hexagonal lattice which is then randomly extended as indicated by the arrows. These points are then connected by an ellipse to create the grain. The red dots indicate the new grain coordinates which are used to calculate the dipolar fields.

The atomic scale model of the medium is made by first making a large single crystal of the desired material (eg $L1_0$ FePt). A template is then used to identify a pseudo granular structure within the single crystal. The starting origin of each of the grains is fixed on a hexagonal lattice, shown by the black dots and dashed lines in the above figure. The starting points are separated by a distance just greater than the desired mean radius for the grains, in this case 1.9 nm. In order to randomise the shapes of the grains, an initial radius of 1.7 nm was chosen, added to which was a randomly chosen distance of $\pm$ 0.5 nm. The random part was added separately to the $+x, -x, +y, -y$ components of the radius, leading to four axes of different lengths, as shown by the black arrows in the figure. The four axes are then connected by an ellipse to form closed shapes. Since the shapes are randomly extended, their centre of mass has also moved. In order to accurately

simulate the dipolar fields, their new centre of mass positions are calculated as the origin for the macrospin magnetic moments, as indicated by the red dots. This leads to a random granular-type structure very similar in appearance to that used in a real recording media.

By repeating this process for each of the points on the original hexagonal lattice, a granular-type structure is generated. This template is superimposed onto the original atomic lattice structure. Atoms which fall within the grains are identified as the magnetic material, and those outside of the grains as packing atoms with no magnetic interactions. Due to the random nature of the generator, it is possible that some grains touch and interact magnetically. Figure. 7.18 shows a plot of the grain size distribution, with a mean grain diameter is 3.40 nm and a standard deviation of 0.28 nm taken from the raw data. The diameter of each particle is calculated by taking the mean of its four axial radii. A visualisation of the end result is inset in Figure. 7.18, where the light spheres indicate the non-magnetic packing atoms, while the dark spheres indicate the magnetic atoms.

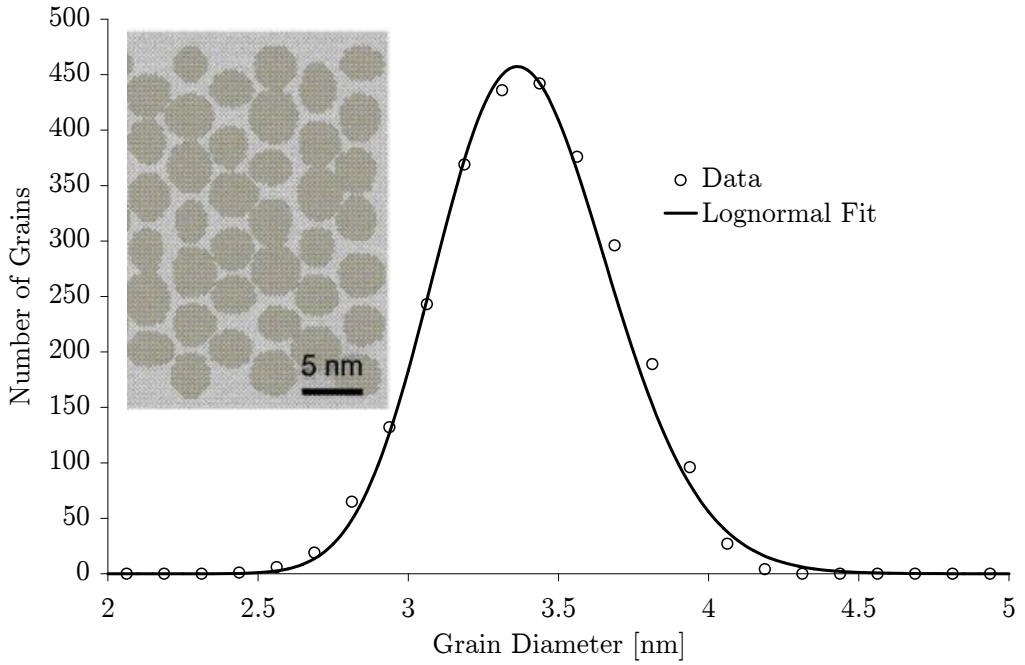

Figure. 7.18: Plot of number of grains vs grain diameter for atomic scale granular recording medium, showing a log normal fit to the data. Inset is a visualisation of an atomic scale granular recording medium for 1TBit/in^2

Hard Disk Write Head Design for HAMR

Modelling of hard disk write heads forms a significant area of physics in its own right [95, 96, 97]. An ideal write head would generate a strong, focused, uniform magnetic field around the field pole which can rapidly change its magnetic

state. Achieving all these characteristics is a continual technical challenge for increasingly large data densities. This model is primarily concerned with the response of the recording media during the HAMR process, and so an ideal head field was used to write the medium. The head was made to be wider than the recording track, so called optical-dominant recording. At the pole edges the field was assumed to decay rapidly with downtrack distance with a $\cos(x)$ profile.

Geometrical Considerations for Head Design for HAMR

Of critical importance for HAMR is the physical arrangement of the laser and field pole, because, on the timescale of the write process, the recording head moves very slowly. This means that there is a considerable lag between the centre of the heat spot and the write head crossing a fixed point on the recording medium. Consequently the temperature under the field pole is lower than the temperature in the centre of the heat spot, and thus grains can undergo substantial cooling during the write process. An optimal design is to place the laser as close as possible to the write field pole, but there are physical limitations to their proximity.

7.5 The Write Process for a Single 3.5nm Grain

The first step in calibrating the recording model for a particular grain size is to investigate the temperature dependence of the general properties of the magnetic grains, such as the magnetisation, and anisotropy energy. For small grain sizes finite size and surface effects can be particularly important, inducing a reduced Curie temperature or enhanced anisotropy, for example. Since we are primarily interested in the challenges in achieving an areal density of 1TBit/in^2, such a density would require 3.5 nm diameter grains (assuming 50 grains per bit and a packing fraction around 90% of that for a perfect hexagonal lattice). Note that this is slightly smaller than might be expected for such a data density, due to the necessity of the grains being isolated by a distance of at least 1-2 atomic radii. A visualisation of a single 3.5 nm cylindrical grain with a height of 5 nm is shown in Figure. 7.19.

Curie Temperature of a 3.5 nm FePt Grain

Determining the Curie temperature of a single grain is important for HAMR so that the laser can be calibrated to heat the medium precisely to the desired temperature. As before the truncated Hamiltonian described in Section 2.6 is used for the following calculations. A standard Monte Carlo metropolis

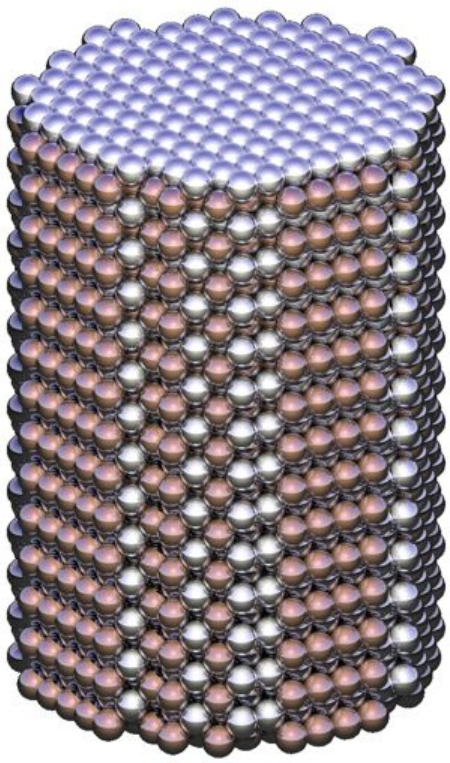

Figure. 7.19: Visualisation of a single 3.5 nm FePt grain showing the $L1_0$ crystal structure and irregular surface features. The light spheres indicate Fe sites, while the dark spheres indicate the Pt sites.

algorithm was used to calculate the equilibrium magnetisation as a function of temperature first by equilibrating the system at the desired temperature and then averaging over 20,000 Monte Carlo steps. A plot of the temperature dependence of the equilibrium magnetisation, M/M_s, is shown in Figure. 7.20. The curve is fitted to an *effective* critical exponent of $\beta = 0.488$ which is calculated from the ratio of core to surface atoms for surface and volume critical exponents. The surface critical exponent arises from the reduction in coordination number at the surface, inducing less critical behaviour in the temperature dependence of the magnetisation [44, 98, 99, 100].

The data show a significantly reduced Curie temperature of 645 K when compared to the bulk material T_c of 700 K, as well as a disordered magnetic tail due to the small system size.

The Influence of Surface Anisotropy on the Coercivity of a 3.5 nm FePt Grain

At such small grain sizes, surface effects can begin to dominate the magnetic properties. One such effect is that of surface anisotropy, which has been investigated in detail in Chapter 5. Although the effects of surface anisotropy can be many and varied, in the case of $L1_0$ FePt, the situation is considerably

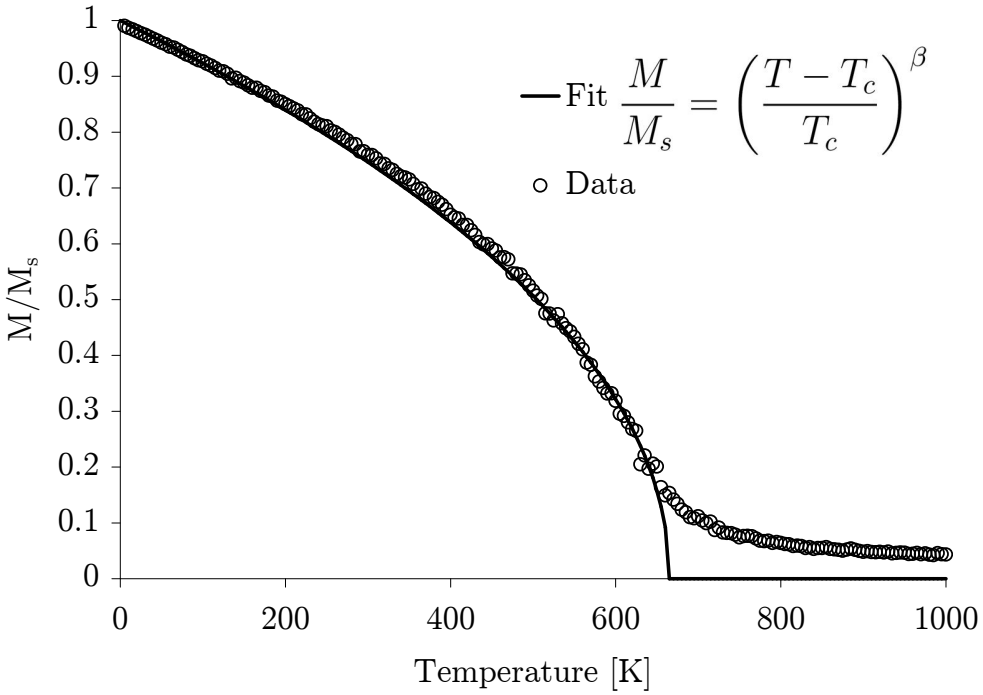

Figure. 7.20: Temperature dependence of the saturation magnetisation for a single 3.5 nm diameter FePt grain. A fit to the data shows a Curie temperature of 665 Kelvin, as well as persistent magnetic order above T_c.

simplified due to the layered crystal structure. This layered structure yields either an easy axis ($K_s < 0$) or easy plane ($K_s > 0$) anisotropy when taking into account the directional vector summation of local atoms within the Néel Model. For 3.5 nm grains, approximately 40% of atoms are on the surface.

The main difficulty with incorporating surface anisotropy within a model system is obtaining a realistic value for the magnitude of the surface anisotropy constant, K_s. The best source of information is from experimental data measuring surface anisotropy at thin film interfaces. A large amount of published data is available from such experiments and a typical value of K_s for an Fe-Ag interface is 0.64 ergs/cm^2, or in atomic-scale units 5.6×10^{-22} Joules/atom at 300 K [101, 102, 103]. The temperature dependence of the anisotropy energy is calculated using the Constrained Monte Carlo technique described in Section 6. Since the local Néel surface anisotropy for the particular structure of $L1_0$ FePt is uniaxial and spherically symmetric, the standard method of holding the macrospin moment at 45° to the z-axis and calculating the restoring torque is perfectly valid for determining the temperature dependence of the anisotropy. To ascertain the effect of the surface anisotropy on the coercivity, the anisotropy field of a single grain was calculated for both positive and negative signs of K_s. For comparison the anisotropy field was also calculated with no surface anisotropy

and also with no core anisotropy, leaving just the surface contributions, as shown in Figure. 7.21.

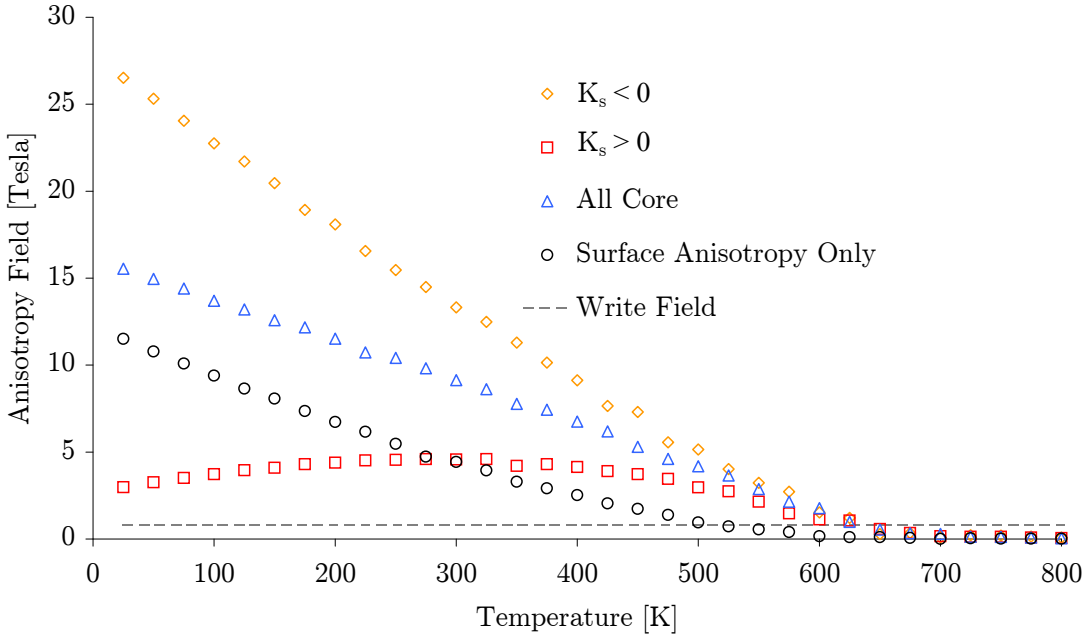

Figure. 7.21: Plot of anisotropy field vs temperature for 3.5 nm FePt grain for different signs of surface anisotropy constant. All core indicates the anisotropy field of the particle if no surface anisotropy is assumed, while the surface anisotropy only is the contribution from the surface to the anisotropy field with the bulk anisotropy deactivated.

In the case of $K_s < 0$, the surface and core anisotropy contributions are additive, giving rise to a zero temperature anisotropy field in excess of 26 Tesla. For the converse case, where $K_s > 0$, the anisotropy energies compete. This results in a strange situation where the anisotropy field initially increases with temperature and then decreases above 300 K. This is due to the stronger temperature dependence of a uniaxial single-ion anisotropy compared with the dominant two-ion anisotropy in FePt [37]. At low temperatures the surface and core anisotropies compete, thus giving a much lower anisotropy field. As the temperature is increased the surface anisotropy becomes weaker and the fractional core anisotropy contribution increases, thus increasing the coercivity. The stronger temperature dependence of the surface anisotropy is due to the fact that surface spins are less strongly exchange coupled and thus have a reduced effective Curie temperature. A distinct, somewhat accidental, benefit of surface anisotropy for HAMR, in the case of $K_s < 0$, is that, due to the stronger temperature dependence of surface anisotropy, the anisotropy field of the material near T_c is almost entirely dependent on the core anisotropy contribution, while at room temperature the anisotropy is enhanced by around

40% compared to bulk, leading to much improved thermal stability for long-term data storage.

Dynamic Effects for a Single Grain for Heat Assisted Writing

In order to create a working model of the HAMR process, parameters such as the time dependence of the temperature and applied field for a single grain first need to be calculated. These are solely determined by the specifics of the model - namely the laser power, thermal conductivities and the write head - laser separation. The temperature and field profiles for a single grain directly in the path of a continuous laser beam are shown in Figure. 7.22. The graph shows that initially, at time t= -2 ns, the temperature of the grain is at room temperature. The temperature then slowly increases as the laser approaches, reaching a maximum near t = 0 ns. As the laser passes over the grain the temperature begins to reduce. The temperature profile is asymmetric due to the write head blocking the laser, which leads to more rapid cooling while the write head passes over the grain. At t = 0.25 ns the write head passes overhead, attempting to orientate the grain during the cooling process. While the external field is acting on the grain, the temperature drops from T_{start} to T_{end}. After the write head has passed, the magnetisation direction of the grain is locked and gradually cools back to room temperature. The entire recording process occurs in a little over 2 nanoseconds due to the speed of the write head assembly.

In order to optimise the HAMR process the ideal temperature under the laser spot needs to be found to maximise the chances of successful reversal. As shown earlier the temperature ideally needs to be just above T_c when the external field from the write pole is overhead, so that the susceptibility is at a maximum, while the cooling rate needs to be sufficiently high so that the grain is in a highly stable magnetic state once the write pole has passed. These temperatures are primarily controlled by the laser power and thermal conductivity of the heatsink material, as described in Section 7.2.

Reversal of a Single Grain during Heat Assisted Writing

Putting all the elements described above together allows the investigation of the model parameters and their effect on the reversal of a single, isolated grain. Before moving to a full model with many grains, one would like to know how robust the reversal process is, which, as illustrated previously, is dependent on the cooling time, maximum temperature, field strength and particle volume. This is done by determining the write success rate by repeatedly performing the reversal on a single grain and counting the number of successful writes. The laser is initialised directly over the grain and then moved away at a speed of 10 ms^{-1}

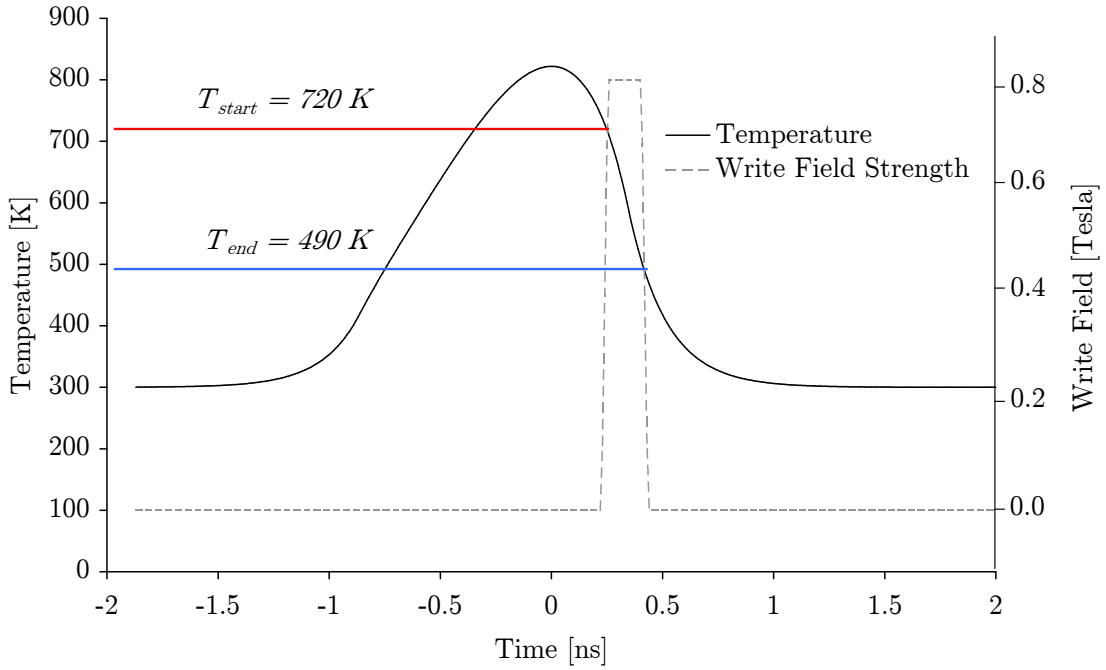

Figure. 7.22: Plot of temperature and external applied field against time for a single grain during HAMR. The temperature profile is asymmetric due to the write head blocking direct laser heating. The temperature of the grain when the write field is first overhead is indicated by the red line, while the temperature of the grain when the field leaves is given by the blue line.

as would occur in a typical device. The write head following the laser, with a field of 1 Tesla, then attempts to orientate the grain magnetisation in the opposite direction to the initial direction. Once the temperature of the grain has returned to room temperature (typically after a time of 1 ns), the laser is deactivated and reset above the grain and the simulation is repeated, but with a different sequence of random numbers for generating the random thermal field. A typical result for these simulations is plotted in Figure. 7.23, showing one of many successive demagnetisation events.

The z-component of magnetisation, indicated by the black line, shows the final recovery direction, in this case in the negative direction indicating a write success. The reversal mechanism is elliptical in nature, since a transverse component of the magnetisation exists at all times during the reversal process. Due to the small size of the grains, the thermal fluctuation of the grain magnetisation length is considerable. The overall write success rate for a single 3.5 nm x 5 nm grain was found to be at a maximum of 90 % for a maximum temperature of 830 K at the centre of the laser pulse. The maximum success rate of only 90% suggests that the use of 3.5 nm grain size is approaching the fundamental limits of conventional magnetic recording technology. This can certainly be avoided by using a stronger write field, or possibly achieving a longer cooling time with less aggressive

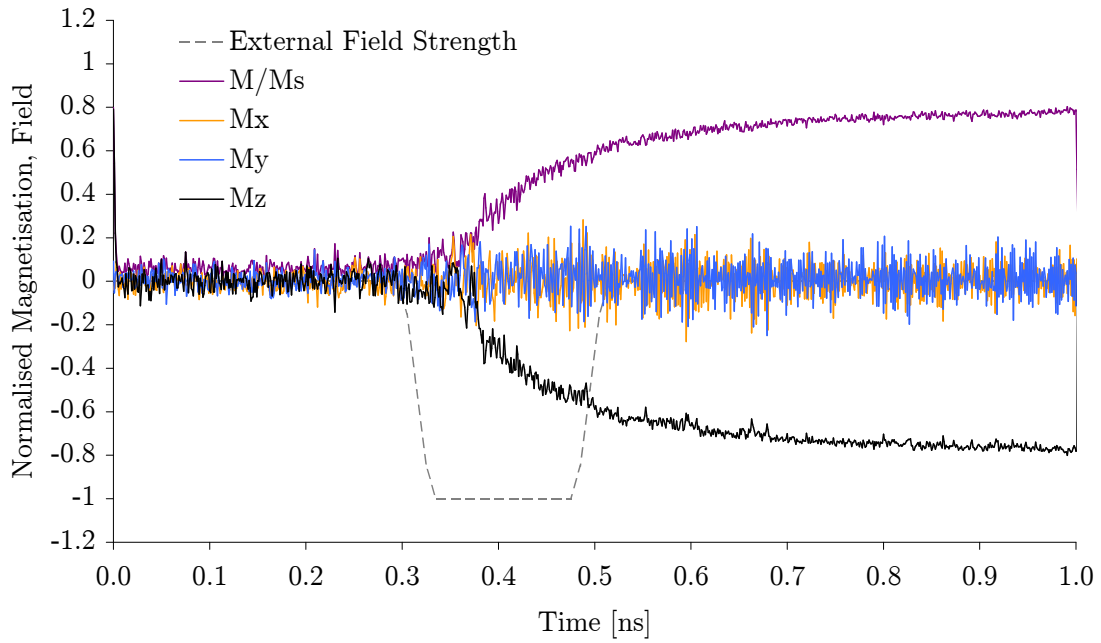

Figure. 7.23: Plot of time dependence of a single grain magnetisation during sequential HAMR. The grey line indicates when the external field from the write head is acting on the grain. The black line, indicating the z-component of the magnetisation, shows that for this particular simulation, the reversal process was successful.

heatsinks.

Nevertheless, the final section of this chapter will present the results for a write simulation for a collection of 120 interacting grains, to see what the final recorded data bits look like.

7.6 The Write Process for Media

Having determined the ideal simulation parameters for a single magnetic grain, a collection of grains can then be modelled to see the effects of inter-grain interactions in the form of exchange and dipolar fields. Exchange interactions between grains tend to reduce the sharpness of the bit edges leading to reading errors, while dipolar fields attempt to disorder the grains in a perpendicular field. These effects further complicate the HAMR process and so understanding their impact on the reliability of HAMR is essential. As mentioned before, the exchange interactions between grains are accounted for on the atomic scale by having touching grains. Another aspect of simulating a larger collection of grains is that the laser heating is in a Gaussian profile, and so a temperature gradient exists across the recording bit. As was demonstrated for the writing process for a single grain, the write success rate is strongly temperature dependent and

so assessing the impact of this temperature gradient on the multi-grain level is important for understanding the fundamental limits of HAMR.

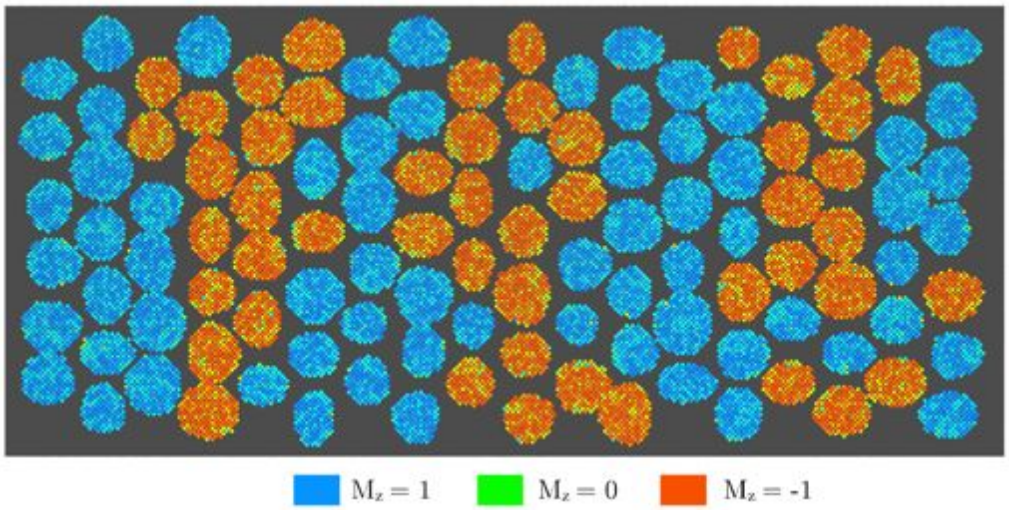

Figure. 7.24: Visualisation of the final magnetisation configuration after write simulation. Red colouring indicates spins in the -z direction, while blue indicates the opposite.

The full media recording model simulates the process of writing alternate bits to the recording media, bringing together all the elements described above. A single simulation involves a single pass of the laser and write head over the medium surface. The magnetic response is then recorded and exported as an image, showing the end configuration of the grains. A typical output is shown above in Figure. 7.24. Red colouring indicates a magnetisation in the negative z-direction, while blue colouring indicates a magnetisation in the opposite direction. Although the bit transitions are blurred, it is possible to discern the transitions. It is interesting to note that wherever grains touch they have the same final magnetisation direction, suggesting that due to the high anisotropy the inter-grain exchange coupling is very strong. Also it is clear that the effects of dipolar fields considerably worsens the write success rate when compared with a single grain.

Conclusions and the Future for HAMR

These simulations have identified some of the huge technical challenges involved with performing successful ultra-high density heat assisted magnetic recording.

The physics and thermodynamics of the reversal process have been investigated in some detail, showing the existence of different reversal modes. Simulations of heat assisted reversal have shown the existence of these modes for different

temperatures. The simulations have been extended through the numerical calculation of the Garanin free energy for a ferromagnet, showing the equilibrium properties of a magnetic system close to the Curie temperature. The analytical calculations show the emergence of a real thermodynamic limit to the heat assisted reversal process occurring for very small grain sizes. The small volume means that the energy barrier between magnetic states is reduced, and so thermal fluctuations prevent a totally reliable reversal process. This limit is very unlikely to be overcome by clever engineering and as such provides the ultimate limit for heat assisted magnetic recording.

Another limitation for heat assisted reversal is the cooling time in the field, which ideally should be as long as possible so that the system can reach equilibrium. This effectively precludes the use of ultra fast laser pulses on conventional recording media, since the pulse induces rapid heating and cooling processes. This effect relates to the blocking temperature, where for a given heating time the magnetisation is locked in a state. Practically this means that the material must be heated very close to T_c in order to see reversal, since it is at this point that the energy barriers become small enough to allow reversal in 100 ps.

Simulations of a single grain showed that the heat assisted reversal process exhibits a visible elliptical reversal mode at elevated temperatures. This aids in the transition between energy states over and above what is expected by the usual theories, which ultimately determines the maximum reversal success rate achievable. The interaction of multiple grains complicates the process of magnetic recording with HAMR but nevertheless illustrates that conventional recording with HAMR is feasible in the Tbit/in^2 regime.

These challenges can likely be overcome to a point with clever engineering and device fabrication improvements. However, the above simulations also outline the fundamental limits to magnetic recording, where moving a few atoms around can make the difference between a functional and non-functional device. At a density of 1-2 TBits/in^2 recording with a conventional granular medium begins to fail as a reliable statistical process, and other techniques such as magnetic random access memory (MRAM) or bit-patterned media (BPM) will be needed to achieve higher areal densities. Using BPM with 4 nm particles with 5 atoms separation between adjacent bits yields an ultimate recording density in the 30 Terabits/in^2 regime.

Conclusions

In this final chapter of the thesis, the results presented previously are summarised, drawing attention to the main conclusions and significant results. The final part then outlines future prospects for atomistic modelling of magnetic systems.

Effects of Structure of the Magnetic Properties of Nanoparticles

The effects of particle shape and structure on the magnetic properties of Co, CoAg, and Fe nanoparticles were investigated by using a combination of Molecular Dynamics and Atomistic magnetic calculations. The structural calculations utilised the Embedded Atom Method, a technique particularly well suited to modelling the structures of metals. Ab-initio calculations of the effective spin Hamiltonian for Co and Fe were used to accurately model the magnetic properties, taking into account any variations in interatomic separation.

The structural calculations revealed a common surface compression for all the particle types, arising from the reduction in coordination number at the surface. For the Co and Fe nanoparticles this compression was shown to cause an increase in the Curie temperature. The structural calculations also revealed that the addition of a monolayer silver coating to Co particles drastically altering the internal structure. The mixed hcp and fcc internal stacking was shown by the magnetic calculations to greatly enhance the anisotropy energy when compared with pure fcc cobalt nanoparticles. This provides a feasible alternative to the assumption that any increase in anisotropy in Co nanoparticles must be due to surface anisotropy.

Surface Anisotropy

Following on from the structural calculations of nanoparticles, the next chapter describes in detail some of the wide range of phenomena caused by surface anisotropy in nanoparticles. The effects of surface faceting, internal crystal structure, particle shape and particle size were all investigated. The surface anisotropy was modelled using the phenomenological Néel surface anisotropy model, and used in combination with the Lagrange Multiplier technique to perform constrained energy minimisation. In order to quantify the results, the effect of surface anisotropy on the energy barrier was determined in each case.

The first investigation was into the effects of nanoparticle shape on the energy barrier. This showed that for weak values of surface anisotropy the effects

were small, with little apparent change in the energy barrier. For very strong surface anisotropy the energy surface was shown to become cubic, arising from spin non-collinearities caused by the underlying crystal symmetry. Elongated particles exhibited very different behaviour, with the energy barrier changing dramatically for all strengths of surface anisotropy. The next part looked at the crystal structure dependence of the energy barrier for nanoparticles with surface anisotropy. This showed that increases in bulk coordination number reduced the strength of the effect of surface anisotropy, and in the case of an hexagonal lattice, six-fold symmetric energy surfaces are generated, illustrating the importance of the underlying crystal symmetry and spin non-collinearities.

The final section investigated the size dependence of the energy barrier and compared the results with published experimental measurements. This revealed that in order to have a consistent size-dependent effect caused by surface anisotropy, the particles must be elongated. A detailed analysis of simple elongated particles found an excellent correlation between the local on-site Néel anisotropy constant, and the macroscopic surface anisotropy energy density, when taking into account the size scaling of the energy barrier.

Constrained Monte Carlo Method

A new constrained Monte Carlo method has been developed, so that the temperature dependence of the magnetocrystalline anisotropy free energy can be easily calculated. The method works by the complementary movement of two random spins, such that the macroscopic magnetic moment of the system is constrained along the desired direction, while allowing it to vary freely in length.

The method has been tested by calculating the temperature dependence of uniaxial and cubic anisotropy energies and comparing the results with the accepted analytical Callen-Callen theory, with the simulations showing excellent agreement at low temperatures. The method was then used to perform the first calculations of the temperature dependence of the surface anisotropy for a thin film, showing that due to the uniaxial nature of the anisotropy, the surface anisotropy follows the surface magnetisation as $K_{\text{surface}} \sim M^3_{\text{surface}}$. The final calculations investigated the temperature dependence of the micromagnetic exchange constant using an atomistic approach. The calculations showed the micromagnetic exchange constant scaling with the system magnetisation as $A \sim M^{1.71}$, although the reason for this scaling behaviour is not known. Nevertheless the calculations give a good basis for micromagnetic simulations utilising a temperature dependent exchange stiffness.

Heat Assisted Magnetic Recording

The final chapter presented simulations of heat assisted magnetic reversal, investigating the magnetic reversal process near the Curie temperature for applications in future hard disk recording technologies. The first section shows that the magnetic reversal probability is highly temperature dependent due to the existence of elliptical and linear reversal mechanisms near and above T_c. Further simulations then showed that the reversal probability is also time dependent, where at constant temperature the system requires a certain amount of time to reach equilibrium. These ideas are then explored further with an analytical description for the angular dependence of the system energy taking into account the change in the magnitude of the magnetisation, allowing the calculation of the Boltzmann distribution for the system. The Boltzmann distributions reveal the volume dependence of the magnetic reversal probability in equilibrium, illustrating the fundamental thermodynamic limit for heat assisted magnetic reversal. The Boltzmann distributions are then related to a size, anisotropy, and field dependent blocking temperature which is then solved graphically. The blocking temperature is shown to reflect the best case condition for the magnetic reversal reliability for a dynamic system, which ultimately depends on the cooling time.

This understanding of the physics behind heat assisted reversal is then applied to a device-like simulation of a granular recording medium designed for a data density in the TBit/in^2 regime. The effect of surface anisotropy within such a system is assessed, and shows that it can potentially enhance the thermal stability. These simulations ultimately show that such a data density is theoretically feasible, provided fairly aggressive error correction methods can be employed.

Future Prospects

Although atomistic magnetic simulations have existed for decades, only recently has it been possible to perform large scale calculations on tens of thousands of spin moments. This thesis has shown how the atomistic simulations are capable of exhibiting a myriad of physical magnetic effects at the nanoscale, not seen with larger scale micromagnetic models. This improvement in the description of magnetic materials allows for a better understanding of magnetic behaviour at the nanoscale.

Nevertheless, a number of assumptions in the atomistic model have yet to be truly tested. The first, which has been touched on in this thesis, is the relationship between structural and magnetic properties. The original Heisenberg model

explicitly included the Coulomb potential, and so an improved atomistic model would include this directly into the Hamiltonian. The problem with this approach is that it then requires assumptions on the interatomic distance dependence of the exchange interactions and anisotropy energy, which is non-trivial for complex materials such as FePt. Another related assumption is the role of damping and thermal fluctuations within the LLG. Currently damping is included phenomenologically and the thermal fluctuations are included with an effective white noise thermal field. In principle both these effects are included within the Coulomb interaction, and so this forms an up and coming area of research.

As for the standard atomistic magnetic calculations, faster computers are enabling the simulation of much more complex and larger systems, such that it will be possible in the near future to model entire devices atomistically, such as a hard disk read and write element. Such models can aid the understanding of experimental results and guide the development of future magnetic technologies. The future prospects for the atomistic model are good, and with continued refinements will continue to provide an essential method to realise new technologies and nanomagnetic devices.

Publications and Presentations

Published Papers

"The influence of shape and structure on the Curie temperature of Fe and Co nanoparticles", R. Evans, U. Nowak, F. Dorfbauer, T. Shrefl, O. Mryasov, R. W. Chantrell, and G. Grochola, Journal of Applied Physics, **99**, 08G703 2006. Also selected for publication in the Virtual Journal of Nanoscience and Technology.

"Effects of surface anisotropy on the energy barrier in cobaltsilver coreshell nanoparticles", F. Dorfbauer, R. Evans, M. Kirschner, O. Chubykalo-Fesenko, R. Chantrell and T. Schrefl, Journal of Magnetism and Magnetic Materials, **316**, 2007, pp791794.

"The Effects of Surface Coating on the Structural and Magnetic Properties of CoAg Core-Shell Nanoparticles", Richard Evans, Florian Dorfbauer, Oleg Myrasov, Oksana Chubykalo-Fesenko, Thomas Schrefl and Roy Chantrell, IEEE Transactions on Magnetics, **43**, Issue 6, 2007, pp3106-3108.

"Effective anisotropies and energy barriers of magnetic nanoparticles with Néel surface anisotropy", R. Yanes , R. Evans, O. Chubykalo-Fesenko, H. Kachkachi, D. A. Garanin and R. W. Chantrell, Physical Review B **76**, 064416, 2007.

Papers under Preparation

"The Physics of Heat Assisted Magnetic Recording", R. F. L. Evans, N. Kazantseva, D. Hinzke, U. Nowak and R. W. Chantrell. To be submitted to Applied Physics Letters, (2008).

"Constrained Monte Carlo Simulation of the Temperature Dependence of Surface Anisotropy", P. Asselin, R. F. L. Evans, R. Yanes, O. Chubykalo-Fesenko, D. Hinzke, U. Nowak and R. W. Chantrell. To be submitted to Physical Review B, (2008).

"Atomistic Simulation of Heat Assisted Magnetic Recording for 1 TBit/in^2", R. F. L. Evans, D. Hinzke, U. Nowak and R. W. Chantrell. To be submitted to Physical Review B, (2008).

"Temperature Dependence of the Micromagnetic Exchange Stiffness", D. Hinzke, U. Atxia, R. F. L. Evans, P. Asselin, O. Chubykalo-Fesenko, O. Myrasov, U. Nowak and R. W. Chantrell. To be submitted to Physical Review B, (2008).

Conference Presentations

"The Influence of Shape and Structure on the Curie temperature of Fe and Co nanoparticles", Magnetism and Magnetic Materials Conference, November 2005, San Jose, California, USA.

"The Effect of The Surface on the Energy Barriers of Magnetic Nanoparticles as Multispin Systems", Joint IEEE Intermag and Magnetism and Magnetic Materials Conference, January 2007, Baltimore, Maryland, USA.

"The Effects of Surface Coating on the Structural and Magnetic Properties of CoAg Core-Shell Nanoparticles", Joint IEEE Intermag and Magnetism and Magnetic Materials Conference, January 2007, Baltimore, Maryland, USA.

Other Presentations

"Surface Anisotropy in Magnetic Nanoparticles", IEEE Magnetics Society Meeting, July 2006, University of Manchester, UK.

"Constrained Montecarlo Techniques and Applications", April 2007, Seagate Research, Pittsburgh, Pennsylvania, USA.

"Atomistic Modelling of Heat Assisted Magnetic Recording", York Magnetics Workshop, June 2008, University of York, UK.

Appendix I - Code Optimisation Techniques

A number of computational "tricks" and techniques have been discovered over the previous three years of my Doctoral studies, which combined have improved code performance by an order of magnitude compared with an un-optimised version. Although these methods are not directly relevant to the remainder of the thesis, they did aid in the computation of all the simulations. In order to summarise and explain these methods without being overly verbose, the appendix includes fragments of example code with a general description, rather than a large body of the computational code, which currently runs in excess of 10,000 lines. Some of these examples are limited to magnetic simulations, while others may well be applicable to other types of problem.

General Computational Techniques

The first section of the appendix addresses general computation methods, such as the normalisation of very small numbers, and optimising memory structure to give the best performance.

Value Normalisation

Generally the atomic scale model deals with numbers which, in everyday terms, are very small, typically being in the range 10^{-21} - 10^{-25}. This creates a problem for computational arithmetic since computers only possess a finite number of digits, which leads to rounding errors when dealing with small numbers. In order to minimise these problems, the parameters used in the model are usually normalised, either to the interatomic exchange energy, J_{ij}, or to the magnitude of the atomic spin moment, μ_s. In my code, all energies and fields are normalised to μ_s. This has the advantage that external fields are always in units of Tesla, enabling the easier extraction of key values such as the anisotropy field. The normalisation process ensures that computation is performed on numbers which are ~ 1, which ensures the best accuracy is conserved for the calculations.

Array Optimisation

The manner in which data is structured in a computational code can greatly affect its performance, so much so that the following improvement yielded an order of magnitude improvement in code runtime. Calculation of the interatomic

exchange energy often comprises a substantial fraction of computation time, due to the sum over a number of neighbouring atoms. A pre-computed neighbour list consisting of a list of atom numbers for each atom is used to identify which atoms are neighbours, and this is then used at runtime to calculate the exchange energy for atom i. A typical section of Fortran 90 code showing the declaration of arrays is given by:

```
1   integer        :: num_atoms
2   integer        :: num_neighbours
3   real(kind=dp)  :: J_ij ! Exchange constant
4
5   integer        :: neighbour_list(1:num_neighbours,1:num_atoms)
6   real(kind=dp)  :: atomic_spin_array(1:3,1:num_atoms)
7   real(kind=dp)  :: atomic_energy_array(1:num_atoms)
```

Here the number of atoms and neighbours, the exchange constant, and three arrays are declared: the first containing the neighbour list, the second containing the vector spin for each atom, and the final array for storing the total energy for the atom. For fully coordinated atoms this form of array structure is fine, however most particles of interest are not fully coordinated, and so an exception must be made for atoms which do not have the number of `num_neighbours`. Since the atom number starts at 1, null neighbours are given an atom number of zero. The standard code for calculating the exchange energy would then be given by:

```
8   integer        :: i,j ! do loop variables
9   real(kind=dp)  :: J_total
10
11  ! Loop over all atoms
12  do i=1,num_atoms
13     J_total = 0.0_dp
14
15     ! Loop over all neighbours
16     do j=1,num_neighbours
17        ! Check if neighbour exists
18        if(j/=0)then
19           ! Calculate exchange energy
20           J_total = J_total + &
21                     J_ij*dot_product(atomic_spin_array(:,i), &
22                     atomic_spin_array(:,neighbour_list(j,i)))
23        else
24           ! If atom is null then exit loop
25           exit
26        end if
27     end do
28
29     ! Store total energy
30     atomic_energy_array(i) = J_total
31  end do
```

Here, the code performs two loops, and calculates the exchange energy for each atom. Note that the `exit` statement at *25* assumes that the neighbour list is ordered so that null neighbours are at the end of the array for each atom. The `if` statement within the inner do loop causes a large performance hit, since the next

segment of code cannot be pipelined until it has been evaluated. Since the result of the `if` statement is known for all atoms prior to the execution of the loop, it is possible to avoid the if statement by pre-computing the number of neighbours each atom has and storing this in a neighbour number array, like so:

```
32    integer :: neighbour_number_array(1:num_atoms)
33    integer :: neighbour_counter
34
35    ! Loop over all atoms
36    do i=1,num_atoms
37       neighbour_counter = 0
38
39       ! Loop over all neighbours
40       do j=1,num_neighbours
41          ! Check if neighbour exists
42          if(j/=0)then
43             ! Add 1 to num_neighbours
44             neighbour_counter = neighbour_counter + 1
45          else
46             ! If atom is null then exit loop
47             exit
48          end if
49       end do
50
51       ! Store num_neighbours
52       neighbour_number_array(i) = neighbour_counter
53    end do
```

This loop is executed only once at the start of the program. This then allows a far more efficient form of the earlier code to be used for the calculation of the exchange energy, given by:

```
54    integer       :: i,j ! do loop variables
55    real(kind=dp) :: J_total
56
57    ! Loop over all atoms
58    do i=1,num_atoms
59       J_total = 0.0_dp
60
61       ! Loop over all existing neighbours
62       do j=1,neighbour_number_array(i)
63             ! Calculate exchange energy
64             J_total = J_total + &
65                       J_ij*dot_product(atomic_spin_array(:,i), &
66                       atomic_spin_array(:,neighbour_list(j,i)))
67       end do
68
69       ! Store total energy
70       atomic_energy_array(i) = J_total
71    end do
```

One further improvement can be made to this code, however, since there are still null neighbours stored in memory. This leads to wasted memory space, as well as a performance penalty due to the way CPU caches load data from main memory. The data comes from the main computer memory in blocks, constituting a cache line, the size of which is architecture dependent. Due to the way the data

is stored, this means that unneeded data is passed to the CPU cache. One way to resolve this issue is to re-order the neighbour list into a single dimension array. This uses a little extra memory as an index to the neighbour list is required, but it does mean that all data loaded to the cache is used, which improves performance by about 10% for a typical problem. The final code for this is given below.

```
72    integer :: total_neighbours
73    integer :: start_index
74    integer :: finish_index
75    integer :: alloc_stat
76    integer :: neighbour_counter
77
78    integer :: index_array(1:2,1:num_atoms) !1-start index
79                                            !2-finish index
80
81    integer, allocatable :: 1D_neighbour_list(:)
82
83    ! Calculate total number of neighbours
84    total_neighbours = 0
85    do i=1,num_atoms
86       total_neighbours = total_neighbours + &
87                          neighbour_number_array(i)
88    end do
89
90    ! Allocate 1D neighbour list
91    allocate(1D_neighbour_list(1:total_neighbours),stat=alloc_stat)
92    if(alloc_stat/=0)stop "Allocate␣1D␣neighbour␣list␣error"
93
94    ! Populate 1D neighbour list
95    neighbour_counter = 0
96    do i=1,num_atoms
97       start_index  = neighbour_counter + 1
98       do j=1,neighbour_number_array(i)
99          ! Store neighbour number in 1D list
100         1D_neighbour_list(neighbour_counter)=neighbour_list(j,i)
101         ! Increment neighbour counter
102         neighbour_counter = neighbour_counter + 1
103      end do
104      finish_index = neighbour_counter
105      ! Store indices in index array
106      index_array(1,i) = start_index
107      index_array(2,i) = finish index
108   end do
109
110   ! Calculate exchange energy
111   do i=1,num_atoms
112      J_total = 0.0_dp
113      ! Loop over atom index numbers
114      do j=index_array(1,i),index_array(2,i)
115            ! Calculate exchange energy
116            J_total = J_total + &
117                      J_ij*dot_product(atomic_spin_array(:,i), &
118                      atomic_spin_array(:,1D_neighbour_list(j)))
119      end do
120      ! Store total energy
121      atomic_energy_array(i) = J_total
122   end do
```

The same technique can be used to improve performance for conditional execution where the outcome can be precomputed, for example where atoms have different site-dependent anisotropies. Another example where such code is useful is for systems with variable exchange constants, by using the index array to precompute the on-site exchange energy.

Atomistic System Generation

An essential part of modelling nanoparticles at the atomic scale is generating particle structures with different shapes and crystal structures. Due to symmetry the best method for generating atomic structures is to use an integer lattice. As will be illustrated later, this also facilitates the use of a very rapid neighbour list generation algorithm. The common crystal structures found in nature are simple cubic (sc), face centred cubic (fcc), body centred cubic (bcc) and hexagonal close packed (hcp). All of these structures can be represented on an integer unit cell with two lattice positions along the y and z axes, and six lattice points along the x-axis, as shown below in Figure. A-1.

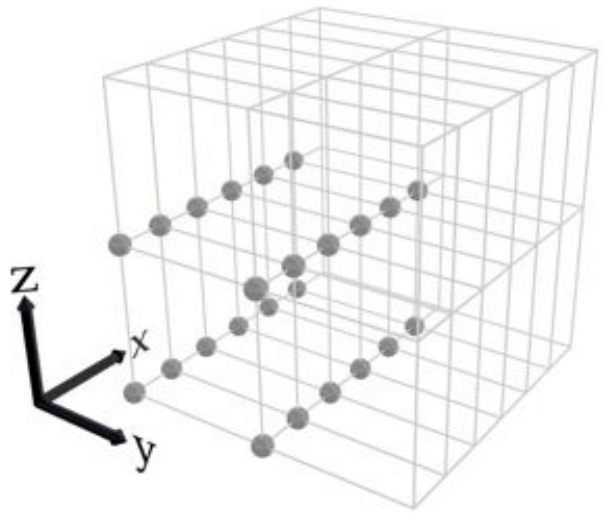

Figure. A-1: Visualisation of integer lattice construction. The grey spheres indicate possible atom positions within the unit cell.

The extra lattice points in the x-axis allow the creation of 111 oriented fcc and hcp lattice structures. A three dimensional integer array is declared which includes all the possible atomic positions. The dimensions of the array indicate the position in space, while the data it contains identifies whether an atom occupies that site. If the integer is set to zero then no atom exists at that site, otherwise the integer is the atom number, which is used later for generating the

usual atom list. The array can also be expanded to include other integer values which can be used to identify different atomic species or whether the atom is a surface atom, for example. An integer lattice for a $10 \times 10 \times 10$ unit cell array is coded as follows:

```
1   integer :: x_dim,y_dim,z_dim
2
3   integer, allocatable :: 3D_coord_array(:,:,:)
4
5   ! Set system dimensions
6   x_dim = 10
7   y_dim = 10
8   z_dim = 10
9
10  ! Allocate 3D coordinate array
11  allocate(3D_coord_array(-3*x_dim:3*x_dim, &
12                          -y_dim:y_dim, &
13                          -z_dim,z_dim),stat=alloc_stat)
14  if(alloc_stat/=0)stop "Allocate 3D coordinate array error"
15
16  ! Initialise array
17  3D_coord_array(:,:,:) = 0
```

The system is positioned at the centre of the coordinate system for convenience. As can be seen, the dimensions of the integer array reflect positions in pseudo-real space. The actual atomic coordinates are simply a multiple of the integer coordinate and a lattice constant. Once the desired size of coordinate array is allocated, it is initialised to zero. The next step is to populate the coordinate array with a non-zero integer, representing the positions of the atoms. The simplest case is that for a simple cubic lattice, since there is only a single atom per unit cell, as shown in Figure. A-2.

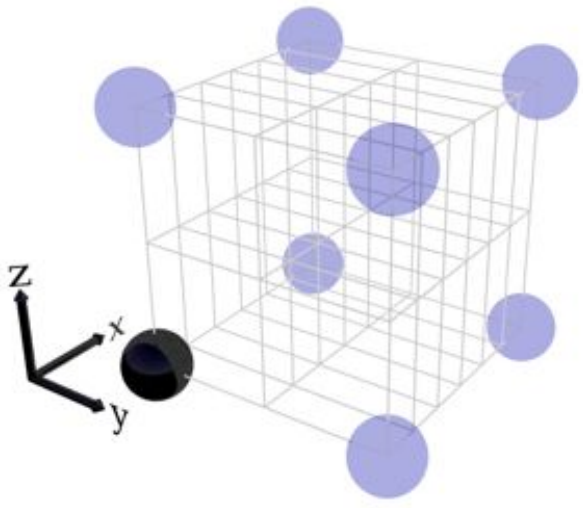

Figure. A-2: Visualisation of simple cubic lattice showing one atom per unit cell. The unit cell is then replicated in 3D space generating the crystal lattice.

The coordinate array is populated with atoms by performing a loop over the lattice sites as follows:

```
18    integer :: atom_number
19    integer :: i,j,k
20
21    atom_number = 1
22
23    do k=-z_dim-1,z_dim-1,2
24       do j=-y_dim-1,y_dim-1,2
25          do i=-x_dim-1,x_dim-1,6
26             3D_coord_array(i,j,k) = atom_number
27             atom_number = atom_number + 1
28          end do
29       end do
30    end do
```

The above code generates the simple cube lattice by taking different step lengths of unit cell length over the coordinate lattice, 2 in the case of y and z, and 6 in the case of the x-dimension. Note that this code also gives each atom a unique identifer which is used later to generate the atom and neighbour lists.

A similar code can be used to generate a 001 orientated fcc lattice, as shown in Figure. A-3.

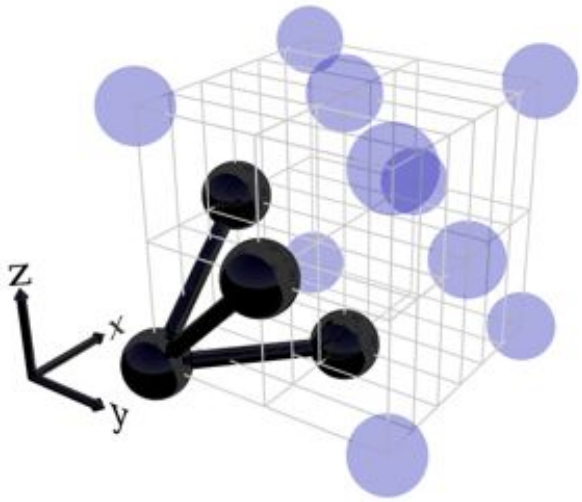

Figure. A-3: Visualisation of face centred cubic lattice with four atoms per unit cell.

The accompanying code to generate an fcc lattice is:

```
31    integer :: atom_number
32    integer :: i,j,k
33
34    atom_number = 1
35
36    do k=-z_dim-1,z_dim-1,2
37       do j=-y_dim-1,y_dim-1,2
38          do i=-x_dim-1,x_dim-1,6
39             3D_coord_array(i,j,k) = atom_number
```

```
40              3D_coord_array(i+3,j+1,k) = atom_number+1
41              3D_coord_array(i+3,j,k+1) = atom_number+2
42              3D_coord_array(i,j+1,k+1) = atom_number+3
43              atom_number = atom_number + 4
44           end do
45        end do
46     end do
```

Here there are four atoms added for each unit cell, and the `atom_number` is incremented accordingly, the *i,j* and *k* modifiers indicate the position of atoms within the unit cell.

The integer lattice method can also be used to generate hcp and 111 fcc lattices, although the physical lattice constant is compressed by a factor $\frac{1}{\sqrt{3}}$ along the *y*-direction and by $\frac{2\sqrt{2}}{3}$ along the *z*-direction. A visualisation of the hcp unit cell is shown in Figure. A-4, followed by the code used to generate the hcp lattice.

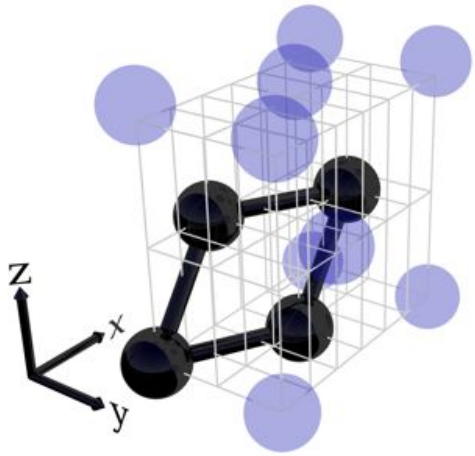

Figure. A-4: Visualisation of hexagonal close packed lattice showing the compressed *y* and *z* axes.

```
47     integer :: atom_number
48     integer :: i,j,k
49
50     atom_number = 1
51
52     do k=-z_dim-1,z_dim-1,2
53        do j=-y_dim-1,y_dim-1,2
54           do i=-x_dim-1,x_dim-1,6
55              3D_coord_array(i,j,k) = atom_number
56              3D_coord_array(i+3,j+1,k) = atom_number+1
57              3D_coord_array(i+2,j,k+1) = atom_number+2
58              3D_coord_array(i+5,j+1,k+1) = atom_number+3
59              atom_number = atom_number + 4
60           end do
61        end do
62     end do
```

Having generated the lattice, the integer coordinates are stored in an atom list, so that the atomic positions can be referenced directly.

Fast Neighbour List Method

Given a particular atomic arrangement, it is necessary to determine which atoms are interacting by creating a so-called "neighbour list". The use of the integer coordinate system described above makes the generation of the neighbour list very efficient, since the locations of the neighbours are stored in a three dimensional coordinate system. This method thus avoids the need to determine the neighbour separation distance which is the usual method for the identification of nearby atoms as neighbours. A typical code segment for calculation of the neighbour list for a simple cubic atomic structure is given by:

```
1   integer :: atom_number
2   integer :: i,j,k
3   integer :: ir !Interaction range
4   integer :: my_coords(1:3)
5   integer :: n_neighbours = 6
6   integer :: nn_counter
7
8   integer :: atom_coord_array(1:3,1:num_atoms)
9   integer :: neighbour_list_array(1:n_neighbours,1:num_atoms)
10
11  ! Set interaction range
12  ir = 2
13
14  do atom_number =1,num_atoms
15     ! Store atom local coordinates
16     my_coords(:) = atom_coord_array(:,atom_number)
17
18     nn_counter = 0
19
20     !loop over all possible neighbour sites in range
21     do k=my_coords(3)-ir,my_coords(3)+ir
22        do j=my_coords(2)-ir,my_coords(2)+ir
23           do i=my_coords(1)-ir*3,my_coords(1)+ir*3
24              ! Check that ir not exceeded
25              if((i*i+j*j+k*k)<ir*ir+1)then
26                 ! Check that atom exists
27                 if(3D_coord_array(i,j,k)/=0)then
28                 nn_counter = nn_counter + 1
29
30                 neighbour_list_array(nn_counter,atom_number) &
31                 = 3D_coord_array(i,j,k)
32                 end if
33              end if
34           end do
35        end do
36     end do
37  end do
```

This method is particularly fast since the inner loops are all very small compared with the size of the system. This means that the neighbour list for

over a million atoms can be generated in less than a second, which is hundreds of times faster than explicitly calculating the distance between all atoms. The above code is also quite general and for correctly tuned interaction range can be used for any crystal structure. Periodic boundary conditions can also be implemented by “wrapping round” the integer arrays to see if an atom is in range.

References

[1] http://www.research.ibm.com.

[2] D. Weller and A. Moser. Thermal effect limits in ultrahigh-density magnetic recording. *Magnetics, IEEE Transactions on*, 35(6):4423–4439, Nov 1999.

[3] H. N. Russell and F. A. Saunders. New Regularities in the Spectra of the Alkaline Earths. *J. Astrophys*, 61:38, January 1925.

[4] W. Heisenberg. Zur theorie des ferromagnetismus. *Z. Phys*, 49:619, 1928.

[5] P. Weiss. Temperature-variation of ferromagnetism. *Compt. Rend*, 143:1136, 1906.

[6] P. Weiss. Hypothesis of the molecular field and ferromagnetism. *J. Phys*, 6:661, 1907.

[7] E. C. Stoner and E. P. Wohlfarth. A mechanism of magnetic hysteresis in heterogeneous alloys. *Phil. Trans. Roy. Soc*, A240:599, 1948.

[8] R. W. Chantrell, K. O'Grady, A. Bradbury, S. W. Charles, and N. Hopkins. The isothermal remanent magnetisation of particulate media. *IEEE Trans. Mag.*, 23:204, 1987.

[9] S. Arrhénius. *Z. Phys. Chem., Lpz*, 4:226, 1889.

[10] L. Néel. *Ann. Geophys.*, 5:99, 1949.

[11] C. P. Bean and J. D. Livingston. Superparamagnetism. *Journal of Applied Physics*, 30(4):S120–S129, 1959.

[12] S. Okamoto, N. Kikuchi, O. Kitakami, T. Miyazaki, Y. Shimada, and K. Fukamichi. Chemical-order-dependent magnetic anisotropy and exchange stiffness constant of fept (001) epitaxial films. *Phys. Rev. B*, 66(2):024413, Jul 2002.

[13] S.H. Charap, Pu-Ling Lu, and Yanjun He. Thermal stability of recorded information at high densities. *IEEE Transactions on Magnetics*, 33(1):978–983, Jan 1997.

[14] W. F. Brown. *Micromagnetics*. Wiley, New York, 1963.

[15] A. Aharoni. *Introduction to the Theory of Ferromagnetism*. Oxford University Press, Oxford, 1996.

[16] Hinzke D. Chantrell R. W. Kazantseva, N. and U. Nowak. Linear and elliptical magnetization reversal close to the Curie temperature. *Submitted to PRL*, 2008.

[17] W. Heitler and F. London. *Z. Phys.*, 44:455, 1927.

[18] W. Gerlach and O. Stern. *Ann. Physik.*, 74:673, 1924.

[19] E. C. Stoner. *Phil. Mag.*, 15:1080, 1933.

[20] M. A. I. Nahid and T. Suzuki. The possible origin of large magnetic anisotropy of Fe_3Pt alloy thin films. *Journal of Applied Physics*, 97:307–+, May 2005.

[21] L. D. Landau and E. M. Lifshitz. Theory of the dispersion of magnetic permeability in ferromagnetic bodies. *Phys. Z. Sowietunion*, 8:153, 1935.

[22] T.L. Gilbert. *Physical Review*, 100:1243, 1955.

[23] F. Dorfbauer. *Simulation of Structure and Magnetic Properties of Nanoclusters*. Diploma Thesis, Institute for Solid State Physics, Vienna University of Technology, 2006.

[24] M. L. Schneider, Th. Gerrits, A. B. Kos, and T. J. Silva. Gyromagnetic damping and the role of spin-wave generation in pulsed inductive microwave magnetometry. *Applied Physics Letters*, 87(7):072509, 2005.

[25] W. F. Brown Jr. *IEEE Trans. Mag.*, 15:1196, 1979.

[26] Peter Jung, Alexander Neiman, Muhammad K N Afghan, Suhita Nadkarni, and Ghanim Ullah. Thermal activation by power-limited coloured noise. *New Journal of Physics*, 7:17, 2005.

[27] Bruno Grossmann and Denis G. Rancourt. Simulation of magnetovolume effects in ferromagnets by a combined molecular dynamics and monte carlo approach. *Phys. Rev. B*, 54(17):12294–12301, Nov 1996.

[28] U. Nowak. Thermally activated reversal in magnetic nanostructures. *Annual Review of Computational Physics IX, ed. by D. Stauer (World Scientific, Singapore 2001) p. 105*, 2001.

[29] William Fuller Brown. Thermal fluctuations of a single-domain particle. *Phys. Rev.*, 130(5):1677–1686, Jun 1963.

[30] Metropolis, N. and Ulam, S. The Monte Carlo Method. *Journal of the American Statistical Association*, 44(247):335–341, sep 1949.

[31] C.P. Robert and G. Casella. *Monte Carlo Statistical Methods (Second Edition)*. Springer-Verlag, New York, 2004.

[32] John S. Thomsen. Logical Relations among the Principles of Statistical Mechanics and Thermodynamics. *Phys. Rev.*, 91(5):1263–1266, Sep 1953.

[33] G. Marsaglia. Choosing a Point from the Surface of a Sphere. *Ann. Math. Stat.*, 43:645–646, 1972.

[34] K Binder. Applications of monte carlo methods to statistical physics. *Reports on Progress in Physics*, 60(5):487–559, 1997.

[35] O. Hjortstam, J. Trygg, J. M. Wills, B. Johansson, and O. Eriksson. Calculated spin and orbital moments in the surfaces of the 3*d* metals Fe, Co, and Ni and their overlayers on Cu(001). *Phys. Rev. B*, 53(14):9204–9213, Apr 1996.

[36] T. J. Klemmer, N. Shukla, C. Liu, X. W. Wu, E. B. Svedberg, O. Mryasov, R. W. Chantrell, D. Weller, M. Tanase, and D. E. Laughlin. Structural studies of $L1_0$ FePt nanoparticles. *Applied Physics Letters*, 81(12):2220–2222, 2002.

[37] O. N. Mryasov, U. Nowak, K. Y. Kushen Ko, and R. W. Chantrell. Temperature-dependent magnetic properties of FePt: Effective spin Hamiltonian model. *Europhys.Lett.*, 69:805–811, 2005.

[38] S.W. Yuan and H.N. Bertram. Fast adaptive algorithms for micromagnetics. *IEEE Transactions on Magnetics*, 28(5):2031–2036, 1992.

[39] D. Hinzke, U. Nowak, R. W. Chantrell, and O. N. Mryasov. Orientation and temperature dependence of domain wall properties in FePt. *Applied Physics Letters*, 90(8):082507, 2007.

[40] A. Iserles. *A First Course in the Numerical Analysis of Differential Equations*. Cambridge University Press, Cambridge, 1996.

[41] José Luis García-Palacios and Francisco J. Lázaro. Langevin-dynamics study of the dynamical properties of small magnetic particles. *Phys. Rev. B*, 58(22):14937–14958, Dec 1998.

[42] P. E. Kloeden and E. Platen. *Numerical Solution of Stochastic Differential Equations*. Springer, Heidelberg, Berlin, 1995.

[43] Makoto Matsumoto and Takuji Nishimura. Mersenne twister: a 623-dimensionally equidistributed uniform pseudo-random number generator. *ACM Trans. Model. Comput. Simul.*, 8(1):3–30, 1998.

[44] K. Binder and P. C. Hohenberg. Surface effects on magnetic phase transitions. *Phys. Rev. B*, 9(5):2194–2214, Mar 1974.

[45] J E Lennard-Jones. Cohesion. *Proceedings of the Physical Society*, 43(5):461–482, 1931.

[46] Murray S. Daw and M. I. Baskes. Embedded-atom method: Derivation and application to impurities, surfaces, and other defects in metals. *Phys. Rev. B*, 29(12):6443–6453, Jun 1984.

[47] X.W. Zhou, H.N.G. Wadley, R.A. Johnson, D.J. Larson, N. Tabat, A. Cerezo, A.K. Petford-Long, G.D.W. Smith, P.H. Clifton, R.L. Martens, and T.F. Kelly. *Acta. Mater.*, 49(19):4005–4015, 2001.

[48] A computer simulation method for the calculation of equilibrium constants for the formation of physical clusters of molecules: Application to small water clusters.

[49] D. J. Evans and B. L. Holian. The Nose-Hoover thermostat. *J. Chem. Phys.*, 83:4069–4074, October 1985.

[50] M. Pajda, J. Kudrnovský, I. Turek, V. Drchal, and P. Bruno. Ab initio calculations of exchange interactions, spin-wave stiffness constants, and curie temperatures of fe, co, and ni. *Phys. Rev. B*, 64(17):174402, Oct 2001.

[51] P. Entel A. V. Postnikov and J.M. Soler. Density functional simulation of small Fe nanoparticles. *Eur. Phys. J. D*, 25:261–270, 2003.

[52] K. Binder et al. *Monte Carlo Methods in Statistical Physics*. Springer-Verlag, Berlin, 1979.

[53] M. E. McHenry, S. A. Majetich, J. O. Artman, M. DeGraef, and S. W. Staley. Superparamagnetism in carbon-coated Co particles produced by the Kratschmer carbon arc process. *Phys. Rev. B*, 49(16):11358–11363, Apr 1994.

[54] S Muller K Heinz and L Hammer. Crystallography of ultrathin iron, cobalt and nickel films grown epitaxially on copper. *Journal of Physics: Condensed Matter*, 11(48):9437–9454, 1999.

[55] Robert Morel, Ariel Brenac, Celine Portemont, Thierry Deutsch, and Lucien Notin. Magnetic anisotropy in icosahedral cobalt clusters. *Journal of Magnetism and Magnetic Materials*, 308(2):296–304, January 2007.

[56] F. Dorfbauer, T. Schrefl, M. Kirschner, G. Hrkac, D. Suess, O. Ertl, and J. Fidler. Nanostructure calculation of CoAg core-shell clusters. volume 99, page 08G706. AIP, 2006.

[57] Matthieu Jamet, Wolfgang Wernsdorfer, Christophe Thirion, Véronique Dupuis, Patrice Mélinon, Alain Pérez, and Dominique Mailly. Magnetic anisotropy in single clusters. *Phys. Rev. B*, 69(2):024401, Jan 2004.

[58] C. Chappert and P. Bruno. Magnetic anisotropy in metallic ultrathin films and related experiments on cobalt films (invited). *Journal of Applied Physics*, 64(10):5736–5741, 1988.

[59] D. Weller, S. F. Alvarado, W. Gudat, K. Schröder, and M. Campagna. Observation of Surface-Enhanced Magnetic Order and Magnetic Surface Reconstruction on Gd(0001). *Phys. Rev. Lett.*, 54(14):1555–1558, Apr 1985.

[60] P. Gambardella, S. Rusponi, M. Veronese, S. S. Dhesi, C. Grazioli, A. Dallmeyer, I. Cabria, R. Zeller, P. H. Dederichs, K. Kern, C. Carbone, and H. Brune. Giant Magnetic Anisotropy of Single Cobalt Atoms and Nanoparticles. *Science*, 300(5622):1130–1133, 2003.

[61] B. Lazarovits, L. Szunyogh, and P. Weinberger. Fully relativistic calculation of magnetic properties of Fe, Co, and Ni adclusters on Ag(100). *Phys. Rev. B*, 65(10):104441, Mar 2002.

[62] D A Eastham and I W Kirkman. Highly enhanced orbital magnetism on cobalt cluster surfaces. *Journal of Physics: Condensed Matter*, 12(31):L525–L532, 2000.

[63] H. Kachkachi and H. Mahboub. Surface anisotropy in nanomagnets: transverse or Néel? *Journal of Magnetism and Magnetic Materials*, 278(3):334–341, 2004.

[64] D. A. Garanin and H. Kachkachi. Surface Contribution to the Anisotropy of Magnetic Nanoparticles. *Phys. Rev. Lett.*, 90(6):065504, Feb 2003.

[65] R. Yanes, O. Chubykalo-Fesenko, H. Kachkachi, D. A. Garanin, R. Evans, and R. W. Chantrell. Effective anisotropies and energy barriers of magnetic nanoparticles with n[e-acute]el surface anisotropy. *Physical Review B (Condensed Matter and Materials Physics)*, 76(6):064416, 2007.

[66] F. Bødker, S. Mørup, and S. Linderoth. Surface effects in metallic iron nanoparticles. *Phys. Rev. Lett.*, 72(2):282–285, Jan 1994.

[67] Chen Chen, Osamu Kitakami, and Yutaka Shimada. Particle size effects and surface anisotropy in Fe-based granular films. *Journal of Applied Physics*, 84(4):2184–2188, 1998.

[68] H. B. Callen and E. Callen. The present status of the temperature dependence of magnetocrystalline anisotropy, and the l(l+1)/2 power law. *Journal of Physics and Chemistry of Solids*, 27(8):1271–1285, 1966.

[69] H. Anton. *Calculus: A New Horizon, 6th ed.* Wiley, New York, 1999 pp 324-327.

[70] George B. Arfken and Hans J. Weber. *Mathematical Methods For Physicists*. Academic Press, 6 edition, June 2005.

[71] P. Bruno. *Physical Origins and Theoretical Models of Magnetic Anisotropy*, volume 24:1-28. IFF-Frienkurs, Forschungszentrum Jlich, 1993.

[72] A. Dinia, N. Persat, and H. Danan. Temperature induced perpendicular magnetic anisotropy in Co/Cu/Co trilayers. *Journal of Applied Physics*, 84(10):5668–5672, 1998.

[73] G. Andre, A. Aspelmeier, B. Schulz, M. Farle, and K. Baberschke. Temperature dependence of surface and volume anisotropy in Gd/W(110). *Surface Science*, 326(3):275–284, 1995.

[74] Á. Buruzs, P. Weinberger, L. Szunyogh, L. Udvardi, P. I. Chleboun, A. M. Fischer, and J. B. Staunton. Ab initio theory of temperature dependence of magnetic anisotropy in layered systems: Applications to thin Co films on Cu(100). *Physical Review B (Condensed Matter and Materials Physics)*, 76(6):064417, 2007.

[75] P. Asselin, R. Evans, D. Hinzke, U. Nowak, and R. W. Chantrell. Study of exchange scaling laws using an atomistic approach. *In preparation for submission to Appl. Phys. Lett.*, 2008.

[76] http://www.samsung.com/global/business/hdd/.

[77] T.W. McDaniel. Ultimate Limits to Thermally Assisted Magnetic Recording. *J. Phys.: Condens. Matter*, 17:R315–332, 2005.

[78] William Fuller Brown. Thermal Fluctuations of a Single-Domain Particle. *Phys. Rev.*, 130(5):1677–1686, Jun 1963.

[79] J.R. Hoinville. Micromagnetic modeling of the thermomagnetic recording process. *IEEE Transactions on Magnetics*, 37:1254–1256, 2001.

[80] E.D. Boerner, O. Chubykalo-Fesenko, O.N. Mryasov, R.W. Chantrell, and O. Heinonen. Moving toward an atomistic reader model. *IEEE Transactions on Magnetics*, 41:936–940, 2005.

[81] U. Nowak, O. N. Mryasov, R. Wieser, K. Guslienko, and R. W. Chantrell. Spin dynamics of magnetic nanoparticles: Beyond Brown's theory. *Physical Review B (Condensed Matter and Materials Physics)*, 72(17):172410, 2005.

[82] D. A. Garanin. Fokker-Planck and Landau-Lifshitz-Bloch equations for classical ferromagnets. *Phys. Rev. B*, 55(5):3050–3057, Feb 1997.

[83] D.A. Garanin and O. Chubykalo-Fesenko. Thermal fluctuations and longitudinal relaxation of single-domain magnetic particles at elevated temperatures. *Physics Review B*, 70(21):212409–+, December 2004.

[84] U. Atxitia, O. Chubykalo-Fesenko, N. Kazantseva, D. Hinzke, U. Nowak, and R. W. Chantrell. Micromagnetic modeling of laser-induced magnetization dynamics using the Landau-Lifshitz-Bloch equation. *Applied Physics Letters*, 91(23):232507, 2007.

[85] M.I. Kaganov, I.M. Lifshitz, and L.V. Tanatarov. *J. Exptl. Theor. Phys. (USSR)*, 31:232, 1957.

[86] S.I. Anisimov, B.L. Kapeliovich, and T.L. Perel'man. *Sov. Phys. JTEP*, 39:375, 1974.

[87] G. L. Eesley. Generation of nonequilibrium electron and lattice temperatures in copper by picosecond laser pulses. *Phys. Rev. B*, 33(4):2144–2151, Feb 1986.

[88] B. Rethfeld, A. Kaiser, M. Vicanek, and G. Simon. Ultrafast dynamics of nonequilibrium electrons in metals under femtosecond laser irradiation. *Phys. Rev. B*, 65(21):214303, May 2002.

[89] S.S. Ghai, W.T. Kim, C.H. Amon, and M.S. Jhon. A novel heat transfer model and its application to information storage systems. *J. Appl. Phys.*, 97:703–705, 2005.

[90] Natalia Kazantseva. *Thesis*. PhD thesis, University of York, UK, 2008.

[91] N. Kazantseva, D. Hinzke, U. Nowak, R. W. Chantrell, U. Atxitia, and O. Chubykalo-Fesenko. Towards multiscale modeling of magnetic

materials: Simulations of fept. *Physical Review B (Condensed Matter and Materials Physics)*, 77(18):184428, 2008.

[92] H. Zeng, S. Sun, R.L. Sandstrom, and Murray. C.B. Chemical ordering of FePt nanoparticle self-assemblies by rapid thermal annealing. *Journal of Magnetism and Magnetic Materials*, 266:227–232, 2003.

[93] Y.J. Tang, J.F. Aubuchon, L.H. Chen, S. Jin, J.W. Kim, Y.H. Kim, and C.S. Yoon. Fabrication and magnetic properties of nanopatterned FePt media. *Journal of Applied Physics*, 99:909, April 2006.

[94] S. Bae, K. Shin, J. Jeong, and J. Kim. Feasibility of FePt longitudinal recording media for ultrahigh density recording. *J. Appl. Phys.*, 87:6953–6955, 2000.

[95] L. Abelmann, S.K. Khizroev, D. Litvinov, J.G. Zhu, J.A. Bain, M.H. Kryder, K. Ramstöck, and C. Lodder. Micromagnetic simulation of an ultrasmall single-pole perpendicular write head. *Journal of Applied Physics*, 87:6636–6638, May 2000.

[96] S. Batra, J.D. Hannay, Zhou Hong, and J.S. Goldberg. Investigations of perpendicular write head design for 1 Tb/in^2. *IEEE Transactions on Magnetics*, 40:319–325, 2004.

[97] J. van Ek, M. Plumer, Zhou Hong, and H.N. Bertram. Micromagnetic recording model of pole-tip saturation effects. *IEEE Transactions on Magnetics*, 36:3975–3983, 2000.

[98] C. S. Arnold and D. P. Pappas. Gd(0001): A Semi-Infinite Three-Dimensional Heisenberg Ferromagnet with Ordinary Surface Transition. *Phys. Rev. Lett.*, 85(24):5202–5205, Dec 2000.

[99] K. D. Sorge, J. R. Thompson, A. Meldrum, T. E. Haynes, S. P. Withrow, J. D. Budai, C. W. White, and L. A. Boatner. High Temperature Magnetic Properties of FePt Nanoparticles Formed by Ion Implantation. *APS Meeting Abstracts*, pages 15005–+, March 2002.

[100] D. P. Landau and K. Binder. Surface and size effects in magnetic phase transitions (invited). *Journal of Applied Physics*, 63(8):3077–3081, 1988.

[101] K. B. Urquhart, B. Heinrich, J. F. Cochran, A. S. Arrott, and K. Myrtle. Ferromagnetic resonance in ultrahigh vacuum of bcc Fe(001) films grown on Ag(001). *Journal of Applied Physics*, 64(10):5334–5336, 1988.

[102] S. T. Purcell, B. Heinrich, and A. S. Arrott. Perpendicular anisotropy at the (001) surface of bulk Fe single crystals. *Journal of Applied Physics*, 64(10):5337–5339, 1988.

[103] F J A den Broeder M T Johnson, P J H Bloemen and J J de Vries. Magnetic anisotropy in metallic multilayers. *Reports on Progress in Physics*, 59(11):1409–1458, 1996.